Durham E-Theses

Beyond the Standard Model through the Higgs Portal

RO, GUNNAR,OYVIND,ISAKSSON

How to cite:

RO, GUNNAR,OYVIND,ISAKSSON (2016) *Beyond the Standard Model through the Higgs Portal*, Durham theses, Durham University. Available at Durham E-Theses Online: http://etheses.dur.ac.uk/11392/

Use policy

Beyond the Standard Model through the Higgs Portal

Gunnar Ro

A thesis presented for the degree of
Doctor of Philosophy

Institute for Particle Physics Phenomenology
Department of Physics
University of Durham
England

October 2015

Beyond the Standard Model through the Higgs Portal

Gunnar Ro

Submitted for the degree of Doctor of Philosophy
October 2015

Abstract

In this thesis, we will investigate the collider phenomenology and cosmological consequences of extensions of the Standard Model (SM) with hidden sectors coupled to the SM via a Higgs portal coupling. We will explore how models with classical scale invariance, where all mass scales are dynamically generated, can address the shortcomings of the SM without destabilising the Higgs mass. The matter-antimatter asymmetry in the Universe and the tiny masses of active neutrinos are addressed in a $U(1)_{B-L}$ extension of the SM with GeV scale right-handed neutrinos. We then investigate a range of models with both Abelian and non-Abelian gauge groups in the hidden sector to show how we can stabilise the Higgs potential and at the same time provide phenomenologically viable dark matter candidates where all scales in the theory have a common origin.

For non-Abelian gauge groups in the hidden sector, we also show that hidden magnetic monopoles can make up a significant fraction of dark matter. The dark matter in this model, which consists of both magnetic monopoles and gauge bosons, has long-range self-interactions which could explain the too-big-to-fail-problem at small scales in the standard cold dark matter scenario. We then study the collider phenomenology of hidden sector models with dark matter candidates through a simplified model framework both at the LHC and at a future 100 TeV collider.

Hidden sector extensions of the SM with a Higgs portal coupling give a rich and predictive model building framework for BSM physics without introducing a large hierarchy of scales.

Declaration

The work in this thesis is based on research carried out at the Institute for Particle Physics Phenomenology, Department of Physics, Durham University, England. No part of this thesis has been submitted elsewhere for any other degree or qualification and it is all my own work unless referenced to the contrary in the text. Chapter 2 is based on work appearing in [1, 2]. Chapter 3 is based on research reported in [1] and Chapter 4 is based on [2]. The text of Chapter 5 is based on work appearing in [3] and Chapter 6 is based on [4]. All these papers were published with Valentin V Khoze, [2] was also written in collaboration with Christopher McCabe and [4] with Michael Spannowsky.

Acknowledgements

Contents

List of Figures

List of Tables

Chapter 1

Introduction

The Standard Model (SM) of particle physics is currently our best description of the fundamental constituents of matter and the forces between them. In this chapter we will provide a short introduction to the theory of the Standard Model together with some of its experimental success. Then we will present the main arguments for why we need to go beyond the Standard Model to explain observed phenomena such as dark matter and the matter-antimatter asymmetry in the Universe.

1.1 The Standard Model

1.1.1 Introduction to the Standard Model

The Standard Model of particle physics is a quantum field theory with a $\mathrm{SU}(3) \times \mathrm{SU}(2) \times \mathrm{U}(1)$ gauge group and a particle content as seen in Table 1.1. The gauge group and the quantum numbers of the particles together determine the forces between the particles. The quantum numbers for the particles in the SM can be seen in Table 1.2. The particles consist of fermions and bosons with half integer and integer spin, respectively. The fermions are divided into quarks, which are charged under the $\mathrm{SU}(3)$ chromodynamic force, and leptons which are not. Both leptons and baryons come in three families, which are successively heavier copies of particles with the same gauge quantum numbers. Each gauge group has corresponding gauge bosons that mediate the forces. In addition to all of the fermions and gauge bosons, there

is one fundamental scalar field in the theory, the Higgs field. The SM Lagrangian, which describes the interactions between all the particles, is schematically given by

$$\mathcal{L} = -\frac{1}{4}F^{\mu\nu}F_{\mu\nu} + i\overline{\psi}\slashed{D}\psi + \overline{\psi}_i y_{ij}\psi_j H + |D^\mu H|^2 + m_h^2 H^\dagger H - \lambda \left(H^\dagger H\right)^2 + h.c. \quad (1.1.1)$$

$F^{\mu\nu}$ is the field strength tensor for each of the three gauge groups. The first term describes the kinetic term for the gauge fields and the self-interactions of the two non-Abelian fields. The second term is the kinetic and gauge interaction term for the fermions, ψ. H is the Higgs scalar field, and the last three terms give the kinetic term and potential for it. The remaining term, which is an interaction between the scalar field and the fermions, is a Yukawa term.

The Lagrangian above is very simplified with all flavour and gauge indices suppressed, and all the gauge interactions hidden in the covariant derivatives D_μ. The covariant derivative is schematically given by

$$D_\mu \psi = \left(\partial_\mu - \sum_{\text{gauge groups}} igA_\mu^i t^i, \right)\psi, \quad (1.1.2)$$

where A_μ^i is a gauge field and t^i is the generator of the gauge group corresponding to the representation of the matter field, which can be read of from Table 1.2.

The Strongly Coupled Sector

Quantum Chromodynamics (QCD) is the gauge theory based on the SU(3) gauge group. Since there are eight generators of the gauge group, QCD has eight gauge bosons called gluons. The gluons can interact with themselves and have both three and four-point vertices since SU(3) is a non-Abelian gauge group. There are six fermions charged under the strong force, the six quarks. They come in two different types, the up-type and the down-type. These types have different electroweak charges, but have the same SU(3) quantum numbers. The quarks are in the fundamental representation of SU(3), so they come in three different colours. At low energy it is impossible to observe free quarks or gluons since QCD is confining: the QCD force becomes so strong that it binds the quarks into composite colour-neutral baryons and mesons. The proton and neutron are baryons made out of three quarks, all of different colour, making the bound state colour neutral. Mesons are made out

	Quarks			Leptons		
Particle	Mass	Q	Particle	Mass	Q
Up quark u	2.3 MeV	$+2/3$	Electron e	0.511 MeV	-1
Charm quark c	1.3 GeV	$+2/3$	Muon μ	106 MeV	-1
Top quark t	173 GeV	$+2/3$	Tau τ	1.7 GeV	-1
Down quark d	4.8 MeV	$-1/3$	Electron neutrino ν_e	< 2.2 eV	0
Strange quark s	95 MeV	$-1/3$	Muon neutrino ν_μ	< 0.17 MeV	0
Bottom quark b	4.2 GeV	$-1/3$	Tau neutrino ν_τ	< 15.5 MeV	0

	Bosons	
Particle	Mass	Q
Higgs boson h	125 GeV	0
Photon γ	0	0
Gluons g	0	0
W bosons $W^\pm$	80.4 GeV	± 1
Z boson Z	91.2 GeV	0

Table 1.1: Mass and electric charge, Q, for the particles in the Standard Model

of a quark and an anti-quark of the same colour, making it colour neutral. There is a whole variety of different mesons and baryons with the lightest being the pion. Confinement is also the reason why QCD is not directly visible in the macroscopic world as a long-distance force. QCD is responsible for holding the nuclei of atoms together, but through the exchange of pions rather than gluons. Since pions have a mass of around 100 MeV the range of the strong nuclear force is about $10\ \text{GeV}^{-1} \approx 1$ fm.

We can explore quarks and gluons experimentally because of asymptotic freedom. At high energy the strong force becomes weaker, and free coloured particles can exist. The strength of a gauge force is determined by the gauge coupling constant, g, in the covariant derivative 1.1.2. When g becomes large, we get confinement and non-perturbative processes, while a small g leads to perturbative behaviour. Due to the particle content in QCD, the evolution of g with energy, as seen in Figure 1.2, is

Field	SU(3)	SU(2)	U(1)$_Y$	U(1)$_{\text{EM}}$
$L_L = \begin{pmatrix} \nu_L \\ l_L \end{pmatrix}$	1	2	-1	0 -1
$Q_L = \begin{pmatrix} u_L \\ d_L \end{pmatrix}$	3	2	1/3	2/3 $-1/3$
l_R	1	1	-2	-1
u_R	3	1	4/3	2/3
d_R	3	1	-2/3	$-1/3$
$H = \begin{pmatrix} \phi \\ h \end{pmatrix}$	1	2	1/2	1 0

Table 1.2: Quantum numbers for the fields of the SM. L and Q are lepton and quark doublets and $l = e, \mu, \tau$, $u = u, c, t$ and $d = d, s, b$.

such that g is large at small energies and decreases at large energies.

The Electroweak Sector

In the electroweak sector we have a product of two gauge groups SU(2)×U(1). Only the left-handed fields are charged under the SU(2) part of the gauge group, making the theory chiral. Both the quarks and the leptons are charged under the electroweak gauge groups as seen in Table 1.2. All the left-handed fields are organised into SU(2) doublets; the quark doublets have one up-type and one down-type left-handed field, while the lepton doublets include one electron-like particle and one neutrino. The Higgs field is a complex scalar doublet charged under the electroweak gauge groups. Since there is only one long range force in addition to gravity in the macroscopic world, the electro-magnetic force, the gauge bosons of the SU(2) part of the electroweak force either have to confine at low energies or be massive. As we see from Table 1.1, the $W^\pm$ and Z bosons have masses in the $80 - 90$ GeV range which leads to a very short range force. An unbroken gauge theory requires massless gauge bosons. Therefore, the electroweak symmetry has to be broken to account for the massive W and Z bosons.

The breaking of the electroweak symmetry is due to the Brout-Englert-Higgs-mechanism [6–8]. Without it, we would not have any heavy gauge bosons or masses for the fermions of the Standard Model. Due to the chiral nature of the SU(2) gauge group, fermion mass terms that couple left and right-handed fields are not gauge-invariant, and are therefore forbidden. The Higgs field is introduced to break the electroweak symmetry and to give masses to fermions and gauge bosons.

As a simple example, we first consider a theory with a U(1) gauge symmetry and a single complex scalar $\Phi = \frac{1}{\sqrt{2}}(\phi_1 + i\phi_2)$. The Lagrangian is given by

$$\mathcal{L} = -\frac{1}{4}F^{\mu\nu}F_{\mu\nu} + |D^\mu\Phi|^2 - V(\Phi), \, V(\Phi) = -m^2\Phi^\dagger\Phi + \lambda\left(\Phi^\dagger\Phi\right)^2. \qquad (1.1.3)$$

The Lagrangian is fully gauge invariant with a covariant derivative $D_\mu = \partial_\mu + igA_\mu$. We can see that the mass-term is negative which would indicate that the scalar field is a Tachyon. To resolve this, we need to expand the Lagrangian around the true vacuum state of the theory. First we find the vacuum

$$\frac{dV(\Phi)}{d\Phi} = 0 \rightarrow \langle\Phi\rangle^2 = \frac{m^2}{\lambda} = v. \qquad (1.1.4)$$

As Φ is a complex scalar field and the vacuum condition only sets the length of Φ, we can choose $\langle\Phi\rangle$ to be real with no imaginary part. We then expand the Lagrangian around the true vacuum $\phi_1 \rightarrow \phi_1 + v$,

$$\mathcal{L} \supset \frac{1}{2}m^2\phi_1^2 + \frac{1}{2}(\partial_\mu\phi_1)^2 + \frac{1}{2}(\partial_\mu\phi_2)^2 + \frac{g^2v^2}{2}A_\mu A^\mu + \sqrt{2}g\langle\Phi\rangle A_\mu\partial^\mu\phi_2. \qquad (1.1.5)$$

This leads to a massive ϕ_1, a massless ϕ_2 and a massive vector boson with mass $m_\gamma = g\langle\Phi\rangle$. A massive vector boson has three degrees of freedom while a massless one only has two. The third degree of freedom of the gauge boson is provided by the massless Goldstone boson ϕ_2. The shifted Lagrangian has an interaction term between the gauge field and the Goldstone boson. We can remove this term and write the Lagrangian in a more canonical form by performing a gauge transformation to the unitary gauge.

$$\mathcal{L} = \frac{1}{2}m^2\phi_1^2 + \frac{1}{2}(\partial_\mu\phi_1)^2 - \frac{1}{4}F^{\mu\nu}F_{\mu\nu} + \frac{g^2v^2}{2}A_\mu A^\mu - V(\phi_1). \qquad (1.1.6)$$

Here we clearly see that there is one massive scalar field, one massive gauge field and no Tachyon.

The Higgs mechanism for a general gauge group works as follows: in the theory we have a scalar field, ϕ, which acquires a vacuum expectation value (vev), $\langle\phi\rangle$, charged under a gauge group with generators t^a. Depending on $\langle\phi\rangle$, the gauge group might be completely broken, as in the U(1) example above, or a sub-group can remain unbroken. All the generators that leave the vacuum invariant

$$t^a\langle\phi\rangle = 0 \qquad (1.1.7)$$

remain unbroken. After the symmetry breaking, the Lagrangian will develop a mass term for the gauge bosons with a mass matrix given by

$$m_{ab}^2 = g^2(t_a\langle\phi\rangle)\cdot(t_b\langle\phi\rangle). \qquad (1.1.8)$$

We can see that the gauge bosons corresponding to the unbroken generators remain massless, and we get one massive gauge boson and one Goldstone mode per broken generator. As before, the third degree of freedom of each gauge bosons is given by the corresponding Goldstone mode. The effect of spontaneous symmetry breaking is therefore that it brakes the original group down to a potentially trivial subgroup where we get as many massive gauge bosons as broken generators and one remaining neutral massive scalar degree of freedom, which in the SM is the Higgs boson. For a given theory, the scalar potential, $V(\phi)$, determines the vacuum state, $\langle\phi\rangle$, which then determines the pattern of the symmetry breaking. Therefore, different potentials can break a gauge group in different ways.

In the Standard Model the SU(2)×U(1) gauge group is broken down to the electro-magnetic (EM) U(1). SU(2)×U(1) has four generators, three from the SU(2) part and one from the U(1) part. We choose the vacuum state to be electrically neutral such that the generator for the EM U(1) is unbroken. Since we then have three broken generators, we get three massive gauge bosons. The original Higgs doublet was a complex SU(2) doublet which had four degrees of freedom: three of these become Goldstone modes, while the last becomes the observable neutral Higgs boson. It is slightly more complicated in the SM since the neutral SU(2) gauge boson W_μ^0 and the hyper-charge boson B_μ will mix and give rise to the Z boson and the photon γ.

The massless fermions in the SM also gain masses by the Higgs mechanism. The Yukawa interactions in the SM Lagrangian provide a mass term for the fermions when $h \to h + v$, as follows

$$\overline{\psi}_i y_{ij} \psi_j H \to \overline{\psi}_i \frac{y_{ij}}{\sqrt{2}} \psi_j v + \overline{\psi}_i \frac{y_{ij}}{\sqrt{2}} \psi_j h. \tag{1.1.9}$$

The fermion mass is then given by $m_f = \frac{y_f}{\sqrt{2}} v$. The Higgs mechanism is the final ingredient to make the SM a phenomenologically viable theory. We have a short-range weak force due the spontaneous symmetry breaking of the electroweak sector, a short-range strong force due to confinement, a long-range electro-magnetic force due to the unbroken U(1) and massive fermions with masses given by their Yukawa couplings to the Higgs field. We will now move on to look at some of the experimental successes of the SM.

1.1.2 Overview of Experimental Successes

The Standard Model has been extensively tested experimentally over the last 40 years. It can successfully explain all the collider data we have observed so far. The discoveries of the $W^\pm$ [9] and Z bosons [10] at UA1 and UA2 at CERN in 1983 and the gluon at DESY in 1979 [11–14] firmly established the Standard Model as a gauge theory with non-Abelian gauge groups. With the discovery of the top quark in 1995 at Fermilab [15], the three-family fermion sector was completely discovered. The one missing piece of the SM matter content, the Higgs Boson, was finally discovered at the LHC in 2012 by the ATLAS and CMS experiments with a mass of about 125 GeV [16, 17].

In addition to discovering the particle content of the Standard Model, we can test the model by measuring and predicting the results of countless collider experiments. Since the SM only has 19 free parameters which have now all been measured, we can make predictions for all collider experiments. There have been no measurements that deviate significantly (at more than 5σ confidence) from the SM prediction. As one can see from the latest measurements from CMS in Figure 1.1, the agreement between observation and prediction is remarkably good over many orders of magnitude in production cross-section.
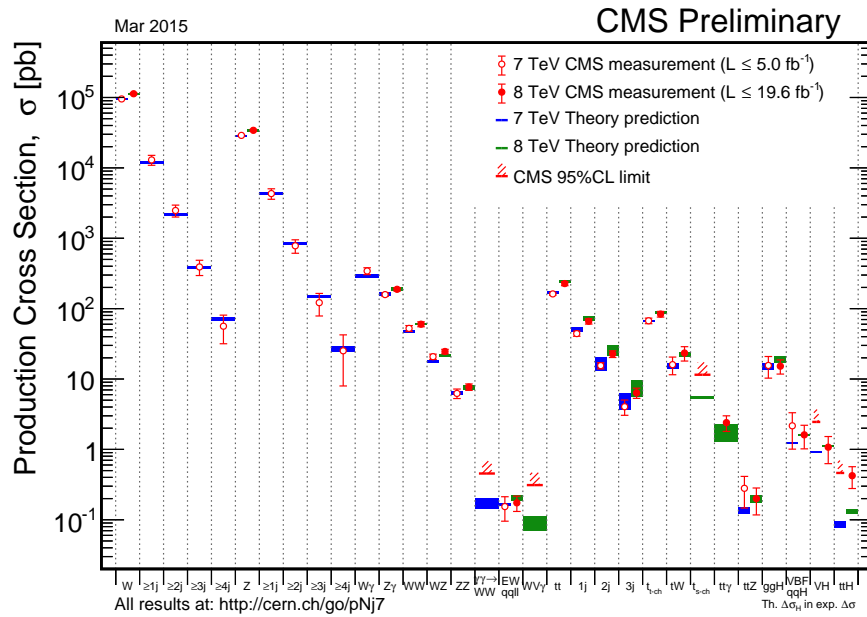
Figure 1.1: Production cross-section for different final states measured at the CMS experiment at the LHC with SM predictions.

This agreement between experiment and theory extends to all aspects of collider physics. In many cases, calculations at multi-loop level are required to achieve a good agreement, as, for example, in the magnetic dipole moment of the electron. One of the most spectacular tests of loop-level calculations comes from the running of the coupling constants with energy. At leading order the coupling constants would not run with energy, but at higher orders they do. One example of the agreement between the calculated and observed running [18] of the strong coupling constant α_s can be seen in Figure 1.2.

1.2   Beyond the Standard Model

Even though the Standard Model is extremely successful and in agreement with all collider experiments, there are many questions it cannot answer. These questions include both observational phenomena that cannot be accommodated in the SM and unanswered theoretical questions. In this section, we will investigate these short-comings of the SM to see what they can tell us about physics Beyond the Standard Model (BSM). First we will consider some of the main observational evidence for
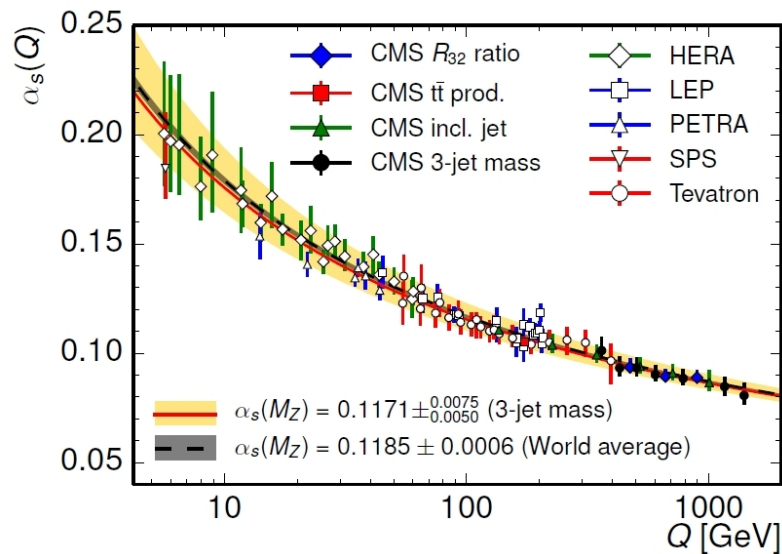
Figure 1.2: The observed and theoretical running of the strong coupling constant α_s.

BSM physics from dark matter, matter-antimatter asymmetry and the stability of the Higgs potential. We will then focus on the hierarchy or naturalness problem. There are many other open questions which we will not cover in any detail. These include why there are three generation of fermions, why a large mass hierarchy of fermions exists, the small neutrino masses, the strong CP-problem and, not least, how to combine the SM with gravity.

1.2.1 Dark Matter

In 1933 Zwicky [19] used the the measured velocity of stars in the Coma galaxy cluster to calculate the mass of the cluster. He discovered that the mass was around 400 times larger than the mass of the luminous stars. This was the first of many observations that show that there is a form of matter in the Universe that we can only detect due to its gravitational effects on visible matter. Zwicky named this mysterious matter "dark matter". We now have evidence for dark matter (DM) from a wide range of length scales, from galaxies to the entire Universe.

At galactic scales, the most compelling evidence comes from rotation curves. The rotation curve of a galaxy shows the circular velocity of stars and gas as a function

of their radial distance. Outside the main concentration of mass, the rotation curve should fall off as $1/\sqrt{r}$ as the Newtonian circular velocity, $v(r)$, is given by

$$v(r) = \sqrt{\frac{GM(r)}{r}}, \tag{1.2.10}$$

where $M(r)$ is the mass distribution and r the radial distance. If the mass distribution of the galaxy were to follow that of the visible stars and gas, we would expect to see this decrease in circular velocity at the outskirts of a galaxy. Instead we see flat rotation curves extending far outside the visible stars and gas. This leads to the conclusion that there exists more matter than we can see with a density profile $\rho \propto 1/r^2$ at large radial distances.

In addition to the original evidence of dark matter discovered by Zwicky, there is a lot of other evidence from galaxy cluster scales. This evidence comes from measuring the mass of galaxy clusters and comparing that to the amount of visible light from the galaxy. The evidence includes using X-rays to determine the temperature profile of the gas in the cluster which, when combined with equations of hydrostatic equilibrium, can provide estimates of the total mass. One can also use gravitational lensing to determine the mass of a cluster by observing how much it bends light originating from behind the cluster. All these measurements, including those on galactic scales, consistently show that there is about five times more mass than can be accounted for by stars and gas.

There have been suggestions that instead of explaining all of these measurements by postulating dark matter, one should instead modify the laws of gravity [20]. This proposal is strongly disfavoured by one of the most spectacular pieces of evidence in favour for dark matter, the Bullet Cluster [21]. The Bullet Cluster is a system consisting of two galaxy clusters that recently collided with each other. From observing the system in visible light, one can see that all the stars just passed through each other as they are too sparsely distributed to interact. X-ray observations show that the gas, which interacts electromagnetically, is left between the two visible galaxies. In addition to these observations, there are observations from gravitational lensing that can tell us how the gravitational mass is distributed. If the only source of mass were normal matter, we would expect most of the matter to be distributed in the

same way as the hot gas since gas makes up the majority of the mass of a galaxy. This would be true even if the laws of gravity were modified to account for the other evidence for dark matter. The measurements show that the majority of the mass is not centred around the gas, but around the stars. This shows that dark matter is a separate form of matter that is, at least mostly, collisionless.

At the cosmological scale, we have evidence for dark matter from the cosmic microwave background (CMB) radiation. By studying the CMB angular power spectrum in combination with data from Big Bang Nucleosynthesis, one can determine both the density of normal matter (baryons) and the density of dark matter. The latest results from the Planck Satellite [22] give a dark matter density of $\Omega_{DM}h^2 = 0.1187 \pm 0.0017$ while the density of baryons is given by $\Omega_b h^2 = 0.022 \pm 0.00028$. We define Ω by

$$\Omega = \frac{\rho}{\rho_{\text{crit}}} \quad \rho_{\text{crit}} = \frac{3H^2}{8\pi G}, \tag{1.2.11}$$

where ρ_{crit} is the critical density which leads to a flat Universe, $h = H/(100\text{km/s/Mpc})$ and H is the Hubble constant. We know that $\Omega_{\text{tot}} \approx 1$ [22]; therefore dark matter makes up about 26% of the energy density of the Universe, five times more than the density of SM baryons.

Having established that dark matter exists, the next question is to determine what it is. Historically, the two main proposed categories have been particulate dark matter, often in the form of weakly interacting massive particles (WIMPS), and massive astrophysical compact halo objects (MACHOS). MACHOS are objects like brown dwarfs or black holes that are made out baryons, but would not be visible like stars. They are now disfavoured as an explanation of dark matter both because the inferred density of baryons is not large enough to support a sufficient density of these objects, and from limits set by micro-lensing surveys which show that MACHOS can not make up the majority of dark matter [23, 24]. The most likely scenario is then that dark matter is made up of weakly interacting particles.

For a particle to be a dark matter candidate, it has to be massive, stable on cosmological time scales and not interact too strongly with baryons or photons. In the Standard Model, the only possible dark matter candidate is the neutrino. As we

will discuss in detail later, its low mass would lead to a very different distribution of the size and mass of dark matter halos than the observed one. Therefore, there are no viable DM candidates in the SM. This is one of the most compelling reasons to investigate BSM physics. We will now investigate what cosmological observations can tell us about the nature of dark matter, and how to incorporate this information into particle physics models.

A viable particle physics model of DM needs to be able to reproduce the observed DM relic density. Different production mechanisms have been discussed in the literature to achieve this (see for example [25]). Here we will focus on the standard thermal freeze-out mechanism which is the most common production mechanism. The discussion follows [26] and [5]. Consider a stable dark matter particle, χ, with mass, m, that in the early Universe is in thermal equilibrium with the SM. As χ is stable, the only way to change the number of χ particles is through pair production or annihilation. As long as the interaction rate of these processes is larger than the expansion rate given by the Hubble parameter H, these interactions can keep the particles in thermal equilibrium. As the Universe expands the Hubble parameter and the interaction rate decreases. When the interaction rate becomes smaller than the Hubble rate, we get chemical decoupling and freeze-out of dark matter. The density becomes too small for the annihilations effectively to change the particle number any more. After freeze-out, the number of dark matter particles will remain constant and the number density will decrease with the normal expansion of the Universe. To study this in detail, we consider the annihilation rate, given by

$$\Gamma_a = \langle \sigma v \rangle n_{\text{eq}}, \tag{1.2.12}$$

where $\langle \sigma v \rangle$ is the thermally averaged annihilation cross-section and n_{eq} is the number density of dark matter while in thermal equilibrium. The thermally averaged cross-section can be calculated from the normal $2 \leftrightarrow 2$ scattering cross-section by following the procedure in [27]. This cross-section together with the mass of the DM particles, are the only particle physics ingredients in the calculation of the relic density.

The mathematical framework to determine the number density of DM particles during the evolution of the Universe, taking annihilations into account, is the Boltz-

mann equation formalism. The Boltzmann equation for a simple DM with only pair annihilation is given by

$$\dot{n} + 3Hn = -\langle\sigma v\rangle \left(n^2 - n_{\mathrm{eq}}^2\right),$$ (1.2.13)

where n is the number density of DM particles. The $3Hn$ term includes the effect of the expanding Universe, and the term with the annihilation cross-section describes the creation and annihilation of DM particles. The evolution with temperature, T, of the Hubble constant is given by

$$H(T) = 1.67 g_\star^{1/2} \frac{T^2}{M_{\mathrm{pl}}},$$ (1.2.14)

where $g_\star$ is the number of relativistic degrees of freedom and M_{pl} is the Planck mass. The equilibrium number density can easily be determined from standard statistical physics and it is $n_{\mathrm{eq}} \propto T^3$ when the DM is relativistic and $n_{\mathrm{eq}} \propto (M_{DM}T)^{\frac{3}{2}} e^{-T/M_{DM}}$ when non-relativistic. If we rewrite the equation using $y = n/s$ and $x = m/T$, where s is the entropy density, we get

$$\frac{dy}{dx} = -\frac{-x\langle\sigma v\rangle s}{H(m)}(y^2 - y_{eq}^2).$$ (1.2.15)

We can see that when $\langle\sigma v\rangle > H$, y and hence the number density are pushed to their thermal equilibrium value, and that when $\langle\sigma v\rangle \ll H$, y remains constant with time. A constant y gives a number density which decreases with T^3 in the same way as the density for normal matter does.

In general, the Boltzmann equation has to be solved numerically, but a good approximation of the final density for the case of s-wave annihilation, when $\langle\sigma v\rangle$ is independent of v, can be found (see e.g. [5, 28]),

$$\Omega_{DM} h^2 = 1.07 \times 10^9 \frac{x_f \, \mathrm{GeV}^{-1}}{(g_{\star s}/\sqrt{g_\star})M_{\mathrm{Pl}} \, \langle\sigma v\rangle}.$$ (1.2.16)

x_f corresponds to the freeze-out temperature and is given by

$$x_f = \log\left(0.038 \frac{g}{\sqrt{g_\star}} M_{\mathrm{Pl}} m \langle\sigma v\rangle\right) - \frac{1}{2} \log\log\left(0.038 \frac{g}{\sqrt{g_\star}} M_{\mathrm{Pl}} m \langle\sigma v\rangle\right).$$ (1.2.17)

For masses around those of the SM an annihilation cross-section of order

$$\langle\sigma v\rangle = 2.3 \times 10^{26} \mathrm{cm}^3/\mathrm{s} = 2 \times 10^{-9} \mathrm{GeV}^{-2}$$ (1.2.18)

will give the observed relic density. This is called the WIMP miracle as weak scale masses and couplings give the correct relic density. In addition to the hierarchy problem discussed below, this is one of the strongest hints of new physics at the weak scale. It should be noted that completely different mass scales can give rise to viable DM scenarios with the correct relic density. Both models with axions, with masses as low as $m_a = 6 \times 10^{-6}$eV (see e.g [29]), and models with WIMPZILLAS, with masses as high as 10^{16} GeV [26], can give the correct relic density.

We can learn more about the nature of dark matter if in addition to the density, we consider the mass distribution of dark matter halos. The information about the size and abundance of DM halos is contained in the dark matter halo mass function, $n(M)$, which determines the number of halos of a certain mass

$$dN = n(M)dM. \qquad (1.2.19)$$

To predict the present-day halo mass function we need an initial distribution at early times and must follow the growth of DM halos over time due to gravitational interactions. The initial distribution can be measured from the CMB[1] and is found to have a power spectrum $P(k) \propto k^n$, where k is the wave-number and the spectral index $n = 0.9603 \pm 0.0073$ [22]. This power spectrum agrees very well with what is predicted in many inflation models. We then need to determine how the halo mass function has evolved until today. One can make some progress analytically, e.g. [30], but the current best predictions come from N-body simulations [31].

The particle physics input into these simulations are the mass and the interactions of DM with itself and with SM particles. Light DM particles have large free-streaming lengths, which leads to a washing away of small scale structure. This was one of the early success of the N-body simulation research programme: it allowed the exclusion of neutrinos as DM due to their small mass [32]. Since light particles will remain relativistic today, they are called hot dark matter (HDM). Most

---

[1]We do not measure the exact initial distribution of the Power Spectrum at the CMB, but at the early time of the CMB we can safely use a linearised theory to calculate the changes from the initial distribution. This gives us good control on the initial distribution from CMB data.

models with HDM are excluded[2]. Particles with masses at the weak scale would be very non-relativistic today and are called cold dark matter (CDM). Due to their heavier mass and lower thermal velocities, these models have short free streaming lengths, and are in agreement with observations of large-scale structure. Figure 1.3 shows the dark matter power spectrum for different dark matter models.
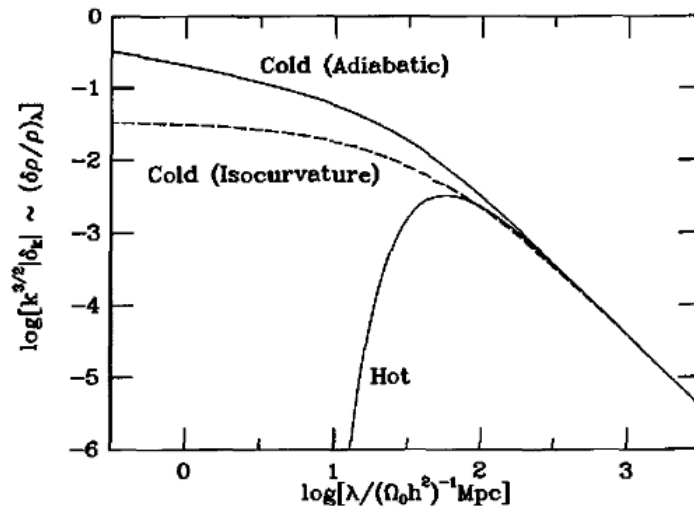
Figure 1.3: Dark matter power spectrum for different classes of dark matter models from [5]. The plot shows the power of fluctuations of a given size (λ). We see that hot dark matter has a strong cut-off for small wavelengths, λ due to free streaming.

The WIMP miracle, together with the good experimental agreement with large scale structure, has made CDM models the leading candidates for dark matter. In addition to the number and mass of dark matter halos, we can also learn about dark matter from the density profile and sub-structure of DM halos. We will explore this in Chapter **5** where we will see that there are some observations that indicate that either warm dark matter or dark matter with self-interactions fits the data on dwarf galaxy scales better than standard cold dark matter. The main observational problem with all of these considerations is of course that we cannot see the DM halos directly. Most of the information we have comes from the visible baryons

---

[2]Axions, even if they are very light, still behave as cold dark matter due their out-of-equilibrium production [29].

embedded in the DM halos. There has been a lot of progress in determining how the visible galaxy relates to the dark halos, and how baryonic physics affects the halo, see e.g. [33] and references therein.

In addition to cosmological experiments, there are three main experimental avenues open to explore dark matter: direct detection, indirect detection and collider experiments. These processes all depend on the same pair annihilation of dark matter into SM fermions process. In direct detection, one looks for recoil energy from collisions between dark matter particles and heavy nuclei, see e.g. [26, 34]. There has been tremendous progress in sensitivity over the last decade, but no convincing signals have been found. The current and projected future limits can be seen in Figure 1.4. For WIMP masses larger than 5-10 GeV, the limits are very strong and future experiments will be able to cover the entire parameter space above the neutrino coherent scattering limit. These DM limits are already very constraining for many models.
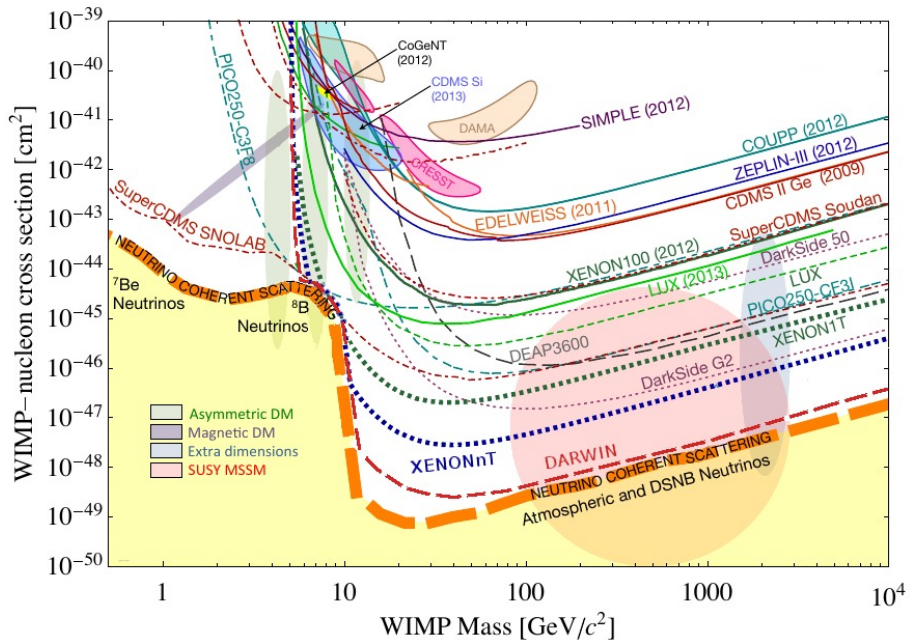
Figure 1.4: Current and future limits from direct detection experiments from [35] adapted from [34]. The current best limits are from the LUX(2013) experiment.

In indirect detection, one looks for high energy photons produced by high energy SM particles after the dark matter annihilates, see e.g. [26, 36]. The annihilation

signal is very sensitive to the density of dark matter, so the most promising place to look would be towards the galactic centre where the DM density is larger. Using gamma rays from the galactic centre, the Fermi-Lat satellite can set limits that are getting close to the annihilation cross-sections needed to reproduce the relic density [37]. In addition to setting limits, using the Fermi-Lat data one can see an excess towards the galactic centre [38] at energies around 1-3 GeV. This excess can be explained by dark matter between 10-100 GeV annihilating to various SM particles with a cross-section around the cross-section that gives the correct relic density, see e.g. [39].

To look for dark matter at colliders, one would search for signals with missing energy recoiling against visible objects. Collider search for mono-jets plus missing energy can give competitive constraints in the low dark matter mass region [40–42]. In this region direct detection experiments lose sensitivity as the recoil energy becomes too small. We will look more at collider searches for dark matter in Chapter **6**.

In BSM particle physics, there is a zoo of proposed dark matter candidates. A small selection includes sterile neutrinos, axions, various supersymmetric partners, composite objects in composite Higgs theories and Kaluza-Klein excitations in extra dimensional models. The main DM candidates we will investigate in this thesis come from BSM extensions with hidden sectors that include either scalars, fermions or vector bosons that couple to the SM via a Higgs portal coupling. Common to all of these models is that they simultaneously try to address multiple problems with the SM, not only provide a DM candidate. If one is mainly interested in dark matter, there are many simple models which include a DM candidate. The simplest such model comes from adding a real scalar singlet, s, with a Z_2 symmetry [43]. The discrete Z_2 symmetry prevents the decay of s. The dark part of the Lagrangian for this model is

$$\mathcal{L}_{DM} = \frac{1}{2}(\partial_\mu s)^2 - \frac{1}{2}m_s s^2 - \lambda_p \left(H^\dagger H\right) s^2, \qquad (1.2.20)$$

where H is the SM Higgs doublet. This model is still experimentally viable [44]. One can also have fairly simple dark matter models where the DM particle is coupled to a mediator which is then coupled to the SM. One example of these models has

fermionic dark matter, χ, and a scalar mediator, ϕ.

$$\mathcal{L}_{DM} = \frac{1}{2}(\partial_\mu \phi)^2 - \frac{1}{2}m_\phi \phi^2 + i\bar{\chi}\slashed{\partial}\chi - m_\chi \bar{\chi}\chi - g_\chi \bar{\chi}\chi\phi. \quad (1.2.21)$$

The mediator could then in general couple to the SM with any or all of following couplings

$$\mathcal{L}_{\text{interaction}} = \left(\kappa_1 W_\mu^+ W^{-\mu} + \kappa_2 Z_\mu Z^\mu - \sum_f \kappa_f \bar{f}f \right) \phi + \lambda_p \phi^2 \left(H^\dagger H \right), \quad (1.2.22)$$

where the fs are the SM fermions and $W^\pm, Z$ the SM gauge bosons. These models are phenomenologically viable, and in Chapter **6** we consider them as simplified models for collider searches for DM.

1.2.2 Matter-Antimatter Asymmetry

When we look out into the the Universe, we see a lot of baryons, but no significant amounts of antibaryons. The trace amounts of antimatter detected in satellite experiments are consistent with all the antimatter in our neighbourhood being produced by collisions of cosmic rays or in astrophysical sources. One possible explanation of this asymmetry could be that baryons and antibaryons somehow separated in the Universe, and large regions of antimatter exist. The problem with this scenario is that the boundaries between matter and antimatter would be visible due to radiation from annihilations. No such boundaries have been discovered [45], which leads us to conclude that the entire observed density in baryons is due to a baryon antibaryon asymmetry. Using data from CMB [46] we find an asymmetry of

$$\eta_b = \frac{n_b - n_{\bar{b}}}{n_\gamma} \approx 6 \times 10^{-10}, \quad (1.2.23)$$

where $n_b, n_{\bar{b}}$ and n_γ are the number densities of baryons, antibaryons and photons respectively. In the thermal plasma of the very early Universe one would expect equal amounts of matter and antimatter. To produce the observed baryon asymmetry we need a process for baryogenesis that fulfils the Sakharov conditions [47]. They are:

1. Baryon number (B) violation

2. Charge conjugation (C) and charge conjugation and parity (CP) violation

3. Out of thermal equilibrium processes

To produce a baryon asymmetry, a process that violates baryon number conservation is clearly needed. Even if such a process exists, the charged conjugated process will also exist and have the same rate unless C and CP are violated. These conditions together are still not enough to generate an asymmetry in thermal equilibrium as any asymmetry will just be washed away by the time-reversed process.

We will start by discussing why baryogenesis is not possible in the SM, before discussing three possible mechanisms for generating an asymmetry in BSM models. Perturbatively, baryon number is a symmetry of the SM, but it can be broken by non-perturbative effects since it is anomalous. Transitions, called Sphalerons, involving transitions between different SU(2) vacua with differing baryon and lepton (L) numbers [48], exist in the SM, and violate B. The SM therefore fulfils the first Sakharov condition. In addition, there is a C and CP violation in the quark sector[3], but it is many orders of magnitude too small to explain the observed baryon asymmetry [49, 50]. The electroweak phase transition could have provided the required out-of-thermal-equilibrium processes if it was a first order phase transition. To get a first order phase transition, the Higgs mass needs to be significantly smaller than the measured 125 Gev [51]. The SM therefore falls short on two out of the three Sakharov conditions, providing another very strong argument for the existence of BSM physics.

There are three main strategies in BSM models to achieve successful baryogenesis:

- **Electroweak Baryogenesis**

  In electroweak baryogenesis the baryon asymmetry is generated during the electroweak phase transition [51,52]. If the phase transition is first-order it will proceed via bubble nucleation. The bubbles spread out with out-of-equilibrium CP-violating processes near the bubble walls with B violation provided by the sphaleron processes. For the asymmetry not to be washed away behind the bubble wall, the phase transition needs to be strongly first-order. To generate

---

[3]And potentially in the lepton sector where the CP phase δ is not constrained.

the observed baryon asymmetry, the problems with SM electroweak baryogenesis need to be addressed. A first-order phase transition requires changes to the scalar potential of the Higgs, and new sources of CP violation require new particles and interactions. Electroweak baryogenesis can be successfully implemented for example in the two Higgs doublet model [53].

- **Grand Unified Baryogenesis**

  Grand unified theories (GUT), based on unifying the SU(3)×SU(2)×U(1) group structure to, for example, SU(5) or SO(10), include gauge bosons that couple leptons to quarks and therefore violate baryon number. GUT models also include many new sources of CP violation. The unification occurs at the energy scale where, due to RG-running, the SM coupling constants become equal. In most models this happens at scales of $10^{15} - 10^{16}$ GeV. The decay of the heavy, B-violating gauge bosons could happen out of thermal equilibrium, thereby fulfilling all of the Sakharov conditions [54]. One of the main problems with GUT baryogenesis is that GUTs also predict a density of magnetic monopoles or gravitinos that would overclose the Universe. This can be solved if inflation happens after GUT symmetry-breaking as inflation would then dilute away all the monopoles. Unfortunately for GUT baryogenesis, this would also dilute away the baryon asymmetry.

- **Leptogenesis**

  Sphaleron processes break both B and L, but not $B-L$ as it is not anomalous in the SM. Therefore if an asymmetry in L existed before the time of the electroweak phase transition, it would be transferred into a baryon asymmetry

$$B = -\frac{36}{25}L. \qquad (1.2.24)$$

  Together with a processes to generate a lepton asymmetry this gives a viable process for he generation of the baryon asymmetry, called leptogenesis [55]. A lepton asymmetry can be produced by the decay of heavy right-handed neutrinos.

We will now consider leptogenesis in more detail. The standard leptogenesis scenario is based on the Type 1 see-saw model for neutrino masses with the following

Lagrangian:

$$\mathcal{L}_I = \mathcal{L}_{SM} + i\overline{N_{R_i}}\slashed{\partial}N_{R_i} - \left(\frac{1}{2}M_i\overline{N_{R_i}^c}N_{R_i} + \epsilon_{ab}Y_{\alpha i}\overline{N_{R_i}}\ell_\alpha^a H^b + h.c.\right), \qquad (1.2.25)$$

where N_i is a right-handed Majorana neutrino with mass M and Y is the Yukawa coupling matrix for the neutrinos. In addition to successfully implement leptogenesis this model can provide an explanation for the small observed neutrino masses without extremely small Yukawa couplings via the see-saw mechanism. If we only consider one generation of neutrinos, we will, after electroweak symmetry breaking, get a mass matrix for the active and sterile neutrino of the following form

$$M_\nu = \begin{pmatrix} 0 & y\langle H\rangle \\ y\langle H\rangle & M \end{pmatrix}, \qquad (1.2.26)$$

where y is the Yukawa coupling and $\langle H\rangle$ the vev of the Higgs field. The eigenvalues of this matrix give a mass for the active neutrino of

$$m_\nu = -\frac{y^2\langle H\rangle^2}{M}. \qquad (1.2.27)$$

With Yukawa couplings of order one and $M \sim 10^{14}$, we can get sub-eV scale mass for the neutrinos in agreement with experiment without small couplings.

In this model leptogenesis proceeds by producing a lepton asymmetry by the out-of-equilibrium decays of the heavy right-handed neutrinos. The Yukawa coupling matrix can have complex phases leading to CP-violation, which together with the lepton number violating Majorana mass term and the electroweak sphalerons will generate a baryon asymmetry. To calculate the resulting baryon asymmetry we, use the Boltzmann formalism as we did for dark matter, see e.g. [56,57]. One needs the cross-sections for the scattering, decay and back reaction of right-handed neutrinos. In a simple version where we consider only one generation of right-handed neutrinos giving rise to the lepton asymmetry, we can find a lower bound on the right-handed neutrino mass to achieve the observed baryon asymmetry [58]

$$M \gtrsim 10^9 \,\text{GeV}. \qquad (1.2.28)$$

One way to lower this bound significantly is to consider two right-handed neutrinos with almost degenerate mass. Lowering the bound on the right-handed neutrinos

to the TeV scales requires significant fine-tuning. Another suggestion to achieve leptogenesis with GeV scale right-handed neutrinos will be explored in detail in Chapter **3**.

1.2.3   Stability of the Higgs Potential

One of the more striking features of quantum field theory (QFT) is the running of the coupling constants of the theory with energy or distance. If we consider measuring the electric coupling by measuring the strength of the electro-magnetic interaction at two distance scales r_1 and r_2 with $r_1 > r_2$, we will find a smaller value of the coupling constant, e, at the larger distance. This is due to the electron-positron pairs in the vacuum screening the charge. This change in coupling constants with scale takes place in all QFTs.

The evolution of coupling constants with energy is related to renormalisation. To compare QFT calculations with experiment, we need to renormalise the theory. We fix the coupling constants at a chosen energy μ to match the experimentally measured value. Physical results should be independent of our choice of scale. We can therefore write down differential equations that capture the change of the coupling constants with μ called renormalisation group equations (RGEs).

Consider a theory with couplings g_i for $i = 1, ..., n$. The RGE equation for g_1 is given by

$$\frac{\partial g_1}{\partial log\mu} = \beta_{g_1}(g_1, g_2, ..., g_n), \tag{1.2.29}$$

where the β-function is a function of all the coupling constants of the theory. All the other g_is have similar differential equations, and together they form a set of coupled differential equations. The β-function appears at the one-loop order, so at tree-level it vanishes. To calculate β-functions one can use the Callan-Symanzik equation. Let $G^{(n)}(x_1, ..., x_n)$ be a connected, renormalised n-point Green's function in a theory with fields ϕ and one coupling constant g. The Callan-Symanzik equation is then

$$\left(\mu \frac{\partial}{\partial \mu} + \beta(g) \frac{\partial}{\partial g} + n\gamma(g) \right) G^{(n)}(x_1, ..., x_n) = 0, \tag{1.2.30}$$

where β is the same function as above and $\gamma(g)$ is the anomalous dimension of the ϕ field. By choosing suitable Green's functions calculated at one loop, one can

calculate both β and γ at one loop. Once β and γ are known we can evolve the couplings constants to any required energy scale.

As shown in Figure 1.2, the RG-running in the SM has been verified experimentally. For the gauge couplings in the SM there are two different patterns of evolution depending on the sign of the β-function. Quantum electrodynamics (QED) has a positive β-function which leads to larger values of e as the energy increases, while QCD has a negative β-function. This results in confinement at low energies and asymptotic freedom at large energies. The coupling constant of the weak $SU(2)$ group also has a negative β-function, but does not confine due to spontaneous breaking of electroweak symmetry. With the measurement of the Higgs mass at the LHC, we now know all the parameters of the SM and can therefore use the RG-equations to evolve the SM up in energy to discover until what energy scale it is valid. At energy scales of $M_{\rm pl}$, we know that quantum gravity effects become important, but any problems with the SM before that would be evidence of new physics.

For the SM to be valid up to the Planck scale, it should not have Landau poles and the scalar potential should be stable. A Landau pole occurs when a coupling constant becomes infinite at a finite energy. This indicates that either new physics is needed to tame the growth in the coupling constant, or that the theory completely changes character in the same way as when QCD confines.

For the potential to be stable, the electroweak vacuum should be the minimum of the potential. The scalar potential, $V(H)$, determines the vacuum state of the theory by its minimum. In the SM, the scalar potential in the unitary gauge is given by

$$V(h) = -\frac{m_h^2}{2}h^2 + \frac{\lambda_H(h)}{4}h^4, \tag{1.2.31}$$

where we consider $\lambda_H(h)$ to be a function of the field value, in order to take into account the running of the coupling when we go to large field values. The negative mass squared gives a minimum away from the origin, and as long as $\lambda_H(h)$ is positive the potential is stable for large values of h. Therefore, for the Higgs potential to remain stable until the Planck scale we need $\lambda_H(h) > 0$ for $h < M_{\rm pl}$. The one-loop

RGE for λ_H in the MS-bar renormalisation scheme is given by

$$
\begin{aligned}
(4\pi)^2 \frac{d\lambda_H}{d\log\mu} &= -6y_t^4 + 24\lambda_H^2 + \lambda_H\left(12y_t^2 - \frac{9}{5}g_1^2 - 9g_2^2\right) \\
&\quad + \frac{27}{200}g_1^4 + \frac{9}{20}g_2^2 g_1^2 + \frac{9}{8}g_2^4,
\end{aligned}
\tag{1.2.32}
$$

where y_t is the top Yukawa coupling, g_1 is the EM gauge coupling and g_2 is the weak SU(2) coupling. As the top Yukawa coupling is the largest of all the couplings, it dominates the running. The negative sign of the top Yukawa term will drive the Higgs coupling towards zero, potentially driving it negative.

The running of the coupling constants in the SM has now been calculated at next-to-next-to-leading order (NNLO) in [59]. With the currently measured values of the Higgs mass and the top mass, the scalar potential seems to be in the interesting metastable regime, just in between stability and instability. In the metastable regime, the electroweak vacuum is a local minimum of the theory, but there is a lower minimum at large field values of order 10^9 GeV. Changing the top mass by about 3σ from its central value could make the potential stable.

A metastable vacuum could still be a problem for the theory. With the scale of the instability found for the current best measured values of the Higgs and top mass, the metastable vacuum would have a lifetime long enough not to be excluded [59]. For this to be a viable scenario, one still would need to explain why the Universe ended up in the metastable vacuum in the first place. There is also a question about how the the Higgs field behaved during inflation. Potentially, both quantum and thermal fluctuations could make a Universe with a metastable Higgs non-viable [60–62]. If the energy scale during inflation is too large, inflation would drive the Universe into the non-electroweak vacuum and the SM would need an extension to survive. We will present an extension to the SM that can help stabilise the Higgs potential in Chapter **4**.

1.2.4 Hierarchy Problem

For the last decades the main theoretical question in the SM has been the naturalness or hierarchy problem. As discovered in 1978 [63], the mass of a scalar field is very

sensitive to any higher energy scales in the theory due to large quantum corrections. This sensitivity would tend to push the mass of the scalar fields up to the highest energy scale in the theory. The Higgs field in the SM is a scalar field, and as such its mass would also be sensitive to large quantum corrections due to new physics at high scales. In this section, we will first discuss the hierarchy problem in more detail and then consider some possible solutions to it.

We will start by considering the quantum corrections to the Higgs mass, m_h^2, from the one loop diagram with an internal top quark. We will start by using a cut-off scale, Λ, to regularise the loop integral. In this regularisation scheme, the corrections are given by

$$\Delta m_h^2 \approx \frac{-y_t^2}{4\pi^2} \left(\Lambda^2 + m_t^2 \, log \left(\frac{\Lambda^2}{m_t^2} \right) - m_t^2 \right), \qquad (1.2.33)$$

where y_t is the top-Yukawa coupling. The corrections are proportional to the Yukawa-coupling, which is why the top quark gives the largest contribution of the SM fermions, and thus we will only consider this contribution. We see that the quantum corrections are quadratically divergent. The observable or renormalised Higgs mass will then be given by a sum of the bare mass m_0 and the corrections

$$m_h^2 = m_0^2 + \Delta m_h^2 = m_0^2 - \frac{y_t^2}{8\pi^2} \Lambda^2. \qquad (1.2.34)$$

From LHC experiments, we know that the Higgs has a mass of $m_h = 125$ GeV. If we now interpret the cut-off Λ as a physical scale and take it to be the Planck scale $M_{\text{pl}} \approx 10^{19}$ GeV, we would need an enormous amount of fine-tuning between m_0, Λ and y_t to achieve the observed Higgs mass. Interpreting the cut-off as physical could mean interpreting it as a maximum momentum or equivalently an inverse lattice spacing. The Planck scale is where quantum gravity effects become important. We know that a theory of quantum gravity is needed at this scale, which is why it is often used to estimate the fine-tuning in the SM, but as we will see below this is not the most useful way of thinking about the hierarchy problem.

The first question to ask is why the Higgs field has this problem, but none of the SM fermions do. If we calculate the one-loop correction to the fermion mass, m_f, we find

$$\delta m_f \propto m_f \, log \left(\frac{\Lambda}{m_f} \right). \qquad (1.2.35)$$

Even for a large Λ this does not introduce fine-tuning as the mass correction is proportional to the mass. This is because fermion masses are technically natural [64]. If a symmetry of the theory is enhanced when a parameter is set to zero, the parameter is technically natural and can naturally be small without any fine-tuning. Fermions have chiral symmetry when they are massless which is why fermion masses are protected from large quantum corrections, and why $\delta m_f \propto m_f$. Scalars have no such protection as the symmetries of the SM would not increase when we set the scalar mass to zero.[4]

If, instead of using a cut-off regulator, we were to calculate the quantum corrections to the Higgs mass using dimensional regularisation, we would find

$$\Delta m_h^2 \approx \frac{-y_t^2 m_t^2}{4\pi^2} \left(\frac{2}{\epsilon} - \gamma_E + log(4\pi) - log\frac{m_t^2}{\mu^2} \right). \tag{1.2.36}$$

The corrections are still divergent, but the $1/\epsilon$ pole corresponds to a logarithmic divergence and not to the quadratic divergence we saw in the cut-off regularisation scheme. Since physics should be independent of regularisation and subtraction schemes, we will define the hierarchy problem in terms of real physical threshold effects, rather than in terms of quadratic divergences. In both regularisation schemes, we find a contribution proportional to m_t^2, which is the threshold contribution. The standard quadratic divergences signal that these threshold corrections will occur, but are not a problem by themselves. This shows that dimensional regularisation does not solve the problem, even if there are no quadratic divergences. The threshold contribution from the top quark is not large enough to require much fine tuning, but new particles could give large contributions. Any new massive particle with mass, M, coupling to the Higgs with coupling y will give a threshold contribution of order $y^2 M^2$. We therefore say that a theory has a hierarchy problem if it has an elementary scalar with mass m coupled to a heavy particle with $y^2 M^2 \gg m^2$.

Another way to understand the same phenomenon is to consider the RG equation for a scalar mass parameter in a simple model with only one fermion with mass, M,

---

[4]In Chapter **2** we will discuss scale invariance, which could represent an increased symmetry of the SM with $m_h = 0$.

coupled to the scalar with a Yukawa coupling, y. The RG equation is given by

$$(4\pi)^2 \frac{\partial m_h^2}{\partial \log \mu} = -16M^2 y^2 + 2\lambda_h m_h^2, \tag{1.2.37}$$

where λ_h is the scalar quartic coupling. We see that the change in Higgs mass induced by the running from μ_0 to μ_1, when $M \gg m_h$, is of the order of

$$\Delta m_h^2 \approx -\frac{16}{(4\pi)^2} y^2 M^2 \log \frac{\mu_1}{\mu_0}. \tag{1.2.38}$$

As long as the RG equations are evolved over a significant range of energies, this will require a large fine-tuning to achieve $m_h \ll M$, leading to the same conclusion as above.[5]

An important way to think about the hierarchy problem is to consider the SM as a low energy effective field theory (EFT) valid up to a cut-off scale Λ. We would then expect contributions to the squared Higgs mass of order Λ^2 as the cut-off corresponds to a heavy particle we have integrated out. Following [65], we will show an example which illustrates both that thinking about thresholds is a more useful way of conceptualising the hierarchy problem, and that some care is needed when thinking about effective field theories and the cut-off contributions to the Higgs mass. Let us consider a simple theory with a scalar field ϕ and two fermions χ and ψ with the following Lagrangian

$$\mathcal{L} = \frac{1}{2}(\partial_\mu \phi)^2 - \frac{1}{2}m_\phi \phi^2 + i\bar{\chi}(\slashed{\partial} - m_\chi)\chi + i\bar{\psi}(\slashed{\partial} - m_\psi)\psi - g_\chi \bar{\chi}\chi\phi - g_\psi \bar{\psi}\psi\phi. \tag{1.2.39}$$

We will consider the situation where the mass of ψ, m_ψ is much larger than the masses of ϕ and χ, respectively m_ϕ and m_χ. Comparing this to the SM, we think of ϕ as the Higgs, χ as the top quark and ψ as a new unobserved particle with a large mass. At energy scales below m_ψ, we can integrate ψ out and consider an effective field theory for ϕ and χ. We can estimate the contribution to the scalar mass in this EFT by

$$m_\phi^2 = m_0^2 + \Delta m_h^2 = m_0^2 - \frac{g_\chi^2}{4\pi^2} \left(\Lambda^2 + m_\chi^2 \log\left(\frac{\Lambda}{m_\chi}\right) - m_\chi^2 \right) \tag{1.2.40}$$

---

[5]There is a factor of two difference between Equation (1.2.38) and what one would expect from (1.2.36) as in the SM the top Yukawa interaction is $\frac{y_t}{\sqrt{2}} h\bar{t}t$.

where we would now treat $\Lambda = m_\psi$ as a physical scale, the cut-off of the EFT. Using this procedure, we would then consider the theory to be fine-tuned if $m_\phi^2 \ll g_\chi^2 m_\psi^2$. Since we know the UV-completion of this EFT, we can calculate the quantum corrections in the full theory

$$m_\psi^2 = m_0^2 + \Delta m_h^2 = m_0^2 - \frac{g_\chi^2}{2\pi^2} \left(\Lambda_1^2 + m_\chi^2 \, log \left(\frac{\Lambda_1^2}{m_\chi^2} \right) - m_\chi^2 \right)$$
$$- \frac{g_\psi^2}{2\pi^2} \left(\Lambda_1^2 + m_\psi^2 \, log \left(\frac{\Lambda_1^2}{m_\psi^2} \right) - m_\psi^2 \right) , \qquad (1.2.41)$$

where Λ_1 is a cut-off regulator that we will take to infinity as there are no other physical scales in the theory. All the divergent pieces are absorbed into the bare coupling as usual during renormalisation, and the logarithmically divergent terms cause the running of the coupling constants. After renormalisation we are still left with mass threshold effects

$$\Delta m_\phi^2 = \frac{g_\chi^2}{8\pi^2} m_\chi^2 + \frac{g_\psi^2}{8\pi^2} m_\psi^2. \qquad (1.2.42)$$

As we can see from this example it is not the presence of the quadratic divergences in the theory, but the mass thresholds that give a hierarchy problem. Another important aspect is that the magnitude of the quantum corrections due to ψ are not given by g_χ and m_ψ as estimated when considering the EFT, but by g_ψ and m_ψ. This means that the theory is unnatural or fine-tuned if $g_\psi^2 m_\psi^2 \gg m_\phi^2$. Coming back to the SM, we can see that solutions of the hierarchy problem do not require top partners [65]. The new threshold effects that would destabilise the Higgs do not need to have anything to do with the top quark.

The hierarchy problem is therefore only a problem if there are any new large scales. The Standard Model by itself is not unnatural since there are no large scales that could destabilise the Higgs mass. If we wanted to extend the SM with, for example, a grand unified theory without supersymmetry, we would get a hierarchy problem, because the large GUT scales couple directly to the Higgs with large couplings. The hierarchy problem is therefore best thought of as a problem which proposed BSM theories need to avoid. Any proposed theory that includes large threshold corrections to the Higgs mass would be unnatural and require fine-tuning.

We characterise the hierarchy problem as one of the main theoretical challenges in particle physics since we know that BSM physics is needed and most of the proposed theories include very large scales coupled to the Higgs with large couplings.

At the Planck scale quantum gravity effects have to become important. If quantum gravity introduces particles with Planck scale masses, e.g micro black holes, that couple strongly to the Higgs, it will lead to extreme amounts of fine tuning. Since the theory of quantum gravity is unknown, it is impossible to predict how gravitational effects would change the Higgs mass. If quantum gravity does not give large contributions to the Higgs mass and there were no other new heavy thresholds in the theory, we will not have a hierarchy problem. This could be characterised as a UV solution to the naturalness problem [66]. We will discuss this possibility further in Chapter **2** in the context of classical scale invariance. Most proposed solutions to the hierarchy problem would instead be characterised as solving the problem in the IR. These theories either do not have elementary scalar fields, or they impose new symmetries that cancel all the quantum corrections to the Higgs mass above the scale of the symmetry. The two main frameworks to address the naturalness problem in the IR are supersymmetry and composite Higgs models. We will now briefly describe both of these approaches.

Supersymmetry (SUSY) refers to models where Lorentz invariance is extended to include a symmetry that transforms bosons to fermions and vice versa. This is the only non-trivial way to extend the Lorentz symmetry of the SM. For an introduction to supersymmetry see [67] and references therein. Supersymmetry gives every particle of the SM a supersymmetric partner with opposite spin statistics, identical masses and quantum numbers. The symmetry also makes the couplings of these new particles match the observed couplings in the SM so that all quadratic divergences to the Higgs mass would vanish. The top quark would have a scalar partner, the stop, which would exactly cancel the top contribution. Since we have not observed any stops or any other supersymmetric partners, supersymmetry would have to be broken. It is possible to break supersymmetry softly not to reintroduce the quadratic divergences. If we consider mass threshold effects instead of quadratic divergences as the source of the hierarchy problem, softly broken SUSY is natu-

ral since any new heavy particle would have a partner that would cancel out the threshold effect. SUSY can only solve the naturalness problem if the scale of SUSY breaking is close to the EW scale. This is often called the little hierarchy problem. After not discovering any signs of SUSY at the first run of the LHC, many minimal SUSY models are now under pressure [68, 69].

The hierarchy problem arose because the SM Higgs boson is an elementary scalar field. In composite Higgs models, the Higgs is instead a bound state of some new fermions, Ψ and $\bar{\Psi}$, charged under a new confining gauge group. This solves the hierarchy problem, since the integral used to calculate the Higgs mass quantum corrections would be cut-off at the scale of confinement, Λ_c, for the new gauge group. Above this scale there are no scalars and therefore no hierarchy problem. This solution to the hierarchy problem, was first proposed in the Technicolor framework in 1979 [63, 70]. Many approaches have adopted this framework, including those where the Higgs is a pseudo-Goldstone boson, see e.g [71]. As with supersymmetry, we see that we have a little hierarchy problem, as the corrections to the squared Higgs mass would be driven by Λ_c^2. If the Higgs is indeed a composite particle, we would expect to see a whole host of other composite particles as in QCD. None of these particles have been discovered, driving the scale of confinement higher and making the little hierarchy problem worse.

There have been other suggested solutions to the hierarchy problem, but an almost universal feature of all these solutions is that they require new physics at the TeV scale not to be very fine-tuned. Of course, as mentioned above, the hierarchy problem itself does not need to be solved at the TeV scale, but if we want to answer the questions of dark matter, baryogenesis etc. without extremely weakly coupled physics, we need particles with masses of TeV or below.

1.3 Outline of the Thesis

The main goal of this thesis is to investigate BSM extensions to the SM that can address the questions about the Standard Model discussed in this introduction. We will study theoretical model-building aspects and both collider and cosmological

phenomenology of hidden sector models. These models extend the SM with a new gauge group which is mainly coupled to the SM via the Higgs portal coupling. In Chapter **2** we will introduce classical scale invariance (CSI) as a model building framework for BSM physics. We will see that all scales in such models will have to be dynamically generated, and that minimal models with few new parameters are viable and can provide solutions to the SM problems. Chapter **2** also includes an overview of classically scale-invariant models studied in the literature.

In Chapter **3** we will study a $U(1)_{B-L}$ CSI extension of the SM in detail. The results presented in this chapter are based on [1]. One appealing feature of this model is that it includes right-handed neutrinos and can explain the active neutrino masses via the see-saw mechanism. The main focus of Chapter **3** will be to implement leptogenesis via neutrino oscillations as suggested in [72] in a classically scale-invariant framework. We will show that this model can successfully generate enough matter-antimatter asymmetry and investigate the available parameter space for the model.

We move on to discussing two of the other open questions in the SM in Chapter **4**, namely dark matter and the stability of the Higgs potential. In this chapter, based on [2], we investigate $U(1)$, $U(1)_{B-L}$ and $SU(2)$ CSI extension to the SM. First we determine the parameter space in which these models can stabilise the Higgs potential. Without adding extra field content, it is only possible in the $SU(2)$ model to stabilise the Higgs potential and not to be excluded by LHC constraints. We therefore also include models with an extra scalar singlet. This scalar singlet can both stabilise the Higgs potential and be a good and viable dark matter candidate. The gauge bosons of the $SU(2)$ theory are also good dark matter candidates. We investigate the available parameter space for all the models where the Higgs potential is stabilised and we get the correct relic density for dark matter.

In Chapter **5** we consider an $SU(2)$ extension of the SM which can support magnetic monopoles based on [3]. A CSI theory with monopoles is interesting as it gives a parametrically larger scale for the mass of the monopoles than the vacuum expectation value of the scalar field. We want to determine if magnetic monopoles in a hidden sector can make up dark matter, and if such models are cosmologi-

cally viable. Models with magnetic monopoles will also include other dark matter candidates and dark radiation. We determine the viable parameter space for the SU(2) SM extension. Due to an unbroken U(1) gauge group, the model has long range dark matter self-interactions which can help to explain the too-big-too-fail and core-vs-cusp problems with the standard cold collisionless dark matter paradigm.

Having studied the cosmological consequences of hidden sector models coupled to the Standard Model via the Higgs portal, in Chapter **6**, based on [4], we will consider what we can learn about these models at the LHC and future colliders. Our main goal will be to study a simplified dark matter model in the two jets plus missing energy final state. This is the signature of the vector boson fusion production of the Higgs or another scalar decaying invisibly. We want to determine the expected reach of the LHC and a future 100 TeV collider, and see if it is possible to learn about the parameters of the hidden sector. The mass of the mediator between the dark sector and the SM is one of the most important parameters at colliders, and we will investigate how well the kinematic information from the two visible jets allows us to differentiate between models with different mediator masses.

Chapter 2

Classical Scale Invariance

Models with classical scale invariance (CSI) have been introduced to explain the shortcomings of the SM in a minimal way, without introducing large scales that would destabilise the Higgs mass. In this chapter, based partly on material from [1, 2], we will discuss how to construct classically scale-invariant BSM models. We will start by discussing scale invariance and what classical scale invariance entails in Section **2.1**. Then we will discuss the Coleman-Weinberg (CW) mechanism used to generate scales radiatively in these models in Section **2.2**. This will show that the classically scale-invariant SM needs to be extended with extra gauge groups or field content to be phenomenologically viable. We will present a minimal extension to the SM, before discussing a wide range of CSI models in Section **2.3**.

2.1 Classical Scale Invariance

We will start by considering scale invariance in quantum field theory. Scale transformations transform the coordinates, x, as

$$x \rightarrow x' = exp(\epsilon)x \,, \tag{2.1.1}$$

where ϵ is a scaling parameter. Scale transformations form an Abelian group with elements $U(\epsilon)$. They act on the fields, $\Phi(x)$, of the theory as

$$\Phi \rightarrow \Phi' = U(\epsilon)\Phi(x)U(\epsilon)^{-1} = \Phi(x) - \epsilon \left(d_\Phi + x_\mu \frac{\partial}{\partial x_\mu} \right) \Phi(x) \,, \tag{2.1.2}$$

where d_ϕ is the scaling dimension of the field and the last equality is for infinitesimal ϵ. In the free theory scalars have scaling dimension $d_\phi = 1$, and fermions have $d_\psi = 3/2$. By considering these transformations, we can see that a free massless theory has a scale-invariant Lagrangian. If we introduce interactions, we find that the Lagrangian is invariant under scale transformations if the interaction terms are dimension four. Any dimensionful parameter, as for example a mass term, $m^2\phi^2$, will break scale invariance.

A theory invariant under scale transformations will have a conserved Noether current, D_μ, corresponding to scale transformations. One can find an expression for this current by using the fact that the symmetric energy momentum tensor can be defined as

$$T^{\mu\nu} = 2\frac{\delta}{\delta g_{\mu\nu}}\int d^4x\mathcal{L}\,,\tag{2.1.3}$$

where $g_{\mu\nu}$ is the spacetime metric. Under scale transformations $\delta g_{\mu\nu} \propto g_{\mu\nu}$, this gives

$$\partial_\mu D^\mu = \delta S \propto \delta g_{\mu\nu}T^{\mu\nu} \propto g_{\mu\nu}T^{\mu\nu} = T^\mu_\mu.\tag{2.1.4}$$

We see that the conservation of the scaling (dilation) current is given by the trace of the energy momentum tensor. Therefore, for a theory to be scale invariant $T^\mu_\mu = 0$. Until now, the analysis has been at tree level. One way of including quantum corrections is to consider the running of the coupling constants, g, of the theory with energy. A scale transformation would change $g \to g + \epsilon\beta(g)$, where $\beta(g)$ is the normal β-function. Including one-loop effects, we find that

$$\partial_\mu D^\mu = T^\mu_\mu = \delta\mathcal{L} = \beta(g)\frac{\partial}{\partial g}\mathcal{L}\,.\tag{2.1.5}$$

For a quantum theory to be scale-invariant, the β-functions have to vanish. If the Lagrangian is scale-invariant but $\beta(g) \neq 0$, scale invariance is anomalously broken, and the theory is classically scale-invariant.

It is possible to extend the group of scale transformations to the conformal group by including special conformal transformations. The distinction between conformal and scale invariance is not important for what follows, and in 4d scale invariance most likely implies conformal invariance, see e.g. [73]. In the literature classical scale invariance is sometimes referred to as classical conformal invariance.

We now turn to classical scale invariance. A theory is classically scale-invariant if there are no dimensionful parameters in the Lagrangian, but $\beta(g) \neq 0$ [74]. This means that even if scale invariance is not an exact symmetry, it is not broken by an arbitrary amount. The breaking of scale invariance is only due to the logarithmic running of coupling constants and the scales this might dynamically generate.[1] We can therefore either view classical scale invariance as softly broken scale invariance or as a classical symmetry which becomes exact in the classical limit of $\hbar \to 0$. When doing calculations in CSI theories we should not use a cut-off regulator since that would break scale invariance [75]. We should instead use a regularisation scheme that does not introduce the UV scale explicitly, for example dimensional regularisation. We will see that models with classical scale invariance can address the hierarchy problem, and be interesting BSM theories.

A separate, but related model building approach is to consider theories with an exact quantum scale invariance of the UV theory, as discussed in [76–78]. Classical scale invariance of the effective theory below the Planck scale does not necessarily assume nor is directly related to a hypothesised conformal invariance of the UV embedding of the SM. UV quantum scale invariance is a more ambitious approach that would make the Higgs mass technically natural and protect it from large quantum corrections. As a solution of the hierarchy problem, this is similar to Supersymmetry. Quantum scale invariance requires that all β-functions become zero in the UV, which requires new physics at the TeV scale. This is because the scale where the β-functions turn over will give corrections to the Higgs mass, even if there are no new heavy particles at this scale [76].

2.2 Coleman-Weinberg Mechanism

We will now review the Coleman-Weinberg mechanism [79] for the generation of scales in a classically massless theory. First, we review the effective action and potential formalism in Section **2.2.1**, and then we calculate the effective potential

---

[1] We will see in detail how scales can be generated in classically scale-invariant theories when we discuss the Coleman-Weinberg mechanism in Section **2.2**.

for a massless U(1) theory in Section **2.2.2**. This will allow us to see how non-zero vacuum expectation values and masses are generated dynamically by radiative corrections.

2.2.1 Effective Action and Potential

By defining the effective action and potential, we will be able to study spontaneous symmetry breaking in a systematic way including quantum corrections. We start from the generating functional in the path integration formulation of quantum field theory, which for a theory with a Lagrangian, $\mathcal{L}$, and a source, $J(x)$, is given by

$$Z[J] = \int \mathcal{D}\phi \exp\left[i \int d^4x \mathcal{L}[\phi] + J\phi\right]. \tag{2.2.6}$$

One can interpret the generating functional as giving the vacuum-to-vacuum transition amplitude in the presence of a source. From the generating functional, we can define the energy functional, $W[J]$,

$$e^{iW[J]} = Z[J] = \langle\Omega|\Omega\rangle_J. \tag{2.2.7}$$

$W[J]$ corresponds to the vacuum energy in the presence of the source J, and it is analogous to the Helmholtz free energy in a condensed matter system. We now define the classical field, ϕ_{cl}, as

$$\phi_{cl} = \frac{\delta W[J]}{\delta J(x)} = \frac{\langle\Omega|\phi(x)|\Omega\rangle_J}{\langle\Omega|\Omega\rangle_J}. \tag{2.2.8}$$

The classical field is a weighted average over all field configurations and dependent on the source $J(x)$. The effective action, $\Gamma[\phi_{cl}]$ is now given by a Legendre transform of the energy functional:

$$\Gamma[\phi_{cl}] = W[J] - \int d^4x J(x)\phi(x). \tag{2.2.9}$$

We can expand the effective action in two very useful ways. The first is as a series of 1PI connected Green's functions[2], Γ^i,

$$\Gamma = \sum_n \frac{1}{n!} \int d^4x_1...d^4x_n \Gamma^{(n)}(x_1,...,x_n)\phi_{cl}(x_1)...\phi_{cl}(x_n). \tag{2.2.10}$$

---

[2]1PI Green's Functions are the sum of all Feynman diagrams which remain connected if one internal line is cut.

The second expansion is in powers of momentum

$$\Gamma = \int d^4x \left[-V(\phi_{cl}) + \frac{1}{2}(\partial_\mu \phi_{cl})^2 Z(\phi_{cl}) + ... \right]. \tag{2.2.11}$$

$V(\phi_{cl})$ is the effective potential, and at tree level it is equal to the normal scalar potential. From Equation 2.2.9, we can see that

$$\frac{\delta \Gamma[\phi_{cl}]}{\delta \phi_{cl}} = -J(x). \tag{2.2.12}$$

We now want to use this relation to study the symmetry breaking properties of our theory. Symmetry breaking occurs if ϕ_{cl} develops a non-zero vacuum expectation value when the source $J(x) = 0$. Therefore, symmetry breaking would happen if

$$\left. \frac{\delta \Gamma[\phi_{cl}]}{\delta \phi_{cl}} \right|_{\phi_{cl} \neq 0} = 0. \tag{2.2.13}$$

From Equation (2.2.11), we can see that, if the theory is translationally invariant, this reduces to

$$\left. \frac{dV(\phi_{cl})}{d\phi_{cl}} \right|_{\phi_{cl} \neq 0} = 0. \tag{2.2.14}$$

This shows that the effective potential is very useful for studying the symmetry breaking properties of a theory. First, the effective potential is calculated to the desired order in perturbation theory. Then we determine that the symmetry is broken if the minimum of the effective potential occurs for $\phi_{cl} \neq 0$.

2.2.2 One Loop Effective Potential for Classically Massless U(1)

We will now use the technique in the previous chapter to study spontaneous symmetry breaking in a classically massless U(1) theory with a complex, charged scalar field. At tree level, the potential only has one minimum at the origin of field space which would leave the U(1) symmetry unbroken. We want to determine if radiative corrections can spontaneously break the U(1) symmetry. This theory has the Lagrangian

$$\mathcal{L} = (D_\mu \Phi)^\dagger (D^\mu \Phi) + \frac{1}{4} F^{\mu\nu} F_{\mu\nu} - \frac{\lambda}{4!} |\Phi|^4, \tag{2.2.15}$$

where the covariant derivative is given by $D_\mu = \partial_\mu - e_{CW} A_\mu$ and the complex scalar by $\Phi = 1/\sqrt{2}(\phi_1 + i\phi_2)$. $F^{\mu\nu}$ is the normal field strength tensor, and e_{CW} is the
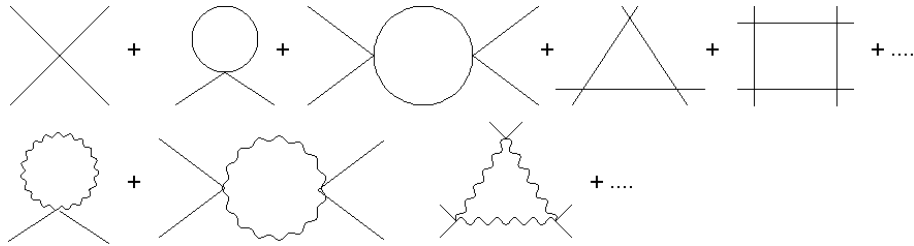
Figure 2.1: Feynman diagrams for the one-loop effective potential of scalar QED, including scalar and gauge boson loops.

gauge coupling. Due to gauge invariance, the effective potential only depends on $\phi_{cl}^2 = \phi_1^2 + \phi_2^2$.

In this section, we will calculate the effective potential following the original calculation in [79] using a cut-off regularisation scheme with cut-off Λ. In Section **2.3.2** we will see that we get the same results if we use dimensional regularisation and the $\overline{\text{MS}}$ subtraction scheme.

From Equations 2.2.10 and 2.2.11, we can see that we can calculate the effective potential as the sum of all 1PI Feynman diagrams with vanishing momentum on the external lines. We show these Feynman diagrams in Figure 2.1. Calculating and summing up the infinite number of Feynman diagrams we get

$$V = \frac{1}{4!}\lambda\phi_{cl}^4 - \frac{1}{2}B\phi_{cl}^2 - \frac{1}{4!}C\phi_{cl}^4 + \frac{1}{2}\int \frac{d^4k}{(2\pi)^4}\ln\left(1 + \frac{\lambda\phi_{cl}^2}{2k^2}\right) + \frac{3}{2}\int \frac{d^4k}{(2\pi)^4}\ln\left(1 + \frac{e_{CW}^2\phi_{cl}^2}{k^2}\right),$$
$$(2.2.16)$$

where B and C are the usual counter-terms needed for renormalisation. We evaluate the UV divergent integral using a cut-off regularisation with cut-off, Λ, to get

$$
\begin{aligned}
V &= \frac{1}{4!}\lambda\phi_{cl}^4 - \frac{1}{2}B\phi_{cl}^2 - \frac{1}{4!}C\phi_{cl}^4 + \frac{\Lambda^2\phi_{cl}^2}{64\pi^2}(\lambda + 6e^2) \\
&\quad + \frac{\lambda^2\phi_{cl}^4}{256\pi^2}\left(\ln\frac{\lambda\phi_{cl}^2}{2\Lambda^2} - \frac{1}{2}\right) + \frac{3\lambda^2\phi_{cl}^4}{64\pi^2}\left(\ln\frac{e_{CW}^2\phi_{cl}^2}{\Lambda^2} - \frac{1}{2}\right)
\end{aligned}
\tag{2.2.17}
$$

We then need to renormalise the theory to remove the divergences. To do this, we impose the following renormalisation conditions

$$\frac{d^2V}{d\phi_{cl}^2} = 0\,,\ \left.\frac{d^4V}{d\phi_{cl}^4}\right|_M = \lambda, \tag{2.2.18}$$

where the first condition is that of a classically massless theory, and the second defines the coupling constant at an arbitrary renormalisation scale, M. Combining

these conditions with Equation 2.2.18, we get an expression for the one loop effective potential

$$V = \frac{1}{4!}\lambda\phi_{cl}^4 + \left(\frac{\lambda^2}{256\pi^2} + \frac{3e_{CW}^4}{64\pi^2}\right)\phi_{cl}^4\left(\ln\frac{\phi_{cl}^2}{M^2} - \frac{25}{6}\right). \tag{2.2.19}$$

We now want to investigate the minima of the effective potential to determine if we get spontaneous symmetry breaking. We will start by considering the pure scalar ϕ^4 theory by setting $e_{CW} = 0$. This gives an effective potential of

$$V = \frac{1}{4!}\lambda\phi_{cl}^4 + \frac{\lambda^2}{256\pi^2}\phi_{cl}^4\left(\ln\frac{\phi_{cl}^2}{M^2} - \frac{25}{6}\right). \tag{2.2.20}$$

It looks as if this potential could develop a minimum away from the origin, but we can only achieve this minimum for a non-zero ϕ_{cl} if

$$\lambda\ln\frac{\phi_{cl}^2}{M^2} \sim -\frac{32}{3}\pi^2. \tag{2.2.21}$$

This is outside the validity of perturbation theory as each higher order is expected to come with a factor of $\lambda\ln\phi_{cl}^2/M^2$, and we must therefore view this minimum as spurious. It would have been possible to anticipate this conclusion as the only way to get a minimum, at non-zero values of ϕ_{cl}, is to balance the λ-term with the λ^2-term.

For scalar QED, we can get symmetry breaking at perturbative couplings as we can now balance λ against e_{CW}^4. It is the interactions of the scalar field with the gauge bosons that will dynamically break the symmetry. As $\lambda \sim e_{CW}^4$ is small, we will for consistency drop the λ^2 term. Keeping the λ and the e_{CW}^4-terms gives the following effective potential

$$V = \frac{1}{4!}\lambda\phi_{cl}^4 + \frac{3e_{CW}^4}{64\pi^2}\phi_{cl}^4\left(\ln\frac{\phi_{cl}^2}{M^2} - \frac{25}{6}\right). \tag{2.2.22}$$

We choose $M = \langle\phi\rangle$, and find that there is a minimum for a non-zero value of ϕ_{cl} if

$$\lambda = \frac{33}{8\pi}e_{CW}^4. \tag{2.2.23}$$

Given this relationship between the coupling constants, we get a final effective potential of

$$V = \frac{3e_{CW}^4}{64\pi^2}\phi_{cl}^4\left(\ln\frac{\phi_{cl}^2}{\langle\phi\rangle^2} - \frac{1}{2}\right). \tag{2.2.24}$$

This potential only depends on e and $\langle\phi\rangle$, not on λ. We have traded a dimensionless coupling constant, λ, for a dimensionful parameter $\langle\phi\rangle$. This phenomenon goes under the name of dimensional transmutation. Using the Coleman-Weinberg mechanism, a scale, $\langle\phi\rangle$, has been generated from a theory with no input mass scales. It is now straightforward to calculate the masses of the particles in the theory. We get one massive vector boson with mass

$$M_A^2 = e_{CW}^2 \langle\phi\rangle^2 \,, \tag{2.2.25}$$

and one massive Higgs boson with mass

$$M_h^2 = \frac{d^2 V}{d\phi^2} = \frac{3e_{CW}^4}{8\pi^2}\langle\phi\rangle^2. \tag{2.2.26}$$

We notice that the Higgs boson mass is parametrically smaller than the gauge boson mass.

2.2.3 Coleman-Weinberg Mechanism and Renormalisation Group Running

It can seem like a strange coincidence, or evidence of fine tuning, that we only get a non-zero vev for ϕ_{cl} when the coupling constants are carefully matched as in Equation (2.2.23). In fact, there is no fine-tuning in this relationship at all [80]. This can be understood by studying the renormalisation group running of the couplings in the U(1) theory considered above. The relevant β-functions are given by [79]

$$\beta_{eCW} = \frac{de}{dt} = \frac{e_{CW}^3}{48\pi^2} \,, \quad \beta_\lambda = \frac{d\lambda}{dt} = \frac{1}{4\pi^2}\left(\frac{5}{6}\lambda^2 - 3e_{CW}^2\lambda + 9e_{CW}^4\right), \tag{2.2.27}$$

where $t = ln\frac{\mu}{M_0}$. We will now consider a situation where at a large energy scale, M_0, we set arbitrary values for the couplings $e_{CW}(M_0) = e_0$ and $\lambda(M_0) = \lambda_0$, and then evolve the couplings down to lower energies. We see that the β-function for λ is positive such that the value of λ will decrease as energy decreases. When λ becomes small, the e^4-term dominates, and the coupling will continue to decrease until it eventually becomes negative. At some energy scale, M_c, the value of λ will be such that

$$\lambda(M_c) = \frac{33}{8\pi}e_{CW}(M_c)^4, \tag{2.2.28}$$

and this is the scale where symmetry breaking happens. It is the positive β-function that drives λ negative and induces spontaneous symmetry breaking. This gives another argument for why we did not get symmetry breaking in the pure scalar field theory. In this theory we have $\beta_\lambda \propto \lambda^2$ which gives a solution of

$$\lambda(t) \propto \frac{1}{t}. \tag{2.2.29}$$

We can see that this solution does not drive λ negative, and would therefore not be able to induce symmetry breaking as above.

To implement the CW mechanism successfully, we need a classically massless theory where a coupling is driven negative by the RG running. This triggers symmetry breaking which dynamically generates scales by dimensional transmutation.

2.3 BSM Models with Classical Scale Invariance

We will now consider how to construct classically scale-invariant models for BSM physics. First, we will discuss classical scale invariance and the hierarchy problem. And then we will show how the SM can be extended in a phenomenologically viable way so that all scales are generated via the CW mechanism in a CSI U(1) extension to the SM. We will then move on to describe different classes of CSI extensions to the SM that have been proposed in the literature, before considering some of the common phenomenological consequences of these models.

2.3.1 Hierarchy Problem in Classically Scale-Invariant Models

Classically scale-invariant models were introduced to address the hierarchy problem [75]. In Section **1.2.4**, we explained how the hierarchy problem is best thought of in terms of mass thresholds of massive particles. In CSI models all scales will be radiatively generated, and in all proposed models there is only one scale. All masses in the theory will be parametrically related to the generated scale. Therefore, a classically scale-invariant theory does not have a hierarchy problem as long as this radiatively generated scale is of the order of the weak scale. For the theory to be

useful, it needs to address the observational problems in the SM with only this scale. In CSI theories all scales are connected at tree level, and, as we will see in the next section, the Higgs mass parameter in the Lagrangian, μ_{SM}, will be given by

$$\mu_{\text{SM}}^2 \propto \lambda_p \langle\phi\rangle^2 \,, \tag{2.3.30}$$

where ϕ is a field that develops a vacuum expectation value due to the CW mechanism, and λ_p is its portal coupling to the Higgs. As long as $\lambda_p \langle\phi\rangle^2 \sim v^2$, the theory will not destabilise the weak scale. This implies new physics around the weak scale unless λ_p is extremely small. A very small λ_p could be technically natural but unappealing unless there is a mechanism to explain such a small coupling constant, as for example due to shift symmetry in [81].

CSI theories do not introduce a naturalness problem, but they do not protect the Higgs mass from new large scales that can appear in for example quantum gravity. This means that any new UV theory beyond the CSI extension needs to be such that it does not reintroduce large corrections to the Higgs mass. Without such large corrections, CSI theories will naturally generate scales that are much smaller than the UV cut-off, Λ_{UV}, of the theory. In the previous section we saw that the scale, $\langle\phi\rangle$, was generated when

$$\lambda(\langle\phi\rangle) = \frac{33}{8\pi} e_{CW}(\langle\phi\rangle)^4. \tag{2.3.31}$$

By solving the RG equations we find a relationship between $\langle\phi\rangle$, which fulfils this relation, and Λ_{UV} [82],

$$\langle\phi\rangle \approx \Lambda_{\text{UV}} \exp\left(\frac{-24\pi^2}{e_{CW}^2(\langle\phi\rangle)}\right). \tag{2.3.32}$$

The exponential suppression is due to the logarithmic running of the coupling constant. This is completely analogous to why Λ_{QCD}, the QCD confinement scale, can naturally be much smaller than the M_{pl}. Dimensional transmutation occurs in QCD and other gauge theories that become strongly coupled. In QCD we trade α_s for Λ_{QCD} in the same way as we did when trading λ for $\langle\phi\rangle$ above. Again, the logarithmic running of the coupling g will lead Λ_{QCD} to be exponentially suppressed from the Λ_{UV}.

Classical scale invariance does not solve the hierarchy problem in the same way as, for example, Supersymmetry. It does require that quantum gravity and any

other new UV physics do not destabilise the Higgs mass. If that is the case, the scales of the theory will naturally be generated at scales exponentially smaller than the UV cut-off, and there will be no fine-tuning.

2.3.2 U(1) CSI Extension of the SM

After the measurement of the mass of the weak vector bosons and the Higgs boson, it is impossible to implement the CW mechanism in the Higgs sector of the SM. As we see from Equations (2.2.25) and (2.2.26), the CW mechanism predicts vector bosons that are significantly heavier than the Higgs bosons, in contradiction with the experimentally observed values. In 1996, Hempfling [83] suggested a minimal, phenomenologically viable extension to the SM where all fundamental mass scales are given by dimensional transmutation. First the SM is made classically massless by setting the Higgs mass to zero, and then it is extended with a U(1) hidden gauge group. There is one new complex scalar field, Φ, which is charged under the hidden gauge group, but is a SM singlet. The hidden sector is coupled to the SM via a Higgs portal coupling, and we have the following scalar potential

$$V_{\text{cl}}(H, \Phi) = \lambda_\phi (\Phi^\dagger \Phi)^2 + \lambda_H (H^\dagger H)^2 - \lambda_{\text{P}} (H^\dagger H)(\Phi^\dagger \Phi) \,. \tag{2.3.33}$$

The Φ field, charged under the hidden U(1) gauge group, can now develop a vacuum expectation value via the CW mechanism as described above. The condition relating the mass of gauge bosons and Higgs bosons now occurs in the hidden sector and therefore has no experimental constraints. The generated scale is then transmitted to the SM due to the Higgs portal coupling and gives a negative mass squared to the SM Higgs

$$\mu_{\text{SM}}^2 = -\lambda_p \langle \Phi \rangle^2. \tag{2.3.34}$$

This allows electroweak symmetry breaking (EWSB) to happen as usual in the SM, giving masses to the fermions and the weak vector bosons. All the masses will be given in terms of the only mass scale in the theory, $\langle \Phi \rangle$. We will now study this example in more detail. We will show how the CW mechanism generates a vev in the hidden sector, and how this vev gets transmitted to the SM. Since both the scalars develop vevs, they will mix. We will calculate the mass eigenstates and the

corresponding mass eigenvalues m_{h_1} and m_{h_2}. In this section we will follow the approach of Ref. [82] by first considering the one-loop contributions in the hidden sector before adding the SM corrections at a later stage. We will also use the $\overline{\text{MS}}$ renormalisation scheme instead of the cut-off scheme calculation presented above.

The complex scalar field, Φ, is given by

$$\Phi = \frac{1}{\sqrt{2}}(\phi + i\phi_2). \qquad (2.3.35)$$

We have the following tree-level scalar potential

$$V_0(h, \phi) = \lambda_\phi (\Phi\Phi^\dagger)^2 + \lambda_H (HH^\dagger)^2 - \lambda_{\text{P}} HH^\dagger \Phi\Phi^\dagger. \qquad (2.3.36)$$

After symmetry breaking, we will be left with two real scalars in the unitary gauge,

$$H = \frac{1}{\sqrt{2}}(0, h), \quad \Phi = \frac{1}{\sqrt{2}}\phi. \qquad (2.3.37)$$

We start by analysing the scale generation in the hidden sector using the one-loop effective potential which in the $\overline{\text{MS}}$ scheme reads, cf. [84],

$$V_1(\phi; \mu) = \frac{\lambda_\phi^{(0)}}{4}\phi^4 + \frac{3}{64\pi^2}e_{\text{CW}}^4(\mu)\phi^4 \left(\log\frac{e_{\text{CW}}^2(\mu)\phi^2}{\mu^2} - \frac{5}{6}\right). \qquad (2.3.38)$$

The potential depends on the RG scale, μ, that appears both in the logarithm and also in the one-loop running CW gauge coupling constant $e_{\text{CW}}(\mu)$. The superscripts indicate a tree level coupling. The running (or renormalised) self-coupling, λ_ϕ, at the RG scale μ is defined via

$$\lambda_\phi(\mu) = \frac{1}{3!}\left(\frac{\partial^4 V_1(\phi; \mu)}{\partial\phi^4}\right)_{\phi=\mu} = \lambda_\phi^{(0)} + \frac{10e_{\text{CW}}(\mu)^4 + 3e_{\text{CW}}(\mu)^4 \log\left(e_{\text{CW}}(\mu)^2\right)}{16\pi^2}.$$
$$(2.3.39)$$

We can now express the effective potential in terms of this renormalised coupling constant by substituting $\lambda_\phi^{(0)} = \lambda_\phi - (10e_{\text{CW}}^4 + 3e_{\text{CW}}^4 \log e_{\text{CW}}^2)/(16\pi^2)$ into eq. (2.3.38), obtaining

$$V_1(\phi; \mu) = \frac{\lambda_\phi(\mu)\phi^4}{4} + \frac{3e_{\text{CW}}(\mu)^4}{64\pi^2}\phi^4 \left(\log\left(\frac{\phi^2}{\mu^2}\right) - \frac{25}{6}\right). \qquad (2.3.40)$$

This is the one-loop effective potential for the hidden sector. It makes the vacuum occur at $\langle\phi\rangle \neq 0$. Minimising the potential (2.3.40) with respect to ϕ at $\mu = \langle\phi\rangle$, gives

the characteristic Coleman-Weinberg-type $\lambda_\phi \propto e_{\mathrm{CW}}^4$ relation between the scalar and the gauge couplings we saw in Section **2.2.2**,

$$\lambda_\phi = \frac{11}{16\pi^2} e_{\mathrm{CW}}^4 \qquad \text{at} \quad \mu = \langle\phi\rangle \, . \tag{2.3.41}$$

The 3! mismatch between this result and the result in [79] and in Equation (2.2.23) is due to the difference in definition of λ_ϕ in the scalar potential. Compare equations (2.2.15) and (2.3.36).

Shifting the CW scalar by its vev $\phi \to \langle\phi\rangle + \phi$, and expanding the effective potential in (2.3.40), we find the mass of ϕ,

$$m_\phi^2 = \frac{3e_{\mathrm{CW}}^4}{8\pi^2} \langle\phi\rangle^2 \, , \tag{2.3.42}$$

and the mass of the Z' U(1) vector boson,

$$M_{Z'}^2 = e_{\mathrm{CW}}^2 \langle\phi\rangle^2 \quad \gg \quad m_\phi^2 = \frac{3e_{\mathrm{CW}}^4}{8\pi^2} \langle\phi\rangle^2 \, . \tag{2.3.43}$$

The $\overline{\mathrm{MS}}$ expressions above are once again identical to those derived in the cut-off scheme in [79, 82].

We now turn to the SM part of the scalar potential (2.3.36), specifically

$$V_0(h) = \frac{\lambda_H}{4} h^4 - \frac{\lambda_{\mathrm{P}}\langle\phi\rangle^2}{4} h^2 \, . \tag{2.3.44}$$

The SM scale μ_{SM}^2 is generated by the CW vev in the second term,

$$\mu_{\mathrm{SM}}^2 = \lambda_{\mathrm{P}}\langle\phi\rangle^2 \, , \tag{2.3.45}$$

and this triggers electroweak symmetry breaking and the appearance of the Higgs vev v. We also need to take the portal coupling into account. In the hidden sector it provides a correction to the CW matching condition (2.3.41) and the CW mass (2.3.42). By including the last term on the *r.h.s* of (2.3.36) to the effective potential in (2.3.38) and (2.3.40), we find a λ_{P}-induced correction to the equations (2.3.41)-(2.3.42), which now read

$$\lambda_\phi = \frac{11}{16\pi^2} e_{\mathrm{CW}}^4 + \lambda_{\mathrm{P}} \frac{v^2}{2\langle\phi\rangle^2} \qquad \text{at} \quad \mu = \langle\phi\rangle \tag{2.3.46}$$

$$m_\phi^2 = \frac{3e_{\mathrm{CW}}^4}{8\pi^2} \langle\phi\rangle^2 + \lambda_{\mathrm{P}} v^2 \tag{2.3.47}$$

We will mainly consider small values of λ_P, so that these corrections are negligible as $\lambda_P v^2/(2\langle\phi\rangle^2) \sim \lambda_P^2/(4\lambda_H) \ll 1$.

Having calculated the masses in the hidden sector, we now move on to compute the SM Higgs mass. We perform the usual shift, $h(x) \to v + h(x)$, and represent the SM scalar potential (2.3.44) as follows,

$$V(h) = \frac{\lambda_H^{(0)}}{4}(v+h)^4 - \frac{\mu_{\text{SM}}^2}{4}(v+h)^2 \,. \tag{2.3.48}$$

The vev, v, is determined by minimising (2.3.48), and the Higgs mass is given by the second derivative of (2.3.48),

$$v^2 = \frac{\lambda_P}{2\lambda_H^{(0)}}\langle\phi\rangle^2\,, \qquad m_h^2 = 2\lambda_H\,v^2\,. \tag{2.3.49}$$

The two scalars, h and ϕ, both have vevs and therefore mix via the mass matrix,

$$M^2 = \begin{pmatrix} 2\lambda_H\,v^2 & -\sqrt{2\lambda_P\lambda_H^{(0)}}\,v^2 \\ -\sqrt{2\lambda_P\lambda_H^{(0)}}\,v^2 & m_\phi^2 \end{pmatrix}\,, \tag{2.3.50}$$

where m_ϕ^2 is given in (2.3.47) (and already includes the λ_P correction). The mass eigenstates are the two Higgs fields, h_1 and h_2 with mass eigenvalues,

$$m_{h_1,h_2}^2 = \frac{1}{2}\left(2\lambda_H v^2 + m_\phi^2 \pm \sqrt{\left(2\lambda_H v^2 - m_\phi^2\right)^2 + 8\lambda_P\lambda_H v^4}\right)\,. \tag{2.3.51}$$

It is easy to see that in the limit where the portal coupling, λ_P, goes to zero, the mixing between the two scalars h and ϕ disappears, and we get m_h^2 and m_ϕ^2 as mass eigenvalues, as one would expect. However, for non-vanishing λ_P, the mass eigenstates h_1 and h_2 are given by

$$\begin{pmatrix} h_1 \\ h_2 \end{pmatrix} = \begin{pmatrix} \cos\theta & -\sin\theta \\ \sin\theta & \cos\theta \end{pmatrix} \begin{pmatrix} h \\ \phi \end{pmatrix}\,, \tag{2.3.52}$$

with a non-trivial mixing angle θ. The SM Higgs with mass $m_{h\,\text{SM}}^2 = \simeq (126\,\text{GeV})^2$ is the eigenstate h_1 which is 'mostly' the h scalar (i.e. $\cos\theta\times$ the scalar coupled to the SM electroweak sector) for small values of the mixing angle,

$$h_{\text{SM}} := h_1 = h\cos\theta - \phi\sin\theta\,, \qquad m_{h_1} = 125.66\,\text{GeV}\,. \tag{2.3.53}$$

In the approximation where $(8\lambda_\text{P}\lambda_H^{(0)}v^4)/(2\lambda_H v^2 - m_\phi^2)^2$ is small, we can expand the square root in (4.1.16) to obtain analytical expressions for the scalar masses:

$$m_{h_1}^2 = m_+^2 = 2v^2\lambda_H \left(1 + \frac{\lambda_\text{P}(\lambda_H^{(0)}/\lambda_H)\,v^2}{2\lambda_H v^2 - m_\phi^2}\right), \quad \text{for} \ \ 2\lambda_H v^2 > m_\phi^2, \quad\quad (2.3.54)$$

$$m_{h_1}^2 = m_-^2 = 2v^2\lambda_H \left(1 - \frac{\lambda_\text{P}(\lambda_H^{(0)}/\lambda_H)\,v^2}{m_\phi^2 - 2\lambda_H v^2}\right), \quad \text{for} \ \ m_\phi^2 > 2\lambda_H v^2. \quad\quad (2.3.55)$$

We can see that a U(1) extension of the CSI SM is a phenomenologically viable BSM model where all the scales are generated via dimensional transmutation. It includes many of the main features of CSI models. The EW scale is transmitted to the Higgs via an extended scalar sector coupled with portal couplings. We are left with two massive neutral scalar fields that mix. It is straightforward to achieve the correct value of the Higgs mass. With the Higgs mass fixed, this simple viable model only has two free parameters which we can take to be the gauge coupling, e_{CW}, and the portal coupling, λ_p. The model is therefore predictive. In Chapter **4** we will investigate both the Higgs vacuum stability and the collider phenomenology of this model.

2.3.3 CSI Extensions of the SM

In this section, we will discuss the different CSI models that have been proposed in the literature. All CSI extensions of the SM start with the SM Lagrangian without the Higgs mass term. Extra field content and potentially new gauge groups are then added to generate scales dynamically. This scale can then be transmitted to the Higgs to trigger electroweak symmetry breaking. There are two main categories of CSI models divided by the strength of the couplings of the new field content. We have already seen examples of weakly coupled models where scales are generated by the CW mechanism, but there are also proposed models where the scale is generated, as in QCD, by confinement when the coupling becomes large (see [85–90]). In this thesis, we will focus on the weakly coupled theories. This class has two main subclasses: one where the CW mechanism is achieved without any extra gauge groups by extending the scalar sector [74, 81, 91–108], and another where we extend the SM with a new gauge group as in the example in the previous section and

in [1, 2, 82, 83, 109–123].

If we consider the theories without extra gauge sectors, there are two main ways to trigger EWSB dynamically. We have already seen that if the SM SU(2) gauge group were to provide the quantum corrections needed to make the CW mechanism work, the Higgs boson mass would have to be much smaller than the mass of the $W^\pm$ and Z bosons. Another problem with the CW mechanism in the SM is that the RG equation for the Higgs self-coupling is dominated by the top Yukawa, making the β-function negative. This will ruin the CW symmetry breaking mechanism as the self coupling will increase with decreasing energy scale and never become negative. The first approach to CSI model building without extra gauge groups is to add extra scalars to the Higgs sector, which can provide large positive contributions to the β-function [74, 91, 93, 96, 98, 102, 103, 105, 124]. In these models, it is a portal type coupling between the scalars that drives the CW mechanism, and therefore we do not get the predicted hierarchy between the SU(2) gauge boson masses and the Higgs mass seen above, making this a phenomenologically viable theory.

As an example, let us consider the approach in Hill [91]. They find that EWSB can be dynamically achieved when the SM is extended with an extra inert[3] Higgs doublet which is portally coupled to the Higgs. We then get an extra contribution to the β-function for the Higgs quartic coupling, λ_H, schematically given by

$$\frac{d\lambda_H}{dlog\mu} \propto \lambda_H^2 - y_t^4 + \lambda_h y_t^2 + \lambda_p^2 ... , \tag{2.3.56}$$

where λ_p is the portal coupling and y_t is the top Yukawa coupling. If λ_p is large enough to overcome the negative contribution from the top Yukawa, the CW mechanism will generate a vev for the Higgs. This gives a prediction for the ratio between the two Higgs masses in the same way as we got a prediction for the ratio of the gauge boson and scalar masses in the U(1) example. The model predicts that the mass of the second Higgs doublet is $m_{h_2} \approx 376$ GeV. This gives a phenomenologically viable and very predictive model, but due to the large portal coupling the model will develop a Landau pole at the ~ 5 TeV scale.

---

[3]A SU(2) doublet that does not get a vev.

In [81, 92, 95, 100, 101, 104, 107, 108] a viable CSI model is achieved by using the CW mechanism to generate a vev for a new scalar field, not the Higgs boson, dynamically. This scalar field is then portally coupled to the Higgs boson, and therefore induces a EWSB by providing a negative mass squared term for the Higgs similarly to the U(1) example above. For a successful CW mechanism, these models will need additional field content in addition to the one new scalar field. For example in [92], there are two new real scalar fields, ϕ_1 and ϕ_2. This gives a scalar potential of

$$V(h, \phi_1, \phi_2) = \lambda_H \frac{1}{4} h^4 + \lambda_1 \frac{1}{4} \phi_1^4 + \lambda_2 \frac{1}{4} \phi_2^4 + \lambda_{H1} \frac{1}{4} \phi_1^2 h^2 + \lambda_{H2} \frac{1}{4} \phi_2^2 h^2 + \lambda_{12} \frac{1}{4} \phi_1^2 \phi_2^2. \quad (2.3.57)$$

We can now organise the coupling constants so that λ_1 will be driven negative at low energy due to the contribution of a large λ_{12} to its β-function. This will lead ϕ_1 to develop a vev which will be transmitted to the Higgs via the portal coupling λ_{H1}. The end result is two massive scalars that mix with each other, as in the previous section, and one additional massive scalar that does not mix. Since the final scalar does not mix with the Higgs, it does not decay and can therefore be a dark matter candidate. This class of models is less minimal, but it can easily incorporate DM and Higgs vacuum stability due to the extra field content.

CSI models with extended gauge sectors differ from each other both in field content and in gauge structure. The simplest models have a new U(1) gauge group as shown above. This model has been studied in [2, 82, 83, 116, 118, 121–123], and we will study Higgs vacuum stability and dark matter in this model in Chapter **4**. A popular extension to this model is to consider the SM extended by a $U(1)_{B-L}$ gauge group [1, 2, 114, 115, 117–120]. All the SM fields are charged under this group with their charge given by their baryon minus lepton number. To be anomaly free, these models require three generations of right-handed neutrinos, and have therefore been studied to explain neutrino mass and leptogenesis as we will see in detail in Chapter **3**. In addition to a U(1) gauge group, extensions with SU(2) groups have been studied in [2, 3, 111, 112]. As we will discuss in Chapter **4**, these models are very interesting because the SU(2) gauge bosons are good dark matter candidates. In [113] they consider a hidden sector consisting of SU(2)×U(1). As long as the CW

mechanism is employed in the hidden sector, these models are phenomenologically viable and have many interesting applications to BSM physics.

2.3.4 Classically Scale-Invariant BSM Physics

As discussed above, for CSI models not to have a hierarchy problem they need to solve the observational questions in the SM without introducing new large scales. Dark matter has been studied in great detail in CSI models, both in the strongly coupled models [85, 87, 90] and in the weakly coupled models [2, 92, 95, 96, 98, 102, 103, 108, 111–113, 121, 122]. In the weakly coupled models, one can implement many different dark matter scenarios. We can have scalar, fermion or vector boson dark matter candidates. In most models this dark matter is coupled to the Higgs via a portal coupling, sometimes directly and sometimes via a scalar mediator. The dark matter candidate is commonly a standard WIMP thermal relic, but also other production mechanisms are possible(see e.g. [103]). If the DM is produced via thermal freeze-out, this can give interesting constraints for these models. The observed relic density can give a lower limit on the Higgs portal coupling so as to not overclose the Universe. The annihilation cross-section, which in many models depends on the portal coupling, can not be too small as then dark matter will freeze out too soon, and be too abundant. This constrains the portal coupling from the opposite side to collider experiments which tends to constrain it form above. In Chapter **4** and **5**, we will investigate CSI models with scalar and vector boson DM, and in Chapter **6** we will discuss LHC phenomenology for models with scalar mediators to fermionic dark matter.

Generating a matter antimatter asymmetry has been much less studied in the context of CSI models. Models with a $U(1)_{B-L}$ gauge group and right-handed neutrinos would be a good starting point for standard leptogenesis, but as discussed in Chapter **1** very heavy right-handed neutrinos are needed, which is incompatible with classical scale invariance. It is possible to reduce the mass of the right-handed neutrinos by fine-tuning their mass difference. This approach, called resonant leptogenesis, has been studied in a CSI framework in [119]. In Chapter **3**, we present a successful approach based on leptogenesis by the oscillation of GeV scale right-

handed neutrinos.

In CSI models the vacuum should be stable[4] up to the Planck scale, without requiring new field content at large energy scales. We will study this in detail for U(1), U(1)$_{B-L}$ and SU(2) models in Chapter **4**. The Higgs vacuum instability has also successfully been addressed in [92, 95, 111, 112, 116]. In all these models the Higgs potential is stabilised by positive contributions to the β-functions of the Higgs self-coupling from portal couplings in an extended Higgs sector.

Inflation has successfully been implemented in CSI models [99, 115, 121, 125]. One example of an inflationary model from [121] is a U(1) CSI extension of the SM with an additional real scalar singlet. This singlet can then successfully play the role of both inflaton and dark matter. The strong CP problem has been addressed in [81, 104]. Axions require a very large scale $\sim 10^{12}$ GeV to solve the strong CP problem. Therefore, a hidden sector that includes an axion has to be extremely weakly coupled. This can potentially be explained by an approximate shift symmetry.

CSI models, unlike for example Supersymmetric models, do not protect the Higgs mass from quantum gravity effects at the Planck scale. Since it is impossible with today's knowledge to determine if quantum gravity will give large corrections to the Higgs mass, this might or might not be considered a problem. There have been some attempts to consider gravity in a CSI framework [106, 120, 125, 126]. The main idea is to think of the Planck mass $M_{\rm pl}$ as the vev of a scalar field, s, that is non minimally coupled to gravity. The Einstein-Hilbert term in the standard general relativity (GR) Lagrangian ($M_{\rm pl}^2 R$ where R is the Ricci scalar curvature) is removed, and we get a scalar-tensor theory for gravity

$$\mathcal{L} = \sqrt{g}\left(-\frac{\epsilon}{2}s^2 R + \mathcal{L}_m\right). \qquad (2.3.58)$$

$\mathcal{L}_m$ is the normal matter Lagrangian, including kinetic terms for s. If the theory dynamically generates a vev for s, $\langle s \rangle = M_{\rm pl}/\sqrt{\epsilon}$, we recover the standard GR Lagrangian. Since $\mathcal{L}_m$ will include a portal coupling, λ_p, between the new scalar s

---

[4]It is possible that meta-stability is sufficient as discussed in Chapter **1**.

and the Higgs boson, this will induce a Higgs mass of

$$M_h^2 = \lambda_p \frac{M_{\mathrm{pl}}^2}{\epsilon} \, . \tag{2.3.59}$$

Getting the observed value for the Higgs mass this requires an extremely small value of λ_p. As λ_p is renormalised multiplicatively, this could be considered to be technically natural. One of the main questions regarding gravitational corrections to the Higgs mass is if microscopic black holes with mass around M_{pl} will give large corrections. In the model discussed in [126], the black holes do not give large contributions to the Higgs mass, since the black holes have to be significantly heavier than M_{pl}. Only black holes with mass just around the Planck scale give a large contribution as the contribution is exponentially suppressed by the black hole entropy.

Classically scale-invariant models come in many shapes and can successfully be used to explain many BSM phenomena. Due to the classical scale invariance, these models often have few new parameters and are predictive. The main consequence of imposing classical scale invariance is that there can not be any large scales in the theory. Therefore, grand unification is incompatible with this approach, and so is standard leptogenesis with right-handed neutrinos with masses of 10^{12} GeV. A very compelling feature of CSI models is that all mass scales have to be dynamically generated. This means that the mass scales of fundamental particles have similar origin as the mass scales of protons and neutrons. If the Planck scale is also dynamically generated, all mass scales in the Universe will be due to dimensional transmutation.

2.3.5   Phenomenology of CSI Models

A common feature of all the weakly coupled CSI models is that they require extended scalar sectors. Either a vacuum expectation value generated for another scalar has to be communicated to the Higgs, or the Higgs needs large positive contributions to the β-function from other scalars. This means that all these CSI models have portal couplings to the Higgs. Higgs portal coupling models have been extensively studied (see e.g. [127, 128]). If the scalar field, s, coupled to the Higgs via the Higgs portal coupling develops a vev, it will mix with the Higgs as described above. We get two

mass eigenstates h_1 and h_2,

$$h_1 = h\cos\theta - s\sin\theta \quad h_2 = s\cos\theta + h\sin\theta \, , \tag{2.3.60}$$

where θ is the mixing angle. This mixing modifies the normal Higgs production cross-sections with a factor $\cos^2\theta$, and it means that h_2 can be produced from and decay to SM fields. This modification of the Higgs coupling allows us to constrain the mixing angle. The signal strengths for Higgs production gives a bound of $\sin\theta < 0.44$ [129]. One can also get a mass dependent bound on θ from the W boson mass, as shown in Figure 3 in Ref. [129]. The constraint comes from the contributions of the heavy second Higgs like scalar, h_2, to the W-boson mass at loop level. In the mass range $m_{h_2} \sim 1$ TeV, the limit becomes $\sin\theta < 0.3$.

If h_2 is lighter than half the Higgs mass, $m_{h_2} < m_h/2 = 62.5$ GeV, then h_1 can very efficiently decay into two h_2s, giving a large invisible branching ratio of the Higgs. Current limits on the invisible branching ratio give a limit on the portal coupling of $\lambda_p \lesssim 10^{-4}$ [82] in this regime. If h_2 can decay into SM particles, we will also get limits from the non-observation of a second SM-like Higgs. We will discuss this further in Chapter **4**.

If $m_{h_2} > 2m_{h_1}$, the $h_2 \to h_1 h_1$ decay is kinematically allowed. This process could then be visible at the 13 TeV LHC [129]. In addition to the extended Higgs sector, most CSI models also have other phenomenological consequences. For models with dark matter, one can look for signals of missing energy at colliders (see Chapter **6**), and at direct and indirect detection. In models where the SM fermions are charged under the hidden gauge group as in the $U(1)_{B-L}$ model, one can look for a Z' boson peak, for example, in the dilepton final state. Other extensions of the basic model will have additional signatures at colliders or at cosmological experiments. Even if CSI models do not have a smoking gun signature, they are predictive and discoverable.

Chapter 3

Leptogenesis and Neutrino Oscillations in the Classically Scale-Invariant Standard Model with the Higgs Portal

In this chapter, based entirely on [1], we will show how to generate a matter anti-matter asymmetry in a classically scale-invariant extension of the Standard Model. This is an important step in establishing CSI extensions of the SM as viable BSM theories. As no supersymmety has been discovered and there is no evidence of any anomalies in the quark flavour sector, the most attractive scenario for generating the baryon asymmetry of the Universe is arguably leptogenesis. Models of leptogenesis also explain neutrino masses elegantly via the see-saw mechanism. As discussed in Section **1.2.2**, in the standard scenario of thermal leptogenesis [55], a lepton asymmetry is generated by decays of heavy right-handed Majorana neutrinos into Standard Model leptons at temperatures much above the electroweak scale. The lepton asymmetry is then reprocessed into the baryon asymmetry by electroweak sphalerons [52, 130] above the electroweak scale.

To generate the observed value of the matter-antimatter asymmetry in the vanilla version of leptogenesis, it is necessary to have extremely heavy masses for sterile neu-

trinos, $M \gtrsim 10^9$ GeV [58, 131]. If this was the full story, classical scale-invariance would be ruled out by $M \ggg v$. Instead, we will adopt an alternative approach to leptogenesis pioneered in [72], and further developed in [132, 133]. In this approach, the lepton flavour asymmetry is produced by oscillations of the right-handed Majorana neutrinos with masses of the order of the electroweak scale or below. This low scale is easily accommodated in a classically scale-invariant setup. We will consider an extension of the SM with a hidden $U(1)_{B-L}$ gauge group which includes GeV scale right-handed neutrinos. This gives a good CSI realisation of this alternative approach to leptogenesis.

The chapter is organised as follows: we will start with a brief introduction of thermal field theory in Section **3.1**. Then, in Section **3.2**, we set up the U$(1)_{B-L}$ extension of the SM model which automatically includes sterile right-handed Majorana neutrinos. The formalism of leptogenesis via Majorana neutrino oscillations is presented in **3.3.1**. Section **3.3.2** adapts and applies theses ideas to our classically scale-invariant models. The matter-antimatter asymmetry is calculated and analysed in Section **3.4** which also contains multiple benchmark points. Conclusions are outlined in Section **3.5**.

3.1 Brief Review of Thermal Field Theory

To calculate expectation values of operators in a QFT at non-zero temperature, we consider a system in a grand canonical ensemble where the system can exchange both energy and particles with a heat reservoir with constant temperature T. When calculating traces by summing over all the states of such an ensemble, each state has a weight of $e^{-\beta H}$ where $\beta = 1/T$ and H is the Hamiltonian of the system. An operator A then has the following expectation value

$$\langle A \rangle = \frac{Tr[e^{-\beta H} A]}{Tr[e^{-\beta H}]} \,. \tag{3.1.1}$$

We can calculate these expectation values using normal QFT techniques, but we evolve the system in imaginary time with periodic or anti-periodic boundary condi-

tions for bosons and fermions respectively. Implementing periodic boundary conditions for time changes integrals over energy to sums over frequencies, $\int d^3k \, d\omega_k \rightarrow \sum_{\omega_k} \int d^3k$. Using these techniques, one can calculate the thermal one-loop potential for a theory [84]

$$V_{\text{one-loop}}^{\text{tot}} = V_{\text{one-loop}}^{T=0} + V_{\text{one-loop}}^{T}, \tag{3.1.2}$$

where $V_{\text{one-loop}}^{T=0}$ is the standard one-loop potential at zero temperature discussed in Chapter **2** and V_{1loop}^{T} is the thermal correction given by

$$V_{\text{one-loop}}^{T} = \frac{1}{2\pi^2 \beta^4} \left(\sum_{i \in \text{bosons}} n_i J_B[m_i^2 \beta^2] + \sum_{j \in \text{fermions}} n_j J_F[m_j^2 \beta^2] \right). \tag{3.1.3}$$

J_B and J_F are the bosonic and fermionic thermal functions, given by

$$J_B[m_i^2 \beta^2] = \int_0^\infty dx \, x^2 \log\left(1 - e^{-\sqrt{x^2 + \beta^2 m^2}}\right), \text{ and} \tag{3.1.4}$$

$$J_F[m_i^2 \beta^2] = \int_0^\infty dx \, x^2 \log\left(1 + e^{-\sqrt{x^2 + \beta^2 m^2}}\right). \tag{3.1.5}$$

At high temperature these function can be expanded as follows,

$$J_B[m^2/T^2] = -\frac{\pi^4}{45} + \frac{\pi^2}{12}\frac{m^2}{T^2} - \frac{\pi}{6}\left(\frac{m^2}{T^2}\right)^{3/2} - \frac{1}{32}\frac{m^4}{T^4}\log\frac{m^2}{a_b T^2} + O\left(\frac{m^6}{T^6}\right), \text{ and} \tag{3.1.6}$$

$$J_F[m^2/T^2] = \frac{\pi^4}{360} - \frac{\pi^2}{24}\frac{m^2}{T^2} - \frac{1}{32}\frac{m^4}{T^4}\log\frac{m^2}{a_f T^2} + O\left(\frac{m^6}{T^6}\right), \tag{3.1.7}$$

where $\log a_b = 5.4076$ and $\log a_f = 2.6351$. In the high temperature limit, the scalar potential of theories with a scalar, ϕ, becomes

$$V^{tot}(\phi, T) = D(T^2 - T_0^2)\phi^2 - ET\phi^3 + \frac{\lambda(T)}{4}\phi^4, \tag{3.1.8}$$

where D, T_0, E and $\lambda(T)$ are calculable constants for a given field content. Both fermions and bosons will contribute to all of these constants, except for E which only gets bosonic contributions due to the m^3/T^3 term in (3.1.6). We see that finite temperature effects induce a thermal correction to the mass squared, proportional to T^2.

3.1.1 Phase Transitions

In the SM, we know that only if the mass-squared term of the Higgs, ϕ, is negative will we get electroweak symmetry breaking. In the previous section, we saw that thermal corrections give a positive contribution to the mass. Therefore, at some temperature in the early Universe, the symmetry is restored and $\langle \phi \rangle = 0$. At some temperature T_{ft} we get a transition between the broken and unbroken phase. Such phase transitions can occur in two distinct ways called first-order and second-order phase transitions. At high temperature the minimum of the potential is at $\phi = 0$ and at zero temperature at $H = v$. The phase transition occurs when these two local minima have equal energy. For the potential in (3.1.8), this is approximately the temperature T_0. For a first order phase transition, the potential has a barrier between the two vacua, while for a second order phase transition no such barrier exists. From equation (3.1.8) we can see that the existence of the barrier depends on the size of the ϕ^3 term.

Since there is no barrier in a second order phase transition, the minimum at the origin becomes a maximum, and any displacement will cause the field to roll down to its new minimum. For a first-order phase transition, the barrier prevents a smooth and fast transition. The phase transition will instead occur when the field can tunnel through the barrier at lower temperature, T_C. This will lead to bubbles of the new phase spreading through the Universe at the speed of light. Interactions in the bubble walls are out of thermal equilibrium and can therefore be very important for baryogenesis as explained in Section **1.2.2**.

One can characterise the strength of the first.order phase transition by ϕ_c/T_c. For the phase transition to be strongly first-order, we require that $\phi_c/T_c \gtrsim 1$. In terms of the potential in equation (3.1.8), the strength of the phase transition is given by

$$\frac{\phi_c}{T_c} = \frac{2E}{\lambda T_C}. \tag{3.1.9}$$

3.2 The B − L Coleman-Weinberg Extension of the Standard Model

We will now extend the minimal U(1) CSI extension in Section **2.3.2** by giving the Standard Model fields a charge under the hidden gauge group. An appealing way to accomplish this to make the hidden U(1) into a $U(1)_{B-L}$ gauge group [109, 110, 134, 135]. All the fields in the theory will then have a charge, under this gauge group, given by their baryon-minus-lepton number.

The Coleman-Weinberg mechanism will work exactly as in section **2.3.2** if we replace e_{CW} with $Q_\phi \, g_{B-L}$, where Q_ϕ is the $B - L$ charge of the scalar field in the hidden sector. The mass of the scalar is therefore given by

$$m_\varphi^2 \;=\; \frac{3}{8\pi^2}\,(Q_\phi\,g_{CW})^2 m_{Z'}^2 \ll m_{Z'}^2\,. \qquad (3.2.10)$$

The massive ($\gtrsim$ few TeV) Z' vector boson now couples to quarks and leptons of the Standard Model proportionally to their $B - L$ charge. The SM Higgs carries no baryon or lepton number, and therefore does not couple to the $U(1)_{B-L}$ sector.

The appeal of this model with a local $U(1)_{B-L}$ group is that the cancellation of gauge anomalies requires the inclusion of three generations of the right-handed neutrinos, ν_{Ri}. These neutrinos carry lepton number $= 1$, and transform under $U(1)_{B-L}$, but are sterile under the SM gauge groups. Finally, the Coleman-Weinberg scalar field ϕ is assigned the $B - L$ charge $= 2$. The interactions of the right-handed neutrinos, ν_{Ri}, are given by

$$\mathcal{L}_{\text{int}}^{\nu_R} \;=\; -\frac{1}{2}\left(Y_{ij}^{\text{M}}\phi\,\overline{\nu_{Ri}^c}\nu_{Rj} \;+\; Y_{ij}^{\text{M}\,\dagger}\phi^\dagger\,\overline{\nu_{Ri}}\nu_{Rj}^c\right) \;-\; Y_{ia}^{\text{D}}\overline{\nu_{Ri}}(\epsilon H)\,l_{La} \;-\; Y_{ai}^{\text{D}\,\dagger}\overline{l_{La}}(\epsilon H)^\dagger\,\nu_{Ri}\,,$$
$$(3.2.11)$$

where Y_{ij}^{M} and Y_{ia}^{D} are 3×3 complex matrices of the Majorana and Dirac Yukawa couplings respectively. The right-handed neutrinos ν_{Ri} are SM singlets (often referred to as sterile neutrinos). They carry lepton number $L = +1$ and their antiparticles, $\overline{\nu_{Ri}}$, have $L = -1$. The charge-conjugate anti-particle, $\overline{\nu_{Ri}^c}$, has the same lepton number $+1$ as the state ν_{Ri}. In the unbroken phase, the lepton number is conserved by all interactions in (3.2.11) when ϕ is assigned lepton number -2. The first two terms

on the right-hand side of (3.2.11) give the only interactions of the CW scalar ϕ with matter fields (apart from its small mixing with the Higgs). No other interactions are possible due to the $L = -2$ charge for ϕ.

Spontaneous breaking of the $B - L$ symmetry by the vev $\langle |\phi| \rangle \neq 0$, generates Majorana masses

$$M_{ij} = Y_{ij}^{\mathrm{M}} \langle |\phi| \rangle, \tag{3.2.12}$$

which lead to interactions that do not conserve lepton number. Importantly, individual lepton flavour is also not conserved: M_{ij} is a complex matrix which induces CP-violating transitions between lepton flavours i and j of the right-handed neutrinos.[1]

The Majorana mass for the right-handed neutrinos gives the standard see-saw mass to the left-handed, active neutrinos. Schematically, this gives the left-handed neutrinos a mass of

$$m_\nu \approx \frac{(Y^D \langle H \rangle)^2}{Y^M \langle \phi \rangle} = \lambda_p \langle \phi \rangle \frac{(Y^D)^2}{Y^M}. \tag{3.2.13}$$

With GeV scale right-handed neutrinos we can achieve the correct, sub eV, masses for the active neutrinos with Dirac Yukawa couplings of the order 10^{-7} – 10^{-8}, cf. Table 3.3. This means that the neutrino Yukawa couplings are not much smaller than the electron Yukawa coupling.

In summary, the single $U(1)_{B-L}$ hidden sector simultaneously incorporates the Coleman-Weinberg scalar, which triggers EWSB, and includes Majorana sterile neutrinos which through the see-saw mechanism give rise to masses of active neutrinos and neutrino oscillations [109, 110]. Furthermore, as will be shown below, the generation of matter-antimatter asymmetry through leptogenesis now becomes possible without any fine-tuning.

---

[1]This is most easily seen in the "Dirac-Yukawa basis" where the Dirac Yukawa matrices Y_{ia}^{D} are diagonalised and real, but not the Majorana ones Y_{ij}^{M}.

3.3 Neutrino Oscillations and Leptogenesis

Leptogenesis is the idea that the baryon asymmetry of the Universe has originated in the lepton, rather than quark sector of the theory. In the standard scenario of thermal leptogenesis [55], one starts with the see-saw Lagrangian involving right-handed neutrinos with Majorana mass terms coupled to the Standard Model left-handed lepton doublets (*cf.* Eq. (3.2.11)),

$$
\mathcal{L}_{\text{int}}^{\nu_R} = -\frac{1}{2}\left(M_{ij}\,\overline{\nu_{Ri}^c}\nu_{Rj} + M_{ij}^\dagger\,\overline{\nu_{Ri}}\nu_{Rj}^c\right) - Y_{ia}^{\text{D}}\overline{\nu_{Ri}}(\epsilon H)\,l_{La} - Y_{ai}^{\text{D}\,\dagger}\,\overline{l_{La}}(\epsilon H)^\dagger\,\nu_{Ri}.
\tag{3.3.14}
$$

It is usually assumed that a lepton asymmetry was generated by decays of heavy right-handed Majorana neutrinos at temperatures much above the electroweak scale. These heavy sterile neutrinos were thermally produced during reheating in the early Universe, and then fell out of thermal equilibrium due to the expansion of the Universe. Their out-of-equilibrium decays into Standard Model leptons and Higgs bosons violate lepton number and CP, thus producing lepton asymmetry, which is then reprocessed into a baryon asymmetry by electroweak sphalerons above the electroweak scale.

The defining phenomenological signature of these models is that the masses of the sterile Majorana neutrinos should be $M \gtrsim 10^9$ GeV [58, 131]. Flavour effects [136] and a resonant enhancement [137] are important and can somewhat lower this bound, but not by many orders of magnitude[2].

3.3.1 Leptogenesis Triggered by Oscillations of Majorana Neutrinos

Akhmedov, Rubakov and Smirnov (ARS) in [72] proposed an alternative physical realisation of the leptogenesis mechanism which allows one to circumvent the $\sim 10^9$ GeV lower bound. In fact, the ARS leptogenesis is intended to work with sterile neutrinos of sub-electroweak Majorana mass-scale. In this section, we will describe how

---

[2]Unless one is willing to fine-tune sterile neutrino masses of different flavours to introduce mass degeneracy $M_i M_j/|M_i^2 - M_j^2| \ggg 1$. This is not the approach we will follow.

leptogenesis in the ARS scenario works in the model defined by Equation (3.3.14), then we extend this to the classically scale-invariant model in Section **3.3.2**.

The generation of matter-antimatter asymmetry proceeds as follows. As in the original mechanism, the right-handed neutrinos are produced thermally in the early Universe through their Yukawa interactions with lepton and Higgs doublets. After being produced, they begin to oscillate, $\nu_{Ri} \leftrightarrow \nu_{Rj}$, between the three different flavour states $i, j = 1, 2, 3$ and interact with the left-handed leptons and Higgs bosons via their Yukawa interactions.

Since the Majorana masses in the ARS scenario are roughly of the electroweak scale or below, they are much smaller than the relevant temperature, T_{osc}, in the early Universe. For this reason, the rate of the total lepton-number violation (i.e. singlet fermions to singlet anti-fermions, $\nu_{Ri} \leftrightarrow \overline{\nu_{Rj}}$, induced by their Majorana masses) is negligible. However, the lepton number of individual flavours is not conserved; complex non-diagonal Majorana matrices induce CP-violating flavour oscillations decays,

$$\nu_{Ri} \leftrightarrow \nu_{Rj} \to l_{Lj} H, \tag{3.3.15}$$

which are out of equilibrium due to smallness of the Yukawa matrices at T_{osc}. Following [72], we now require that by the time the temperature cools down to T_{EW}, where electroweak sphaleron processes freeze out, two of the neutrino flavours, i.e. ν_{R2} and ν_{R3}, equilibrate with their Standard Model counterparts, $l_{L2,3} H$, while the remaining flavour (call it the 1$^{\text{st}}$ or e-flavour) does not.[3] In terms of the decay rates for the three sterile neutrino flavours this implies,

$$\Gamma_2(T_{EW}) > H(T_{EW}) \,, \quad \Gamma_3(T_{EW}) > H(T_{EW}) \,, \quad \Gamma_1(T_{EW}) < H(T_{EW}) \tag{3.3.16}$$

where H is the expansion rate of the Universe given by the Hubble 'constant'

$$H(T) = \frac{T^2}{M_{\text{Pl}}^*} \,, \qquad M_{\text{Pl}}^* \equiv \frac{M_{\text{Pl}}}{\sqrt{g_*}\sqrt{4\pi^3/45}} \simeq 10^{18}\,\text{GeV} \tag{3.3.17}$$

---

[3]The opposite case where only one flavour equilibrates before the sphaleron freeze-out can be treated similarly. Essentially, *both* cases can be treated by not imposing any constraint on Γ_2, i.e. by simply dropping the first equation in (3.3.16).

and M_{Pl}^* is the reduced Planck mass. These conditions determine the relevant values of the Yukawa couplings via,

$$\sum_a Y_{ia}^{\text{D}} Y_{ai}^{\text{D}\,\dagger} \frac{\gamma_{av} T_{EW}}{H(T_{EW})} \sim 1 \quad => \quad \sum_a Y_{ia}^{\text{D}} Y_{ai}^{\text{D}\,\dagger} \simeq \frac{2.0}{\gamma_{\text{av}}} \times 10^{-16} \simeq 4 \times 10^{-14}\,. \tag{3.3.18}$$

γ_{av} is a dimensionless constant depending on the couplings of the theory, see Equation (3.3.23). As a result of this washout of the second and the third lepton flavours, the corresponding lepton doublets are processed by electroweak sphalerons into baryons, while the first flavour of right-handed neutrinos is not transferred to the active leptons fast enough before the electroweak sphaleron shuts down. (If the sphaleron had not frozen out below T_{EW}, all three flavours would have had enough time to thermalise and the net lepton and baryon asymmetry would have been zero.)

In the ARS approach[4], the interactions of sterile Majorana neutrinos ν_{Ri} with the thermal plasma are described by the 3×3 density matrix ρ_{ij} with the evolution equation [138]

$$i\frac{d\rho}{dt} = [\mathcal{H}, \rho] - \frac{i}{2}\{\Gamma, \rho\} + i\Gamma^{\text{p}}\,, \tag{3.3.19}$$

where $\mathcal{H}$ is the Hermitian effective Hamiltonian, and Γ and Γ^{p} are the destruction and production rates of ν_{Ri}. In the Yukawa basis at temperatures much higher than the Majorana mass, the effective Hamiltonian, in the ultra relativistic limit $T \gg M_i$, is of the form

$$\mathcal{H} = k(T) + U\frac{\hat{M}^2}{2k(T)}U^{\dagger} + V(t)\,. \tag{3.3.20}$$

U is the mixing matrix which relates the Yukawa basis with the mass eigenstate basis where the Majorana masses are diagonal, $\hat{M}^2 = \text{diag}(\hat{M}_1^2\,, \hat{M}_2^2\,, \hat{M}_3^2)$, and $k(T) \simeq T$ is the neutrino momentum.

The first term on the right-hand side of (3.3.20) is the kinetic energy, which in the relativistic limit is equal for all the neutrinos, and therefore does not contribute to (3.3.19). The second term is the free Hamiltonian describing sterile neutrino oscillations. It originates from a tree-level diagram of ν_{Ri} to ν_{Rj} propagation with two helicity flips $\propto (M/2)^2$ connected by the propagator $2/k(T)$. We can also

---

[4]Reader primarily interested in the final expression for the lepton asymmetry can skip directly to Eqs. (3.3.28)-(3.3.31) which summarise the main result as derived in Ref. [133].

view the first two terms as the ultra-relativistic expansion of $E = \sqrt{p^2 + m^2} \approx p + \frac{m^2}{2p}$. The third term in (3.3.20) is the potential due to coherent forward scattering processes [72],

$$V = \mathrm{diag}\,(V_1, V_2, V_3) \,, \qquad V_i = \frac{1}{8}(Y_i^{\mathrm{D}})^2\, T \,. \tag{3.3.21}$$

These processes arise from one-loop diagrams with an internal lepton and Higgs doublet. Such diagrams, c.f Section **3.1**, give a thermal correction to the mass squared $M_T^2 \propto (Y^D)^2 T^2$ which in the relativistic limit gives an effective potential proportional to M_T^2/T.

For the destruction rates of the sterile neutrinos in (3.3.19), ARS take the dominant Higgs-mediated two-to-two processes involving a lepton and a top-anti-top pair,

$$\Gamma = \mathrm{diag}\,(\Gamma_1, \Gamma_2, \Gamma_3) \,, \qquad \Gamma_i \sim \frac{9 y_t^2}{64\pi^3}(Y_i^{\mathrm{D}})^2\, T \tag{3.3.22}$$

where y_t is the top Yukawa. The two-to-two process is dominant as the one-to-two process is suppressed by M/T. The dimensionful part of the two body decay of the sterile neutrinos is given by its mass and not T. Taking all the processes into account, the destruction (or relaxation) rates of sterile neutrinos can be accounted for as follows [133],

$$\Gamma_i = \sum_a Y_{ia}^{\mathrm{D}} Y_{ai}^{\mathrm{D}\,\dagger}\, \gamma_{av}\, T \tag{3.3.23}$$

Here γ_{av} is the dimensionless quantity inferred from the rates tabulated in Ref. [139], it has a weak dependence on temperature, so that at $T = 5 \times 10^5$ GeV, $\gamma_{av} \simeq 3 \times 10^{-3}$ while at electroweak temperature, $\gamma_{av}(T_{EW}) \simeq 5 \times 10^{-3}$. Following [133], we will use (3.3.23) for the relaxation rate (we also note that this expression is written in the basis-independent form).

The final ingredient appearing in the ARS kinetic equation (3.3.19) is the production rate Γ^{p} which is determined in terms of the destruction rate Γ above and the equilibrium density matrix, $i\Gamma^{\mathrm{p}} = i\Gamma\rho^{\mathrm{eq}} = i\exp(-\mathrm{k}/T)\,\Gamma$ [72].

The production of the asymmetry starts at the time t_{osc} which corresponds to the temperature T_{osc} when the sterile neutrinos have performed at least one oscillation. This happens when the difference of the eigenvalues of the free Hamiltonian in

(3.3.20) becomes of the order of the Hubble constant [72],

$$\frac{|M_i^2 - M_j^2|}{2T_{\text{osc}}} = 2\pi\, H(T_{\text{osc}}) \quad => \quad T_{\text{osc}} = \left(\frac{|M_i^2 - M_j^2|M_{\text{Pl}}^*}{4\pi} \right)^{1/3} \tag{3.3.24}$$

Lepton flavour asymmetry is converted by electroweak sphalerons to baryon asymmetry until the process ends at $T_{EW} \simeq 140$ GeV, when the sphalerons freeze out. By this time, two of the three flavours of right handed neutrinos are in equilibrium with their left-handed partners while the third flavour is still out of equilibrium, as in Eq. (3.3.16).

Now, by integrating the kinetic equation for the sterile neutrino density matrix (3.3.19) between t_{osc} to t_{EW}, the authors of [72] were able to derive an expression for the number density $n_1 := \rho_{11}$ of the first flavour right-handed neutrinos. The asymmetry in this unequilibrated flavour, which will be reprocessed into a baryon asymmetry, is given by $n_L = n_1 - n_{\bar{1}}$. Up to an overall numerical factor and combining the neutrino mixing matrix angles together with the CP phase δ into a Jarlskog invariant $J = s_{12}c_{12}s_{13}c_{13}^2 s_{23}c_{23}\sin\delta$, the functional form of the generated lepton asymmetry over the entropy density of the Universe, s, reads schematically[5]

$$\text{ARS}: \quad \frac{n_L}{s} \sim J\, \frac{\Delta(Y^D)^2\Delta(Y^D)^2\Delta(Y^D)^2\,(M_{\text{Pl}}^*)^2}{|\Delta M^2|^{1/3}|\Delta M^2|^{1/3}|\Delta M^2|^{1/3}}\, \gamma_{av} \tag{3.3.25}$$

Seven years after ARS, in Ref. [132], Asaka and Shaposhnikov (AS) extended this approach by including the back-reaction of active neutrinos on the sterile neutrinos. Specifically, the authors of [132] have solved the kinetic equation (3.3.19) for the 12×12 density matrix whose components describe the mixing of all active and sterile neutrinos and anti-neutrinos,

$$\rho = \begin{pmatrix} \rho_{ij} & \rho_{i\bar{j}} & \rho_{ib} & \rho_{i\bar{b}} \\ \rho_{\bar{i}j} & \rho_{\bar{i}\bar{j}} & \rho_{\bar{i}b} & \rho_{\bar{i}\bar{b}} \\ \rho_{aj} & \rho_{a\bar{j}} & \rho_{ab} & \rho_{a\bar{b}} \\ \rho_{\bar{a}j} & \rho_{\bar{a}\bar{j}} & \rho_{\bar{a}b} & \rho_{\bar{a}\bar{b}} \end{pmatrix} \simeq \begin{pmatrix} \rho_{ij} & 0 & 0 & 0 \\ 0 & \rho_{\bar{i}\bar{j}} & 0 & 0 \\ 0 & 0 & \rho_{ab} & 0 \\ 0 & 0 & 0 & \rho_{\bar{a}\bar{b}} \end{pmatrix} \tag{3.3.26}$$

Here the elements of the density matrix which mix sterile with active (anti-)neutrinos are neglected as they describe correlations between particles of very different masses.

---

[5]We will write down a precise and improved expression in Eq. (3.3.31) below.

Also the elements mixing neutrinos with anti-neutrinos are dropped as they give lepton number (or helicity) flips. The resulting ρ-matrix is an extension of the simple 3×3 sterile-to-sterile density matrix ρ_{ij} (and its CP-conjugate $\rho_{\bar{i}\bar{j}}$) used by ARS, as reviewed above.

The functional form of the generated lepton asymmetry computed by AS is given by (*cf.* Eq. (3.3.25)),

$$\text{AS}: \qquad \frac{n_L}{s} \sim \tilde{J} \, \frac{Y^D \, Y^D \, \Delta(Y^D)^2 \, (M_{\text{Pl}}^*)^{4/3}}{|\Delta M^2|^{1/3}|\Delta M^2|^{1/3}} \, \gamma_{av}^2 \,, \qquad (3.3.27)$$

where $\tilde{J}$ is a certain combination of mixing angles and CP phases.

Quite remarkably, the functional form of the Asaka-Shaposhnikov result in (3.3.27) was fully reproduced by the recent, more technical derivation of the lepton asymmetry by Drewes and Garbrecht (DG) in [133]. Their approach is based on a systematic application of non-equilibrium QFT methods (the Schwinger-Keldysh formalism [140,141]) to the calculation of the lepton flavour asymmetry (see also [142,143]). It is this result of [133] (which in the following section will be adapted to the case of the Coleman-Weinberg $B - L$ model with the $\langle \phi \rangle$-induced and thermally corrected Majorana masses) which we will use for our calculation of the resulting matter-antimatter asymmetry.

Having noted the fact that the non-equilibrium calculation of [133] reproduces the parametric form (though with a different numerical factor) of the more intuitive formalism of AS based on the density matrix, we can now proceed to simply state the equation which determines the generation of lepton asymmetry in [133],

$$\frac{d}{dz} \frac{n_{La}}{s} = \frac{2 \, S_{aa}}{s T_{EW}} \,, \qquad (3.3.28)$$

where n_{La} is the produced charge density of active lepton number of flavour a (particles minus anti-particles), $s = \frac{2\pi^2}{45} g_* T^3$ is the entropy density of the Universe and the 'time' variable z is defined via $z := T_{EW}/T$. On the right-hand side we have the source term given by the expression [133],

$$\frac{2 \, S_{aa}}{s T_{EW}} = -\sum_c \sum_{i \neq j} i \, \frac{Y_{ai}^{D\dagger} Y_{ic}^{D} Y_{cj}^{D\dagger} Y_{ja}^{D} - Y_{ai}^{D\,t} Y_{ic}^{D*} Y_{cj}^{D\,t} Y_{ja}^{D*}}{M_{ii}^2 - M_{jj}^2} \, \frac{M_{\text{Pl}} T_{EW}}{z^2} \, \gamma_{av}^2 \times 7.3 \times 10^{-4} \,.$$

$$(3.3.29)$$

To determine the lepton asymmetry, we integrate $\int_{z_{\text{osc}}}^{1} 2\, S_{aa}/(sT_{EW})\, dz$ using the expression in (3.3.29). The lower limit, z_{osc}, corresponds to the early temperature T_{osc} in (3.3.24) where the oscillations of sterile neutrinos start competing with the Hubble rate,

$$z_{\text{osc}}^3 := \left(\frac{T_{EW}}{T_{\text{osc}}}\right)^3 = 8\pi \sqrt{\frac{\pi^3 g_*}{45}} \frac{T_{EW}^3}{M_{\text{Pl}}|M_{ii}^2 - M_{jj}^2|} \, . \tag{3.3.30}$$

The upper integration limit $z = 1$ is the electroweak phase transition temperature, T_{EW} where the sphaleron freezes out. The integral gives the desired lepton asymmetry, which is the main result of [133],

$$\text{DG}: \quad \frac{n_{La}}{s} = -\sum_{c}\sum_{i \neq j} i\, \frac{Y_{ai}^{\text{D}\dagger}Y_{ic}^{\text{D}}Y_{cj}^{\text{D}\dagger}Y_{ja}^{\text{D}} - Y_{ai}^{\text{D}\,\text{t}}Y_{ic}^{\text{D}*}Y_{cj}^{\text{D}\,\text{t}}Y_{ja}^{\text{D}*}}{\text{sign}(M_{ii}^2 - M_{jj}^2)} \tag{3.3.31}$$

$$\times \left(\frac{M_{\text{Pl}}^2}{|M_{ii}^2 - M_{jj}^2|}\right)^{\frac{2}{3}} \gamma_{av}^2 \times 1.2 \times 10^{-4} \, .$$

3.3.2 Leptogenesis in Classically Massless Models

The focus of this thesis is BSM models with classical scale invariance. In these models no explicit mass scales are allowed in the Lagrangian as they would break classical scale invariance, and hence all masses have to be generated dynamically, e.g. by vacuum expectation values of scalars induced by the Coleman-Weinberg field.

In the minimal $B - L$ model, Majorana masses M_{ij} for right-handed neutrinos are generated by the vev $\langle\phi\rangle$ of the Coleman-Weinberg field[6] in Eq. (3.2.12). There are two effects which need to be taken into account. One is that at temperatures above the critical temperature $T_{B-L} \sim \langle|\phi|\rangle$, the spontaneously broken $U(1)_{B-L}$ gauge symmetry is restored, so that in the unbroken phase the Coleman-Weinberg field vev vanishes, $\langle|\phi|\rangle = 0$. Secondly, due to interactions of right-handed neutrinos with ϕ and with the $B - L$ gauge bosons, Z', there are also thermal corrections to the mass which need to be taken into account, cf. Section **3.1**.

---

[6]In more general settings, the sterile neutrinos could couple to a different scalar which would get its vev through a portal coupling to the Coleman-Weinberg field. In this paper we concentrate on the minimal case where the scalar responsible for the Majorana mass of sterile neutrinos is the Coleman-Weinberg field itself. Extensions with more scalars are straightforward.

To do this we write down the effective Hamiltonian (3.3.20) in the form

$$\mathcal{H} = \frac{M^2}{2T} + V^{\mathrm{M}}(T) + V^{\mathrm{D}}(T) \,, \tag{3.3.32}$$

where the first term is the tree-level effect of Majorana mass insertions as before. It is now given by

$$\frac{M^2}{2T} = \frac{|Y^{\mathrm{M}}|_{ij}^2 \, |\langle\phi\rangle|^2}{2T} \, \Theta(T_{B-L} - T) \simeq \frac{|Y^{\mathrm{M}}|_{ij}^2 \, |\langle\phi\rangle|^2}{2T} \, \Theta(\langle|\phi|\rangle - T) \,. \tag{3.3.33}$$

Here the theta-function accounts for the transition to the unbroken phase at temperatures above $T_{B-L} \sim \langle|\phi|\rangle$.

The second term on the right-hand side of (3.3.32) takes into account the thermal mass, M_T, from the new self-energy diagrams for the right-handed neutrino due to interactions with the Coleman-Weinberg scalar ϕ and the Z' bosons,

$$V^{\mathrm{M}} = \frac{M_T^2}{2T} = \frac{1}{32}|Y^{\mathrm{M}}|_{ij}^2 \, T + \frac{1}{8}g_{B-L}^2 \, \delta_{ij} \, T \,. \tag{3.3.34}$$

The third term, V^{D}, in (3.3.32) is the already accounted for effect of Dirac Yukawa interactions in (3.3.21)-(3.3.23).

In summary, the new effects on Majorana masses are taken into account automatically by making the substitution in the source term (3.3.29):

$$\frac{M_{ii}^2 - M_{jj}^2}{2T} \longrightarrow \frac{1}{2T} \left((|Y^{\mathrm{M}}|_{ii}^2 - |Y^{\mathrm{M}}|_{jj}^2)(|\langle\phi\rangle|^2 \, \Theta(\langle|\phi|\rangle - T) + 2T(V_{ii}^{\mathrm{M}} - V_{jj}^{\mathrm{M}}) \,, \tag{3.3.35}$$

which amounts to

$$\Delta M^2 := \Delta M_0^2 \longrightarrow \Delta M^2(T) := \Delta|Y^{\mathrm{M}}|^2 \left(|\langle\phi\rangle|^2 \, \Theta(\langle|\phi|\rangle - T) + \frac{1}{16}T^2 \right) \,, \tag{3.3.36}$$

where the zero-temperature contribution is ΔM_0^2, which can also be written as $\Delta|Y^{\mathrm{M}}|^2|\langle\phi\rangle|^2$. We further note that the Z' contributions to V^{M} are flavour-independent and cancel out in $\Delta M^2(T)$.

In Fig. 3.1(a) we plot the effective $\Delta M^2(T)$ given by the right-hand side of (3.3.36) as a function of temperature. For future convenience we have smoothened the step-function to account for a more physical behaviour near the phase transition. Essentially, the non-vanishing mass in the broken phase on the left is connected at

3.1(a)   3.1(b)
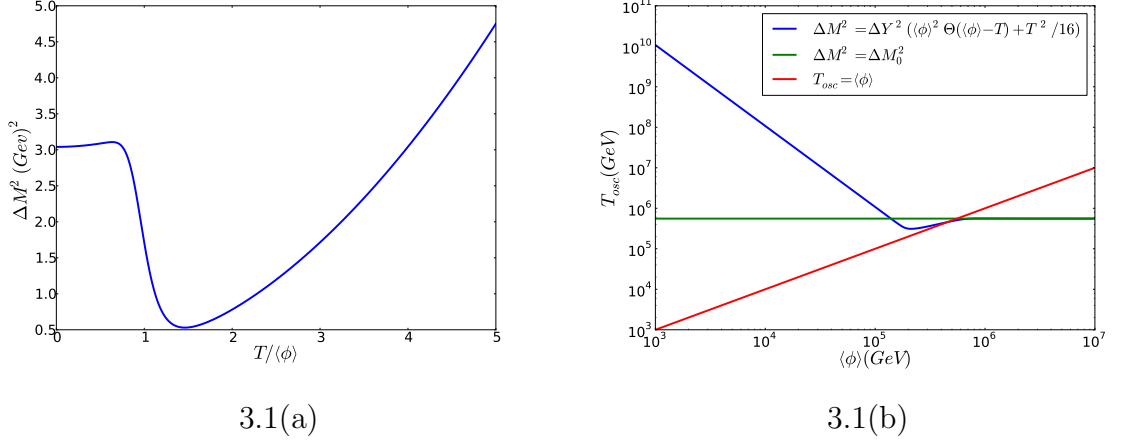
Figure 3.1:   Left panel shows the effective thermal mass squared difference $\Delta M^2(T)$ given by (3.3.36) with smoothened theta-function (and the initial value taken to be $\Delta M_0^2 = 3\,\text{GeV}^2$) as the function of the temperature over $\langle|\phi|\rangle$ [8]. On the right panel, the blue curve sketches the initial temperature T_{osc} as the function of $\langle|\phi|\rangle$ showing the transition between the unbroken ($T_{\text{osc}} > \langle|\phi|\rangle$) and the broken ($T_{\text{osc}} < \langle|\phi|\rangle$) phase. The horizontal green line gives the value of T_{osc} computed in the regime of [133] via (3.3.24). On the right of the plot, the blue and green curves coincide.

$T/\langle|\phi|\rangle \sim 1$ by a finite-width bubble wall to the unbroken phase where the mass receives only a thermal contribution.

In the original DG formulation ($z = T_{EW}/T$) we integrate the source term

$$\text{DG}: \qquad \frac{M_{\text{Pl}} T_{EW}}{\Delta M^2} \left(\int_{z_{\text{osc}}}^{1} \frac{dz}{z^2} \right). \qquad (3.3.37)$$

In our model, after the substitution (3.3.36), we have two separate regimes that we need to deal with separately. The first is when $T_{\text{osc}} > T_{B-L} = \langle|\phi|\rangle$, and the second is the opposite case when $T_{\text{osc}} < T_{B-L}$. For the first case we get

$$\frac{M_{\text{Pl}} T_{EW}}{\Delta |Y^{\text{M}}|^2} \left(\int_{z_{\text{osc}}}^{T_{EW}/\langle|\phi|\rangle} \frac{dz}{T_{EW}^2/16} + \int_{T_{EW}/\langle|\phi|\rangle}^{1} \frac{dz}{|\langle\phi\rangle|^2 z^2 + T_{EW}^2/16} \right), \qquad (3.3.38)$$

and for the second case

$$\frac{M_{\text{Pl}} T_{EW}}{\Delta |Y^{\text{M}}|^2} \left(\int_{z_{\text{osc}}}^{1} \frac{dz}{|\langle\phi\rangle|^2 z^2 + T_{EW}^2/16} \right). \qquad (3.3.39)$$

---

[8] $\langle|\phi|\rangle$ denotes the vev at zero temperature

The oscillation temperature is determined in a similar manner to what was done before in (3.3.24). For the $T_{\mathrm{osc}} > \langle|\phi|\rangle$ case, it is given by

$$\langle|\phi|\rangle < T_{\mathrm{osc}} := \frac{\Delta|Y^{\mathrm{M}}|^2 M_{\mathrm{Pl}}^*}{64\pi} = \frac{\Delta|M_0|^2 M_{\mathrm{Pl}}^*}{64\pi \langle|\phi|\rangle^2}, \tag{3.3.40}$$

while for the case with $T_{\mathrm{osc}} < \langle|\phi|\rangle$, the oscillation temperature is approximately the same as in (3.3.24) with the mass given by the vev, $\langle|\phi|\rangle$. The thermal corrections to the mass are small when $T < \langle\phi\rangle$,

$$T_{\mathrm{osc}} = \left(\frac{\Delta|Y^M|^2 \langle\phi\rangle^2 M_{\mathrm{Pl}}^*}{4\pi}\right)^{1/3}. \tag{3.3.41}$$

To calculate the final lepton asymmetry, we integrate the source terms from $z_{\mathrm{osc}} = T_{EW}/T_{\mathrm{osc}}$. The final result for the lepton flavour asymmetry in both cases is

$$\frac{n_{La}}{s} = -\gamma_{av}^2 \times 7.3 \times 10^{-4} \sum_c \sum_{i \neq j} i \left(Y_{ai}^{\mathrm{D}\dagger} Y_{ic}^{\mathrm{D}} Y_{cj}^{\mathrm{D}\dagger} Y_{ja}^{\mathrm{D}} - Y_{ai}^{\mathrm{D}\mathrm{t}} Y_{ic}^{\mathrm{D}*} Y_{cj}^{\mathrm{D}\mathrm{t}} Y_{ja}^{\mathrm{D}*}\right) \times \mathcal{I}_{ij}, \tag{3.3.42}$$

where $\mathcal{I}_{ij}$ are the integrals of the source term for the two regimes. When $T_{\mathrm{osc}} > \langle|\phi|\rangle$, this integral is given by

$$\mathcal{I}_{ij} = \frac{16}{\sum_k (Y_{ik}^{\mathrm{M}\dagger} Y_{ki}^{\mathrm{M}} - Y_{jk}^{\mathrm{M}\dagger} Y_{kj}^{\mathrm{M}})} \frac{M_{\mathrm{Pl}}}{\langle|\phi|\rangle} \left(1 - \frac{\langle|\phi|\rangle}{T_{\mathrm{osc}}} + \frac{1}{4}\tan^{-1}\left(\frac{4\langle|\phi|\rangle}{T_{EW}}\right) - \frac{1}{4}\tan^{-1}(4)\right), \tag{3.3.43}$$

The low-temperature case (3.3.38) is treated similarly. We note that in the case where T_{osc} approaches $\langle|\phi|\rangle$ (or falls below it), the first integral in (3.3.38) disappears, since $T_{EW}/\langle|\phi|\rangle \to z_{\mathrm{osc}}$, in agreement with (3.3.39). This is manifested by the cancellation between the first and the second term inside the brackets in (3.3.43), so that for $T_{\mathrm{osc}} \leq \langle|\phi|\rangle$, we get

$$\mathcal{I}_{ij} = \frac{4}{\sum_k (Y_{ik}^{\mathrm{M}\dagger} Y_{ki}^{\mathrm{M}} - Y_{jk}^{\mathrm{M}\dagger} Y_{kj}^{\mathrm{M}})} \frac{M_{\mathrm{Pl}}}{\langle|\phi|\rangle} \left(\tan^{-1}\left(\frac{4\langle|\phi|\rangle}{T_{EW}}\right) - \tan^{-1}\left(\frac{4\langle|\phi|\rangle}{T_{\mathrm{osc}}}\right)\right), \tag{3.3.44}$$

with T_{osc} in this case given by (3.3.24).

The dependence of T_{osc} on the value of $\langle|\phi|\rangle$ is plotted on the right panel of Fig. 3.1 in blue. The red diagonal line is the $T_{\mathrm{osc}} = \langle|\phi|\rangle$ boundary separating the broken from the unbroken phase. The horizontal green line gives the value of T_{osc}

in the regime of [133] given by (3.3.24). It is valid for low temperatures (high vevs) $T_{\mathrm{osc}} \leq \langle |\phi| \rangle$ i.e. to the right of the diagonal red line where the blue line coincides with the horizontal green line. On the other hand, at high temperatures, $T_{\mathrm{osc}} > \langle |\phi| \rangle$, the blue line depicting T_{osc} is determined by the right-hand side of Eq. (3.3.40). In the transitional region where all three lines meet, the blue line of T_{osc} briefly drops below the green line prediction of [133]. This dip is a consequence of the local minimum on Fig. 3.1(a) which corresponds to the drop in the effective mass squared when one passes from the broken to the unbroken phase.

3.4 Baryon Asymmetry and Phenomenology

Equations derived in the previous section, (3.3.42),(3.3.43), compute the lepton flavour asymmetry generated in the classically scale-invariant Standard Model $\times$ U(1)$_{B-L}$. Electroweak sphalerons process this lepton flavour asymmetry into baryon asymmetry of the Universe (BAU). As explained in Sec. **3.3.1**, in order to achieve a non-vanishing value of BAU it is required that at the time of electroweak phase transition two of the flavours of sterile neutrinos are equilibrated with their SM decay products, but it is essential that the remaining flavour is not. Thus if the inequalities (3.3.16) are satisfied, a BAU is produced $\sim -n_{Le}$. The baryon asymmetry can be estimated as [133]

$$\frac{n_b}{s} \simeq -\frac{3}{14} \times 0.35 \times \frac{n_{Le}}{s}. \tag{3.4.45}$$

The observed value of the asymmetry is $n_b^{\mathrm{obs}}/s = (8.75 \pm 0.23) \times 10^{-11}$.

First we would like to determine the range of the parameters in our model for which the required baryon asymmetry is generated. In the neutrino sector we use the standard Casas-Ibarra parametrisation [144] of the see-saw Dirac Yukawa couplings,

$$Y^{D\dagger} = U_\nu \cdot \sqrt{m_\nu} \cdot \mathcal{R} \cdot \sqrt{M} \times \frac{\sqrt{2}}{v}, \tag{3.4.46}$$

where m_ν and M are diagonal masses of active and Majorana neutrinos respectively, and $v = 246$ GeV. The active-neutrino-mixing matrix U_ν is the PMNS matrix which contains six real parameters, including three measured mixing angles and three CP-phases. The matrix $\mathcal{R}$ is parametrised by three complex angles ω_{ij}.

3.2(a) $M(\text{GeV})$ 3.2(b) n_b/n_b^{obs}
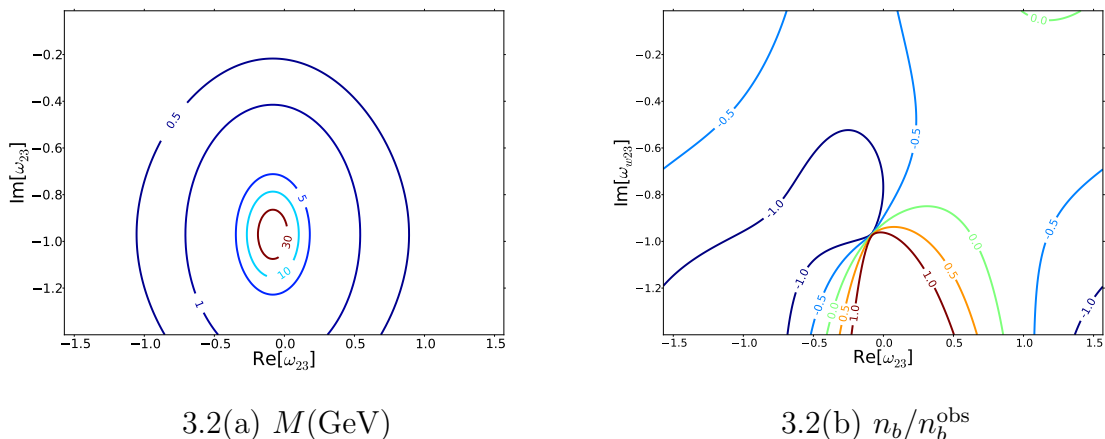
Figure 3.2:   Left panel shows maximal values of Majorana masses in GeV for which the wash-out bound in Eq. (3.4.47) can be achieved. The panel on the right shows contours for the baryon asymmetry produced, normalised to the observed value. Majorana masses used in 3.2(b) are taken from 3.2(a) for each value of $Re[\omega_{23}]$ and $Im[\omega_{23}]$. In both plots we vary $Re[\omega_{23}]$ and $Im[\omega_{23}]$ keeping other parameters of the model fixed at indicative values as in Ref. [133], detailed in the Tables 3.1 and 3.2.

In our analysis we will choose and fix the values of m_ν consistent with the solar and atmospheric neutrino mass differences. We also choose a generic value for the three CP-phases. We then vary the unknown complex angles ω_{ij} over the parameter space. To keep things as simple as possible, we will choose a 2-dimensional subspace on which we vary the real and imaginary parts of the complex angle ω_{23}, while keeping ω_{12} and ω_{13} fixed. For easy comparison, our 2-d slice of the ω-space is the same as in [133] (it can be read off Scenarios 1-3 and 5-7 in Tables 3.1 and 3.2 below). For completeness, we will also comment on the results of varying the other complex angles and CP phases of the parameter space.

Different choices of the three Majorana masses will characterise different benchmark points. Since in our case the Majorana particle mass (we drop the subscript 0 in what follows) is $M = Y^M \langle \phi \rangle$, there is an additional scale $\langle \phi \rangle$ which we will vary and specify[9].

---

[9]Phenomenologically, it makes sense to use $\langle \phi \rangle$ and M as the two independent parameters, rather than, say Y^M and $\langle \phi \rangle$.
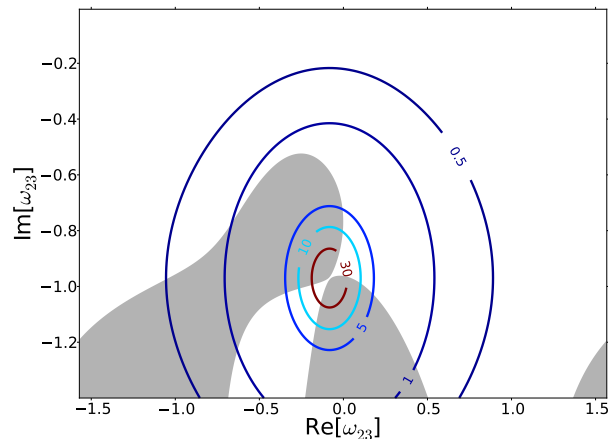
Figure 3.3: Superposition of the Majorana mass contours in GeV satisfying the wash-out bound with the baryon asymmetry produced with shaded regions denoting the required baryon asymmetry from Fig. 3.2

First we would like to determine the range of allowed values of Majorana masses for sterile neutrinos. We start by considering the models where $T_{\text{osc}} \ll \langle \phi \rangle$ which is equivalent to the model with a majorana mass term in the Lagrangian. The wash-out rates for the lepton flavours $a = e, \mu, \tau$ are given by Γ_a, and we require that

$$\frac{\Gamma_e}{H(T_{EW})} := \frac{1}{2} \sum_i Y_{ei}^{\text{D}\,\dagger} Y_{ie}^{\text{D}} \, \gamma_{av} \, \frac{T_{EW}}{H(T_{EW})} < 1 \,. \tag{3.4.47}$$

Figure 3.2(a) shows mass contours in GeV of the lightest Majorana neutrino flavour, such that the wash-out rate =1 is achieved. This can be interpreted as an upper bound on Majorana masses for which (3.4.47) is satisfied. Quite clearly from this perspective it is straightforward to realise M in the region from a few 100 MeV to above 30 GeV, or even up to a TeV. BBN constrains the lower limit to $M > 200$ MeV, so we have

$$200 \, \text{MeV} \, < \, M \, \lesssim \, \text{few} \times 100 \, \text{GeV} \,. \tag{3.4.48}$$

For the model to be viable, we also need to produce enough baryon asymmetry. Figure 3.2(b) plots the ratio n_b/n_b^{obs}. The baryon asymmetry here is computed using Eq. (3.3.31) derived for the simple Majorana mass model [133], where the values of M at each point on the parameter space are taken from Fig. 3.2(b). Below we will also compute the asymmetry in the classically scale-invariant Standard Model $\times$

3.4(a) Wash-out

3.4(b) n_b/n_b^{obs}
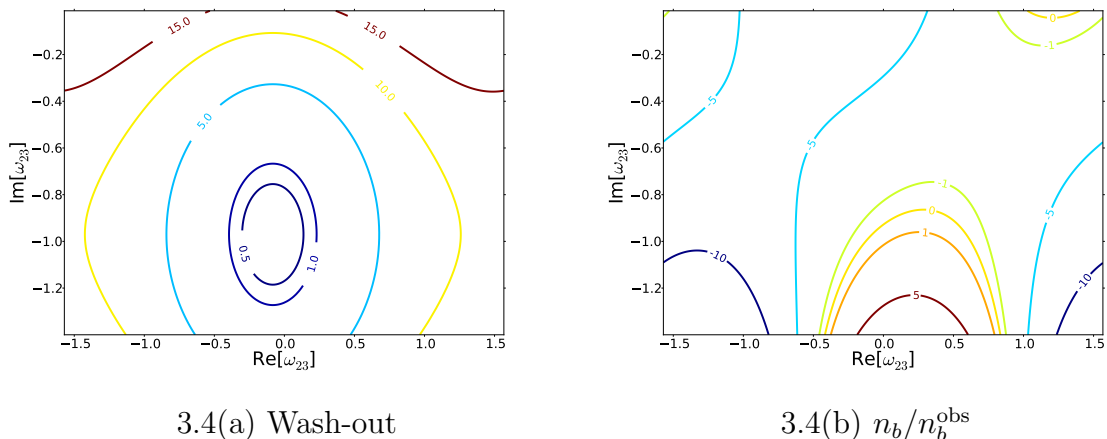
Figure 3.4: The wash-out rate (left panel) and the normalised baryon asymmetry computed in the classically scale-invariant $B - L$ model. The values of model parameters are defined in the text.

$U(1)_{B-L}$. To generate the observed asymmetry we need to be inside the $+1$ or -1 contours in Fig. 3.2(b).

Figure 3.3 depicts the superposition of the two panels of Fig. 3.2. It can be seen that the required baryon asymmetry (the area inside the two shaded contours in Fig. 3.3) is indeed generated in the above mass range.

Figures 3.2 and 3.3 were obtained by varying the real and imaginary parts of ω_{23} while keeping other parameters fixed. We have also checked that desired amounts of the wash-out and the baryon asymmetry are produced in sizeable regions of the parameter space when other complex angles and CP phases are varied. In our benchmark points described in the tables below, the fixed parameters were chosen inside these regions.

In Table 3.1 we present our first four benchmark scenarios. The lepton flavour asymmetry n_{La}/s with $a = e, \mu, \tau$ in all four cases in this table is calculated using Eq. (3.3.31) in the simple Majorana mass model in the formalism of [133]. We also show the wash-out rates for the three flavours, $\Gamma_a/H(T_{EW})$ and the value of the oscillation temperature.

In Scenarios 1, 2 & 3 we vary Majorana masses M_i of sterile neutrinos from ~ 500 MeV (Scenario 1) through ~ 4 GeV (Scenario 2) to $\sim 200 - 300$ GeV (Scenario 3).

	Scenario 1	Scenario 2	Scenario 3	Scenario 4
M_1	0.5 GeV	3.6 GeV	200.0 GeV	1.0 GeV
M_2	0.6 GeV	4.0 GeV	250.0 GeV	2.0 GeV
M_3	0.7 GeV	4.4 GeV	300.0 GeV	3.0 GeV
m_1	0.0 meV	0.0 meV	0.0 meV	2.5 meV
m_2	8.7 meV	8.7 meV	8.7 meV	9.1 meV
m_3	49.0 meV	49.0 meV	49.0 meV	49.0 meV
s_{12}	0.55	0.55	0.55	0.55
s_{23}	0.63	0.63	0.63	0.63
s_{13}	0.16	0.16	0.16	0.16
δ	$-\pi/4$	$-\pi/4$	$-\pi/4$	π
α_1	0	0	0	$-\pi$
α_2	$-\pi/2$	$-\pi/2$	$-\pi/2$	π
ω_{12}	1+2.6i	1+2.6i	1+2.6i	-1+1.5i
ω_{13}	0.9+2.7i	0.9+2.7i	0.9+2.7i	0.5+2.6i
ω_{23}	0.3-1.5i	-1.2i	-0.05-0.975i	π-2.4i
$n_{Le}/(s \times 2.5 \times 10^{-10})$	-4.4	-6.7	-5	-8.3
$n_{L\mu}/(s \times 2.5 \times 10^{-10})$	39	32	108	32
$n_{L\tau}/(s \times 2.5 \times 10^{-10})$	-34	-25	-103	-24
$\Gamma_e/H(T_{EW})$	0.68	0.64	0.84	0.59
$\Gamma_\mu/H(T_{EW})$	68	290	1×10^4	410
$\Gamma_\tau/H(T_{EW})$	220	920	4×10^4	150
T_{osc}	2×10^5 GeV	5×10^5 GeV	10^7 GeV	5×10^5 GeV

Table 3.1: Four benchmark points corresponding to different ranges of Majorana masses.

For convenience, the values of active neutrino masses in these three scenarios are chosen to be the same as in Scenario I in [133]. The same applies to the choices of mixing angles. The main lesson of these benchmark points is to demonstrate the range of variation of Majorana masses in (3.4.48).

The fourth Scenario in Table 3.1 is included for completeness as it reproduces
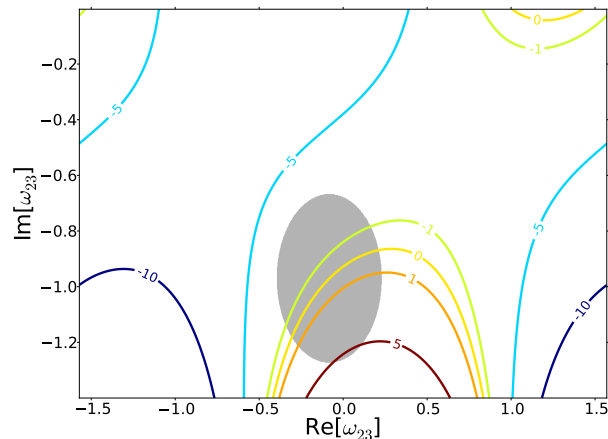
Figure 3.5: Superposition of the wash-out rate ≤ 1 (inside the shaded ellipse) with the baryon asymmetry produced from Fig. 3.4

Scenario II of [133] and has a different selection of active neutrino mass values from Scenarios 1-3.

Having established the likely range of Majorana masses, we now proceed to the analysis of the the classically scale-invariant Standard Model $\times$ CW$_{B-L}$ where the matter-antimatter asymmetry is computed using the formalism of Section **3.3.2**.

The right panel of Figure 3.4 shows the baryon asymmetry (normalised to its observed value) computed using Eqs. (3.3.42)-(3.3.43). The values of Majorana masses are chosen in the GeV range: $M_1 = 3.6$ GeV, $M_2 = 4.0$ GeV and $M_3 = 4.4$ GeV, precisely as in Scenario 2 in Table 3.1. The value of the Coleman-Weinberg vev is chosen $\langle|\phi|\rangle = 10^5$ GeV, which corresponds to a Higgs portal coupling of $\lambda_P = \frac{1}{2}\left(\frac{125\,\text{GeV}}{\langle|\phi|\rangle}\right)^2 \simeq 0.78 \times 10^{-6}$. To achieve the required BAU we must be either below the $+1$ contour or above the -1 curve. This amounts to almost the entire area of Fig. 3.4(b) being available.

The left plane of Fig. 3.4(a) shows the wash-out rate contours for the same choice of parameters. Here we have to be inside the $+1$ ellipse for baryogenesis to succeed. The superposition of this wash-out ≤ 1 contour with the baryon asymmetry, calculated and depicted in Fig. 3.4(b), is shown in Fig. 3.5.

In the above example, we chose a relatively large CW vev, $\langle|\phi|\rangle = 10^5$ GeV, not
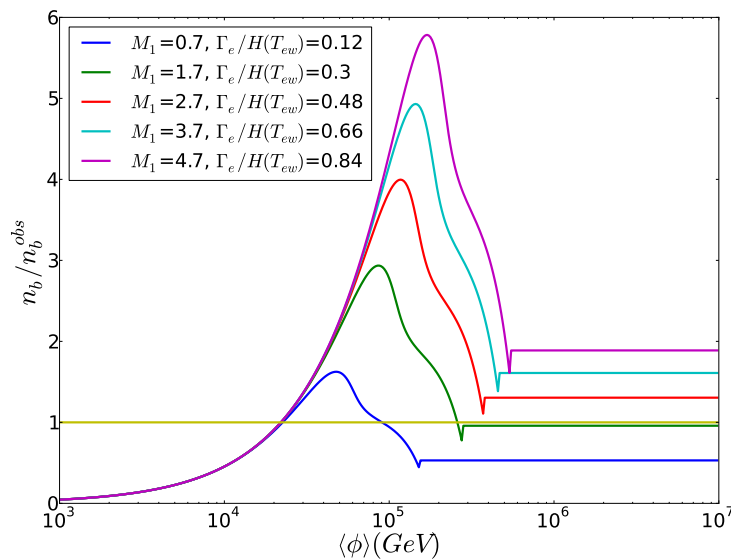
Figure 3.6: Baryon asymmetry (normalised by the observed value) as a function of $\langle|\phi|\rangle$ for masses between 0.7 GeV and 4.7 GeV. The wash-out rates for the electron neutrino flavour (all less than 1 as required) are also shown in the legend.

much below the value of $T_{\rm osc} = 5 \times 10^5$ GeV computed for these GeV-scale values of M_i's. As a result, we ended up with a rather small value of the Higgs portal coupling, $\lambda_P \sim 10^{-6}$.

A natural and important question to ask is how much freedom we have to lower $\langle|\phi|\rangle$ (and thus raise λ_P) while keeping other parameters, such as the Majorana masses fixed. Figure 3.6 plots the baryon asymmetry (divided by the observed value) as the function of $\langle|\phi|\rangle$ for the range of masses between 0.7 GeV and 4.7 GeV (from bottom to top). The figure also indicates the values of wash-out rates $\Gamma_e/H(T_{EW}) < 1$. The flat distributions on the right of the plot correspond to values of $\langle|\phi|\rangle$ reaching and exceeding the relevant values of temperature $T_{\rm osc}$ where leptogenesis begins. These constant values of the generated baryon asymmetry agree with those computed using the non-dynamical Majorana masses in the formalism of [133] reviewed above in Section **3.3.1**. To the left of the plateau on Fig. 3.6 there is a small dip followed by a broad peak which emerges largely due to the first integral in (3.3.38). This integral describes the situation before the symmetry breaking where the only source of mass for the right-handed neutrinos is due to

thermal corrections. The smaller mass means that a larger asymmetry is generated. The small dip is the reflection of the dip in the oscillation temperature T_{osc} in the middle of Fig. 3.1(b).

Finally, to the left of the plot on Fig. 3.6, at small values of $\langle |\phi| \rangle$, all contours converge and tend to zero uniformly and independently of the values of M's. To understand this point, note that according to (3.3.42),(3.3.43),

$$n_b \sim \frac{(Y^{\mathrm{D}})^4}{(Y^{\mathrm{M}})^2} \frac{M_{\mathrm{Pl}}}{\langle |\phi| \rangle} \sim \frac{\langle |\phi| \rangle \, m^2 M_{\mathrm{Pl}}}{v^4} \to 0 \,, \quad \text{as } \langle |\phi| \rangle \to 0 \,, \tag{3.4.49}$$

independently of M.

As a result, Fig. 3.6 shows that independently of the values of the chosen Majorana masses, the contours cross the observed value of baryon asymmetry (normalised at 1) for values of $\langle |\phi| \rangle \simeq 1.2 \times 10^4$ GeV. This gives $\lambda_P \simeq 0.5 \times 10^{-4}$.

Tables 3.2 and 3.3 detail three new benchmark points (Scenarios 5, 6 & 7) where lepton flavour asymmetry is generated in the classically scale-invariant $B - L$ model with the Majorana masses in the GeV range. In these scenarios we successively lower the vev of the Coleman-Weinberg filed $\langle |\phi| \rangle$ from 10^5 to 3.4×10^3 GeV. The second column, Scenario 6 gives the values of the portal coupling $\lambda_{\mathrm{P}} \simeq 10^{-5}$, which is in agreement with the presently available Higgs data constraints and can be probed by the future experiments [82].

The third column (Scenario 7) in the Tables 3.2 and 3.3 enters the regime where λ_{P} approaches 10^{-3}. (To achieve this we brought the three Majorana masses closer together relative to Scenarios 5 and 6, thereby introducing some fine-tuning.) We also show the values of the Majorana Y^{M} and the average value of the Dirac Yukawa $\langle Y^{\mathrm{D}} \rangle$ couplings[10] along with the ranges for g_{B-L}, or equivalently, the Z' vector boson mass, and the self-coupling of the CW scalar. The lower bound on the Z' mass in Table 3.3 is the experimental bound $M_{Z'} \geq 3.5$ TeV, which is then translated into the lower bounds on g_{B-L} via

$$m_{Z'} = Q_\phi \cdot g_{B-L} \langle |\phi| \rangle = 2 \, g_{B-L} \langle |\phi| \rangle \,. \tag{3.4.50}$$

The upper bounds on $M_{Z'}$ in Table 3.3 follow from the requirement of perturbativity

---

[10]The latter is computed as the average of $\sqrt{2} m M / v$.

	Scenario 5	Scenario 6	Scenario 7
$\langle\phi\rangle$	$10^5\,\mathrm{GeV}$	$2.5\times10^4\,\mathrm{GeV}$	$3.4\times10^3\,\mathrm{GeV}$
M_1	$3.6\,\mathrm{GeV}$	$3.6\,\mathrm{GeV}$	$3.96\,\mathrm{GeV}$
M_2	$4.0\,\mathrm{GeV}$	$4.0\,\mathrm{GeV}$	$4.0\,\mathrm{GeV}$
M_3	$4.4\,\mathrm{GeV}$	$4.4\,\mathrm{GeV}$	$4.04\,\mathrm{GeV}$
m_1	$0.0\,\mathrm{meV}$	$0.0\,\mathrm{meV}$	$0.0\,\mathrm{meV}$
m_2	$8.7\,\mathrm{meV}$	$8.7\,\mathrm{meV}$	$8.7\,\mathrm{meV}$
m_3	$49.0\,\mathrm{meV}$	$49.0\,\mathrm{meV}$	$49.0\,\mathrm{meV}$
s_{12}	0.55	0.55	0.55
s_{23}	0.63	0.63	0.63
s_{13}	0.16	0.16	0.16
δ	$-\pi/4$	$-\pi/4$	$-\pi/4$
α_1	0	0	0
α_2	$-\pi/2$	$-\pi/2$	$-\pi/2$
ω_{12}	1+2.6i	1+2.6i	1+2.6i
ω_{13}	0.9+2.7i	0.9+2.7i	0.9+2.7i
ω_{23}	0.3-1.5i	-1.2i	-0.04-0.976i
$n_{Le}/(s\times2.5\times10^{-10})$	-18	-5	-6.6
$n_{L\mu}/(s\times2.5\times10^{-10})$	99	27	41
$n_{L\tau}/(s\times2.5\times10^{-10})$	-81	-22	-34
$\Gamma_e/H(T_{EW})$	0.64	0.64	0.67
$\Gamma_\mu/H(T_{EW})$	290	290	304
$\Gamma_\tau/H(T_{EW})$	920	920	960
T_{osc}	$10^6\,\mathrm{GeV}$	$7.5\times10^7\,\mathrm{GeV}$	$9.8\times10^7\,\mathrm{GeV}$

Table 3.2: Three benchmark points in the classically scale-invariant $B-L$ model corresponding to Majorana masses in the GeV range, with the values of the Coleman-Weinberg vev $\langle|\phi|\rangle = 10^5$, 2.5×10^4 and 3.4×10^3 GeV.

in the coupling $\alpha_{B-L} \leq 0.1$, which gives $g_{B-L} \lesssim 1.1$. For the CW self-coupling λ_ϕ the lower bounds are determined by the smallest possible value of g_{B-L},

$$\lambda_\phi = \frac{33}{8\pi^2}(Q_\phi \cdot g_{B-L})^4 = \frac{33}{8\pi^2}(2\,g_{B-L})^4. \qquad (3.4.51)$$

	Scenario 5	Scenario 6	Scenario 7
$\langle\phi\rangle$	$10^5\,\mathrm{GeV}$	$2.5\times10^4\,\mathrm{GeV}$	$3.4\times10^3\,\mathrm{GeV}$
λ_p	8×10^{-7}	10^{-5}	0.7×10^{-3}
Y_1^{M}	3.6×10^{-5}	1.4×10^{-4}	1.2×10^{-3}
Y_2^{M}	4×10^{-5}	1.6×10^{-4}	1.2×10^{-3}
Y_3^{M}	4×10^{-5}	1.8×10^{-4}	1.2×10^{-3}
$\langle Y^{\mathrm{D}}\rangle$	4×10^{-8}	4×10^{-8}	4×10^{-8}
$M_{Z'}$	$3.5\,\mathrm{TeV}<M_{Z'}<220\,\mathrm{TeV}$	$3.5\,\mathrm{TeV}<M_{Z'}<56\,\mathrm{TeV}$	$3.5\,\mathrm{TeV}<M_{Z'}<7.4\,\mathrm{TeV}$
g_{B-L}	$0.0175<g_{B-L}<1.1$	$0.15<g_{B-L}<1.1$	$0.5<g_{B-L}<1.1$
λ_ϕ	$5\times10^{-4}<\lambda_\phi$	$0.04<\lambda_\phi$	$0.4<\lambda_\phi$

Table 3.3: The range of coupling constants corresponding to benchmark points in Table 3.2.

3.5 Conclusions

In this chapter we have shown that in a $U(1)_{B-L}$ CSI extension of the SM, it is possible to generate the observed value of the matter-antimatter asymmetry. This model needs right-handed neutrinos to cancel the anomalies in the new gauge group. The matter antimatter asymmetry is generated via oscillations of right-handed Majorana neutrinos with masses in the window roughly between 200 MeV and 500 GeV. The model also includes a $B-L$ Z' boson which has a current exclusion limit of $M_{Z'}\geq 3.5$ TeV, but with a large discovery potential at the LHC [135].

The presently available Higgs data provide valuable constraints on the parameter space of the model, and future experimental data on Higgs decays will further constrain model parameters in the Higgs sector [82]. Additional experimental constraints will come from searches for sub-TeV-scale sterile neutrinos via a combination of neutrinoless double beta decay, electroweak precision data, LHC searches and high intensity frontier experiments (see e.g. [145, 146] for recent reviews). At the high intensity frontier, one can look for missing energy in meson decay, or in the appearance of leptons at detectors along the beam-line if the right-handed neutrinos are heavier than a few GeV. At the LHC, one can discover right-handed Majorana neu-

trinos by looking for same sign dileptons as the Majorana mass term breaks lepton number. All these experimental signatures and the relatively few new parameters in the model make this a predictive BSM model.

These results support the BSM model-building strategy which is based on classically scale-invariant extensions of the SM with portal-type interactions involving the Higgs field as well as other microscopic scalars. These theories can successfully address the matter-antimatter asymmetry of the Universe.

Chapter 4

Higgs Vacuum Stability from the Dark Matter Portal

The main motivation of this chapter, based exclusively on [2], is to study the link between the stability of the electroweak vacuum and the properties of dark matter in classically scale-invariant extensions of the Standard Model (*CSI ESM*). As for all CSI ESM models, we expect expect a *common origin* of all mass scales, i.e. the EW scale relevant to the SM and the scales of new physics. In this chapter we will investigate extending the SM with a U(1), U(1)$_{B-L}$ or SU(2) gauge group with or without adding an extra scalar singlet.

On a model by model basis, we will first determine the regions of parameter space where the SM Higgs vacuum is stabilised and the extended Higgs sector phenomenology is consistent with the LHC exclusion limits. Then we investigate dark matter phenomenology, compute the relic abundance and impose direct-detection constraints for vector and scalar components of dark matter from current and future experiments.

Our discussion and computations in Sections **4.3** and **4.4** are based on the CSI ESM model-building features and results derived in Section **4.1**, and on solving the renormalisation group equations in Section **4.2**.

4.1 CSI ESM Building and Generation of the EW Scale

In this section we will describe all the CSI ESM models we are considering in this chapter. We will start with a brief recap of the U(1) model from Section **2.3.2**, and then move on to the U(1)$_{B-L}$, also considered in Chapter **3**. Then we extend the hidden gauge group to a non-Abelian SU(2) gauge group, before adding a singlet scalar to the theory. For all these theories we will use the following for the SM scalar potential

$$V(H)_{\mathrm{SM}} = -\frac{1}{2}\mu_{\mathrm{SM}}^2 H^\dagger H + \lambda_{\mathrm{SM}}(H^\dagger H)^2 \,. \qquad (4.1.1)$$

4.1.1 CSI U(1)$_{\mathrm{CW}} \times$ SM

As we discussed in Section **2.3.2**, in the minimal U(1) CSI extension to the SM the Coleman-Weinberg mechanism dynamically creates a vev for Φ, a complex scalar field charged under the hidden U(1). This vev is then transmitted to the SM via the Higgs portal coupling, generating a negative mass-squared term for the Higgs which will trigger EWSB. This theory is specified by the following tree-level scalar potential

$$V_{\mathrm{cl}}(H, \Phi) = \lambda_\phi(\Phi^\dagger\Phi)^2 + \lambda_H(H^\dagger H)^2 - \lambda_{\mathrm{P}}(H^\dagger H)(\Phi^\dagger\Phi) \,. \qquad (4.1.2)$$

In the unitary gauge we are left with two real singlet scalars

$$H = \frac{1}{\sqrt{2}}(0, h) \,, \quad \Phi = \frac{1}{\sqrt{2}}\phi \,, \qquad (4.1.3)$$

and a tree-level scalar potential of

$$V_0(h, \phi) = \frac{\lambda_\phi^{(0)}}{4}\phi^4 + \frac{\lambda_H^{(0)}}{4}h^4 - \frac{\lambda_{\mathrm{P}}^{(0)}}{4}h^2\phi^2 \,, \qquad (4.1.4)$$

where the superscripts indicate that the corresponding coupling constants are the tree-level quantities.

The Effective potentials and running couplings in this chapter will always be computed in the $\overline{\mathrm{MS}}$ scheme. Following Section **2.3.2**, we find the one-loop potential

in the hidden sector

$$V_1(\phi;\mu) = \frac{\lambda_\phi(\mu)\phi^4}{4} + \frac{3e_{\mathrm{CW}}(\mu)^4}{64\pi^2}\phi^4\left(\log\left(\frac{\phi^2}{\mu^2}\right) - \frac{25}{6}\right). \tag{4.1.5}$$

This dynamically generates a vev for ϕ, and we get the characteristic relation between the scalar and the gauge couplings,

$$\lambda_\phi = \frac{11}{16\pi^2}e_{\mathrm{CW}}^4 \qquad \text{at} \quad \mu = \langle\phi\rangle, \tag{4.1.6}$$

and the mass of ϕ and Z', the U(1) vector boson

$$M_{Z'}^2 = e_{\mathrm{CW}}^2\langle\phi\rangle^2 \quad \gg \quad m_\phi^2 = \frac{3e_{\mathrm{CW}}^4}{8\pi^2}\langle\phi\rangle^2. \tag{4.1.7}$$

The SM scale μ_{SM}^2 is generated by the CW vev in the second term of equation (4.1.2)

$$\mu_{\mathrm{SM}}^2 = \lambda_{\mathrm{P}}\langle\phi\rangle^2, \tag{4.1.8}$$

and this triggers in turn the appearance of the Higgs vev v.

The presence of the portal coupling in the potential (4.1.4) provides a correction to the CW matching condition and masses

$$\lambda_\phi = \frac{11}{16\pi^2}e_{\mathrm{CW}}^4 + \lambda_{\mathrm{P}}\frac{v^2}{2\langle\phi\rangle^2} \qquad \text{at} \quad \mu = \langle\phi\rangle \tag{4.1.9}$$

$$m_\phi^2 = \frac{3e_{\mathrm{CW}}^4}{8\pi^2}\langle\phi\rangle^2 + \lambda_{\mathrm{P}}v^2 \tag{4.1.10}$$

in full agreement with the results of [82]. In this chapter, we consider small values of λ_{P} so that these corrections are negligible, since $\lambda_{\mathrm{P}}v^2/(2\langle\phi\rangle^2) \sim \lambda_{\mathrm{P}}^2/(4\lambda_H) \ll 1$.

Our next task is to compute the Higgs mass including the SM radiative corrections. To proceed, we perform the usual shift, $h(x) \to v + h(x)$, and represent the SM scalar potential as follows,

$$V(h) = \frac{\lambda_H^{(0)}}{4}(v+h)^4 - \frac{\mu_{\mathrm{SM}}^2}{4}(v+h)^2 + \frac{1}{2}\Delta m_{h,\mathrm{SM}}^2 h^2, \tag{4.1.11}$$

where for overall consistency we have also included one-loop corrections to the Higgs mass arising in the Standard Model,

$$\Delta m_{h,\mathrm{SM}}^2 = \frac{1}{16\pi^2}\frac{1}{v^2}\left(6m_W^4 + 3m_Z^4 + m_h^4 - 24m_t^4\right) \approx -2200\,\mathrm{GeV}^2. \tag{4.1.12}$$

These corrections are dominated by the top-quark loop and are therefore negative. The appearance of v^2 in the denominator of $\Delta m^2_{h,\mathrm{SM}}$ is slightly misleading, and it is better to recast it as

$$\Delta m^2_{h,\mathrm{SM}} = 2\Delta\lambda_H v^2, \quad \text{where} \quad \Delta\lambda_H \simeq -0.018. \tag{4.1.13}$$

The vev v is determined from (4.1.11) by minimisation and setting $h(x) = 0$, and thus the last term in (4.1.11) does not affect the value of v. However, it does contribute to the one-loop corrected value of the Higgs mass. We have

$$v^2 = \frac{\lambda_\mathrm{P}}{2\lambda_H^{(0)}} \langle\phi\rangle^2, \qquad m_h^2 = 2\lambda_H v^2, \qquad \lambda_H = \lambda_H^{(0)} + \Delta\lambda_H \simeq \lambda_H^{(0)} - 0.018, \tag{4.1.14}$$

where λ_H is the one-loop corrected value of the self-coupling.

As we saw in Section **2.3.2**, h and ϕ both have vevs and hence mix via the mass matrix,

$$M^2 = \begin{pmatrix} 2\lambda_H v^2 & -\sqrt{2\lambda_\mathrm{P}\lambda_H^{(0)}}\, v^2 \\ -\sqrt{2\lambda_\mathrm{P}\lambda_H^{(0)}}\, v^2 & m_\phi^2 \end{pmatrix}, \tag{4.1.15}$$

where m_ϕ^2 is given in (4.1.10) (and already includes the λ_P correction).[1] The mass eigenstates are the two Higgs fields, h_1 and h_2, with the mass eigenvalues,

$$m^2_{h_1,h_2} = \frac{1}{2}\left(2\lambda_H v^2 + m_\phi^2 \pm \sqrt{\left(2\lambda_H v^2 - m_\phi^2\right)^2 + 8\lambda_\mathrm{P}\lambda_H^{(0)} v^4}\right). \tag{4.1.16}$$

The mass eigenstates h_1 and h_2 are given by

$$\begin{pmatrix} h_1 \\ h_2 \end{pmatrix} = \begin{pmatrix} \cos\theta & -\sin\theta \\ \sin\theta & \cos\theta \end{pmatrix} \begin{pmatrix} h \\ \phi \end{pmatrix} \tag{4.1.17}$$

with a non-trivial mixing angle θ. The SM Higgs is the scalar that is 'mostly' the h scalar (i.e. $\cos\theta\times$the scalar coupled to the SM electroweak sector)

$$h_\mathrm{SM} := h_1 = h\cos\theta - \phi\sin\theta, \qquad m_{h_1} = 125.66\,\mathrm{GeV}. \tag{4.1.18}$$

---

[1]The mass mixing matrix (4.1.15) is equivalent to the mass matrix derived in [82] which was of the form: $M^2 = \begin{pmatrix} m^2_{h,0} + \Delta m^2_{h,\mathrm{SM}} & -\kappa\, m^2_{h,0} \\ -\kappa\, m^2_{h,0} & m^2_{\phi,0} + \kappa^2 m^2_{h,0} \end{pmatrix}$ in terms of $m^2_{h,0} = 2\lambda_H^{(0)} v^2$ and $m^2_{\phi,0} = 3e_\mathrm{CW}^4\langle\phi\rangle^2/(8\pi^2)$, with $\kappa = \sqrt{\lambda_\mathrm{P}/(2\lambda_H^{(0)})}$.

The SM Higgs self-coupling constant, λ_{SM}, appearing in the SM Higgs potential (4.1.1) can be inferred from $m_{h_1}^2 = 2\lambda_{\text{SM}}v^2$, but it is not the relevant or primary parameter in our model, λ_H is.

In our computations for the RG evolution of couplings and the analysis of Higgs potential stabilisation carried out in this chapter, we solve the initial condition (4.1.18) for the eigenvalue problem of (4.1.15) numerically without making analytical approximations. However, we show some simple analytic expressions to illuminate our approach.

In the approximation where $(8\lambda_{\text{P}}\lambda_H^{(0)}v^4)/(2\lambda_H v^2 - m_\phi^2)^2$ is small we can expand the square root in (4.1.16) and obtain:

$$m_{h_1}^2 = m_+^2 = 2v^2\lambda_H \left(1 + \frac{\lambda_{\text{P}}(\lambda_H^{(0)}/\lambda_H)\,v^2}{2\lambda_H v^2 - m_\phi^2}\right), \quad \text{for } 2\lambda_H v^2 > m_\phi^2, \qquad (4.1.19)$$

$$m_{h_1}^2 = m_-^2 = 2v^2\lambda_H \left(1 - \frac{\lambda_{\text{P}}(\lambda_H^{(0)}/\lambda_H)\,v^2}{m_\phi^2 - 2\lambda_H v^2}\right), \quad \text{for } m_\phi^2 > 2\lambda_H v^2. \qquad (4.1.20)$$

Note that our requirement of assigning the SM Higgs mass value of 126 GeV to the 'mostly h state' selects two different roots of (4.1.16) in the equations above, depending on whether the h state or the ϕ state is lighter. As a result, there is a 'discontinuity of the SM Higgs identification' with $m_{h_1}^2 > 2v^2\lambda_H$ in the first equation, while $m_{h_1}^2 < 2v^2\lambda_H$ in the second equation. Similarly, the value of λ_H is smaller or greater than the perceived value of λ_{SM} in the SM, in particular,

$$\lambda_{\text{SM}} = \lambda_H \left(1 - \frac{\lambda_{\text{P}}(\lambda_H^{(0)}/\lambda_H)\,v^2}{m_\phi^2 - 2\lambda_H v^2}\right), \quad \text{for } m_\phi^2 > 2\lambda_H v^2. \qquad (4.1.21)$$

One concludes that in the case of the CW scalar being heavier than the SM Higgs, it should be easier to stabilise the SM Higgs potential, since the initial value of λ_H here is larger than the initial value of the λ_{SM} coupling and as such, it should be useful in preventing λ_H from going negative at high values of the RG scale.[2]

---

[2]This point has been noted earlier in the literature in [147,148], [111] in the context of assisting the stabilisation of the SM Higgs by integrating out a heavy scalar. In our case the second scalar does not have to be integrated out. In fact, the required stabilising effect arises when the second scalar is not much heavier than the SM Higgs, which manifests itself in keeping the denominator in (4.1.21) not much greater than the square of the EW scale.

On a more technical note, in our computations we also take into account the fact that the requirement of stability of the Higgs potential at high scales goes beyond the simple condition $\lambda_H(\mu) > 0$ at all values of μ, but should be supplemented by the slightly stronger requirement emerging from the tree-level stability of the potential (4.1.4), which requires that $\lambda_H > \lambda_P^2/(4\lambda_\phi)$.

In the following Sections **4.1.2-4.1.4**, we extend the construction above to models with more general hidden sectors. First of all, the G_{CW} Coleman-Weinberg sector can be extended so that SM fermions are charged under G_{CW}, and secondly G_{CW} can also be non-Abelian. In addition, these CSI ESM models can include a gauge singlet with portal couplings to the Higgs and the CW scalar field. In Sections **4.3** and **4.4** we will investigate the combination of constraints arising from the Higgs vacuum stability, collider exclusions, and dark matter searches and phenomenology.

4.1.2 CSI $U(1)_{B-L} \times SM$

As in Chapter **3**, we will extend the simple $U(1)$ hidden sector to the $B - L$ theory originally introduced in [134]. The $U(1)_{B-L} \times SM$ theory is a particularly appealing CSI ESM realisation, since the gauge anomaly of $U(1)_{B-L}$ cancellation requires that the matter content of the model automatically includes three generations of right-handed Majorana neutrinos. All SM matter fields are charged under the $U(1)_{B-L}$ gauge group with charges equal to their baryon minus lepton number. In addition, the CW field ϕ carries a $B - L$ charge of 2 and its vev generates the Majorana neutrino masses and the mass of the $U(1)_{B-L}$ Z' boson. The standard see-saw mechanism generates masses of visible neutrinos and also leads to neutrino oscillations.

The scalar field content of the model is the same as before, with H being a complex doublet and $\Phi = \frac{1}{\sqrt{2}}(\phi + i\phi_2)$, a complex singlet under the SM. The tree-level scalar potential is given by (4.1.2) which in the unitary gauge takes the form (4.1.4). Our earlier discussion of the mass gap generation in the CW sector, EWSB and the mass spectrum structure, proceeds precisely as in the previous sections, with the substitution $e_{CW} \to 2\,e_{B-L}$. The one-loop corrected potential (4.1.5) becomes:

$$V_1(\phi) = \frac{\lambda_\phi}{4}\phi^4 + \frac{3}{64\pi^2}(2e_{B-L})^4\phi^4\left(\log\frac{4e_{B-L}^2\phi^2}{\mu^2} - \frac{5}{6}\right) - \frac{\lambda_P}{4}h^2\phi^2\,. \qquad (4.1.22)$$

Minimising it at $\mu = \langle \phi \rangle$ gives the matching condition for the couplings, and the expansion around the vacuum at $\langle \phi \rangle$ determines the mass of the CW scalar field (cf. (4.1.9)-(4.1.10)),

$$\lambda_\phi = \frac{11}{\pi^2} e_{\mathbf{B-L}}^4 + \lambda_{\mathrm{P}} \frac{v^2}{2\langle \phi \rangle^2} \qquad \text{at} \quad \mu = \langle \phi \rangle \qquad (4.1.23)$$

$$m_\phi^2 = \frac{6 e_{\mathbf{B-L}}^4}{\pi^2} \langle \phi \rangle^2 + \lambda_{\mathrm{P}} v^2 \qquad (4.1.24)$$

in agreement with [1]. The expressions for the Higgs field vev, v, and the Higgs mass, m_h, are unchanged and given by (4.1.14). The mass mixing matrix is the same as in (4.1.15) with m_ϕ^2 given by (4.1.24).

4.1.3   CSI $SU(2)_{\mathrm{CW}} \times$ SM

One can also use a non-Abelian extension of the SM in the CSI ESM general framework. In this section we concentrate on the simple case where the CW group is $SU(2)$, and for simplicity we assume that there are no additional matter fields (apart from the CW scalar Φ) charged under this hidden sector gauge group. This model was previously considered in [111] and subsequently in [112]. The novel feature of this model is the presence of a vector dark matter candidate, the $SU(2)$ Coleman-Weinberg gauge fields [111].

The classical scalar potential is the same as before,

$$V_{\mathrm{cl}}(H, \Phi) = \lambda_\phi (\Phi^\dagger \Phi)^2 + \lambda_H (H^\dagger H)^2 - \lambda_{\mathrm{P}} (H^\dagger H)(\Phi^\dagger \Phi), \qquad (4.1.25)$$

where Φ as well as the Higgs field H are complex doublets of the $SU(2)_{\mathrm{CW}}$ and the $SU(2)_{\mathrm{L}}$ respectively. In the unitary gauge for both of the $SU(2)$ factors we have,

$$H = \frac{1}{\sqrt{2}}(0, h), \; \Phi = \frac{1}{\sqrt{2}}(0, \phi). \qquad (4.1.26)$$

The one-loop corrected scalar potential (4.1.5) now becomes

$$V_1(\phi) = \frac{\lambda_\phi}{4} \phi^4 + \frac{9}{1024 \, \pi^2} g_{\mathrm{CW}}^4 \phi^4 \left(\log \frac{g_{\mathrm{CW}}^2 \phi^2}{4\mu^2} - \frac{5}{6} \right) - \frac{\lambda_{\mathrm{P}}}{4} h^2 \phi^2, \qquad (4.1.27)$$

where g_{CW} is the coupling of the $SU(2)$ CW gauge sector. Minimising at $\mu = \langle \phi \rangle$

gives:

$$\lambda_\phi = \frac{33}{256\,\pi^2}\,g_{\text{cw}}^4 + \lambda_{\text{P}}\frac{v^2}{2\langle\phi\rangle^2} \qquad \text{at} \quad \mu = \langle\phi\rangle \tag{4.1.28}$$

$$m_\phi^2 = \frac{9}{128\,\pi^2}\,g_{\text{cw}}^4\,\langle\phi\rangle^2 + \lambda_{\text{P}}v^2\,. \tag{4.1.29}$$

The Higgs mass is then again given by Equation (4.1.14).

4.1.4 CSI ESM ⊕ Singlet

All Abelian and non-Abelian CSI extensions of the SM introduced above can be easily extended further by adding a singlet degree of freedom, a one-component real scalar field $s(x)$. Such extensions by a real scalar were recently shown in [121] to be instrumental in generating the slow-roll potential for cosmological inflation when the scalar $s(x)$ is non-minimally coupled to gravity. The two additional features of models with the singlet, which are particularly important for the purposes of this chapter, are that the singlet portal coupling to the Higgs will provide an additional (and powerful) mechanism for the Higgs stabilisation, and that the singlet $s(x)$ is also a natural candidate for scalar dark matter.

The gauge singlet s-field is coupled to the ESM models of Sections **4.1.1-4.1.3** via scalar portal interactions with the Higgs and the CW field Φ,

$$V_{\text{cl}}(H,\phi,s) = \frac{\lambda_{Hs}}{2}H^\dagger H s^2 + \frac{\lambda_{\phi s}}{2}\Phi^\dagger \Phi s^2 + \frac{\lambda_s}{4}s^4 + V_{\text{cl}}(H,\Phi)\,. \tag{4.1.30}$$

Equations (4.1.2) and (4.1.30) describe the general, renormalisable and gauge-invariant scalar potential for the three classically massless scalars as required by classical scale invariance. The coupling constants in the potential (4.1.30) are all taken to be positive. Thus the potential is stable and the positivity of λ_{Hs} and $\lambda_{\phi s}$ ensures that no vev is generated for the singlet $s(x)$. Instead, the CW vev $\langle\phi\rangle$ generates a mass term for the singlet,

$$m_s^2 = \frac{\lambda_{Hs}}{2}\,v^2 + \frac{\lambda_{\phi s}}{2}\,|\langle\phi\rangle|^2\,. \tag{4.1.31}$$

In the vacuum state we get the following values for the scalar fields: $s = 0$, $\phi = \langle\phi\rangle$ and $H = \frac{v}{\sqrt{2}} = \sqrt{\frac{\lambda_{\text{P}}}{\lambda_{\text{H}}}}\,|\langle\phi\rangle|$.

4.2 RG Evolution

To determine the regions of parameter space where the CSI ESM models have a stable Higgs vacuum, we need to evolve the couplings in energy using the RG equations. In this section, we first specify the RG equations for all CSI ESM theories of interest, with and without the additional singlet, and then fix the initial conditions for the RG evolution.

Following this more technical build up in the present section, the Higgs vacuum stability and collider constraints on the Higgs-sector phenomenology will be analysed in Section **4.3**.

4.2.1 Standard Model $\times$ U(1)$_{\mathrm{CW}}$

This is the simplest scale-invariant extension of the SM. The hidden sector is an Abelian U(1) which couples only to the CW scalar (of charge 1) and no other matter fields. We now proceed to write down the renormalisation group equations for this model.

The scalar couplings λ_H, λ_ϕ and λ_{P} are governed by:

$$
\begin{aligned}
(4\pi)^2 \frac{d\lambda_H}{d\log\mu} = {} & -6y_t^4 + 24\lambda_H^2 + \lambda_{\mathrm{P}}^2 + \lambda_H\left(12y_t^2 - \frac{9}{5}g_1^2 - 9g_2^2 - 3g_{\mathrm{mix}}^2\right) \\
& + \frac{27}{200}g_1^4 + \frac{9}{20}g_2^2 g_1^2 + \frac{9}{8}g_2^4 + \frac{3}{4}g_2^2 g_{\mathrm{mix}}^2 \\
& + \frac{9}{20}g_1^2 g_{\mathrm{mix}}^2 + \frac{3}{8}g_{\mathrm{mix}}^4
\end{aligned}
\tag{4.2.32}
$$

$$
(4\pi)^2 \frac{d\lambda_\phi}{d\log\mu} = 20\lambda_\phi^2 + 2\lambda_{\mathrm{P}}^2 - 12\lambda_\phi\, e_{\mathrm{CW}}^2 + 6e_{\mathrm{CW}}^4
\tag{4.2.33}
$$

$$
(4\pi)^2 \frac{d\lambda_{\mathrm{P}}}{d\log\mu} = \lambda_{\mathrm{P}}\left(6y_t^2 + 12\lambda_H + 8\lambda_\phi - 4\lambda_{\mathrm{P}} - 6e_{\mathrm{CW}}^2 \right.
\tag{4.2.34}
$$

$$
\left. -\frac{9}{10}g_1^2 - \frac{9}{2}g_2^2 - \frac{3}{2}g_{\mathrm{mix}}^2\right) - 3g_{\mathrm{mix}}^2 e_{\mathrm{CW}}^2\,.
$$

$$
\tag{4.2.35}
$$

The RG equation for the top Yukawa coupling, y_t, is

$$
(4\pi)^2 \frac{dy_t}{d\log\mu} = y_t\left(\frac{9}{2}y_t^2 - \frac{17}{20}g_1^2 - \frac{9}{4}g_2^2 - 8g_3^2 - \frac{17}{12}g_{\mathrm{mix}}^2\right)\,.
\tag{4.2.36}
$$

Finally, e_{CW}, g_{mix} and g_i denote the gauge couplings of the $\text{U}(1)_{\text{CW}} \times \text{SM}$, which obey

$$(4\pi)^2 \frac{de_{\text{CW}}}{d \log \mu} = \frac{1}{3} e_{\text{CW}}^3 + \frac{41}{6} e_{\text{CW}} g_{\text{mix}}^2 \tag{4.2.37}$$

$$(4\pi)^2 \frac{dg_{\text{mix}}}{d \log \mu} = \frac{41}{6} g_{\text{mix}} \left(g_{\text{mix}}^2 + 2g_1^2 \right) + \frac{1}{3} e_{\text{CW}}^2 g_{\text{mix}} \tag{4.2.38}$$

$$(4\pi)^2 \frac{dg_3}{d \log \mu} = -7 g_3^3 \,, \tag{4.2.39}$$

$$(4\pi)^2 \frac{dg_2}{d \log \mu} = -\frac{19}{6} g_2^3 \,, \tag{4.2.40}$$

$$(4\pi)^2 \frac{dg_1}{d \log \mu} = \frac{41}{10} g_1^3 \,. \tag{4.2.41}$$

A characteristic feature of the Abelian ESM theory is g_{mix}, the kinetic mixing of the two Abelian factors, $\text{U}(1)_{\text{CW}} \times \text{U}(1)_Y$. For a generic matter field φ transforming under both $\text{U}(1)$'s with the charges Q^{CW} and Q^Y, the kinetic mixing is defined as the coupling constant g_{mix} appearing in the the covariant derivative,

$$D_\mu \varphi = \partial_\mu \varphi + i \sqrt{\frac{3}{5}} g_1 Q^Y A_\mu^Y + i (g_{\text{mix}} Q^Y + e_{\text{CW}} Q^{\text{CW}}) A_\mu^{\text{CW}} \,. \tag{4.2.42}$$

Kinetic mixing is induced radiatively in so far as there are matter fields transforming under both Abelian factors. In what follows, we will for simplicity choose $g_{\text{mix}}(\mu = M_t) = 0$ at the top mass.

4.2.2   Standard Model $\times$ $\text{U}(1)_{\text{B-L}}$

The RG equations in the $\text{B} - \text{L}$ theory are the appropriate generalisation of the equations above. These equations were first derived in [149], and they were also discussed recently in [109]. In our conventions the RG evolution in the CSI $\text{U}(1)_{\text{B-L}} \times$ SM theory with the classical scalar potential (4.1.2) is determined by the set of RG equations below:

$$(4\pi)^2 \frac{d\lambda_H}{d \log \mu} = r.h.s. \,(4.2.32) \tag{4.2.43}$$

$$(4\pi)^2 \frac{d\lambda_\phi}{d \log \mu} = 20\lambda_\phi^2 + 2\lambda_P^2 - 48\lambda_\phi e_{\text{B-L}}^2 + 96 e_{\text{B-L}}^4 - Tr[(y^M)^4]$$
$$+ 8\lambda_\phi Tr[(y^M)^2] \tag{4.2.44}$$

$$(4\pi)^2 \frac{d\lambda_P}{d \log \mu} = \lambda_P \left(6y_t^2 + 12\lambda_H + 8\lambda_\phi - 4\lambda_P - 24 e_{\text{B-L}}^2 - \frac{9}{10} g_1^2 - \frac{9}{2} g_2^2 - \frac{3}{2} g_{\text{mix}}^2 \right.$$
$$\left. + 4Tr[(y^M)^2] \right) - 12 g_{\text{mix}}^2 e_{\text{B-L}}^2 \,. \tag{4.2.45}$$

The Yukawas for the top quark and for the three Majorana neutrinos are evolved via

$$(4\pi)^2 \frac{dy_t}{d\log\mu} = y_t \left(\frac{9}{2}y_t^2 - \frac{17}{20}g_1^2 - \frac{9}{4}g_2^2 - 8g_3^2 - \frac{17}{12}g_{\text{mix}}^2 - \frac{2}{3}e_{\text{B-L}}^2 \right.$$
$$\left. -\frac{5}{3}g_{\text{mix}}e_{\text{B-L}} \right) \tag{4.2.46}$$

$$(4\pi)^2 \frac{dy_i^M}{d\log\mu} = y_i^M \left(4(y_i^M)^2 + Tr[(y^M)^2] - 6e_{\text{B-L}}^2 \right) , \tag{4.2.47}$$

and the gauge couplings are evolved by Equations (4.2.41) together with

$$(4\pi)^2 \frac{de_{\text{B-L}}}{d\log\mu} = 12e_{\text{B-L}}^3 + \frac{32}{3}e_{\text{B-L}}^2\, g_{\text{mix}} + \frac{41}{6}e_{\text{B-L}}\, g_{\text{mix}}^2 \tag{4.2.48}$$

$$(4\pi)^2 \frac{dg_{\text{mix}}}{d\log\mu} = \frac{41}{6}g_{\text{mix}} \left(g_{\text{mix}}^2 + \frac{6}{5}g_1^2 \right) + 2\frac{16}{3}e_{\text{B-L}} \left(g_{\text{mix}}^2 + \frac{3}{5}g_1^2 \right)$$
$$+12e_{\text{B-L}}^2\, g_{\text{mix}} . \tag{4.2.49}$$

4.2.3 Standard Model $\times$ U(1)$_{\text{B-L}}$ $\oplus$ Singlet

When discussing the Higgs vacuum stability, we will soon find out that the size of the available region on the CSI ESM parameter space will depend significantly on whether or not the theory includes an additional singlet field. We are thus led to extend the RG equations above with an extra singlet.

The scalar self-couplings and portal couplings in this model are governed by the following equations,

$$(4\pi)^2 \frac{d\lambda_H}{d\log\mu} = r.h.s.\,(4.2.43) + \frac{1}{2}\lambda_{Hs}^2 \tag{4.2.50}$$

$$(4\pi)^2 \frac{d\lambda_\phi}{d\log\mu} = r.h.s.\,(4.2.44) + \frac{1}{2}\lambda_{\phi s}^2 \tag{4.2.51}$$

$$(4\pi)^2 \frac{d\lambda_P}{d\log\mu} = r.h.s.\,(4.2.45) - \lambda_{Hs}\lambda_{\phi s} \tag{4.2.52}$$

$$(4\pi)^2 \frac{d\lambda_s}{d\log\mu} = 18\lambda_s^2 + \lambda_{\phi s}^2 + 2\lambda_{Hs}^2 \tag{4.2.53}$$

$$(4\pi)^2 \frac{d\lambda_{Hs}}{d\log\mu} = \lambda_{Hs} \left(6y_t^2 + 12\lambda_H + 6\lambda_s + 4\lambda_{Hs} - \frac{9g_1^2}{10} - \frac{9g_2^2}{2} \right)$$
$$-2\lambda_P\lambda_{\phi s} \tag{4.2.54}$$

$$(4\pi)^2 \frac{d\lambda_{\phi s}}{d\log\mu} = \lambda_{\phi s} \left(12\lambda_\phi + 6\lambda_s + 4\lambda_{\phi s} - 18e_{\text{B-L}}^2 \right) - 4\lambda_P\lambda_{Hs}. \tag{4.2.55}$$

The rest of the RG equations are the same as before. The equations for the Yukawa couplings are given in (4.2.46)-(4.2.47), and the equations for the gauge

couplings are given by Equations (4.2.41) together with (4.2.48)-(4.2.49). As always, we set $g_{\rm mix}(\mu = M_t) = 0$.

Note that it is easy to derive a simple formula (Equation (4.2.58) below) which computes the coefficients in front of scalar couplings on the right-hand sides of the RG equations. First, let us write the classical scalar potential in the form

$$V_0 = \sum_\varphi \frac{\lambda_\varphi}{4} (\vec{\varphi}^2)^2 + \sum_{\varphi < \varphi'} \frac{\lambda_{\varphi\varphi'}}{4} (\vec{\varphi}^2)(\vec{\varphi}'^2) \,, \tag{4.2.56}$$

where in our case $\varphi = \{h, \phi, s\}$, and the second sum is understood as a sum over the three pairs of indices, (h, ϕ), (h, s) and (ϕ, s). The notation $\vec{\varphi}$ denotes the canonically normalised real components of the Higgs, $\vec{h} = (h_1, \ldots, h_4)$, the complex doublet $\vec{\phi} = (\phi_1, \ldots, \phi_4)$ and the real singlet $\vec{s} = s$. In general we denote the number of real components of each of the species of $\vec{\varphi}$ and N_φ. It is then easy to derive an expressions for the scalar-coupling contributions to all the self-interactions by counting the contributing four-point 1PI diagrams involving 2 scalar vertices. For the beta functions of the self-couplings we get

$$(4\pi)^2 \frac{d\lambda_\varphi}{d\log\mu} \ni 2(N_\varphi + 8)\, \lambda_\varphi^2 + \sum_{\tilde\varphi} \frac{N_{\tilde\varphi}}{2}\, \lambda_{\varphi\tilde\varphi}^2 \,, \tag{4.2.57}$$

and the portal couplings are governed by

$$(4\pi)^2 \frac{d\lambda_{\varphi\varphi'}}{d\log\mu} \ni \sum_\varphi 2(N_\varphi + 2)\, \lambda_\varphi \lambda_{\varphi\varphi'} + \sum_{\varphi'} 2(N_{\varphi'} + 2)\, \lambda_{\varphi\varphi'} \lambda_{\varphi'} + \sum_{\tilde\varphi} N_{\tilde\varphi}\, \lambda_{\varphi\tilde\varphi} \lambda_{\varphi'\tilde\varphi} + 4\, \lambda_{\varphi\varphi'}^2 \tag{4.2.58}$$

This formula is valid for all of the CSI ESM examples considered in this chapter.

4.2.4 Standard Model× $\mathbf{SU(2)}_{\rm CW}$

We can also write down the relevant renormalisation group equations for the classically scale-invariant Standard Model $\times$ $SU(2)_{\rm CW}$ theory with a scalar potential given by Equation (4.1.25). These RG equations were first derived in [111, 112]. For scalar

self-couplings λ_H and λ_ϕ, and the portal coupling λ_P we have:

$$
(4\pi)^2 \frac{d\lambda_H}{d\log\mu} = -6y_t^4 + 24\lambda_H^2 + 2\lambda_P^2 + \lambda_H\left(12y_t^2 - \frac{9}{5}g_1^2 - 9g_2^2\right) + \frac{27}{200}g_1^4
$$
$$
+ \frac{9}{20}g_2^2 g_1^2 + \frac{9}{8}g_2^4 \tag{4.2.59}
$$

$$
(4\pi)^2 \frac{d\lambda_\phi}{d\log\mu} = 24\lambda_\phi^2 + 2\lambda_P^2 - 9\lambda_\phi\, g_{\rm cw}^2 + \frac{9}{8}g_{\rm cw}^4 \tag{4.2.60}
$$

$$
(4\pi)^2 \frac{d\lambda_P}{d\log\mu} = \lambda_P\left(6y_t^2 + 12\lambda_H + 12\lambda_\phi - 4\lambda_P - \frac{9}{2}g_{\rm cw}^2\right.
$$
$$
\left. - \frac{9}{10}g_1^2 - \frac{9}{2}g_2^2\right), \tag{4.2.61}
$$

where the top Yukawa coupling obeys

$$
(4\pi)^2 \frac{dy_t}{d\log\mu} = y_t\left(\frac{9}{2}y_t^2 - \frac{17}{20}g_1^2 - \frac{9}{4}g_2^2 - 8g_3^2\right), \tag{4.2.62}
$$

and $g_{\rm cw}$, $g_{3,2,1}$ are the gauge couplings of the $SU(2)_{\rm cw} \times SU(3) \times SU(2) \times U(1)$,

$$
(4\pi)^2 \frac{dg_{\rm cw}}{d\log\mu} = -\frac{43}{6}g_{\rm cw}^3 - \frac{1}{(4\pi)^2}\frac{259}{6}g_{\rm cw}^5 \tag{4.2.63}
$$

$$
(4\pi)^2 \frac{dg_3}{d\log\mu} = -7g_3^3 \tag{4.2.64}
$$

$$
(4\pi)^2 \frac{dg_2}{d\log\mu} = -\frac{19}{6}g_2^3 \tag{4.2.65}
$$

$$
(4\pi)^2 \frac{dg_1}{d\log\mu} = \frac{41}{10}g_1^3, \tag{4.2.66}
$$

where for the $U(1)$ coupling we use the normalisation $g_1^2 = \frac{5}{3}g_Y^2$.

All running couplings are computed in the $\overline{\rm MS}$ scheme, and furthermore we use the physical freeze-out condition for the $SU(2)_{\rm cw}$ degrees of freedom at the RG scales below their mass shell. In other words, the $SU(2)_{\rm cw}$ contributions to the β-functions for $g_{\rm cw}$, λ_ϕ and λ_P will be set to zero when $\mu < M_{Z'} = \frac{1}{2}g_{\rm cw}\langle\phi\rangle$.

4.2.5 Standard Model $\times$ SU(2)$_{\rm cw}$ $\oplus$ singlet

RG-equations for the three scalar self-couplings now take the form:

$$
(4\pi)^2 \frac{d\lambda_H}{d\log\mu} = -6y_t^4 + 24\lambda_H^2 + 2\lambda_P^2 + \frac{1}{2}\lambda_{Hs}^2 + \lambda_H\left(12y_t^2 - \frac{9}{5}g_1^2 - 9g_2^2\right)
$$
$$
+ \frac{27}{200}g_1^4 + \frac{9}{20}g_2^2 g_1^2 + \frac{9}{8}g_2^4 \tag{4.2.67}
$$

$$
(4\pi)^2 \frac{d\lambda_\phi}{d\log\mu} = 24\lambda_\phi^2 + 2\lambda_P^2 + \frac{1}{2}\lambda_{\phi s}^2 - 9\lambda_\phi\, g_{\rm cw}^2 + \frac{9}{8}g_{\rm cw}^4 \tag{4.2.68}
$$

$$
(4\pi)^2 \frac{d\lambda_s}{d\log\mu} = 18\lambda_s^2 + 2\lambda_{\phi s}^2 + 2\lambda_{Hs}^2, \tag{4.2.69}
$$

and for the three portal couplings we have

$$(4\pi)^2 \frac{d\lambda_{\mathrm{P}}}{d\log\mu} = \lambda_{\mathrm{P}} \left(6y_t^2 + 12\lambda_H + 12\lambda_\phi - 4\lambda_{\mathrm{P}} - \frac{9}{2}g_{\mathrm{CW}}^2 - \frac{9}{10}g_1^2 \right. \quad (4.2.70)$$
$$\left. - \frac{9}{2}g_2^2 \right) - \lambda_{Hs}\lambda_{\phi s}$$

$$(4\pi)^2 \frac{d\lambda_{Hs}}{d\log\mu} = \lambda_{Hs} \left(6y_t^2 + 12\lambda_H + 6\lambda_s + 4\lambda_{\mathrm{Hs}} - \frac{9}{10}g_1^2 - \frac{9}{2}g_2^2 \right) \quad (4.2.71)$$
$$- 4\lambda_{\mathrm{P}}\lambda_{\phi s}$$

$$(4\pi)^2 \frac{d\lambda_{\phi s}}{d\log\mu} = \lambda_{\phi s} \left(12\lambda_\phi + 6\lambda_s + 4\lambda_{\phi s} - \frac{9}{2}g_{\mathrm{CW}}^2 \right) - 4\lambda_{\mathrm{P}}\lambda_{Hs} . \quad (4.2.72)$$

4.2.6 Initial Conditions and Stability Bounds

To solve the RG equations and determine the RG evolution of the couplings of our models, we first need to specify the initial conditions for all the couplings.

First, we specify the initial conditions for the SM coupling constants at M_t: The initial values for the top Yukawa coupling y_t and the SM gauge couplings are taken from [59],

$$y_t(\mu = M_t) = 0.93558 + 0.00550 \left(\frac{M_t}{\mathrm{GeV}} - 173.1 \right) + -0.00042 \frac{\alpha_3(M_z) - 0.1184}{0.0007}$$
$$- 0.00042 \frac{M_W - 80.384\,\mathrm{GeV}}{\mathrm{GeV}} \pm 0.00050_{\mathrm{th}} \quad (4.2.73)$$

$$g_3(\mu = M_t) = 1.1666 \quad\quad\quad\quad\quad\quad\quad\quad\quad\quad\quad\quad\quad\quad\quad\quad (4.2.74)$$
$$+ 0.00314 \frac{\alpha_3(M_z) - 0.1184}{0.0007} - 0.00046 \left(\frac{M_t}{\mathrm{GeV}} - 173.1 \right)$$

$$g_2(\mu = M_t) = 0.64822 \quad\quad\quad\quad\quad\quad\quad\quad\quad\quad\quad\quad\quad\quad\quad\quad (4.2.75)$$
$$+ 0.00004 \left(\frac{M_t}{\mathrm{GeV}} - 173.1 \right) + 0.00011 \frac{M_W - 80.384\,\mathrm{GeV}}{\mathrm{GeV}}$$

$$g_1(\mu = M_t) = \sqrt{\frac{5}{3}} \left(0.35761 + 0.00011 \left(\frac{M_t}{\mathrm{GeV}} - 173.1 \right) - \quad\quad (4.2.76) \right.$$
$$\left. 0.00021 \frac{M_W - 80.384\,\mathrm{GeV}}{\mathrm{GeV}} \right).$$

In our numerical analysis we will always assume the central values for M_t and M_W.

The CW portal coupling, λ_P and the CW gauge coupling are taken as the two free input parameters specifying the two-dimensional BSM parameter space of our U(1) or SU(2) × SM theories. When an additional singlet field $s(x)$ is present, the input parameters also include λ_{Hs}, λ_s and $\lambda_{\phi s}$.

The input values of the two remaining couplings, the Higgs self-coupling λ_H, and the self-coupling of the CW scalar, λ_ϕ, are then determined from the value of the SM Higgs mass and from the CW matching condition, (4.1.9), respectively. To find λ_H, we numerically compute the eigenvalues of the mass matrix (4.1.15), and set $m_{h_1} = 125.66$ GeV, as was outlined in Equation (4.1.18). We then iteratively solve for $\lambda_\phi(\mu = M_t)$ by running it from the top mass scale to $\mu = \langle \phi \rangle$, and checking that we fulfil the CW matching relation (4.1.9) at the latter scale.

Having thus specified the initial conditions for all couplings at the low scale, $\mu = M_t$, we run them up to the high scale, $\mu = M_{Pl}$, by numerically solving the RG equations. To determine the region of parameter space where the Higgs potential is stable, we check that the conditions

$$4\lambda_H(\mu)\,\lambda_\phi(\mu) \,>\, \lambda_P^2(\mu)\,, \qquad \lambda_H(\mu) \,>\, 0\,, \quad \text{for all } \mu \leq M_{Pl}\,, \qquad (4.2.77)$$

arising from the positive definiteness of Equation (4.1.2), are fulfilled. We also check that the model remains perturbative, requiring that all the scalar and gauge couplings are bounded by an order-one constant all the way to the Planck scale,

$$\lambda_i(\mu) \,<\, \text{const}\,\mathcal{O}(1) = 3\,, \qquad (4.2.78)$$

where for concreteness we chose a conservative numerical value of the upper bound = 3; in practice our results do not depend significantly on this choice.

4.3   Higgs Physics: Stability and Phenomenology

It is well known that in the Standard Model, the Higgs self-coupling becomes negative at $\mu \sim 10^9$ GeV, making the SM Higgs potential unstable below the Planck scale [59, 150] (see also [151, 152] for a review of earlier work). This effect can be seen in Figure 4.1 which shows the solution of RG equations in the limit where all Higgs portal interactions are switched off.
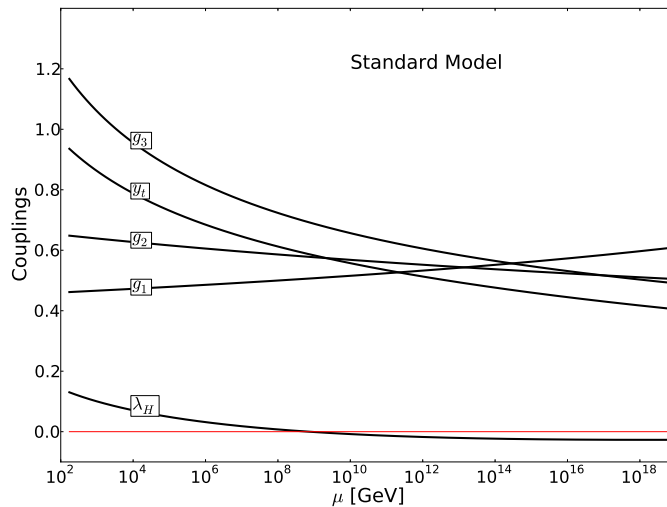
Figure 4.1: RG evolution in the Standard Model. The Higgs self-coupling turns negative at $\mu \gtrsim 10^9$ GeV, thus signalling that the SM Higgs potential becomes unstable below the Planck scale. In this and all other Figures we use $M_t = 173.1$ GeV.

For our classically scale-invariant extensions of the SM to be meaningful and practical natural theories valid all the way up to the Planck scale, the Higgs potential has to be stabilised.[3] There are two mechanisms, both relying on the Higgs portal interactions, to achieve this:

1. The SM Higgs is the mixed mass eigenstate h_1 between H and the CW scalar as dictated by Equation (4.1.18). As we explained at the end of Section **4.1.1**, in the case where the second scalar is heavier than the Higgs, $m_{h_2} > m_{h_1}$, the initial value of the Higgs self-coupling λ_H is larger than in the SM, cf. Equation (4.1.21), and this helps with the Higgs stabilisation [111, 147, 148].

2. The portal couplings of other scalars to the Higgs, such as λ_P and λ_{Hs} contribute positively to the beta function of λ_H as can be seen e.g. from the RG

---

[3]In this chapter we will concentrate on the more conservative case of absolute stability. Another phenomenologically acceptable possibility analysed recently in [59] is that the SM vacuum is metastable, with a lifetime much greater than the age of the Universe. In that case one would also have to argue why after reheating the Universe ended up in the metastable vacuum near the origin, for example following the approach of [153].
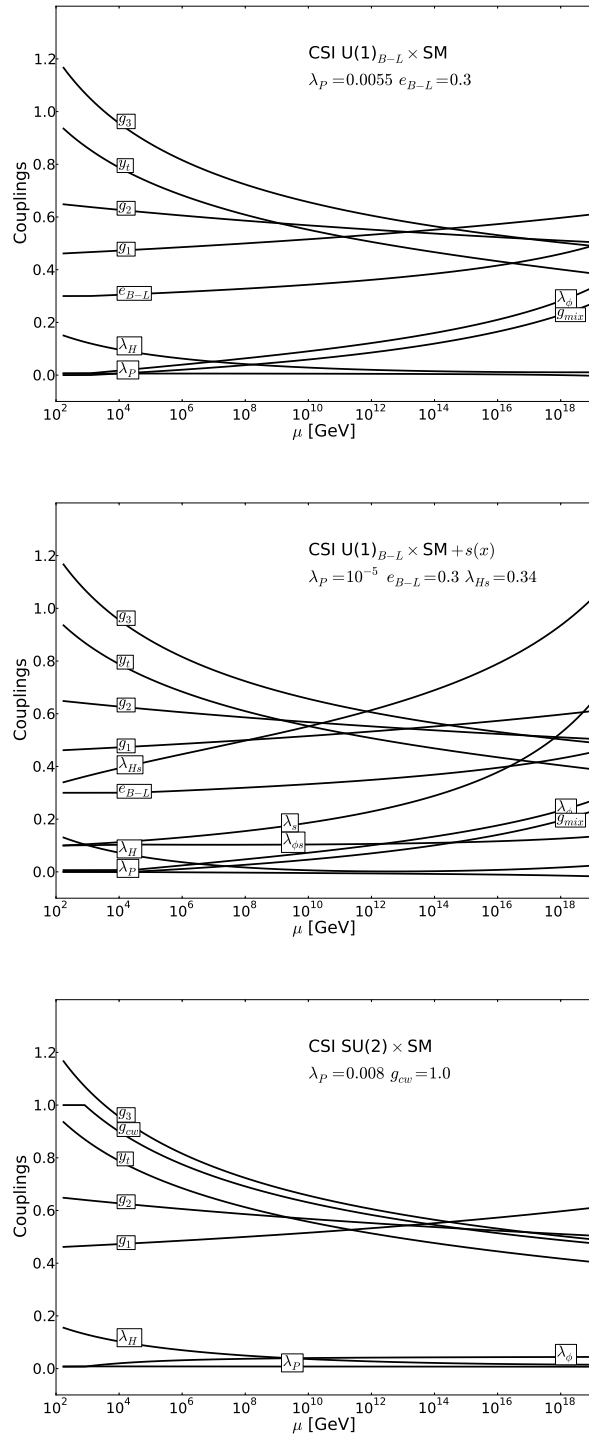
Figure 4.2: RG evolution in CSI ESM theories with (a) E = U(1)$_{\mathbf{B-L}}$, (b) E = U(1)$_{\mathbf{B-L}}$ + $s(x)$, and (c) E = SU(2)$_{\mathbf{CW}}$. With these initial conditions the Higgs coupling λ_H stays positive and satisfies the tree-level stability bound (4.2.77).

equation (4.2.67) in the $SU(2)_{CW}$ + scalar case, where $\beta_{\lambda_H} \ni 2\lambda_P^2 + \frac{1}{2}\lambda_{Hs}^2$. This effect (due in particular to the otherwise unconstrained but still perturbative λ_{Hs} coupling) will be instrumental in achieving the Higgs stability in models with an extra scalar [154, 155].

Examples of RG running for some specific input values of parameters for three different classes of models which result in stable Higgs potential are shown in Figure 4.2. Cases (a) and (c) give an example of mechanism (1), and the model with an additional scalar in case (b) is a representative of mechanism (2) at work.

In the rest of this section, we will quantify the regions of the parameter spaces for individual models where the scalar potential is stabilised. We will also combine these considerations with the current LHC limits applied to the extended Higgs sectors of our Higgs portal theories in a model-by-model basis.

4.3.1   CSI $U(1)_{CW} \times SM$

In this theory mechanism (1) is operational for stabilising the Higgs potential in a region of the two-dimensional parameter space of the model described by λ_P and the CW gauge coupling. As shown in Figure 4.3, we get a wedge shaped region inside the black contour, inside which the Higgs potential is stable.

Higgs stabilisation in this region can be traced to the initial value of λ_H being enhanced compared to the SM due to mixing between h and the CW scalar field. The wedge shape can be understood as follows. The upper edge of the wedge follows the mass contour where $m_{h_2} > m_h$, since the enhancement of the initial value of λ_h only happens when $m_{h_2} > m_{h_1}$ (see (4.1.21)). The mechanism is only effective when the two masses are not too far from each other (cf. the denominator of the second term in Equation (4.1.21)). The lower contour of the wedge signifies when the mass difference becomes too large. The effect is enhanced when the off-diagonal element is larger as we get more mixing. This explains why the stability wedge in Figure 4.3 is wider for larger values of λ_P. We get an upper limit on $e_{CW} \approx 0.9$ since for larger values we find a Landau pole before the Planck scale.

Higgs sector phenomenology of this model in the context of LHC, LEP, future colliders and low energy measurements was analysed recently in [82]. In particular,
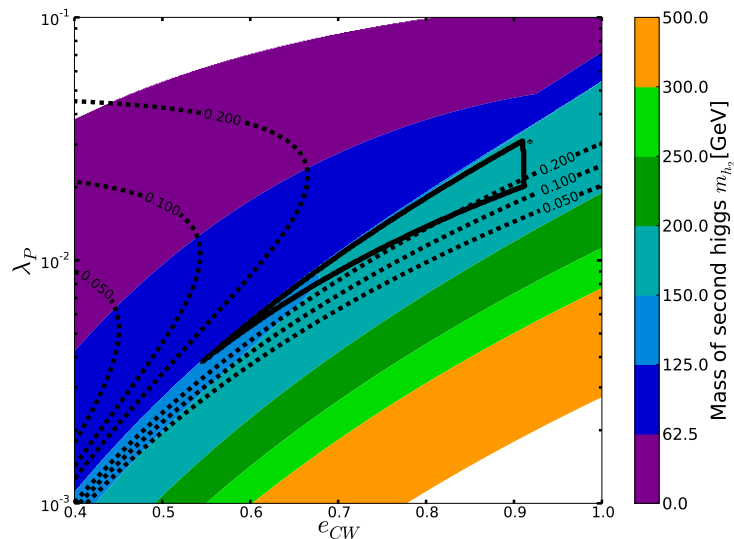
Figure 4.3: Parameter space in the minimal $U(1)_{CW} \times SM$ classically scale-invariant theory. The black wedge-shaped contour shows the region of the (λ_P, e_{CW}) parameter space of the model where the Higgs potential is stabilised. The dotted lines represent contours of fixed values $\sin^2\theta = 0.05$, 0.1 and 0.2 of the Higgs mixing angle. Finally, the colour-coding indicates the mass of the second scalar h_2 in GeV.

it was shown there that in the part of the parameter space where the second scalar is light, 10^{-4} GeV $< m_{h_2} < m_{h_1}/2$, the presently available Higgs data (and specifically the limits on the invisible Higgs decays) constrain the model quite tightly by placing an upper limit on the portal coupling at $\lambda_P \lesssim 10^{-5}$.

However, from Figure 4.3 we see that the Higgs stability in the minimal model (and more generally in all portal models without additional scalar $s(x)$, i.e. relying on the stabilisation mechanism (1)) requires the second scalar to be heavier than the SM Higgs, $m_{h_2} > m_{h_1}$ (see also Figures 4.4, 4.5). Thus Higgs stability pushes these models into the region of the parameter space with a heavier second scalar, precisely where the collider limits on invisible Higgs decays and on the non-observation of other Higgs-like states are much less stringent.

Collider limits which do constrain the stability region in Figure 4.3 are exclusion limits on the heavier Higgs production normalised to the expected SM cross-section at this Higgs mass. In all Higgs portal models we consider in this chapter, the

expected cross-section for the h_2 scalar is given by the SM cross-section multiplied $\sin^2\theta$ of the mixing angle. With the currently available ATLAS and CMS data for the search of the heavier Higgs boson at integrated luminosity of up to 5.1 fb^{-1} at $\sqrt{s} = 7$ TeV and up to 5.3 fb^{-1} at $\sqrt{s} = 8$ TeV, the observed signal strength in the units of the SM cross-section for the heavier Higgs is roughly at the level of 10^{-1}, or slightly above, as can be seen from plots in [156–158]. This gives an upper limit on the mixing angle $\sin^2\theta \lesssim 0.1$.

The contours of constant values of $\sin^2\theta = 0.05$, 0.1 and 0.2 are shown on Figure 4.3 as dotted lines. As we can see for $\sin^2\theta \lesssim 0.1$, there is no overlap left between what is allowed by the collider limits and what is consistent with the Higgs stability in this model. We thus conclude that the combination of the Higgs potential stabilisation and the LHC limits on the heavier Higgs essentially rule out the minimal $U(1)_{\mathrm{CW}} \times$ SM theory. This conclusion is based on a one-loop RG analysis with the methodology we adopted for the initial values, and on the use of the central value for the top mass. As such there is an intrinsic theoretical uncertainty in the exact position and size of the wedge. By lowering the top mass from its central value by 1 GeV, the wedge in Figure 4.3 would touch the $\sin^2\theta = 0.1$ contour, making the model viable in a limited corner of parameter space.

Instead, to get a stable viable model with the current central value of the top mass and without relying upon the sub-leading RG effects, we will simply extend the theory by adding a singlet $s(x)$ in Sections **4.3.3** and **4.3.5**.

4.3.2 CSI $\mathbf{U(1)_{B-L} \times SM}$

One way to extend the minimal model is to allow for interactions of the hidden sector with the SM fermions. As we have seen already, a simple implementation of this idea is described by the $U(1)_{\mathbf{B-L}} \times$ SM classically scale-invariant theory. We proceed to solve the RG equations in this model and search for a region of parameter space where the scalar potential is stable, with the results shown in Figure 4.4.

The stability region in Figure 4.4 is shorter along the horizontal $e_{\mathbf{B-L}}$–direction than in the minimal CW model of Figure 4.3 above. This is caused by the slope of the $\mathrm{B-L}$ gauge coupling being steeper than for the minimal $U(1)_{\mathrm{CW}} \times$ SM theory, due to
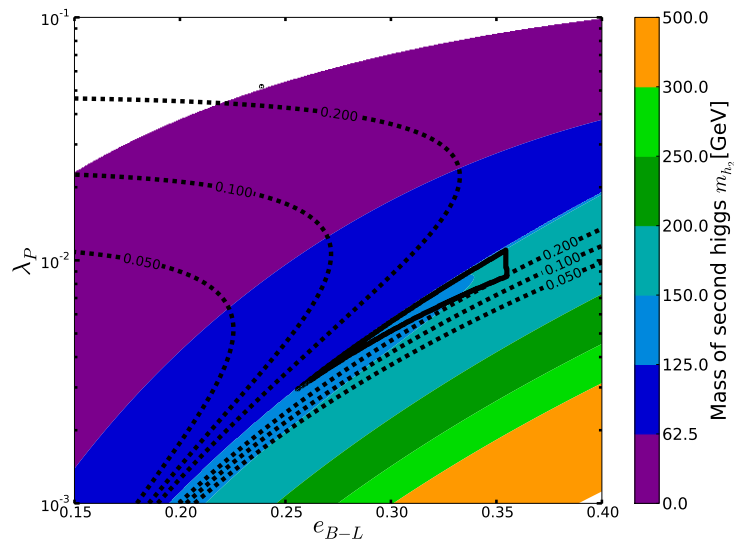
Figure 4.4: Parameter space of the $U(1)_{\mathbf{B-L}} \times$ SM theory showing the region where the Higgs potential is stabilised and the $\sin^2 \theta$ contours. The legend is the same as in Figure 4.3.

the SM quarks and leptons which are now charged under the $U(1)_{\mathbf{B-L}}$ gauge group. We therefore get a Landau pole before the Planck scale if $e_{\mathbf{B-L}}(\mu = m_t) \gtrsim 0.35$, and this shortens the allowed region.

The width of the stability wedge reflects the fact that in the $B - L$ model the CW scalar ϕ has a $B - L$ charge of two. Therefore, one would expect that the width of the stability region for the $B - L$ model at a fixed value of the gauge coupling, say at $e_{\mathbf{B-L}} = 0.3$, should be of similar size to the stability region of the pure $U(1)$ CW sector at twice the value of the coupling, i.e. at $e_{\mathrm{CW}} = 0.6$, which is indeed the case.

Collider exclusion limits of $\sin^2 \theta \lesssim 0.1$ are indicated in Figure 4.4 as before by the dotted lines showing contours of constant $\sin^2 \theta = 0.05$, 0.1 and 0.2. We see that the combination of the Higgs potential stabilisation and the LHC limits on the heavier Higgs rules out also the $U(1)_{\mathbf{B-L}} \times$ SM theory without an additional singlet.

In the $U(1)_{\mathbf{B-L}}$ model we also have a Z' boson which couples to the Standard Model fermions. The ATLAS and CMS experiments give lower limits for $M_{Z'}$ of

about 3 TeV [159, 160]. This implies

$$M_{Z'} = 2e_{\mathbf{B-L}} \langle \phi \rangle = 2e_{\mathbf{B-L}} \sqrt{\frac{2\lambda_H}{\lambda_p}} v \,, \qquad (4.3.79)$$

and therefore

$$\sqrt{\lambda_{\mathrm{P}}} < \frac{2v\sqrt{2\lambda_H}}{3\,\mathrm{TeV}} e_{\mathbf{B-L}} \implies \lambda_p \lesssim (0.1\,e_{\mathbf{B-L}})^2 \,. \qquad (4.3.80)$$

For $e_{\mathbf{B-L}} = 0.35$ we find that $\lambda_{\mathrm{P}} \lesssim 10^{-3}$, which is clearly outside the stability wedge of the $\mathrm{B-L}$ model. Therefore Higgs stabilisation in the minimal $\mathrm{U(1)}_{\mathbf{B-L}} \times \mathrm{SM}$ theory is also not compatible with the collider limits on Z'.

4.3.3 CSI U(1)$_{\mathbf{B-L}} \times$ SM $\oplus$ singlet

When we add a real scalar $s(x)$ to the $\mathrm{U(1)}_{\mathrm{CW}}$ or $\mathrm{U(1)}_{\mathbf{B-L}} \times$ SM theory, the scalar potential is stabilised by mechanism (2) which relies on a positive shift in the β-function for λ_H,

$$\beta_{\lambda_H} \ni +\frac{\lambda_{Hs}}{2} \,. \qquad (4.3.81)$$

We have checked that the stabilisation occurs on the entire $(\lambda_{\mathrm{P}}, e)$ 2d parameter space for values of $\lambda_{Hs} \sim 0.34$ or above, as can be seen from the left table in Table 4.1.

4.3.4 CSI SU(2)$_{\mathrm{CW}} \times$ SM

Solving RG equations in the non-Abelian CW theory coupled to the SM gives the Higgs stability region shown in Figure 4.5 together with the $\sin^2 \theta$ exclusion contours. The stability wedge is now shifted to larger values of g_{CW}, as ϕ has an equivalent charge of $1/2$. From Figure 4.5, we conclude that the combination of the Higgs potential stabilisation and the LHC limits on the heavier Higgs leaves a small corner of the parameter space available in the minimal SU(2)$_{\mathrm{CW}} \times$ SM theory.

4.3.5 CSI SU(2)$_{\mathrm{CW}} \times$ SM $\oplus$ singlet

The Higgs potential in the SU(2)$_{\mathrm{CW}} \times$ SM model can be stabilised on the entire 2d plane $(\lambda_{\mathrm{P}}, g_{\mathrm{CW}})$ by extending the model with a vev-less singlet $s(x)$ portally

λ_{P}	$e_{\mathbf{B-L}}$	λ_{Hs}		λ_{P}	g_{CW}	λ_{Hs}
10^{-5}	0.1	0.34		10^{-5}	0.8	0.35
10^{-5}	0.2	0.34		10^{-5}	1.4	0.35
10^{-5}	0.3	0.33		10^{-5}	2.0	0.35
0.0001	0.1	0.35		0.0001	0.8	0.35
0.0001	0.2	0.34		0.0001	1.4	0.35
0.0001	0.3	0.33		0.0001	2.0	0.35
0.001	0.1	0.35		0.001	0.8	0.34
0.001	0.2	0.29		0.001	1.4	0.35
0.001	0.3	0.33		0.001	2.0	0.35

Table 4.1: Minimal values of λ_{Hs} needed to stabilise the Higgs potential in the CSI ESM $\oplus$ singlet models with $\lambda_s = 0.1$ and $\lambda_{\phi s} = 0.01$. Left Table: $\mathrm{U(1)_{B-L}}$. Right Table: $\mathrm{SU(2)_{CW}}$.
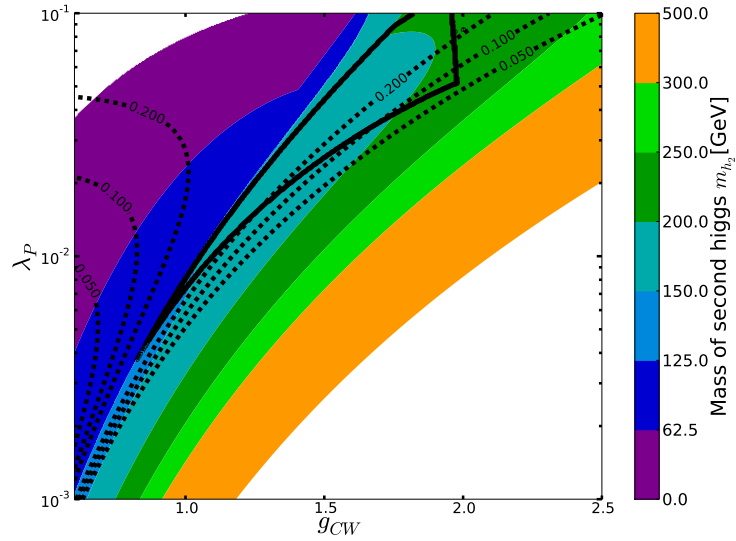

Figure 4.5: Parameter space of the $\mathrm{SU(2)_{CW}} \times \mathrm{SM}$ theory showing the region where the Higgs potential is stabilised and the $\sin^2\theta$ contours. The legend is the same as in Figure 4.3.

coupled to the Higgs, as in Equation (4.3.81). The table on the right in Table 4.1 shows the critical value of λ_{Hs} for this stabilisation mechanism to work in the CSI $\mathrm{SU(2)_{CW}} \times \mathrm{SM} \oplus$ singlet model.

Before we conclude this section, we would like to make one further comment. We have shown that the minimal Higgs portal models without an additional scalar are largely ruled out by the combination of Higgs (in)stability and the LHC constraints (except for a small region of the parameter space still available in the non-Abelian model). At the same time we showed that if these models include an additional scalar field with a portal coupling $\lambda_{Hs} \sim 0.35$, the Higgs stability restrictions are completely lifted and the models are completely viable.

The question arises if this conclusion would also apply to models without an additional scalar, but instead with a relatively large Higgs-CW portal coupling, $\lambda_{\rm P} \sim 0.3$, so that β_{λ_H} would instead receive a positive contribution from $2\lambda_{\rm P}^2$. This approach would not work for the following reason: In order not to get a large mixing angle $\sin^2\theta > 0.1$ in this case, we require that the second scalar is quite heavy, $m_{h_2} > 300$ GeV. This in turn requires a large CW gauge coupling of $g_{\rm CW} \approx 3.5$. Such a large gauge coupling leads to a large value for λ_ϕ at the scale of $\langle\phi\rangle$. λ_ϕ therefore develops a Landau pole already at low scales making the theory non-viable.

4.4 Dark Matter Physics: Relic Abundance and Constraints

Having demonstrated that the Higgs sector can be stabilised and that it is in agreement with all current observations, we now show that this framework can accommodate the observed dark matter density of the Universe. In the scenarios that we have studied, there are two potential dark matter candidates. The first candidate is a vector dark matter candidate [161–163] given by the triplet of gauge bosons, Z'_i, of the $SU(2)_{\rm CW}$ sector, considered recently in [111, 112]. These particles have the same mass, $M_{Z'}$, and are stable because of an unbroken global $SO(3)$ 'custodial symmetry' which also ensures that each component has the same relic abundance. The second candidate is the singlet scalar particle, s, coupled to the Higgs through

the Higgs portal.[4] This is a much studied dark matter candidate [43, 44, 165–170] that is stable because of an automatic Z_2 symmetry of the classically scale-invariant SM$\times$G$_{\mathrm{CW}}$ theory with the real singlet [121].[5]

Having argued that the vector triplet and scalar particles are stable and therefore potential dark matter candidates, we must calculate the relic abundance in order to show that they can saturate, or form a component of the observed dark matter abundance. We take $\Omega_{\mathrm{DM}}h^2 = 0.1187 \pm 0.0017$, the value inferred from Planck+WP+HighL+BAO data [22]. Owing to reasonable couplings to the Standard Model particles, the scalar and vector dark matter components are in thermal equilibrium with the Standard Model degrees of freedom in the early Universe. Their abundance is therefore determined by the thermal freeze-out mechanism. To calculate it, we must solve the Boltzmann equation, which is [171, 172],

$$\frac{dn_i}{dt} + 3Hn_i = -\langle\sigma_{ii}v\rangle\left(n_i^2 - n_i^{\mathrm{eq}\,2}\right) - \sum_{j,k}\langle\sigma_{ijk}v\rangle\left(n_in_j - \frac{n_k}{n_k^{\mathrm{eq}}}n_i^{\mathrm{eq}}n_j^{\mathrm{eq}}\right)\,, \quad (4.4.82)$$

where n_i is the number density of one component χ_i of the dark matter abundance, $\langle\sigma_{ii}v\rangle$ is the usual annihilation cross-section term for reactions of the form $\chi_i\chi_j \to XX$, where X is a particle in equilibrium with the thermal bath, and $\langle\sigma_{ijk}v\rangle$ is the cross-section for the semi-annihilation reaction $\chi_i\chi_j \to \chi_kX$.

4.4.1 Vector Dark Matter

We first consider the case of vector dark matter only, which is similar to Hambye's model [161], except that here there are no explicit μ terms. This model is interesting as it was the first example of a model containing both annihilation and semi-annihilation processes, as shown in Figure 4.6.

The annihilation cross-section is dominated by the lower four diagrams of Figure 4.6, which contribute to the process $Z_i'Z_i' \to h_2h_2$. The leading order terms

---

[4]Magnetic monopoles are also a possible third dark matter candidate [164]; we will come back to this possibility in a SU(2) model with an adjoint scalar in Chapter **5**.

[5]The $s \to -s$ symmetry of the potential Equation (4.1.30) is an automatic consequence of scale-invariance and gauge invariance, which does not allow odd powers of H and Φ.
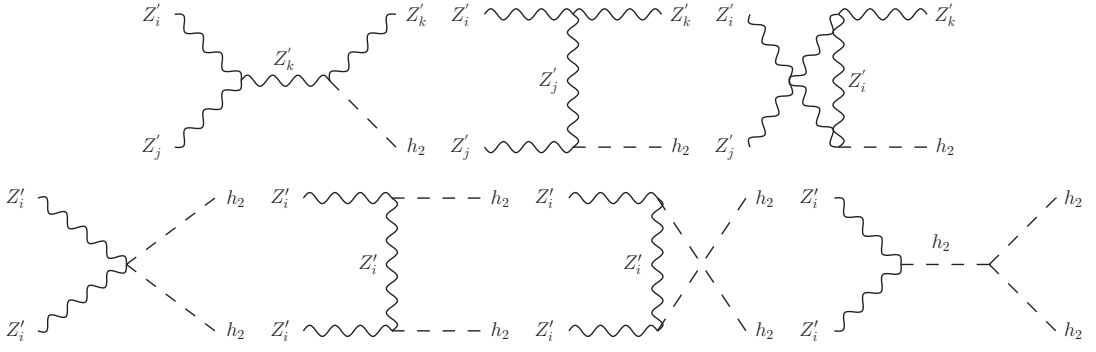
Figure 4.6:   The upper three diagrams show the process $Z'_i Z'_j \to Z'_k h_2$, which is the dominant contribution to the semi-annihilation cross-section. The process $Z'_i Z'_j \to Z'_k h_1$ also occurs but is suppressed by $\tan^2 \theta$. The lower four diagrams show the processes that dominate the annihilation of $Z'_i Z'_i$. Other diagrams are suppressed by at least one power of $\sin \theta$ or λ_{P}.

contributing to the non-relativistic (s-wave) cross-section from these diagrams are

$$\langle \sigma_{ii} v \rangle = \frac{11 g^4_{\mathrm{CW}} - 60 g^2_{\mathrm{CW}} \lambda_\phi + 108 \lambda^2_\phi}{2304 \pi} \frac{\cos^4 \theta}{M^2_{Z'}} + \mathcal{O}\left(\frac{m^2_{h_2}}{M^2_{Z'}}, \sin \theta, \lambda_{\mathrm{P}} \right) . \tag{4.4.83}$$

In our numerical work, we include all sub-leading terms in this cross-section as well as the contributions from $Z'_i Z'_i \to h_1 h_1$, $Z'_i Z'_i \to \bar{f} f$, $Z'_i Z'_i \to W^+ W^-$ and $Z'_i Z'_i \to Z^0 Z^0$, all of which are suppressed by at least one power of $\sin \theta$ or λ_{P}.

The diagrams that contribute to the semi-annihilation process are shown by the upper three diagrams in Figure 4.6. In the non-relativistic limit, the (s-wave) cross-section for $Z'_i Z'_j \to Z'_k h_2$ is

$$\langle \sigma_{ijk} v \rangle = \frac{3 g^4_{\mathrm{CW}}}{128 \pi} \frac{\cos^2 \theta}{M^2_{Z'}} \left(1 - \frac{m^2_{h_2}}{3 M^2_{Z'}} \right)^{-2} \left(1 - \frac{10 m^2_{h_2}}{9 M^2_{Z'}} + \frac{m^4_{h_2}}{9 M^4_{Z'}} \right)^{3/2} . \tag{4.4.84}$$

There is also a subdominant process $Z'_i Z'_j \to Z'_k h_1$ whose cross-section is obtained from Equation (4.4.84) by substituting $m_{h_2} \to m_{h_1}$ and $\cos \theta \to \sin \theta$. For completeness, we include this in our numerical work. Comparing Equations (4.4.83) and (4.4.84), we observe that $\langle \sigma_{ijk} v \rangle \sim 5 \langle \sigma_{ij} v \rangle$ and therefore the semi-annihilation processes dominate.

The global custodial symmetry ensures that the vector triplet is degenerate in mass and each Z'_i contributes one-third to the relic abundance. That is the total abundance $n_{Z'}$ is related to the individual components by $n_{Z'} = 3 n_{Z'_1} = 3 n_{Z'_2} = 3 n_{Z'_3}$.

It should also be clear that $\langle \sigma_{11} v \rangle = \langle \sigma_{22} v \rangle = \langle \sigma_{33} v \rangle := \langle \sigma v \rangle_{\text{ann}}$ and $\langle \sigma_{123} v \rangle = \langle \sigma_{132} v \rangle = \langle \sigma_{213} v \rangle = \langle \sigma_{231} v \rangle = \langle \sigma_{312} v \rangle = \langle \sigma_{321} v \rangle := \langle \sigma v \rangle_{\text{semi-ann}}$. Therefore, the Boltzmann equation for the total abundance is

$$\frac{dn_{Z'}}{dt} + 3H n_{Z'} = -\frac{\langle \sigma v \rangle_{\text{ann}}}{3} \left(n_{Z'}^2 - n_{Z'}^{\text{eq}\,2} \right) - \frac{2\langle \sigma v \rangle_{\text{semi-ann}}}{3} n_{Z'} \left(n_{Z'} - n_{Z'}^{\text{eq}} \right) . \quad (4.4.85)$$

We solve this equation numerically by the method outlined in [173].

The coloured regions in the upper and lower panels of Figure 4.7 show the total relic abundance of the vector triplet as a fraction of the observed abundance. For instance, in the lower left (blue) part of the upper panel, the abundance exceeds the observed value and is therefore excluded. The thick black wedge indicates the region where the Higgs potential is stabilised up to the Planck scale (as in Figure 4.5). We see that for most of the wedge, the vector triplet contributes between 1% and 100% of the total dark matter abundance. However, when we combine this with the LHC constraint on $\sin^2 \theta$, we see from Figure 4.7 that the vector dark matter component contributes less than 10% to the total relic abundance, and we need to add another dark matter component. The lower panel in Figure 4.7 shows the dark matter fraction as a function of $M_{Z'}$ and m_{h_2}. We see that the $M_{Z'}$ have to lie between 500 GeV and 1000 GeV for the model to have a stable Higgs vacuum.

Also shown in the upper panel are the direct detection current constraints from LUX [174] and the projected limits from LZ [34]. At a direct detection experiment, a vector Z'_i can elastically scatter with a nucleon N via exchange of h_1 or h_2. The resulting spin-independent scattering cross-section for this to occur is

$$\sigma_N^{\text{SI}} = \frac{g_{\text{CW}}^2 \sin^2 2\theta}{16\pi} \frac{f_N^2 m_N^2 \mu_{\text{red}}^2}{v^2} \left(\frac{1}{m_{h_2}^2} - \frac{1}{m_{h_1}^2} \right)^2 , \quad (4.4.86)$$

where $f_N := \langle N \sum_q m_q \bar{q} q \rangle N / m_N \approx 0.295$ is the Higgs-nucleon coupling [175], m_N is the nucleon mass and μ_{red} is the vector-nucleon reduced mass. When setting a limit from the experimental data, we account for the fact that the the vector triplet forms a subcomponent of the total dark matter density over much of the parameter space of interest. We make a scaling ansatz that the fraction of the local dark matter density $\rho_{Z'}/\rho_{\text{DM}}$ is the same as the fraction of the dark matter relic abundance $\Omega_{Z'}/\Omega_{\text{DM}}$. After taking into account this scaling, the limits from LUX and LZ are

shown in Figure 4.7 by the lines with the appropriate label. In the upper panel, the regions above and to the left of the lines are excluded.

We have also checked that the when applied to the lower panel, the LUX exclusion limit excludes the entire lower island. Therefore, while the current LUX limits do not constrain the region where the Higgs potential is stabilised, the projected LZ limit excludes all of this region.

4.4.2   Singlet Scalar Dark Matter

We have previously motivated the introduction of a real singlet scalar field to allow the Higgs potential to be stabilised over a much larger range of the parameter space. Providing a candidate to saturate the observed dark matter abundance provides a second motivation. The two examples of CSI ESM with a U(1) Coleman-Weinberg sector, which we have considered in Sections **4.3.1** and **4.3.2**, do not have a dark matter candidate. This is because the $U(1)_{\mathrm{CW}}$ gauge boson is unstable, owing to its kinetic mixing with hypercharge, and the only scalar field present, ϕ_{CW}, mixes with the SM Higgs. The $SU(2)_{\mathrm{CW}}$ sector does have a stable component in the form of the Z'_i triplet, but we have seen (cf. left panel in Figure 4.7) that after LHC constraints have been taken into account, the vector triplet can only account for sub-component of the total dark matter abundance in the region where the Higgs potential is stabilised. Therefore, in the case of an SU(2) extended Standard Model, an additional dark matter component is also required.

We first study the case where the singlet forms all of the dark matter (as required in the U(1) case) before turning to the case where it forms a sub-component (as required in the SU(2) case).

In the CSI $U(1)_{\mathbf{B-L}} \times$ SM $\oplus$ singlet model, the ATLAS and CMS limit $M_{Z'} \gtrsim 3$ TeV implies that λ_{P}, and therefore $\sin\theta$, is small. As a result, the diagrams that dominantly contribute to the total annihilation cross-section $\langle \sigma v \rangle_{\mathrm{s,ann}}$ are those shown in Figure 4.8. The Z_2 symmetry of this theory ensures that all semi-annihilation processes vanish, so that the Boltzmann equation describing the evolution of the
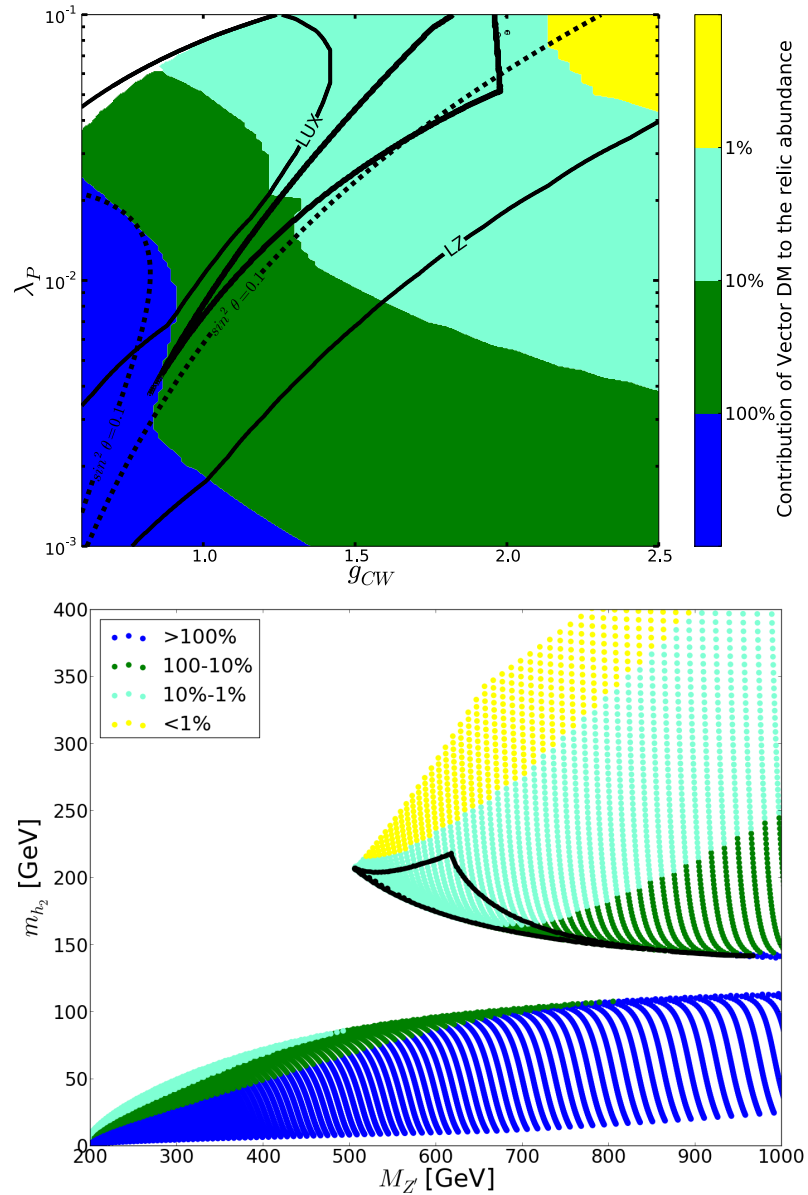
Figure 4.7:   The coloured contours and the wedge-shaped regions in black in both panels indicate when the vector triplet forms more or less than 100%, 10% and 1% of the observed dark matter abundance, and the parameter values where the Higgs potential is stabilised respectively. Also shown in the upper panel are the LUX and projected LZ limits (the region above these lines is excluded), which account for the fact that the dark matter is a subcomponent of the total density in much of the parameter space, and the limit $\sin^2\theta = 0.1$. The lower panel shows that the vector mass should lie between 500 GeV and 1 TeV to improve Higgs stability.
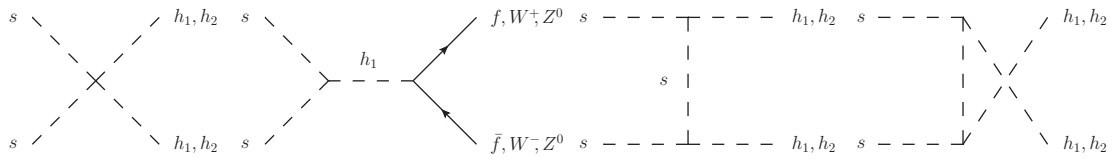
Figure 4.8: The leading contributions to the scalar annihilation cross-section $\langle \sigma v \rangle_{\text{s,ann}}$. Other diagrams are suppressed by at least one power of $\sin\theta$.
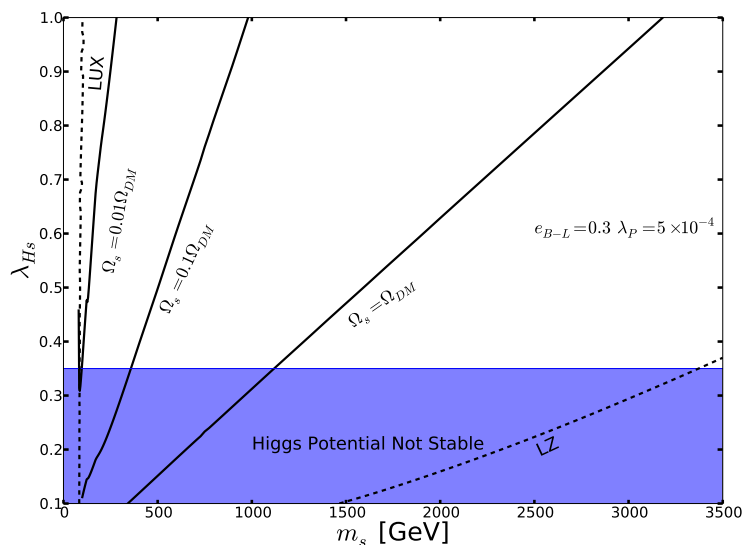

Figure 4.9: Scalar dark matter (m_s, λ_{Hs}) plane in the CSI U(1)$_{\mathbf{B-L}} \times$ SM $\oplus$ singlet model. The solid lines show the fraction of the total DM density the scalar singlet makes up. The dotted lines show the direct detection constraints from LUX and the project limits from LZ. In the shaded region the extra singlet does not stabilise the Higgs potential.

scalar number density n_s is the usual one:

$$\frac{dn_s}{dt} + 3Hn_s = -\langle \sigma v \rangle_{\text{s,ann}} \left(n_s^2 - n_s^{\text{eq}\,2} \right) \ . \tag{4.4.87}$$

The main parameters of our singlet dark matter models are the scalar dark matter mass, m_s, and its coupling, λ_{Hs}, to the Higgs field. We solve the Boltzmann equation numerically, and the results are displayed in Figure 4.9 on the (m_s, λ_{Hs}) plane. In this figure, we have initially fixed $e_{\mathbf{B-L}} = 0.3$ and $\lambda_{\mathrm{P}} = 5 \times 10^{-4}$ resulting in a mixing angle $\theta \approx 5 \times 10^{-3}$ and mass $M_{Z'} = 3.6$ TeV. When $e_{\mathbf{B-L}}$ and λ_{P} are chosen so that $M_{Z'}$ lies above the bounds from direct searches by ATLAS and CMS, we

find that the positions of the lines are not sensitive to the values of $e_{\mathrm{B-L}}$ and λ_{P}. The coupling constant $\lambda_{\phi s}$ can be traded in for m_s^2 (cf. Equation (4.1.31)) so that the only remaining free parameters are m_s and λ_{hs} (the quadratic coupling λ_s plays no role in the Born-level freeze-out calculation). For each value of m_s, the value of λ_{Hs} that gives 100%, 10% or 1% of the observed dark matter density Ω_{DM} is shown in Figure 4.9. The region below $\lambda_{Hs} \sim 0.34$ is excluded because for these values of λ_{Hs}, the real scalar does not help to stabilise the Higgs potential (cf. Table 4.1). We also impose that $\lambda_{Hs} \lesssim 1$ in order that λ_{Hs} does not develop a Landau pole before the Planck scale. For the singlet scalar to saturate the observed dark matter density, we find that its mass should lie in the range between 1 TeV and 3.2 TeV. In this range, the annihilation channel $ss \to Z'Z'$ is not allowed kinematically, justifying its exclusion from the diagrams in Figure 4.8.

Finally, we also show the current direct detection constraints from LUX and the projected limits from LZ. The scalar can scatter at a direct detection experiment through a t-channel exchange of h_1 and h_2, and the resulting spin-independent scattering cross-section to scatter off a nucleon N is

$$
\sigma_N^{\mathrm{SI}} = \frac{\lambda_{Hs}^2 \cos^4\theta}{4\pi} \frac{f_N^2 m_N^2 \mu_{\mathrm{red}}^2}{m_s^2 m_{h_1}^4} \left[1 - \tan\theta \left(\frac{\lambda_{\phi s}}{\lambda_{Hs}} - \frac{m_{h_1}^2}{m_{h_2}^2} \left(\frac{\lambda_{\phi s}}{\lambda_{Hs}} + \tan\theta \right) \right) \right]^2 . \quad (4.4.88)
$$

As in the case of the vector triplet, we account for the fact that the scalar makes up a sub-component of the dark matter in much of the parameter space. While the current LUX limit constrains low values of m_s where the scalar density Ω_s is very low, the projected LZ limits should constrain the full parameter space of interest.

4.4.3 Scalar and Vector Dark Matter

Finally, we consider the CSI $\mathrm{SU(2)_{CW}} \times$ SM $\oplus$ singlet model in which the dark matter is comprised of both the singlet scalar and vector triplet. In this case we solve the Boltzmann equations (4.4.85) and (4.4.87) as before, but we now include the annihilation process $ss \to Z_i' Z_i'$ or the reverse process, depending on which is kinematically allowed.

Figure 4.10 shows the results on the $(g_{\mathrm{CW}}, \lambda_{\mathrm{P}})$ plane for $\lambda_{Hs} = 0.36$ and $\lambda_{Hs} = 1.0$ in the upper and lower panels respectively. The coloured contours indicate the values
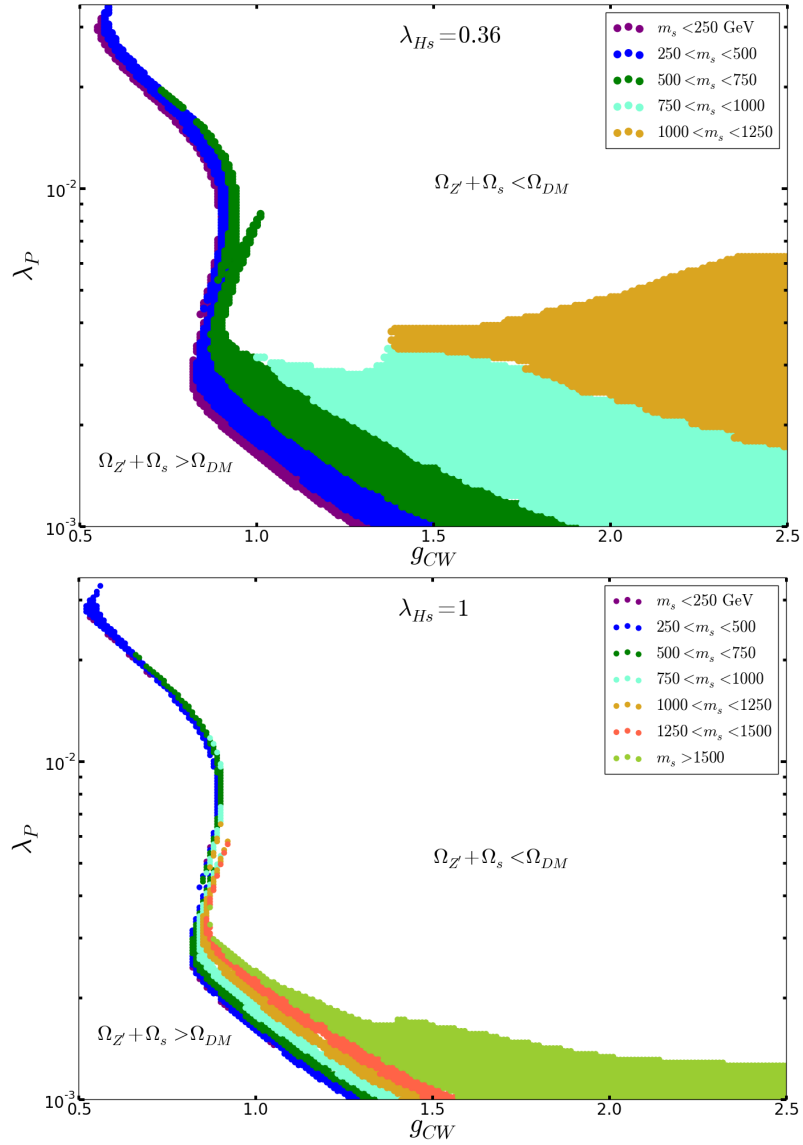
Figure 4.10: The plots show the available parameter space where the scalar and vector dark matter together make up the total dark matter density in the CSI $SU(2)_{CW} \times SM \oplus$ singlet model. The colour-coded regions show the scalar dark matter mass in GeV. In the white regions the combined density is either larger or smaller than the observed dark matter density. In the upper plot we fixed $\lambda_{Hs} = 0.36$, and in the lower plot $\lambda_{Hs} = 1$.

of m_s that is chosen to give a total density of vector and scalar dark matter saturating the observed value, i.e. $\Omega_{Z'} + \Omega_s = \Omega_{DM}$. There is a limited portion of the parameter space in which the vector and scalar make up all of the dark matter, and this region is smaller in the case where λ_{Hs} is bigger. These results can be understood with

reference to Figures 4.7 and 4.9. From Figure 4.7, we observe that in the upper right corner of the upper panel, the vector density is very small, so that the scalar should make up most of the density. From the lower panel, we also see that in this region, $M_{Z'} \lesssim 1$ TeV, which because $g \approx 2$, implies that $\langle \phi \rangle \lesssim 1$ TeV. Now, from Figure 4.9, we see that for $\lambda_{Hs} = 0.36$, we require $m_s \approx 1$ TeV in order that $\Omega_s \approx \Omega_{\text{DM}}$. However, given that $m_s^2 \approx \lambda_{\phi s} |\langle \phi \rangle|^2 / \sqrt{2}$ (cf. Equation (4.1.31)), we see that we cannot achieve $m_s \approx 1$ TeV unless $\lambda_{\phi s} \gtrsim 1$, in which case it develops a Landau Pole before the Planck scale. Figure 4.9 also allows us to see why the parameter space is smaller for a larger λ_{Hs}. This is because the value of m_s that is required to obtain $\Omega_s \approx \Omega_{\text{DM}}$ is larger for a larger λ_{Hs} and this is more difficult to do, again because of the perturbativity restriction on $\lambda_{\phi s}$.
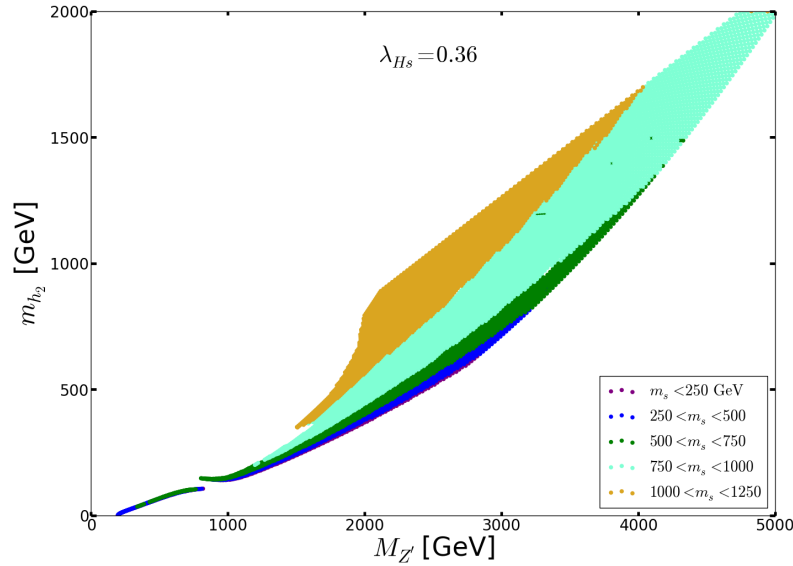

Figure 4.11: The region on the mass plane $(M_{Z'}, m_{h_2})$ where the combined density of the scalar and vector dark matter equals the observed dark matter density. The colours show the scalar dark matter mass in GeV and in the white regions the combined density is either larger or smaller than the observed dark matter density. Here, we have fixed $\lambda_{Hs} = 0.36$.

Figure 4.11 shows the vector and Coleman-Weinberg scalar mass, and contours of the scalar mass in which the total density is saturated. This plot has $\lambda_{Hs} = 0.36$. We see that both the vector and the scalar are required to be around the TeV scale.

4.5 Conclusions

Classically scale-invariant extensions of the Standard Model constitute a highly pre-dictive and minimal model building framework. In this CSI ESM set-up, all mass scales have to be generated dynamically and should therefore have a common origin. These models have to address all the sub-Planckian shortcomings of the Standard Model. In this chapter, we have analysed the CSI ESM theories from the perspective of solving the instability problem of the SM Higgs potential and at the same time providing viable dark matter candidates.

In simple CSI models with Abelian hidden sectors, we identified regions of pa-rameter space where the SM Higgs potential is stabilised all the way up to the Planck scale. These are the wedge-shaped regions in Figures 4.3 and 4.4. When combined with LHC constraints on heavier Higgs bosons, we found that these regions did not survive (see dotted lines in Figures 4.3 and 4.4).

In the case of a non-Abelian SU(2) hidden sector in Figure 4.5, a small part of the parameter space with the stable Higgs potential is compatible with the LHC constraints.

We then argued that by adding a real scalar singlet with a portal coupling to the Higgs $\lambda_{Hs} \gtrsim 0.35$, all of our CSI ESM models have a stable Higgs potential and are consistent with the LHC exclusion limits on extended Higgs sectors.

For Abelian models the singlet, of mass m_s, is the only dark matter candidate, and Figure 4.9 shows the available parameter space on the (m_s, λ_{Hs}) plane. If this singlet contributes 100% of the total observed dark matter density, its mass lies between 1 TeV and 3 TeV. The LUX direct detection limits do not yet constrain the model, however the projected reach of LZ would cover all of the viable parameter space.

In non-Abelian models we have two possible components of dark matter: the singlet and the hidden sector SU(2) gauge bosons, Z_i'. Without the singlet, the combination of Higgs stability and LHC constraints implies that vector dark matter contributes less than 10% of the observed relic density, as can be seen in Figure 4.7. Thus, to saturate the dark matter density and stabilise the Higgs potential, we are required to have a singlet dark matter component. Finally, we have investigated the

phenomenology of two-component dark matter. The viable regions of parameter space are shown in Figures 4.10 and 4.11. Typically, both components have a mass close to 1 TeV.

We see that CSI ESM models are viable and predictive. They provide a non-trivial link between the electroweak scale, including the Higgs vacuum stability, and the nature and origin of dark matter. Furthermore, future dark matter direct detection and collider experiments will be able to explore a significant fraction of their parameter space.

Chapter 5

Dark Matter Monopoles, Vectors and Photons

In this chapter, based on [3], we will continue to investigate models where the SM is extended with a hidden or dark sector. This sector only couples to the SM via a Higgs portal, and we are interested in dark sectors that include dark matter particles. In Chapter 4, we saw examples of scalar and vector boson dark matter candidates. If the dark sector is of the Georgi-Glashow type, with non-Abelian gauge groups and adjoint scalars, 't Hooft-Polyakov monopoles [176, 177] will be part of the particle spectrum of the theory.

The motivation of this chapter is to investigate the cosmological consequences of magnetic monopoles in the dark sector. We will determine if monopoles can contribute to the observed dark matter relic density, and how large their contribution could be. It will also be very important to discuss which additional features emerge from a dark sector for it to be able to support monopoles. Therefore, we will consider the cosmological and phenomenological properties of a minimal and complete model based on a SU(2) dark sector with an adjoint scalar.

The cosmological production rate of magnetic monopoles and their contributions to dark matter were discussed previously [178]. We will incorporate these results in our analysis. More recently, dark sector monopoles and vector bosons were considered in [179], with the authors of [179] concluding that the monopole contribution to

the dark matter density should be negligible. This does not agree with our findings in Section **5.2**.

The chapter will be organised as follows: in Section **5.1** we introduce the model with monopoles, and discuss issues regarding dynamic mass generation. The model will necessarily include massless hidden sector photons. In Section **5.2** we will discuss cosmological constraints on this dark radiation. We then move on to calculate the dark matter relic density of both monopole and vector boson dark matter in Section **5.3**. Due to the unbroken U(1) remaining in the dark sector, the dark matter will have long range self interactions. We discuss the inconsistencies at small scales in the cold collisionless dark matter (CCDM) framework, and how the self-interacting dark matter in our model could help explain these problems in Section **5.4**.

5.1 The Model

Consider the Standard Model extended by a hidden (a.k.a. dark) sector which contains an $SU(2)_D$ gauge group and a scalar field Φ in the adjoint representation of $SU(2)_D$. [1] The Lagrangian for the dark sector is:

$$\mathcal{L}_D = -\frac{1}{2}\mathrm{Tr}F'_{\mu\nu}F'^{\mu\nu} + \mathrm{Tr}(D_\mu\Phi(D^\mu\Phi)^\dagger) - \lambda_\phi\mathrm{Tr}(\Phi\Phi^\dagger)^2 + m^2\,\mathrm{Tr}(\Phi\Phi^\dagger)\,, \quad \Phi = \phi_a\frac{\sigma_a}{2}.$$
(5.1.1)

$F'_{\mu\nu}$ is the field strength of the $SU(2)_D$ gauge field $A'_\mu = A'^a_\mu\frac{\sigma_a}{2}$, the covariant derivative is $D_\mu\Phi = \partial_\mu\Phi + ig_D[A'_\mu, \Phi]$, where g_D is the gauge coupling, and $\sigma_{a=1,2,3}$ are the Pauli matrices.

The Φ-field also couples to the SM via the Higgs portal interaction,

$$\mathcal{L}_{\mathrm{HP}} = \lambda_{\mathrm{P}}(H^\dagger H)\mathrm{Tr}(\Phi\Phi^\dagger)\,.$$
(5.1.2)

In the absence of other matter fields in the dark sector, this is the only interaction between the SM and the dark sector. In particular, there is no kinetic mixing between the non-Abelian dark sector $SU(2)_D$ and the SM gauge groups.

---

[1]This is the simplest model containing topologically stable monopoles. More complicated models with gauge groups of larger rank would be possible, but this simple model captures all the main features of models with dark matter monopoles

The scalar potential in our dark-sector Lagrangian (5.1.1) contains a negative mass-squared term, $-m^2 \operatorname{Tr}(\Phi\Phi^\dagger)$, for the adjoint scalar. This will lead to a a non-trivial vacuum $\langle\Phi\rangle \neq 0$ which breaks the $SU(2)_D$ gauge symmetry to $U(1)_D$. Using gauge freedom, we can set

$$\langle\Phi\rangle = \langle\phi_3\rangle\frac{\sigma_3}{2}\,, \quad \text{where} \quad \langle\phi_3\rangle = w = m/\sqrt{\lambda_\phi}\,. \tag{5.1.3}$$

After symmetry breaking in the dark sector, we get two massive gauge bosons $W'_\pm$ with mass $M_{W'} = g_D w$, one massive scalar $m_\phi = \sqrt{2}m$ and one massless gauge boson γ'. $SU(2)_D$ has been broken, but an unbroken $U(1)_D$ gauge group remains.

The effect of symmetry breaking is communicated from the dark sector to the SM via the Higgs portal interaction (5.1.2), which can generate the μ_{SM}^2 term in the SM effective potential,

$$V(H)_{SM} = -\frac{1}{2}\mu_{SM}^2 HH^\dagger + \lambda_{SM}(HH^\dagger)^2\,. \tag{5.1.4}$$

If μ_{SM}^2 was absent at tree level, the dark sector will generate a contribution $\mu_{SM}^2 = \lambda_{\mathrm{P}}\langle|\Phi|\rangle^2$, and triggers electroweak symmetry breaking with the Higgs vev and mass,

$$v = \frac{\mu_{SM}}{(2\lambda_{SM})^{1/2}} \simeq 246\,\mathrm{GeV}\,, \qquad m_{h\,SM} = \mu_{SM} \simeq 126\,\mathrm{GeV}\,. \tag{5.1.5}$$

In the next section, we will see that the dark sector will include magnetic monopoles. In addition there are two other components of cosmological significance; dark photons γ' and dark massive vector bosons $W'_\pm$. Massless γ' photons will contribute to the density of radiation in the Universe, and the massive $W'_\pm$ together with the magnetic monopoles will be the dark matter candidates in our model.

5.1.1 Monopoles

Magnetic monopoles are objects with a net magnetic charge. One can easily extend Maxwell's equations to include magnetic charge

$$\nabla \cdot E \;=\; 4\pi\rho_e \tag{5.1.6}$$

$$\nabla \cdot B \;=\; 4\pi\rho_m$$

$$\nabla \times E \;=\; -\frac{1}{c}\frac{\partial B}{\partial t} - \frac{4\pi}{c}J_m$$

$$\nabla \times B \;=\; \frac{1}{c}\frac{\partial E}{\partial t} + \frac{4\pi}{c}J_e\,,$$

where E and B are the electric and magnetic field, ρ_e and ρ_m the electric and magnetic charge density, and J_e and J_m the electric and magnetic current. No magnetic monopoles corresponding to the SM U(1) gauge group have ever been discovered. In 1931, Dirac [180] introduced the first magnetic monopoles in a quantum theory. He studied magnetic monopoles in a U(1) gauge theory, and discovered the famous result that product of magnetic charge, g_m, and electric charge, g_e, is quantised

$$g_m g_e = 2\pi n \,. \tag{5.1.7}$$

Dirac's monopoles are divergent towards the centre of the monopole and therefore not well behaved states in QFT. In 1974, Polyakov and 't Hooft independently discovered how to get viable magnetic monopoles in quantum field theory by considering a SU(2) theory with an adjoint scalar [176,177]. At long distances these SU(2) monopoles behave exactly like the Dirac monopoles, but they have a complicated SU(2) structure at the centre which smooths out the divergences.

For the potential to be bounded, we need $|\Phi|^2 = m^2/\sqrt{\lambda_\phi}$ at the two-sphere at infinity. This makes the Higgs field a map from $S^2 \to S^2$, so it has a conserved topological charge, N. This topological charge makes the monopoles stable and it also gives the magnetic charge of the monopoles

$$g_m = \frac{4\pi}{e} N \,. \tag{5.1.8}$$

Monopoles are stable, extended particle like field configurations. Their mass is bounded from below by the Bogomolny bound [181],

$$M_{\mathrm{m}} \geq \frac{4\pi}{g_D} w = \frac{M_{W'}}{\alpha_D} \,, \tag{5.1.9}$$

When $\lambda_\phi \to 0$, we get BPS monopoles, which saturates the Bogomolny bound for the mass. More generally, away from the BPS limit, the monopole mass is given by $M_{\mathrm{m}} = \frac{M_{W'}}{\alpha_D} f(\lambda_\phi/g_D^2)$ where f is a smooth monotonically increasing function from $f(0) = 1$ to $f(\infty) \simeq 1.787$, see e.g. [182]. We will therefore use the Bogomolny bound as a reasonable approximation for the monopole mass for all values of λ_ϕ. We will be interested in the possibility that monopoles can make up dark matter. Some additional applications of monopoles to dark matter physics were discussed

in [183] where TeV-scale monopoles in a hidden sector gave a decaying dark matter candidate due to a small kinetic mixing and a hidden photon mass. In our settings there are no heavy messenger fields between the two sectors to induce the kinetic mixing and the monopoles are stable. In [184] it was pointed out that there is a region of parameter space in supersymmetric models where invisible monopoles can be the dark matter. On the opposite side of the spectrum, [164] considered galaxy-sized 't Hooft-Polyakov magnetic monopoles.

5.1.2 Mass-Scale Generation

What is the origin of the m^2 term in (5.1.1)?

(1.) We can choose to make the full theory classically scale-invariant (CSI). In this case all input mass scales of the classical Lagrangian are set to zero, and thus $m_{\text{cl}}^2 \equiv 0$. The vacuum expectation value $\langle \Phi \rangle = w \neq 0$ is then generated radiatively via the Coleman-Weinberg (CW) mechanism [79]. In Section **5.1.3** we outline how this works in massless Georgi-Glashow theory. The dark gauge symmetry is broken by $\langle \Phi \rangle$ and this can be recast as generating an effective m^2 term in (5.1.1) in the CSI Standard Model $\times SU(2)_D$ theory. This is a minimal scenario where dynamical mass generation occurs directly in the dark sector, i.e. we have identified the mass-scale-generating sector with the dark sector, $SU(2)_{CW} = SU(2)_D$.

(2.) A complementary approach is to keep the mass-scale-generating sector and the dark sector distinct. Then interactions between the two sectors would transmit the mass scale from the mass-scale-generating sector to the dark sector. For example, in CSI settings we can think of a SM $\times SU(2)_D \times G_{CW}$ model, where G_{CW} is the Coleman-Weinberg gauge sector which generates the vev $\langle \varphi_{CW} \rangle$ for the CW scalar field. This radiatively generated scale is then transmitted to the dark sector scalar and to the SM Higgs field via scalar portal interactions, $\mathcal{L}_{\text{Portal}} \ni \lambda_{CWD} |\varphi_{CW}|^2 \operatorname{Tr}(\Phi\Phi^\dagger) + \lambda_{CWH} |\varphi_{CW}|^2 (H^\dagger H)$ such that $\lambda_{CWD} |\langle \varphi_{CW} \rangle|^2 = m^2$ in (5.1.1).[2] In the above, G_{CW} is an example of the mass-generating sector. In

---

[2]In this scenario the induced SM Higgs mass parameter in (5.1.4) is $\mu_{SM}^2 = \lambda_{CWH} \langle |\varphi_{CW}| \rangle^2 + \lambda_{\text{P}} \langle |\Phi| \rangle^2$.

general, it does not have to be reliant on the CW mechanism, as the mass scale can arise from any dimensional transmutation-type dynamical argument, including a strongly coupled sector.

(3.) It is equally possible to treat m^2 as an input parameter and not consider CSI at all, without invalidating any of the cosmological arguments that will follow.

Our reason for distinguishing between the first two classes of models is the effect on the cosmological production of magnetic monopoles. The monopole production rate [185, 186] will depend on the nature of the phase transition in the dark sector when the temperature in the early Universe falls below the critical temperature of $SU(2)_D$. In the Coleman-Weinberg sector the phase transition is first order, while in the Standard Model sector the electroweak phase transition is very weakly first order or second order [84, 187, 188]. The distinction can be traced to the value of the scalar self-coupling constant: in CW models λ is small relative to the gauge coupling (resulting in CW scalar masses being one-loop suppressed relative to W' masses); in the SM this is not the case, with the Higgs being heavier than W and Z.

5.1.3 Coleman-Weinberg Mechanism with an Adjoint Scalar

In this section we will show how an adjoint scalar in a SU(2) CSI extension of the SM will dynamically acquire a vev via the Coleman-Weinberg mechanism [79]. The classically massless SU(2) theory with an adjoint scalar (5.1.1) was in fact one of the examples considered in the original paper of Coleman and Weinberg [79]. In a gauge where $\phi_{1,2} = 0, \phi_3 = \phi$, they find a contribution from the gauge bosons to the effective potential of the form

$$V_{W'} = \frac{3g_D^4}{32\pi^2}\phi^4 \left(\log \frac{\phi^2}{\langle\phi\rangle^2} - \frac{25}{6} \right) . \tag{5.1.10}$$

This is twice the result of the Abelian U(1) case as there now two massive vector bosons, $W'_\pm$. This is also to be compared with the case of SU(2)$_D$ with a *fundamental* scalar, considered in Section **4.1.3**, where all three gauge bosons got a mass.

Combining the one-loop expression (5.1.10) with tree level potential we get

$$V = \frac{\lambda_\phi}{4}\phi^4 + \frac{3g_D^4}{32\pi^2}\phi^4 \left(\log \frac{\phi^2}{\langle\phi\rangle^2} - \frac{25}{6}\right), \qquad (5.1.11)$$

which has a non-trivial minimum with a vev for ϕ when

$$\lambda_\phi(\langle\phi\rangle) = \frac{11}{8\pi^2} g_D^4(\langle\phi\rangle). \qquad (5.1.12)$$

With the adjoint scalar acquiring a vev, the $SU(2)_D$ gauge group is broken to $U(1))_D$, and we end up with two massive gauge bosons $W'_\pm$, a massless gauge boson γ', and one massive scalar field $\phi = \phi_3$, neutral under $U(1)_D$. The masses are given by

$$M_{W'} = g_D\langle\phi\rangle, \qquad m_\phi^2 = \frac{3g_D^2\langle\phi\rangle^2}{4\pi^2}. \qquad (5.1.13)$$

As for all the other CSI extensions of the SM considered in Chapter 4, the vev of ϕ is transmitted via the Higgs portal coupling to the SM, triggering EWSB. The two neutral scalars will again mix with each other.

5.2 Dark Radiation and N$_{\text{eff}}$

The massless dark photon, γ', that remains after the breaking of $SU(2)_D$ to $U(1)_D$ is a new relativistic particle. In this section we will determine the contribution of γ' to the effective number of relativistic degrees of freedom and apply experimental constraints.

During both Big Bang Nucleosynthesis (BBN) and recombination the evolution of the Universe depends on the density of relativistic particles,

$$\rho_{\text{rel}} = g_\star(T) \times \frac{\pi^2}{30} T^4, \qquad (5.2.14)$$

where $g_\star$ counts the number of all relativistic degrees of freedom. Following standard notation (see e.g. [189] for more detail) $g_\star$ is given by

$$g_\star(T) = \sum_{m_i < T} C_i\, g_i \times \left(\frac{T_i}{T}\right)^4, \qquad (5.2.15)$$

where the sum is over all degrees of freedom, T_i and m_i are the temperature and the mass of particle i, the coefficients are $C_i = 1$ for bosons and $C_i = 7/8$ for fermions,

and g_i denotes internal degrees of freedom (e.g. for SM photons $g_\gamma = 2$, counting two transverse polarisations, and for each flavour of SM neutrino $g_\nu = 2$). This expression is conventionally rewritten in terms of the effective number of neutrinos, N_{eff}:

$$g_\star = g_\gamma + \frac{7}{8} g_\nu N_{\text{eff}} \times \left(\frac{T_\nu}{T}\right)^4 = 2 + \frac{7}{8} 2 N_{\text{eff}} \left(\frac{4}{11}\right)^{\frac{4}{3}} \tag{5.2.16}$$

$$\Delta N_{\text{eff}} \simeq 2.2 \, \Delta g_\star. \tag{5.2.17}$$

In the Standard Model, $N_{\text{eff}} = 3.046$ and not $N_{\text{eff}} = 3$, due to non instantaneous annihilation of electrons and positrons. Any new relativistic particles from BSM theories would increase N_{eff}, making it a useful probe of new physics. Recently the Planck Collaboration found $N_{\text{eff}} = 3.30 \pm 0.27$ at the time of recombination from a combination of CMB and Baryon Acoustic Oscillation data [22]. There is also a limit on N_{eff} from Helium abundance at BBN (T=1MeV), $N_{\text{eff}} = 3.24 \pm 1.2(95\%)$.

γ' is a relativistic particle and contributes to N_{eff}. If the dark photon was in thermal equilibrium with the SM photon, $T_{\gamma'} = T$, then Equation (5.2.15) would give $\Delta g_\star = 2$, leading to $\Delta N_{\text{eff}} \simeq 4.4$, which is ruled out by the Planck data.

However, this is not what happens in our case where the SM and the hidden sector have no direct mediators and interact only via the Higgs portal. The two sectors will lose thermal contact after the $SU(2)_D$ phase transition to the broken phase and before BBN. The interactions between dark photons and the SM will have to proceed through γ' coupled to virtual W' bosons, which in turn are coupled to virtual scalars ϕ which have a small mixing with the SM Higgs through the Higgs portal coupling. This interaction rate will be negligible with respect to the Hubble constant, $\Gamma < H = T^2/M_{\text{Pl}}^\star$, and the hidden sector will be colder than the SM.

Following [189], we will model this situation in terms of two sectors that had the same temperature when all the degrees of freedom were relativistic, and then decoupled at temperature T_D. The temperature, T_M, is the temperature at either recombination or BBN. Assuming that entropy is conserved within each sector we have,

$$\frac{g_{\star s}^h(T_M^h) T_M^{h3}}{g_{\star s}^h(T_D) T_D^3} = \frac{g_{\star s}^{sm}(T_M) T_M^3}{g_{\star s}^{sm}(T_D) T_D^3}, \tag{5.2.18}$$

where the superscript h refers to the hidden sector and sm to the Standard Model. The number of relativistic degrees of freedom, $g_{\star s}$, making up the entropy in the Universe is given by the expression (*cf.* Equation (5.2.15)),

$$g_{\star s}(T) = \sum_{m_i < T} C_i \, g_i \times \left(\frac{T_i}{T} \right)^3 . \tag{5.2.19}$$

In the hidden sector $g_{\star s}^h$ counts only γ' plus relativistic particles that will decay into γ'. Hence,

$$g_{\star s}^h(T_D) = 2 + n \qquad \text{and} \qquad g_{\star s}^h(T_{BBN}^h) = g_{\star s}^h(T_{CMB}^h) = 2 \, , \tag{5.2.20}$$

where n denotes the number of relativistic particles in the hidden sector, in addition to the two polarisations of γ', at the time when the two sectors decouple (i.e. before the phase transition to the broken phase). The number of SM degrees of freedom at the decoupling temperature is

$$g_{\star s}^{sm}(T_D) = 106.75 \, , \tag{5.2.21}$$

and at the time of measurements,

$$g_{\star s}^{sm}(T_{BBN}) = 2_\gamma + \frac{7}{8}(4_{e^\pm} + (3 \times 2)_\nu) = 10.75 \, , \tag{5.2.22}$$

$$g_{\star s}^{sm}(T_{CMB}) = 2_\gamma + \frac{7}{8}(3.046 \times 2)_\nu \times \frac{4}{11} = 3.94 \, . \tag{5.2.23}$$

From Equations (5.2.17), (5.2.15), (5.2.18) we deduce ΔN_{eff} at the time of measurement (BBN or CMB),

$$\Delta N_{\text{eff}}(T_M) = 2.2 \, \Delta g_\star(T_M) = 2.2 \times g_{\gamma'} \times \left(\frac{T_M^h}{T_M} \right)^4 = 4.4 \times \left(\frac{g_{\star s}^h(T_D)}{g_{\star s}^h(T_M^h)} \frac{g_{\star s}^{sm}(T_M)}{g_{\star s}^{sm}(T_D)} \right)^{4/3} , \tag{5.2.24}$$

so that

$$\Delta N_{\text{eff}}(T_{CMB}) = 0.022 \times (2 + n)^{4/3} \tag{5.2.25}$$

$$\Delta N_{\text{eff}}(T_{BBN}) = 0.08 \times (2 + n)^{4/3}. \tag{5.2.26}$$

In a model with only a dark photon in the hidden sector, we would have $n = 0$, leading to $\Delta N_{\text{eff}}(T_{CMB}) = 0.05$ and $\Delta N_{\text{eff}}(T_{BBN}) = 0.2$, which is very similar to the result in [190].

We can now get a limit on the number of degrees of freedom, n, in the dark sector which annihilate into γ'.[3] Since the neutral scalar, ϕ, does not couple to the dark photon, the lowest value of n we can have in the Georgi-Glashow dark sector is $n = 6$, given by the three polarisations of $W'^{\pm}$. Additional matter fields or higher rank gauge groups would increase n appropriately.

From the Planck limit $\Delta N_{\text{eff}} < 0.8 (2\sigma)$ at T_{CMB}, we get an upper limit $n < 14(2\sigma)$. A stronger limit $n \lesssim 7$ follows from the data on Helium abundance at BBN. We conclude that our $SU(2)_D$ gauge theory with an adjoint scalar is consistent with the current available constraints on N_{eff}. At the same time additional degrees of freedom in the dark sector are disfavoured.

For the minimal case, $n = 6$, arising from $W'_{\pm}$ contributions (and assuming that their entropy does not leak to the SM particles[4]) our model predicts

$$\Delta N_{\text{eff}}(T_{CMB}) = 0.022 \times (2 + 6)^{4/3} = 0.35 \,, \tag{5.2.27}$$

which could be ruled out by Planck measurements as the projected sensitivity in ΔN_{eff} is 0.044.

5.3 Dark Matter Relic Density

In our model there are two dark matter candidates. The massive gauge bosons $W'_{\pm}$ are carriers of (dark) electric charge of the unbroken $U(1)_D$, and as such they are stable. They provide a vector dark matter (VDM) candidate. The dark magnetic (anti-)monopoles $M'_{\text{mg}\pm}$ carry topological magnetic charge of $U(1)_D$ and serve as a candidate for monopole dark matter (MDM). The combined contribution of

---

[3]Even if some of these particles have a relic density of the right order of magnitude to give the correct dark matter density, almost all of the entropy in the species will have been transferred, since freeze-out normally happens at $T = M/20$. The vector bosons $W'_{\pm}$ can annihilate to both γ' and ϕ. Since ϕ mixes with the SM Higgs, this entropy will leak to the Standard Model particles, which could effectively increase $g^{sm}_{\star s}(T_D)$. The fraction of the entropy transferred to γ' is given by the branching ratio $\Gamma_{W'_{\pm} \to \gamma'}$ which is assumed to dominate over the entropy transfer to the SM.

[4]Since ϕ mixes with the SM Higgs, there is some entropy exchange between the two sectors, which can increase $g^{sm}_{\star s}(T_{CMB})$.
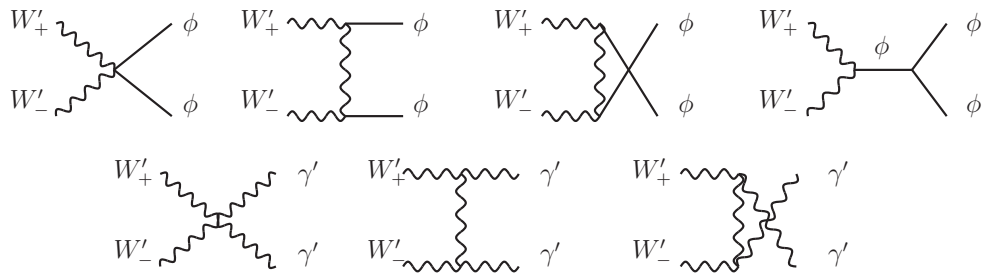
Figure 5.1: Diagrams giving the dominant contribution to the $W'_\pm$ annihilation cross-section.

VDM and MDM should amount to (or not exceed) the observed total dark matter abundance $\Omega_{DM}h^2 = 0.1187 \pm 0.0017$ measured by the Planck Satellite [22].

5.3.1 Dark Gauge Bosons: Sommerfeld Enhancement and Relic Density

Models of dark matter with non-Abelian dark sectors interacting with the visible SM sector only weakly, for example via portal interactions, are popular approaches to dark matter (see e.g. [191–193]). In Chapter **4** and in [111,112], dark matter from a completely broken dark SU(2) sector was discussed. As the SU(2) group in our model is broken down to a U(1), we have two vector boson DM candidates, $W'_\pm$. W'_+ and W'_- can annihilate into two dark photons γ' or into two ϕ scalars. The dominant contribution to their annihilation is given by the Feynman diagrams in Figure 5.1. Using these diagrams, we have computed the leading-order non-relativistic s-wave annihilation cross-section,[5]

$$\langle \sigma v \rangle_{\text{pert}} = \frac{1579\,g_D^4}{2304\pi M_{W'}^2} - \frac{5\,g_D^2\,\lambda_\phi}{192\pi M_{W'}^2} + \frac{3\,\lambda_\phi^2}{64\pi M_{W'}^2}\,. \tag{5.3.28}$$

This leading order perturbative cross-section is further enhanced at low velocities by the Sommerfeld effect [194–198], which arises from multiple dark photon exchanges

---

[5]For simplicity, in the analytic expression on the *r.h.s.* of (5.3.28) we have assumed that $m_\phi \ll M_{W'}$. We have checked that the inclusion of effects due to scalar masses does not make a noticeable change in our numerical results.
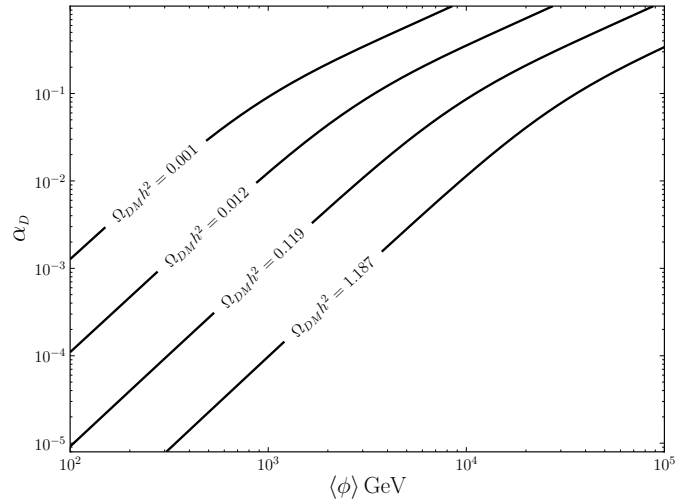
Figure 5.2: Contours of the relic density of vector dark matter.

in the t-channel between the incoming W'_+ and W'_-. As a result we have

$$\langle \sigma v \rangle = S \, \langle \sigma v \rangle_{\text{pert}} \,, \tag{5.3.29}$$

where the multiplicative Sommerfeld factor [194, 198] is

$$S = \frac{\alpha_D \pi}{v} \frac{1}{1 - \exp\left[-\frac{\alpha_D \pi}{v}\right]} \,, \tag{5.3.30}$$

and becomes relevant in the non-relativistic regime where the 'perturbative' factor $\frac{\alpha_D \pi}{v}$ is no longer small.

The relic density of vector dark matter is found by solving the Boltzmann equations,

$$\frac{dn_i}{dt} + 3Hn_i = -\langle \sigma v \rangle \left(n_i^2 - n_i^{eq\,2} \right), \tag{5.3.31}$$

where n_i for $i = 1, 2$ is the density of W'_+ and W'_- with $n_1 = n_2$. Then the combined $W'_\pm$ density, n, is twice that, $n = 2n_1 = 2n_2$. It satisfies the equation

$$\frac{dn}{dt} + 3Hn = -\langle \sigma v \rangle_{\text{eff}} \left(n^2 - n^{eq\,2} \right) \quad , \quad \text{where} \quad \langle \sigma v \rangle_{\text{eff}} := \frac{\langle \sigma v \rangle}{2} \,. \tag{5.3.32}$$

Using this Boltzmann equation we can now write down the standard s-wave solution for the dark matter abundance (see e.g. [5, 28]),

$$\Omega_{VDM} \, h^2 = 1.07 \times 10^9 \frac{x_f \, \text{GeV}^{-1}}{(g_{\star s}/\sqrt{g_\star}) M_{\text{Pl}} \, \langle \sigma v \rangle_{\text{eff}}} \,, \tag{5.3.33}$$

where $x_f := M_{W'}/T_f$ and T_f is the freeze-out temperature. The expression for x_f is

$$x_f = \log\left(0.038\frac{g}{\sqrt{g_\star}}M_{\text{Pl}}M_{W'}\langle\sigma v\rangle_{\text{eff}}\right) - \frac{1}{2}\log\log\left(0.038\frac{g}{\sqrt{g_\star}}M_{\text{Pl}}M_{W'}\langle\sigma v\rangle_{\text{eff}}\right),$$
(5.3.34)

where $g = 6$ is the number of $W'_\pm$ degrees of freedom.

The relic density of $W'_\pm$, given by Equations (5.3.33)-(5.3.34), is shown in Figure 5.2 on the two-dimensional plane (α_D, w) of the dark sector parameter space. In the CW case $\lambda_\phi \ll \alpha_D$, and the scalar self-coupling λ_ϕ plays no role. We have also considered a more general case with $\lambda_\phi/\alpha_D =$ fixed, for example $= 4$ similarly to the SM value, and continued to scan over α_D and $\langle\phi\rangle$. We have found no noticeable difference in the relic density behaviour in Figure 5.2.

The relic density curves in Figure 5.2 are seen to be bending at higher values of α_D. This is the consequence of the Sommerfeld enhancement factor in (5.3.30). In the perturbative regime $\frac{\alpha_D\pi}{v} \ll 1$, $S = 1$, but changes to $S = \frac{\alpha_D\pi}{v}$ in the regime of larger gauge coupling or equivalently lower velocities. This gives the bending of the contours seen in the figure. We estimate the velocity in (5.3.30) by $v = \sqrt{T_f/M_{W'}} = 1/\sqrt{x_f}$. In scanning over the parameter space in Figure 5.2, we found x_f changing between 15 and 25, which gave the range of velocities $0.2 \lesssim v \lesssim 0.25$ in the Sommerfeld S factor.

5.3.2 Dark Monopoles

Production of Monopoles

Monopoles are topological defects which are produced during a phase transition in the early Universe. First we need to determine the order of the phase transition of the $SU(2)_D$ dark sector relevant for the monopole production. At sufficiently high temperature, the only minimum of the effective potential of the dark sector $V_D(\phi, T)$ is at the origin $\phi = 0$ (here ϕ is the dark sector scalar in the unitary gauge) and the $SU(2)_D$ symmetry is restored. As the Universe expands, a second minimum appears, and at the critical temperature, $T = T_c$, the values of V_D in the two minima become equal. The phase transition is of the first order if there is a barrier separating the two minima at critical temperature. If on the other hand there is no potential barrier

between the minima, the phase transition is of the second order.

As already noted in section **5.1.2**, the character of the phase transition depends on whether the dark sector is of the CW-type or not. We illustrate this point by writing the one-loop thermal potential from Section **3.1**

$$V_D(\phi, T) = D(T^2 - T_0^2)\phi^2 - ET\phi^3 + \frac{\lambda_T}{4}\phi^4 \,, \tag{5.3.35}$$

with the parameters in our case (i.e. the model of (5.1.1)) given by

$$D = \frac{g_D^2}{4} \,, \quad E = \frac{g_D^3}{2\pi} \,, \quad T_0 = \frac{1}{4D}(\sqrt{2}m^2 - \frac{g_D^4}{2\pi}w^2) \,, \quad \lambda_T = \lambda_\phi - \frac{3g_D^4}{8\pi^2}\log\frac{g_D^2 w^2}{a_B T^2} \tag{5.3.36}$$

and $a_B \simeq e^{3.91}$. We reach the critical temperature, T_c, when the values of V_D in the two minima become equal,

$$T_c^2 = \frac{T_0^2}{1 - E^2/(\lambda_T D)} \,, \quad \phi_c = \frac{2ET_c}{\lambda_{T_c}} \,, \tag{5.3.37}$$

with ϕ_c being the value of the field in the second minimum at this instance. The strength of the first order phase transition is conventionally characterised by the dimensionless order parameter ϕ_c/T_c, which can be thought of as the separation between the two vacua in units of temperature. We have

$$\frac{\phi_c}{T_c} = \frac{2E}{\lambda_{T_c}} = \frac{g_D^3}{\pi(\lambda_\phi + \frac{3g_D^4 \times 3.91}{8\pi^2})} \,. \tag{5.3.38}$$

Strongly first order phase transitions have $\phi_c/T_c \gtrsim 1$. The phase transition is weakly first order if the vacua at 0 and ϕ_c are near each other, and changes to a second order phase transition for $\phi_c/T_c \ll 1$.

To have a second order phase transition we need:

$$\frac{g_D^3}{\pi} \ll \lambda_\phi + \frac{3g_D^4 \times 3.91}{8\pi^2}. \tag{5.3.39}$$

In the Coleman-Weinberg settings $\lambda_\phi = \frac{11g_D^4}{8\pi^2}$, which implies

$$\text{CW}: \quad \frac{\phi_c}{T_c} = \frac{1}{g_D}\frac{8\pi}{22.73} = \frac{1}{3.2\sqrt{\alpha_D}} \gg 1 \quad \text{for } \alpha_D \ll 0.1 \,, \tag{5.3.40}$$

which gives a strongly first order phase transition for a weakly coupled CW sector, as expected.

The production of magnetic monopoles in the early Universe can be estimated using the Kibble limit [185]. It is a lower limit on the density of magnetic monopoles created cosmologically, and it is expressed in terms of the horizon volume. As we will show the limit applies to both a first and second-order phase transition,

$$\frac{n_\mathrm{m}}{T^3} \geq \left(\frac{T_c}{\sqrt{\frac{45}{4\pi^3 g_\star}} M_\mathrm{Pl}} \right)^3 . \tag{5.3.41}$$

First we justify this bound for phase transitions of the second order [182, 185]. During the phase transition, the ϕ_a field changes from 0 to $|\phi|^2 = w^2$. The direction of ϕ_a is the same inside a volume ζ^3 where ζ is the correlation length. At the critical temperature ζ diverges, but, due to causality, information can only be exchanged inside the horizon. The correlation length will therefore be frozen in at the horizon scale $d_h \simeq H^{-1}$, and we will get a domain structure with ϕ_a in different domains pointing in different directions. At domain intersection points, the random orientation of the scalar field, given a non-trivial topology, can give rise to magnetic monopoles with a probability p close to 1. We can estimate the density of monopoles created [182]:

$$n_\mathrm{m} \propto p\, \zeta^{-3} \sim \zeta^{-3} \quad , \quad \text{where} \quad \zeta < d_h = H^{-1} , \tag{5.3.42}$$

and equation (5.3.41) follows.

If the phase transition in the dark sector is first-order, a potential barrier is formed between the symmetric and the symmetry-breaking vacua. Below the critical temperature the symmetric vacuum is meta-stable. Bubbles of the symmetry breaking vacuum will nucleate and expand. Inside each bubble the scalar field will have a random orientation. When the bubbles collide they can create magnetic monopoles. The density of magnetic monopoles will therefore be proportional to the density of bubbles. Since the bubbles cannot propagate faster than the speed of light, the size of a bubble is limited by the horizon size. We therefore get a very similar bound [5] on the density of magnetic monopoles as from the Kibble argument in Equation (5.3.41), enhanced by a logarithmic factor [199]:

$$\mathrm{first-order\ ph.\,tr.}: \quad \frac{n_\mathrm{m}}{T^3} \geq \left[\frac{T_c}{\sqrt{\frac{45}{4\pi^3 g_\star}} M_\mathrm{Pl}} \log \left(\frac{\sqrt{\frac{45}{4\pi^3 g_\star}} M_\mathrm{Pl}}{T_c} \right)^4 \right]^3 . \tag{5.3.43}$$

For a second order phase transition, the Kibble bound was refined by Zurek [186] with an argument relying on a careful analysis of the timescales involved in the phase transition. A system undergoing a phase transition is characterised by a relaxation time τ, and a correlation length ζ,

$$\tau = \frac{\tau_0}{\sqrt{|\epsilon(T)|}} \;, \quad \text{and} \quad \zeta = \zeta_0 \, |\epsilon(T)|^{-\nu} \;, \tag{5.3.44}$$

where

$$\epsilon(T) := \frac{T - T_c}{T_c} \;, \tag{5.3.45}$$

and $1/2$ and ν are the critical exponents describing the degree of divergence of τ and ζ in the proximity of the critical temperature T_c. At a time t close to the critical point, t_c, one has $t - t_c \propto \epsilon(T) \to 0$ where the proportionality constant is the quenching time-scale,

$$\tau_Q := \frac{t - t_c}{\epsilon(T)} \;. \tag{5.3.46}$$

At the time $t_\star$ when the time interval to the critical point becomes equal to the relaxation time τ, the system is no longer able to re-adjust to changes in the temperature quickly enough. This leads to the correlation length freezing out at this time. We have

$$|t_\star - t_c| = \tau(t_\star) = \tau_0 \, |\epsilon(t_\star)|^{-1/2} \;, \tag{5.3.47}$$

with the *l.h.s.* being via (5.3.46) also $= \tau_Q \, |\epsilon(t_\star)|$, which implies that

$$|\epsilon(t_\star)|^{3/2} = \tau_0/\tau_Q \;, \quad \text{and} \quad \zeta(t_\star) = \zeta_0 \, |\epsilon(t_\star)|^{-\nu} = \zeta_0 \, |\tau_0/\tau_Q|^{2\nu/3} \;. \tag{5.3.48}$$

In our case $\tau_Q = H(T_c)^{-1}$ and for the remaining constants, from the Landau-Ginzburg theory one estimates [178] that $\zeta_0 \simeq \tau_0 \sim 1/(\sqrt{\lambda_\phi} T_c)$. The classical value for the critical exponent ν is $1/2$, but quantum corrections can modify this value.

The second equation in (5.3.48) is the correlation length at the freeze-out temperature $t_\star$. It is a more accurate replacement of the Kibble-limit estimate $\zeta < d_h = H(T_c)^{-1}$.

The monopole relic density from the Zurek mechanism today is then given by the following expression [178, 186] (for conversion factors see Equations (5.3.69)-(5.3.70)),

$$\text{second} - \text{order ph. tr.} : \quad \frac{n_{\rm m}}{T^3} \simeq 10^{-2} \left(\frac{M_{\rm m}}{1 \text{ TeV}} \right) \left(\frac{30 \, T_c}{M_{\rm Pl}} \right)^{\frac{3\nu}{1+\nu}} \;, \tag{5.3.49}$$

or (using numerical conversion Equations (5.3.69)-(5.3.70)),

$$\text{second} - \text{order ph. tr.}: \quad \Omega_{\mathrm{m}} h^2 = 1.5 \times 10^9 \left(\frac{M_{\mathrm{m}}}{1 \text{ TeV}} \right) \left(\frac{30 \, T_c}{M_{\mathrm{Pl}}} \right)^{\frac{3\nu}{1+\nu}} \quad (5.3.50)$$

Zurek's argument above is also valid for various condensed matter systems where the effect has been experimentally confirmed [200, 201].

The main difference between Zurek's result (5.3.49)-(5.3.50) and the Kibble lower limit (5.3.41) or (5.3.43), is the power p of the $(T_c/M_{\mathrm{Pl}})^p$ suppression factor. It reduces from $p = 3$ in the Kibble bound to the $p = 3\nu/(1 + \nu) \simeq p_{\mathrm{cl}} = 1$ for $\nu_{\mathrm{cl}} = 1/2$ in the Zurek bound. This makes it possible for relatively light monopoles with masses starting in the few hundred TeV range, to contribute significantly to dark matter, as can be inferred from Figure 5.4 in section **5.3.2**. The Kibble bound would require monopoles to be at least in the 10^{11} GeV range or above to play a non-negligible role in the dark matter relic abundance (*cf.* Figure 5.3).

Evolution of Monopoles

Magnetic monopoles are stable and cannot decay due to conservation of their dark magnetic charge. Once created, the density of magnetic monopoles can therefore only be changed by monopole-anti-monopole annihilation.

We will now estimate the density of monopoles taking these annihilations into account. In the diffusion approach [202–204], the motion of monopoles in a plasma of electrically charged particles, in our case $W'_{\pm}$, is described by a Brownian walk with thermal velocities $v_T = \sqrt{T/M_{\mathrm{m}}}$ and a mean free path l_{free},

$$l_{\mathrm{free}} = v_T \, t_{\mathrm{free}} = \sqrt{\frac{T}{M_{\mathrm{m}}}} \frac{M_{\mathrm{m}}}{T \sum_i n_i \sigma_i} , \quad (5.3.51)$$

where σ_i is the classical cross-section for large-angle scattering of a light particle with a monopole,

$$\sigma_i = \frac{g_{mD}^2 \, q_i^2}{(4\pi)^2 T^2} , \quad (5.3.52)$$

n_i is the number density and the sum is over all spin states. The number density for relativistic particles is [5]

$$n_i = \frac{\zeta(3)}{\pi^2} T^3 , \quad (5.3.53)$$

and for non relativistic particles of mass M_i the number density is

$$n_i = \left(\frac{M_i T}{2\pi}\right)^{\frac{3}{2}} \exp\left(-\frac{M_i}{T}\right) . \tag{5.3.54}$$

It is convenient to define the dimensionless quantity B,

$$B := T^{-1} \sum_i n_i \sigma_i , \quad \text{so that}: \quad l_{\text{free}} = \frac{1}{B}\sqrt{\frac{T}{M_{\text{m}}}}\frac{M_{\text{m}}}{T^2} \tag{5.3.55}$$

The attractive Coulomb force between the monopoles and antimonopoles makes them drift towards each other during their random walk in the electric plasma. Their drift velocity is determined from the balance between the monopole-antimonopole attraction and the drag force of the plasma. It is given by [204],

$$v_{\text{drift}}(r) = \frac{1}{B}\frac{g_{mD}^2}{T^2 \, r^2} . \tag{5.3.56}$$

Monopoles drift toward antimonopoles through the plasma. The drag force dissipates monopole energy, and if the mean free path is less than the capture radius,

$$l_{\text{free}} \leq l_{\text{capt}} = g_{mD}^2/(4\pi T) , \tag{5.3.57}$$

a monopole-antimonopole bound state is formed which ultimately annihilates to ordinary elementary states. The relevant time scale for the formation of the bound state is $t_{\text{drift}} = r/v_{\text{drift}} = 1/\Gamma_{\text{drift}}$. Therefore, the monopole-antimonopole annihilation cross-section is given by,

$$\sigma = \frac{\Gamma_{\text{drift}}}{n_{\text{m}}} = \frac{v_{\text{drift}}(r)}{n_{\text{m}}r} = \frac{1}{B}\frac{g_{mD}^2}{T^2} . \tag{5.3.58}$$

The resulting density of monopoles after annihilation is determined by a Boltzmann equation [203],

$$\frac{d}{dx}\frac{n_{\text{m}}}{s} = \frac{\sigma}{H(x)\,x}\left(\frac{n_{\text{m}}}{s}\right)^2 , \quad \text{where} \quad x := \frac{M_{\text{m}}}{T} \tag{5.3.59}$$

with σ on the right hand side given by (5.3.58). The solution is known analytically [203]. It quickly becomes independent of the initial conditions at x_0, resulting in,

$$\frac{n_{\text{m}}}{s}(x) \simeq \frac{2\pi B}{g_{mD}^2}\frac{\sqrt{\frac{45}{4\pi^3 g_\star}}M_{\text{m}}}{M_{\text{Pl}}}\frac{1}{x} . \tag{5.3.60}$$

If following [203], we assume that the the plasma consists of particles that are relativistic from x_0 to x_f where x_f corresponds to the temperature where l_{free} and l_{capt} become equal,

$$x_f^{-1} = \left(\frac{4\pi}{g_{mD}^2} \right)^2 \frac{1}{B^2} \,, \tag{5.3.61}$$

the result for the final number density of monopoles is in agreement with [203],

$$\frac{n_{\text{m}}}{s}(x_f) \simeq \frac{2\pi}{Bg_{mD}^2} \left(\frac{4\pi}{g_{mD}} \right)^2 \frac{\sqrt{\frac{45}{4\pi^3 g_\star}} M_{\text{m}}}{M_{\text{Pl}}} \,. \tag{5.3.62}$$

This diffusive capture process is effective only as long as the mean free path is smaller than the capture radius. At lower temperatures, where l_{free} exceeds l_{capt}, the rate of monopoles-antimonopole annihilation cannot compete with the expansion of the Universe and the monopole density freezes out at the value at x_f.

There is an important difference between the more standard application of the diffusion method described above, where GUT monopoles were propagating in the plasma of very light relativistic electrons and positrons, and our model. In our case the plasma is made up of $W'_\pm$ with masses $M_{W'} = g_D \langle \phi \rangle$ much closer to the monopoles of the same dark sector. Thus, the particles in the plasma will become non-relativistic fairly soon after the phase transition, when

$$x_{\text{nr}} = \frac{M_{\text{m}}}{T_{\text{nr}}} = \frac{M_{\text{m}}}{M_{W'}} = \frac{1}{\alpha_D} = \frac{4\pi}{g_{mD}^2} \,. \tag{5.3.63}$$

After x_{nr} the density of the plasma will decrease exponentially, as per (5.3.54), and the mean free path will therefore exponentially increase. The final monopole density in our model will thus be cut off at x_{nr}

$$\frac{n_{\text{m}}}{s}(x_{\text{nr}}) \simeq \frac{B}{2} \frac{\sqrt{\frac{45}{4\pi^3 g_\star}} M_m}{M_{pl}} \,. \tag{5.3.64}$$

Current Density of Monopoles

To determine the current density in monopoles we first have to determine the type of the dark sector phase transition, and then compute the initial monopole production density accordingly. If the initially produced density is lower than the estimated density after monopole-antimonopole annihilation (5.3.64), the effect of annihilations
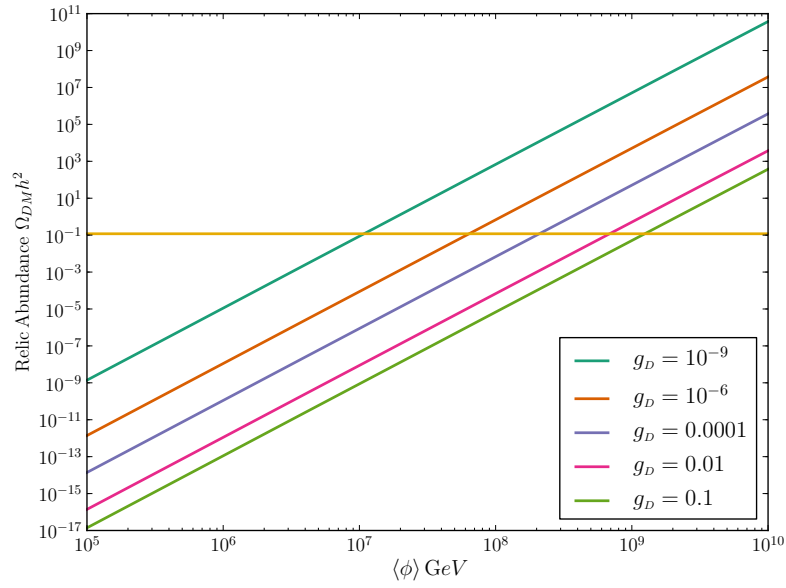
Figure 5.3: The relic density of monopoles produced cosmologically during a first order phase transition as a function of the dark scalar vev $w = \langle \phi \rangle$ and for different values of the dark gauge coupling g_D.

is unimportant and the initial monopole density survives. If, on the other hand, the initial density is higher than the annihilation density, the final monopole density is set by the monopole-antimonopole annihilations expression.

The conversion from monopole density, n_{m}/s or n_{m}/T, to $\Omega_{\mathrm{m}}h^2$ is as normal given by

$$\Omega_{\mathrm{m}}h^2 \;=\; \rho_{\mathrm{m}} \; \frac{1}{\rho_{\mathrm{crit}}h^{-2}} \,, \tag{5.3.65}$$

$$\rho_{\mathrm{m}}h \;=\; \frac{n_{\mathrm{m}}}{s}\, M_{\mathrm{m}}\, s_0 = \frac{n_{\mathrm{m}}}{T^3}\, M_{\mathrm{m}}\, T_0^3 \,, \tag{5.3.66}$$

where subscript 0 refers to the current time or temperature and the normalisation factors are given by

$$\rho_{\mathrm{crit}}h^{-2} \;=\; 1.9 \times 10^{-29}\mathrm{gcm}^{-3} = 7.53 \times 10^{-47}\,\mathrm{GeV}^4 \,, \tag{5.3.67}$$

$$s_0 \;=\; \frac{2\pi^2}{45}g_\star(t = t_0)\, T_0^3 \,, \tag{5.3.68}$$

with $T_0 = T_{CMB} = 2.73\,\mathrm{K} = 2.35 \times 10^{-13}\,\mathrm{GeV}$ and $g_\star(t = t_0) = 2$ in the dark sector
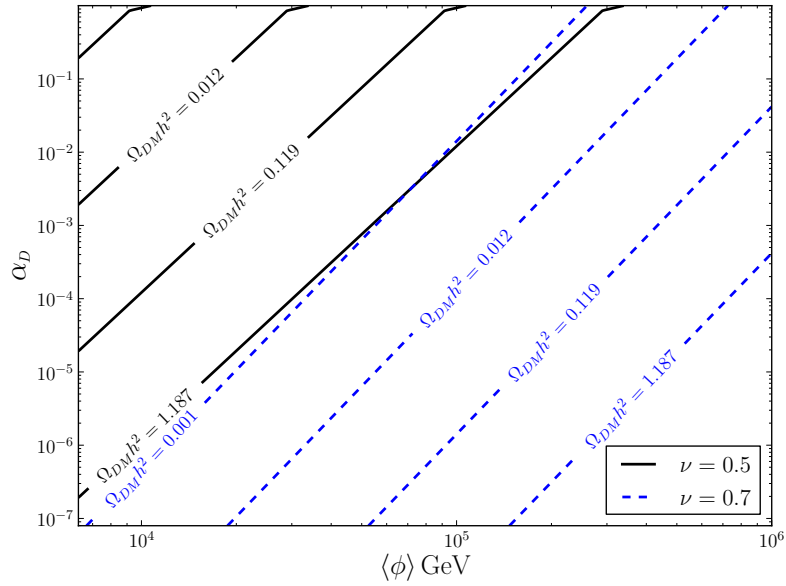
Figure 5.4: The relic density of monopoles after a second order phase transition. Results are shown on the dark sector gauge-coupling–vev plane for two different values for the critical exponent, $\nu = 0.5$ (in black) and $\nu = 0.7$ (in blue).

and 3.94 in the SM. Thus

$$\Omega_{\mathrm{m}} h^2 = \frac{n_{\mathrm{m}}}{s} \times \frac{M_{\mathrm{m}}}{1\,\mathrm{TeV}} \times 1.5 \times 10^{11}, \tag{5.3.69}$$

$$= \frac{n_{\mathrm{m}}}{T^3} \times \frac{M_{\mathrm{m}}}{1\,\mathrm{TeV}} \times 1.7 \times 10^{11}. \tag{5.3.70}$$

The current relic density of monopoles for a first-order phase transition, computed using (5.3.43), is shown in Fig 5.3. We see that relic density depends strongly on the dark scalar field vev $w = \langle \phi \rangle$ as this sets both the mass of the monopoles and the critical temperature of the phase transition. The density increases with lower coupling g_D as the mass of the monopoles increase.

The current relic density for a second-order phase transition, based on (5.3.49)-(5.3.50) combined with (5.3.64), is plotted in Figure 5.4 for two values of the critical exponent, $\nu = 0.5$ and $\nu = 0.7$.

For a second order phase transition we can see that we have two components of dark matter both with a significant fraction of the observed relic density. The combined relic density can be seen in Figure 5.5 for $\nu = 0.5$ and in Figure 5.6 for $\nu = 0.6$.
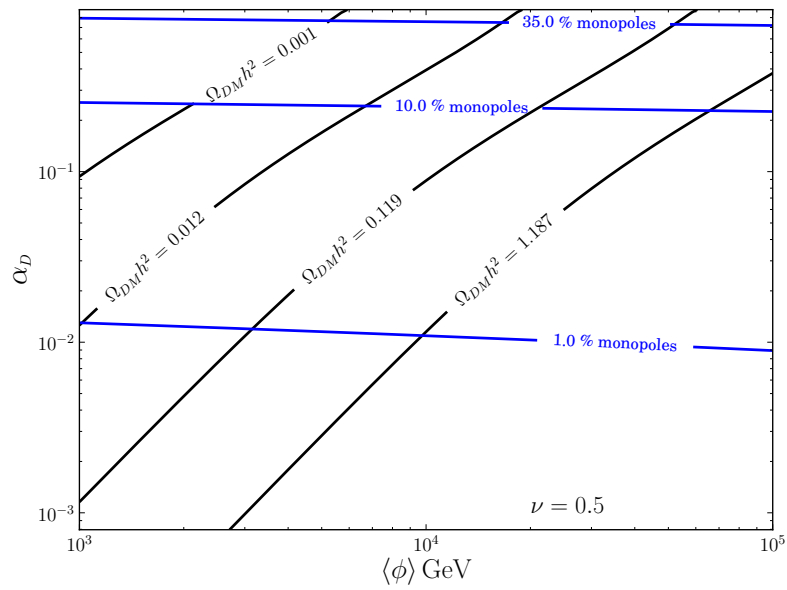
Figure 5.5: Combined relic density of vector and monopole components of dark matter after a second order phase transition with the critical exponent $\nu = 0.5$. The blue lines show the relative fraction of monopoles.
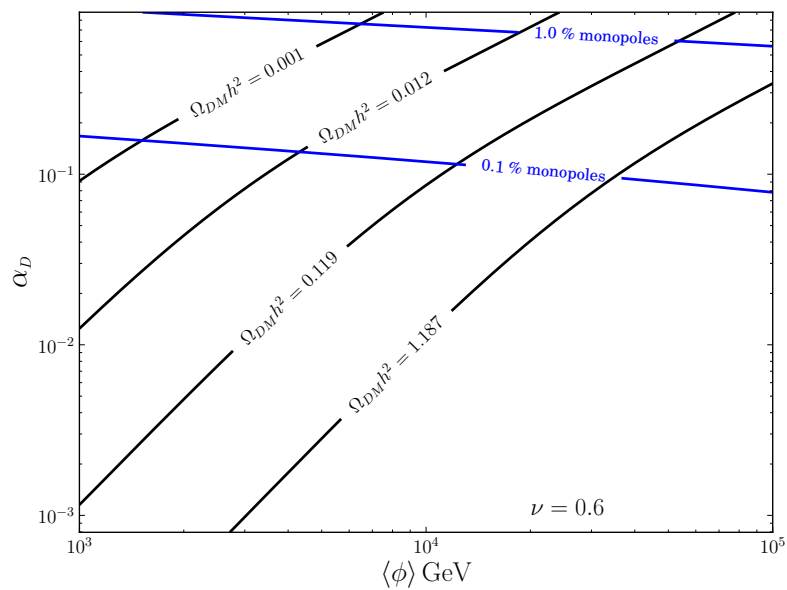

Figure 5.6: Combined relic density for monopole and vector dark matter with $\nu = 0.6$. Blue contours show the fraction of monopoles alone.

Dark sector monopoles and vector bosons were also considered recently in [179]. The authors of [179] have concluded based on their Figure 8 that achieving a

monopole abundance of 10% of the observed dark matter relic density would require what they describe as a 10^{-2} % fine-tuning. Our results in Figures 5.5-5.6 do not support such a conclusion. It follows from our Figure 5.5 that the contour of the observed relic density value $\Omega_{\mathrm{DM}}h^2 = 0.119$ can readily intersect the 10% monopole abundance contour, and even the 35% monopole abundance contour, and so on.

5.4 Self-Interacting Dark Matter

Due to the unbroken $U(1)_D$ symmetry, we will have long-rage forces acting between the dark matter particles. Vector dark matter is electrically charged under the $U(1)_D$, while the magnetic monopoles have magnetic charges. This self-interacting dark matter provides a framework which can solve the cosmological problems of collisionless cold dark matter (CCDM) at small scales [205]. Numerical simulations [206] based on CCDM are very successful in describing the large scale structure of the Universe at scales $\gg 1$ Mpc. However, observations on galactic and subgalactic scales $\lesssim 1$ Mpc are in conflict with the structure formation predicted by such simulations.

Collisionless dark matter predicts that density distributions of dwarf galaxy halos should have a cusp in the centre while observationally flat cores have been found [207, 208]; this is the core-vs-cusp problem. Cold dark matter simulations also predict too many too large subhalos in the Milky Way halo [209, 210]. In particular, simulations which use collisionless dark matter predict $\mathcal{O}(10)$ subhalos with velocities $v > 30$ km/s, but no halos have been observed with $v > 25$ km/s. This is known as the 'too-big-to-fail' problem, as these large subhalos are too big not to develop visible galaxies. These discrepancies might still be explained by baryonic effects.

In order to address these problems with small-scale structure, models of self-interacting dark matter have been proposed and studied in recent literature. References [211–216] considered long-range Yukawa interactions between cold dark matter mediated by a light vector or scalar bosons. The effects of an unbroken $U(1)$ symmetry with a massless force carrier were considered in [28, 217, 218].

The result of self-interactions is a transfer of energy between dark matter parti-

cles. This effect is captured by the transfer cross-section defined by,

$$\sigma_{\rm T} = \int d\Omega \, (1 - \cos\theta) \, \frac{d\sigma}{d\Omega} \,, \tag{5.4.71}$$

where $d\sigma/d\Omega$ is the usual differential cross-section. The $(1 - \cos\theta)$ factor takes into account the energy transferred in the collision. Even though our model contains a microscopically massless force carrier γ' in a plasma it is described by a Yukawa potential

$$V(r) = \frac{\alpha_e}{r} e^{-m_{\gamma'} r} \,, \tag{5.4.72}$$

where the effective mass of γ' is due to its interactions with the plasma and given by the inverse of the Debye length $l_{\rm D}$,

$$m_{\gamma'} = \frac{1}{l_{\rm D}} = \frac{(4\pi\alpha_D\rho)^{1/2}}{M_{\rm DM}\, v} \,. \tag{5.4.73}$$

Here ρ is the dark matter density in a galaxy and v is its velocity. Since the density ρ is small, the effective mass $m_{\gamma'}$ will be small, and we can use the classical Coulomb limit $M_{\rm DM} v / m_{\gamma'} \gg 1$ for both the attractive and repulsive potential with the result [215, 219, 220],

$$\sigma_{\rm T} = \frac{16\pi\alpha_D^2}{M_{\rm DM}^2 \, v^4} \log\left(1 + \frac{M_{\rm DM}^2 \, v^2}{2\alpha_D m_{\gamma'}^2}\right) \,. \tag{5.4.74}$$

If the energy transfer is large enough, self interacting dark matter could flatten out the cores of dwarf galaxies and decrease the number of large subhalos by collisional stripping, solving the core-vs-cusp and the too-big-too-fail problems. On the other hand, if the cross-section is too large, the effects could be seen on larger scales and would be ruled out.

The limits on this cross-section come from comparing observations to simulations. One obvious constraint is from the Bullet cluster which gives an upper limit on the cross-section, $\sigma_{\rm T}/M_{\rm DM} < 1.25$ cm^2/g [221]. Since the transfer cross-section is very strongly velocity-dependent, it is important that this bound is imposed in the relevant velocity range $v \sim 1000$ km/s. There are also constraints of $\sigma_{\rm T}/M_{\rm DM} \lesssim 0.1$ to 1 cm^2/g from Milky Way scales in the velocity range of 200 km/s [215]. These limits come from considering the shape of galaxies. Self-interactions tend to
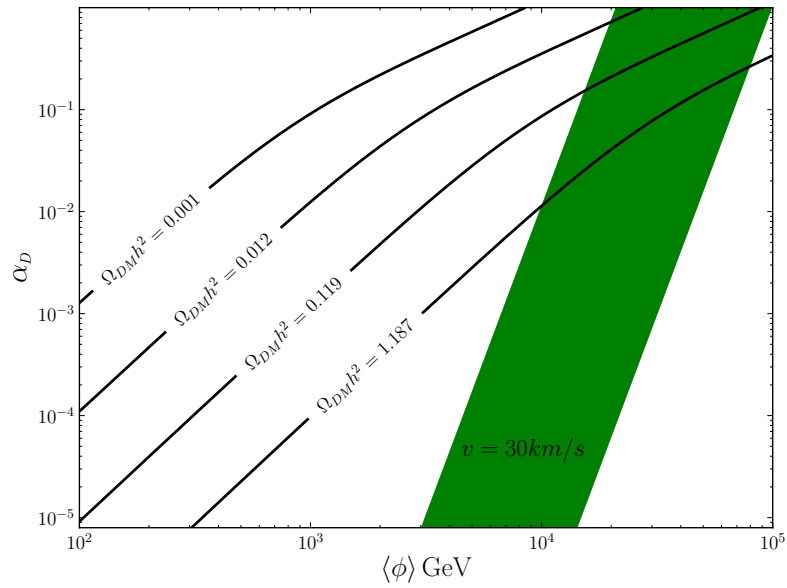
Figure 5.7: Vector dark matter transfer cross-section and relic density. The green region shows the region in parameter space where σ_T/m_{DM} is in the interval between 0.1 and 10 cm^2/g at velocity $v = 30$ km/s, relevant for solving the core-cusp problem and the too-big-too-fail problem.
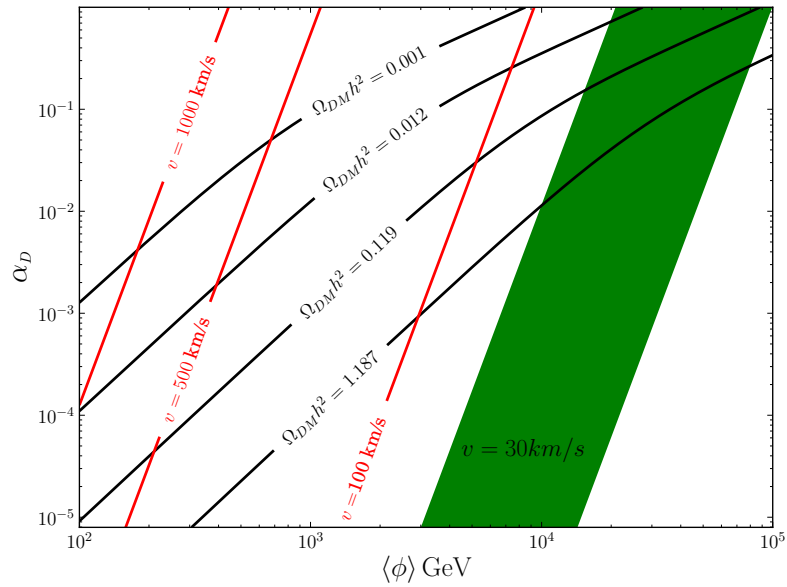

Figure 5.8: Same as in Figure 5.7 but with additional contours (in red) showing $\sigma_T/m_{DM} = 1$ at higher velocities: $v = 100$km/s, $v = 500$km/s and $v = 1000$km/s.
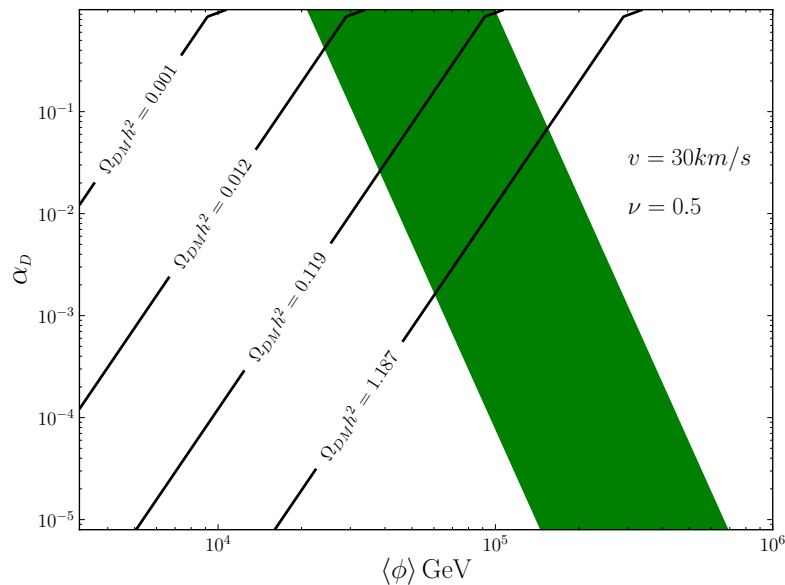
Figure 5.9: Monopole dark matter transfer cross-section and the relic density contours for the critical exponent $\nu = 0.5$. The region in green shows the region in parameter space where σ_T/m_{DM} is in the interval between 0.1 and 10 cm²/g at velocity $v = 30$ km/s relevant for solving the core-vs-cusp problem and the too-big-too-fail problem.

make galaxies more spherical, so the observation of elliptical galaxies together with N-body simulations can give limits on the energy transfer.

To solve the too-big-to-fail problem one needs a cross-section of the order of $\sigma_T/M_{DM} \sim 0.1 - 10$ cm²/g [214–216] at the velocity scale of dwarf galaxies ($v \sim 10-30$ km/s). By comparing this to the limits from larger scale structures one finds that there might be a small region of parameter space left for a theory with velocity independent cross-section of around $\sigma_T/M_{DM} \sim 0.6$ cm²/g [214, 215].

In this chapter we consider a velocity-dependent cross-section which, if the cross-section is around 1 cm²/g at velocities of $v \sim 10-30$ km/s, it will be much smaller at the velocities relevant for the shapes of galaxies or the bullet cluster. Therefore, there is no contradiction between the cross-sections needed to solve the too-big-too-fail problem and the constraints from the ellipticity of galaxies.

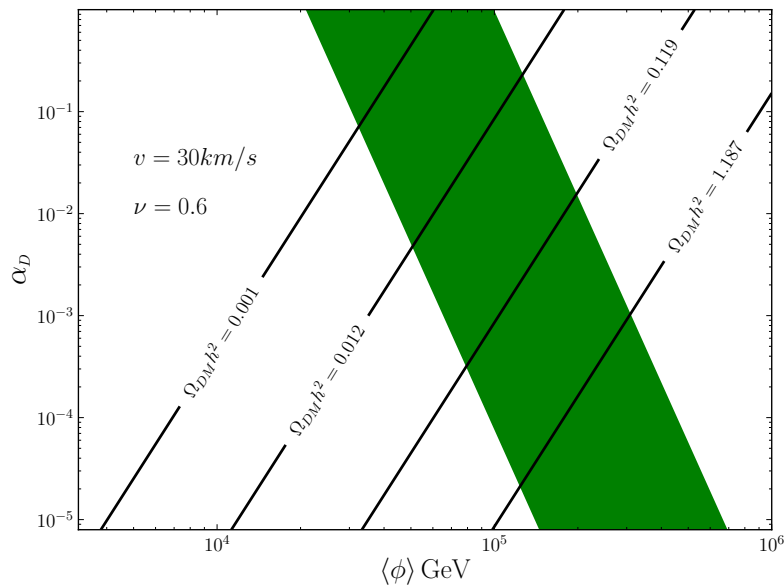In Figure 5.7, we show the region of parameter space of our model where the

Figure 5.10: Monopole dark matter as in Figure 5.9 with the critical exponent value $\nu = 0.6$.

transfer cross-section for vector dark matter is in the desired region $\sigma_{\mathrm{T}}/M_{\mathrm{DM}} = 0.1 - 10\ \mathrm{cm}^2/\mathrm{g}$ at $v - 30\ \mathrm{km/s}$, which can help solving these problems at dwarf galaxy scales. This is superimposed with the contours of the relic density for vector dark matter in our model. In Figure 5.8 we overlay this with the contours of $\sigma_{\mathrm{T}}/m_{DM} = 1$ at other velocities. It readily follows from these considerations that the upper bound constraint from the Milky Way and from Bullet cluster at $v \sim 200$ to km/s are satisfied by the self-interacting VDM in the regime where the relic density is in agreement with observations and the dwarf-galaxy-scale problems are addressed.

Monopole self-interactions are obtained by replacing the electric with the magnetic Coulomb law, $\alpha_D \rightarrow \alpha_{mD} = 1/\alpha_D$, which gives the limits seen in Figures 5.9 and 5.10 for monopole dark matter produced in a model with a second order phase transition.

5.5   Conclusions

In this chapter we have investigated a SU(2) dark extension to the SM with an adjoint scalar. This model includes two dark matter candidates and a new relativistic

degree of freedom contributing to dark radiation. The dark matter candidates are heavy vector bosons and magnetic monopoles. Magnetic monopoles are produced during phase transitions in the early Universe, and we find that they can make up a significant fraction of dark matter in our model.

The unbroken U(1) subgroup that remains after symmetry breaking in the hidden sector contributes to dark radiation and provides long range self-interactions between the dark matter particles. We found that the minimal model we considered satisfies the observational constraints on N_{eff} and on the transfer cross-section at large velocities. At the same time, the self-interacting vector and monopole DM intrinsic to our model can produce the right size of transfer cross-sections relevant for addressing problems with CCDM at dwarf galaxy scales. The dark matter in our model has two components with different self-interactions, and there are interactions between the two components. To study the cosmological consequences of this in any more detail would require the use of N-body simulations.

Chapter 6

Spectroscopy of Scalar Mediators to Dark Matter at the LHC and at 100 TeV

The existence of dark matter is one of the most compelling arguments for BSM physics. DM candidates have been proposed in many different BSM models and can have a rich and varying phenomenology. However, assuming dark matter can be produced at colliders a generic feature is the existence of collider signatures with missing energy, as stable dark matter particles leave the detector unobserved. In this chapter, based entirely on [4], we will investigate the two-jets-plus-missing-energy final state at the LHC and a future 100 TeV collider.

6.1 Introduction

To discover missing energy signals at colliders, the invisibly decaying particle needs to recoil against reconstructable objects. Searches for mono-jets and mono-photons, where the dark matter recoils against a visible jet or photon, have been carried out at Run 1 of the LHC [222–224]. These studies have so far not discovered any evidence for an excess of missing energy events, but can in parts of the parameter space be as or more constraining than limits from direct and indirect detection [225–230]. It is thus important to formulate and extend the searches for dark matter at the LHC

for Run 2 and beyond.

Dark matter can be produced at colliders via an exchange of a mediator particle which connects the colliding SM partons to the dark sector. A viable and simple approach to characterise and interpret dark matter searches at colliders relies on using simplified models with four basic types of mediators: vectors, axial-vectors, scalars and pseudo-scalars (see white papers [229–231] for early reviews and references). The mediator is a dynamical degree of freedom in this approach which is the correct description for dark matter searches at the LHC as the energy transfer in the collision can typically exceed the mediator masses. Following the Higgs discovery, there is a renewed interest in the role of scalar degrees of freedom and the possibilities provided by extended Higgs sectors in searches for new physics. Of particular interest to dark matter searches are models with scalar and pseudo-scalar mediators whose reach at the LHC was studied recently in [40–42]. It was found that the LHC at 14 TeV will provide a complementary coverage to the low-energy experiments in dark matter searches, and it is the only experiment to probe dark sectors if the invisible particles produced are not stable at cosmological scales. These studies have been performed using the mono-jet-plus-missing-energy topology [222–224].

In this chapter, we will study simplified models with scalar mediators in the two-jets-plus-missing-energy topology to determine their collider limits and discovery potential by analysing their kinematics of the final state jets. For scalar mediators, mono-jet searches predominantly rely on the gluon fusion production channel [40, 41]. The presence of a second jet allows for more non-trivial kinematics in the final state. Using VBF type cuts, one can suppress more of the background and the contribution from the gluon fusion production channel. This makes the weak boson fusion processes dominant instead, and allows us to capture mediators with suppressed couplings to fermions. The kinematic information in the two jets+MET final state should also allow us to study the mediator mass which will be the main focus of this chapter. In a slightly different context, the idea of exploring two-jet kinematics to learn more about the SM–DM interactions has also been implemented in [232].

We consider a simplified model with a scalar mediator whose SM couplings are

proportional to the SM Higgs. We start by defining the models in Section **6.2** before briefly considering the DM phenomenology in Section **6.3**. We then move on to consider the phenomenology at the LHC in Section **6.4** and at a future 100 TeV collider in Section **6.5**.

6.2 Models

In the unitary gauge, the Standard Model (SM) contains just a single scalar-field degree of freedom, the neutral scalar Higgs h. At tree level, h interacts with the massive vector bosons, $W^{\pm}$ and Z^0 and all the SM fermions, f. The linear interactions of h with the other SM particles can be written in the form,

$$\mathcal{L}_h^{SM} \supset \left(\frac{2M_W^2}{v} W_{\mu}^+ W^{-\,\mu} + \frac{M_Z^2}{v} Z_{\mu} Z^{\mu} - \sum_f \frac{m_f}{v} \bar{f}f \right) h \,. \qquad (6.2.1)$$

We want to extend the SM by introducing a scalar mediator particle ϕ which couples to the SM degrees of freedom as well as to fermionic dark matter particles χ via

$$\mathcal{L}_{\phi} \supset -g_{\chi} \, \bar{\chi}\chi \, \phi \,. \qquad (6.2.2)$$

For the purpose of this chapter, the spin of the dark matter particle is not relevant, i.e. the dark matter particle could instead be a vector or a scalar particle. There are two types of settings where the additional scalar ϕ can appear in interactions with the Standard Model. First, it can be an additional Higgs doublet for example coming from a two-Higgs doublet model or more generally any scalar field transforming non-trivially under the $SU(2)_L$ of the SM. Alternatively, the ϕ scalar mediator can be a singlet under the Standard Model. In the latter case it interacts with the SM degrees of freedom only via the mixing with the SM Higgs, h. The interactions of ϕ with the SM are subject to experimental constraints on the mixing angle $\sin^2\theta \lesssim 0.15$ (see [129,233]) arising from experimental bounds on the SM Higgs to invisible decays and other Higgs data.

First in section **6.2.1** we consider the more constrained singlet-mixing case, and then in section **6.2.2** we define the less constrained generic Higgs-like scenario. The upshot is that both of these cases will be described by the same simplified model of

Equation (6.2.13) with the scaling parameter κ being either unconstrained $\kappa \sim 1$ or small $\kappa \lesssim 0.15$.

6.2.1 The Singlet Mixing Model

In the implementation of the model ϕ is a Standard-Model singlet neutral scalar, and the visible SM sector and the 'invisible' χ sector are coupled to each other only via the mixing between the two neutral scalars ϕ and h, as in the Higgs portal model. The states of definite masses, h_1 and h_2, are

$$h = h_1 \cos\theta + h_2 \sin\theta\,, \qquad \phi = -h_1 \sin\theta + h_2 \cos\theta\,, \qquad (6.2.3)$$

where θ is the mixing angle. Combining Equations (6.2.1)-(6.2.3) we obtain a simplified model for invisible Higgs decays involving two Higgs-like neutral scalars h_1 and h_2:

$$\begin{aligned}
\mathcal{L}_{h_1,h_2} = &\left(\tfrac{2M_W^2}{v} W_\mu^+ W^{-\mu} + \tfrac{M_Z^2}{v} Z_\mu Z^\mu - \sum_f \tfrac{m_f}{v} \bar{f}f\right) \left(h_1 \cos\theta + h_2 \sin\theta\right) \\
&-g_\chi \bar{\chi}\chi\left(h_2 \cos\theta - h_1 \sin\theta\right) - \tfrac{1}{2}m_{h_1}^2 h_1^2 - \tfrac{1}{2}m_{h_2}^2 h_2^2 - m_\chi \bar{\chi}\chi\,. \quad (6.2.4)
\end{aligned}$$

The first scalar mass eigenstate, h_1, plays the role of the observed SM Higgs boson, and we also assume that the mediator h_2 is always heavier than the SM Higgs,

$$m_{h_2} > m_{h_1} = 125\,\mathrm{GeV}\,. \qquad (6.2.5)$$

If h_2 is lighter than h_1, h_2 will not contribute to the final state with two jets and missing energy as we discuss below. A light second scalar can be very interesting for other final states. With this Lagrangian we can produce h_2 as in the SM via both the gluon-fusion and the vector-boson-fusion mechanisms, with the corresponding SM cross-sections rescaled by $\sin^2\theta$. Similarly the h_1 production rates are rescaled relative to the SM by a factor of $\cos^2\theta$ which is $\simeq 1$ for sufficiently small values of the mixing angle.

If both mediators can be produced on-shell in either channel, the cross-section for $\bar{\chi}\chi+$ two-jet production in the narrow width approximation can be written as,

$$\sigma_{\mathrm{DM}}^{(i)} = \sigma_{h_i}\, \mathrm{Br}_{h_i \to \bar{\chi}\chi}, \qquad (6.2.6)$$

where σ_{h_i} is the production cross-section for h_i + two jets and $\mathrm{Br}_{h_i\to\bar{\chi}\chi}$ are the branching ratios,

$$\sigma_{h_1} = \sigma_{\mathrm{SM}}\cos^2\theta\,, \quad \sigma_{h_2} = \sigma_{\mathrm{SM}}\sin^2\theta\,, \tag{6.2.7}$$

$$\mathrm{Br}_{h_1\to\bar{\chi}\chi} = \frac{\sin^2\theta\,\Gamma_{\phi\to\bar{\chi}\chi}}{\sin^2\theta\Gamma_{\phi\to\bar{\chi}\chi} + \cos^2\theta\,\Gamma_{h\to\mathrm{SM}}} = \sin^2\theta\,\frac{\Gamma_{\phi\to\bar{\chi}\chi}(m_{h_1})}{\Gamma_{h_1}^{\mathrm{tot}}}\,, \tag{6.2.8}$$

$$\mathrm{Br}_{h_2\to\bar{\chi}\chi} = \frac{\cos^2\theta\,\Gamma_{\phi\to\bar{\chi}\chi}}{\cos^2\theta\,\Gamma_{\phi\to\bar{\chi}\chi} + \sin^2\theta\,\Gamma_{h\to\mathrm{SM}}} = \cos^2\theta\,\frac{\Gamma_{\phi\to\bar{\chi}\chi}(m_{h_2})}{\Gamma_{h_2}^{\mathrm{tot}}}\,, \tag{6.2.9}$$

where

$$\Gamma_{\phi\to\bar{\chi}\chi} = \frac{g_\chi^2 m_\phi}{8\pi}\left(1 - \frac{4m_\chi^2}{m_\phi^2}\right)^{\frac{3}{2}}. \tag{6.2.10}$$

For dark matter masses below the kinematic threshold of both mediators, $2m_\chi < m_{h_1} < m_{h_2}$, both mediators can be on-shell, and in principle both channels for the dark matter production are open. Due to the different size of the decay widths, the lighter Higgs will dominate, as can be seen from (6.2.6)-(6.2.9),

$$\sigma_{\mathrm{DM}}^{(1)}/\sigma_{\mathrm{DM}}^{(2)} \propto \frac{\Gamma_{h_2}^{\mathrm{tot}}}{\Gamma_{h_1}^{\mathrm{tot}}} \gg 1\,. \tag{6.2.11}$$

The SM Higgs has a very narrow width of 0.0068 GeV, and due to the limits on the Higgs to invisible branching ratio we know that this width, $\Gamma_{h_1}^{\mathrm{tot}}$, cannot increase by more than 35% [234]. The reason the Higgs width is so small is that all the fermions are coupled to the Higgs via Yukawa couplings, so that we cannot have light fermions with large couplings coupled to the Higgs. The total decay width of the second scalar, $\Gamma_{h_2}^{\mathrm{tot}}$, on the other hand, can easily be large as can be inferred from Figure 6.1. Even for $g_\chi = 0.1$ the total width of h_2 will be an order of magnitude larger than the h_1 Higgs width. Hence, for light dark matter only the h_1 Higgs mediator is relevant when both channels are open.

For heavier dark matter, $m_{h_1} < 2m_\chi < m_{h_2}$, only the h_2 channel is open and it is efficiently described by the simplified model

$$\mathcal{L} = \sin\theta\left(\frac{2M_W^2}{v}W_\mu^+W^{-\,\mu} + \frac{M_Z^2}{v}Z_\mu Z^\mu - \sum_f \frac{m_f}{v}\bar{f}f\right)h_2 \tag{6.2.12}$$

$$- g_\chi\,\bar{\chi}\chi h_2 - \frac{1}{2}m_{h_2}^2 h_2^2 - m_\chi\bar{\chi}\chi\,.$$

Finally, if dark matter masses are higher than m_{h_2} it cannot be produced via an on-shell mediator exchange, and the resulting rate of its production is too small to be observed.
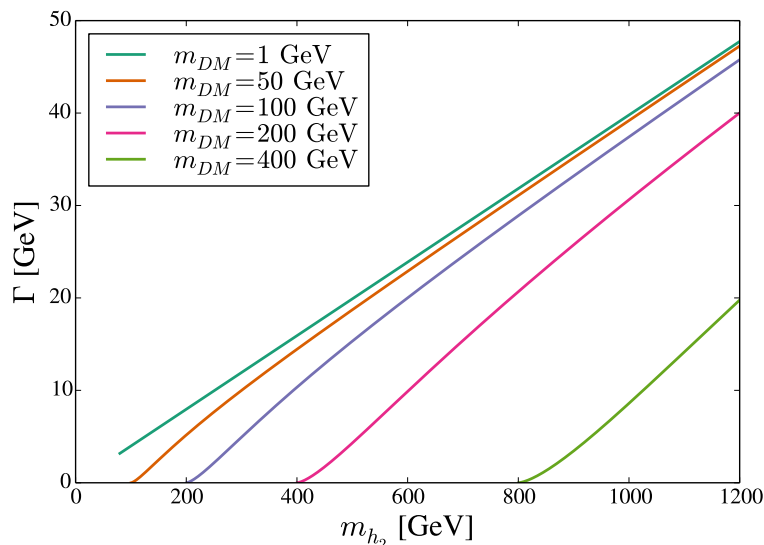
Figure 6.1: The decay width of h_2 into $\bar{\chi}\chi$ with $g_{\text{DM}} = 1$.

Current limits on $\sin^2\theta$ mainly come from two sources, the Higgs signal strengths and the electroweak precision tests, for recent papers see [82, 128, 129, 233, 235]. Limits from Higgs signal strength measurements constrain $\cos^2\theta$ directly [129]. This leads to a bound $\sin\theta < 0.44$, independent of the mass of h_2. The electroweak precision tests, mainly the W boson mass, give a mass-dependent constraint on $\sin\theta$ shown in Figure 3 in [129]. In the mass range around 1 TeV, the limit becomes $\sin\theta < 0.3$. We also note that the limits coming from a non-observation of the second SM-Higgs-like state are not directly applicable for h_2 in our case, due to its large branching ratio to invisibles.

We will only consider these limits in the context of the singlet-mixing simplified model with the κ-parameter $\kappa = \sin^2\theta$. In the simplified model framework we do not know what other particle content there is, and additional degrees of freedom could modify both the SM Higgs signal and the loop corrections to the W-mass.

Recent discussion of theory models for dark matter based on mass mixing between the scalar singlet mediator and the SM Higgs can be found in [2,3,88,111–113] and Chapters **4** and **5**.

6.2.2   Generic Higgs-like Scalar Mediator Model

More generally, scalar mediators to dark sector can also arise from an independent additional Higgs doublet or Higgs multiplet for example in the two-Higgs-doublet models. We choose a simplified model for a generic scalar mediator by assuming that it has the same interactions with the SM vector bosons and fermions as the SM Higgs, but scaled by an overall scaling factor κ which is a free parameter of the simplified model,

$$
\begin{aligned}
\mathcal{L} = & \sqrt{\kappa} \left(\frac{2M_W^2}{v} W_\mu^+ W^{-\mu} + \frac{M_Z^2}{v} Z_\mu Z^\mu - \sum_f \frac{m_f}{v} \bar{f}f \right) \phi \qquad (6.2.13) \\
& - g_\chi \bar{\chi}\chi\phi - \frac{1}{2}m_m^2\phi^2 - m_\chi\bar{\chi}\chi .
\end{aligned}
$$

In general, the scalar mediator can couple with a different strength to the SM vector bosons and to SM fermions, thus introducing additional parameters into the simplified model (6.2.13). For clarity and simplicity, we will use the minimal model (6.2.13) with a single scaling factor. Here, $\kappa = 1$ corresponds to the normal SM Higgs couplings. In general we consider values of $\kappa \lesssim 1$ since it is difficult from a model-building perspective to increase the coupling to gauge bosons with additional Higgs singlets or doublets. The simplified model for the more constrained singlet mixing case is described by the same Lagrangian with $\kappa = \sin^2\theta \lesssim 0.15$. In this simplified model framework, we do not introduce a direct coupling between the SM Higgs and $\chi\bar{\chi}$, as this interaction can be easily captured with giving ϕ the same mass as the Higgs.

6.3   Comments on the Relic Density and Direct Detection Constraints

Simplified models for dark matter are introduced to capture the main aspects of dark matter collider phenomenology without being complete models. It is therefore customary not to impose constraints from relic density or direct detection stringently. Still, the model introduced above in Equation (6.2.13) is a valid model that could have cosmologically viable dark matter. Therefore, to give an indication of

constraints for models of this type, we calculate the relic density and direct detection constraints assuming that

- (i) the dark sector fermions $\bar{\chi} \, \chi$ which enter the simplified model definition (6.2.13) is *cosmologically* stable dark matter and not merely one of the dark sector degrees of freedom which are long-lived on a collider scale;

- (ii) the dark matter particles annihilate predominantly via the mediator interaction specified in (6.2.13), and there are no other DM annihilation channels beyond the simplified model (6.2.13) or that they are highly suppressed.

We stress that if either of these additional assumptions is not satisfied, the relic density and direct detection-related constraints discussed in this section will not apply. These are strong assumptions that can easily be evaded in many well motivated DM models.

We will now require that the dark matter does not overclose the Universe, and that the direct detection cross-section is sufficiently small not to have been observed so far. We calculate the relic density and direct detection limits using the MadDM [236, 237] with the simplified model (6.2.13). The computed relic density is compared to the observed relic density from the Plank Satellite [22] of $\Omega h^2 = 0.1199 \pm 0.0027$, and the direct detection cross-sections are compared to the limits from the LUX experiment [174].

Figure 6.2 shows the contours of the computed relic density and the direct detection exclusions on the mediator mass – dark matter mass plane and for various values of g_{DM} and κ. For the direct detection constraint we have assumed that the DM density interacting with the detector is given by the canonical value, even if the DM in our model is only a sub-component of the total DM density in this region of parameter space. Therefore, the direct detection limits on our model are weaker than what is shown in the figure in the region of parameter space where the calculated DM density is smaller than the observed value.

As for the collider phenomenology at the LHC and at future colliders, we will be interested in heavy mediators with the dark matter mass and the dark matter coupling largely unconstrained, as long as the scalar mediators have a large branching

ratio to dark matter. From Figure 6.2 we can see that all these models easily avoid direct detection constraints, and as long as the dark matter mass is quite heavy we can have mediator masses up to 2500 GeV without over-closing the Universe. For $g_{\text{DM}} = 4$ and a heavy mediator $M_{\text{med}} \simeq 2.5$ TeV, we need $m_\chi \gtrsim 400$ GeV to have viable dark matter (another way to put it is that only the DM which is more than 6 times lighter than the mediator is constrained here). For smaller couplings the minimal DM mass increases accordingly (as can be seen from the second and third plots in Fig. 6.2) not to overclose the Universe for the heaviest mediators, but this is not a problem for the models we will consider in the rest of the chapter. We will therefore now turn to collider phenomenology where we will study models which, if we interpreted as complete models, can provide a viable dark matter candidate.

We conclude that the relic density and direct detection considerations can provide useful constraints on our simplified model under certain assumptions. This provides an important complementarity to the collider phenomenology we will now study. If the LHC or future colliders can resolve and probe the mediator mass-scale and a signal with missing energy is discovered, one of the main open questions will be if the signal results in the production of cosmological dark matter and what is its particle identity.

6.4 Collider Limits on Scalar Mediators with two Jets and MET at the LHC

To derive collider limits on models with scalar mediators to dark matter sectors, and to distinguish between models with different mass scales, we will use a search strategy based on final states with missing transverse energy plus two jets. There are four main kinematic quantities associated with the $\not{E}_T$-plus-two-jets signatures: the missing transverse momentum $\not{p}_T$, the jets' invariant mass M_{jj}, the azimuthal angle between the tagging jets $\Delta\phi_{jj}$ and the jets' pseudo-rapidity difference $\Delta\eta = \eta_{j1} - \eta_{j2}$.
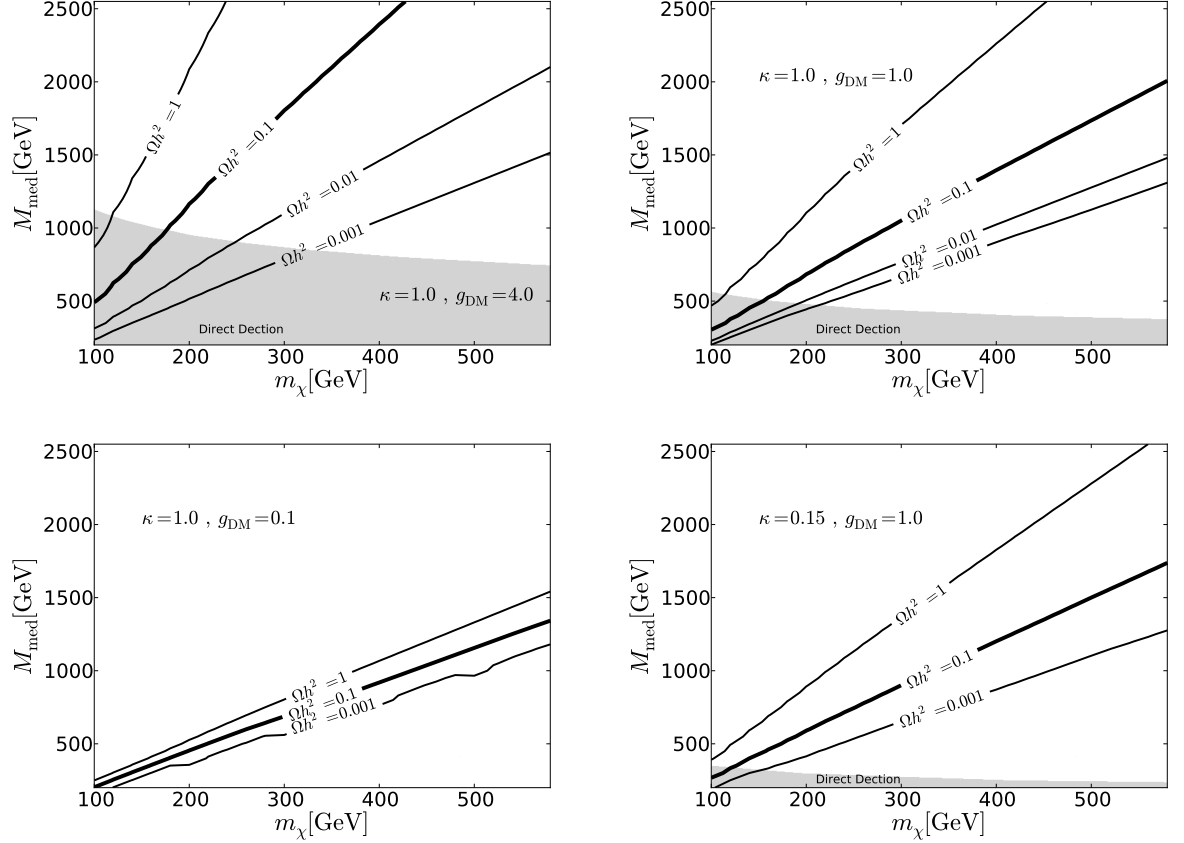
Figure 6.2:   Dark matter relic density and direct detection constraints for our
simplified model for dark matter for various values of g_{DM} and κ. The lines give
relic density contours and the grey region shows the area excluded by direct detection
constraints.

In terms of these we impose the VBF cuts [238, 239],

$$\displaystyle{\not}p_T > 100\,\mathrm{Gev}\,,\quad M_{jj} > 1200\,\mathrm{GeV}\,,\quad \Delta\phi_{jj} < 1\,,\quad \Delta\eta > 4.5\,,\quad p_{T,j} > 40\,\mathrm{GeV}\,,$$

$$(6.4.14)$$

to separate the signal and background. Here $p_{T,j}$ is the transverse momentum of each
jet defined by using the anti-kt jet algorithm with $R = 0.4$. We reconstruct jets using
Fastjet [240, 241]. After imposing these cuts, the main production channel of the
scalar mediator is largely reduced to weak vector boson fusion (WBF), leaving only
a small contribution from the gluon fusion (GGF) channel (*cf.* Table 6.1). Despite
of the relative smallness of the GGF process after cuts (6.4.14), one should not be
tempted to approximate them by the Higgs-gluon effective vertex. The inclusion of
finite top-quark mass effects in the top-loop in the GGF production is known to be

important (in the context of DM searches at the LHC this was emphasised in [242]), especially for heavier scalar mediators where the heavy top mass approximation breaks down. We therefore simulate both the WBF and GGF contributions to the signal with VBFNLO [243–245], which includes the full top-loop dependence to GGF.

The background is simulated at leading order using MadGraph [246]. Both signal and background are then showered with Herwig++ [247]. The main backgrounds are Z + two jets with the Z decaying to neutrinos and $W^{\pm}$ + two jets where the W decays to a neutrino and a missing lepton. We count the lepton as missed if it has $|\eta_l| > 2.5$ or $p_T < 10$ GeV. We have also checked that the $\bar{t}t$ background is negligible after the cuts. The projected LHC exclusion limits for these final states have been studied previously in [238,239,248,249] in the context of an invisible branching ratio for the SM Higgs.

6.4.1 Width Effect on Differential Distributions

In Figure 6.3 we can see the effect of varying the width of the mediator on the differential distributions of M_{jj} and $\Delta\phi_{jj}$, for a mediator with $M_{\mathrm{med}} = 800$ GeV. A smaller width leads to a slightly broader M_{jj} tail and flatter $\Delta\phi_{jj}$ distribution. For reasonably small total widths this effect is not very large. We will therefore use the narrow width approximation where we produce the mediator on-shell with subsequent decay to $\bar{\chi}\chi$, with a branching ratio determined by the coupling constants and dark matter mass when we simulate the signal.

6.4.2 Exclusion Limit Reach at the LHC

Our first goal is to establish the projected LHC exclusions for models with scalar mediators based on the two jets and $\not{E}_T$ final states. We aim to evaluate the upper limit on the mediator mass for the model to be within the LHC reach.

The left panel in Table 6.1 shows the cross-sections for the signal at the LHC at the 13 TeV centre-of-mass energy, assuming a 100% branching ratio of the scalar mediators to dark matter and $\kappa = 1$. The cross-sections for SM backgrounds are
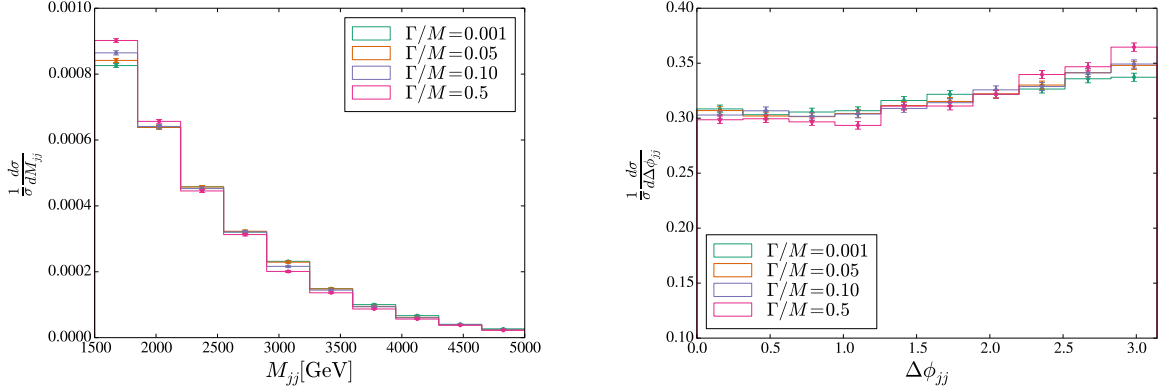
Figure 6.3: Kinematic distributions for different values of the mediator width at $\sqrt{s} = 13$ TeV when $M_{\text{med}} = 800$ GeV.

M_{med}	VBF	GGF	Total
125 GeV	89	17	107
250 GeV	61	13	74
500 GeV	26	10	36
750 GeV	12	3	15
1000 GeV	6.0	0.7	6.7
1500 GeV	2.0	0.1	2.1

Background	Cross-section(fb)
Zjj	128
W$^+$jj	116
W$^-$jj	40

Table 6.1: Cross-sections (fb) at partonic level after VBF cuts in (6.4.14) at 13 TeV.

shown in the table on the right. Using these one can calculate the simple projected exclusion limits for these models from a standard cut-and-count procedure.

For our analysis, we will use the differential cross-sections to perform a binned log-likelihood analysis [250] to compute confidence levels (CLs) for experimental exclusions [251]. In the four plots of Figure 6.4, we show the normalised differential distributions for signal and background as functions of the four kinematic variables M_{jj}, $\not{p}_T$, $\Delta\eta$, $\Delta\phi_{jj}$. These kinematic distributions are plotted for different values of the mediator mass ranging from $M_{\text{med}} = 125$ GeV to 1500 GeV[1].

---

[1]Compared to differential distributions at e^+e^- colliders [252, 253], at the LHC differences between the models are less pronounced and more difficult to exploit.
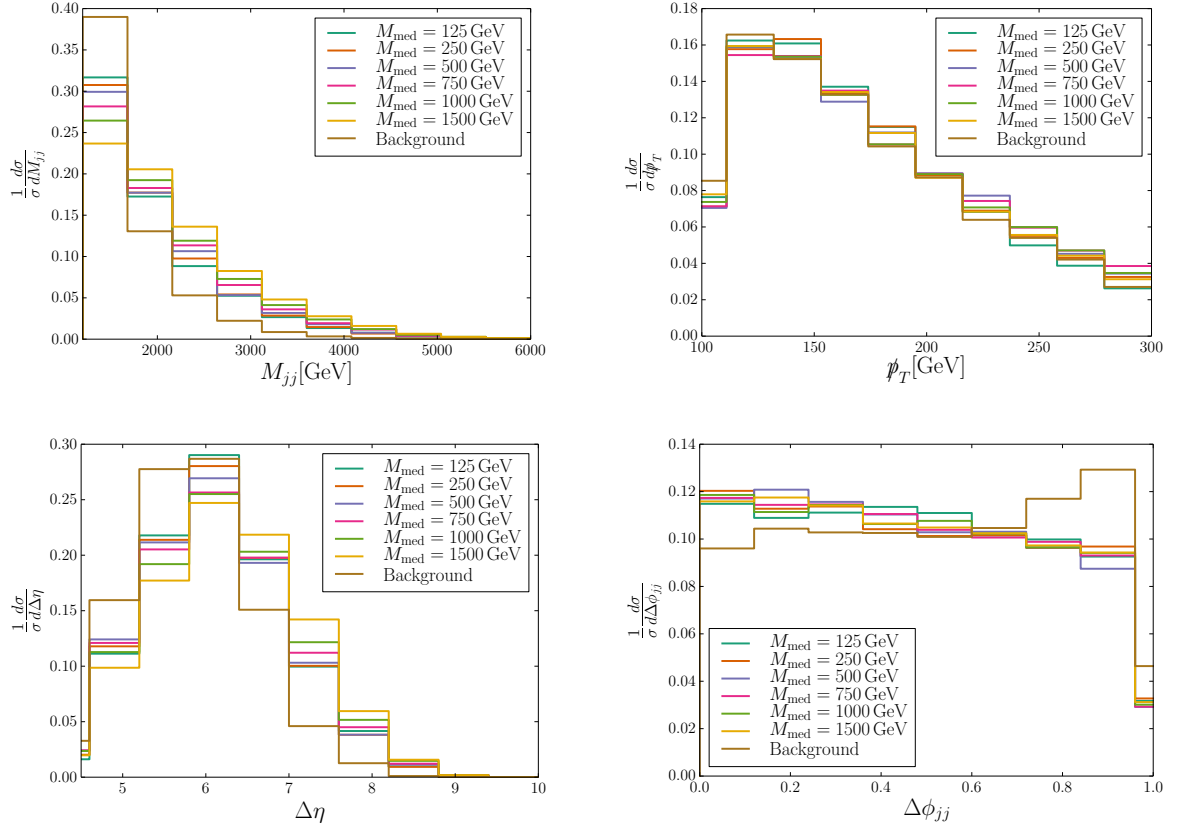
Figure 6.4: Kinematic distributions for different values of the mediator mass for the signal, and for the background at the LHC. M_{jj} distributions are shown on the top left panel, $\not{p}_T$ is on top right right, $\Delta\eta$ and ϕ_{jj} distributions are on the bottom left and right panels respectively.

The differences in the shapes of the kinematic distributions for models with different values of $M_{\rm med}$ can be used to differentiate between them. The binned log-likelihood technique for computing confidence levels is based on regarding each bin in a histogram for the measured variable as an independent search channel to be combined with all others. Systematic uncertainty is taken into account by running many pseudo Monte Carlo experiments where the normalisation of the background histogram is varied randomly. The significance is then given by the fraction of these experiments that has a smaller likelihood ratio than that for the expected background distribution. We use the M_{jj} distribution (the $\Delta\eta$ distribution gives similar results) with ten bins both to determine the signal exclusion limits, and later to distinguish between different signal models.
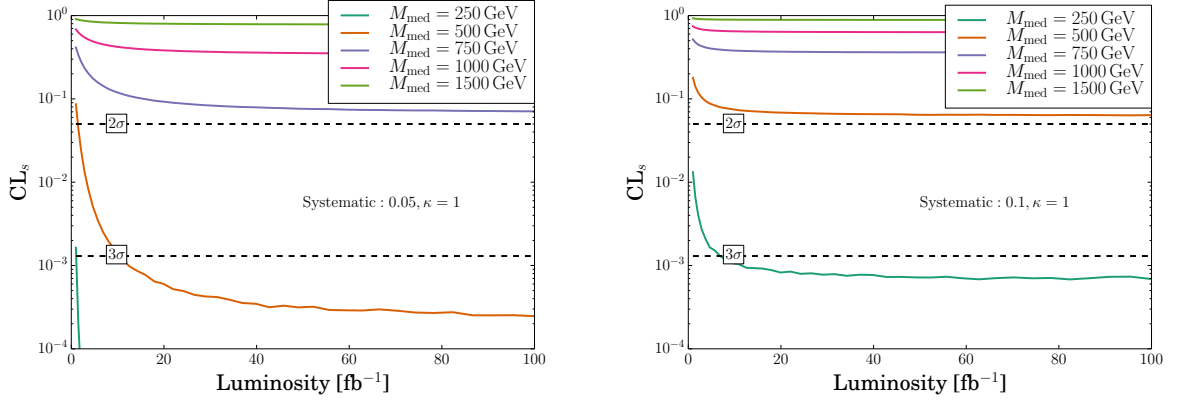
Figure 6.5: We characterise the LHC reach for models with different values of M_{med} by computing confidence levels for excluding signals from the SM backgrounds. We consider models with $\kappa = 1$, and on the left panel use a systematic uncertainty of 5%. The panel on the right corresponds to a 10% systematic uncertainty.

In Figures 6.5-6.7, we show the LHC reach for excluding scalar mediator models for different values of mediator masses. The plots in Figure 6.5 apply to generic models with $\kappa = 1$ and assume a 5% and a 10% level of systematic uncertainty. Figure 6.6 shows the LHC exclusion contours in the context of the mediator-Higgs mixing models. We set $\kappa = 0.15$ and assume a 1% and a 5% systematic uncertainty. Plots in Figure 6.7 show the LHC exclusion limits without fixing the κ parameter to a specific value. Here we allow κ to float so that for each model the computed cross-section is set equal to a cross-section that corresponds to a 30% invisible branching ratio for the 125 GeV Higgs.

The conclusions we draw is that, for generic scalar mediator models with $\kappa \simeq 1$, with the 13 TeV LHC, we can probe models with mediator masses up to $M_{\text{med}} \approx 750$ GeV (assuming a 5% level of systematic uncertainty). For the models with a small κ, in particular the models associated with the Higgs–singlet-mediator mixing where $\kappa = \sin^2\theta \lesssim 0.15$, we can probe up to $M_{\text{med}} \approx 500$ GeV (with an optimistic 1% systematic uncertainty). Not surprisingly, the decrease in cross-section at small values of κ makes it very hard to reach to the higher mediator masses in the Higgs portal-type mixing model realisations at the LHC.
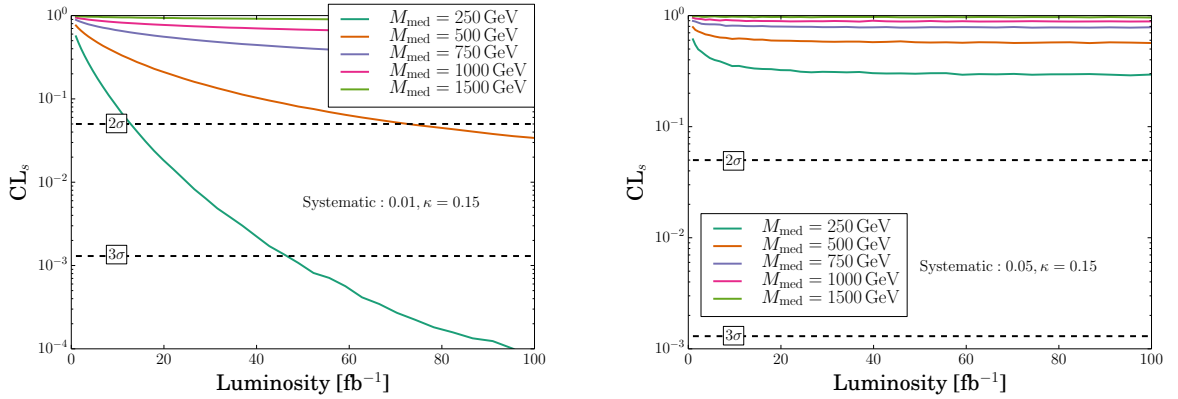
Figure 6.6:   The LHC reach for different M_{med} models with $\kappa = 0.15$ in terms of
confidence levels to exclude signal from SM background. On the left panel we use
a systematic uncertainty of 1%, and the panel on the right corresponds to a 5%
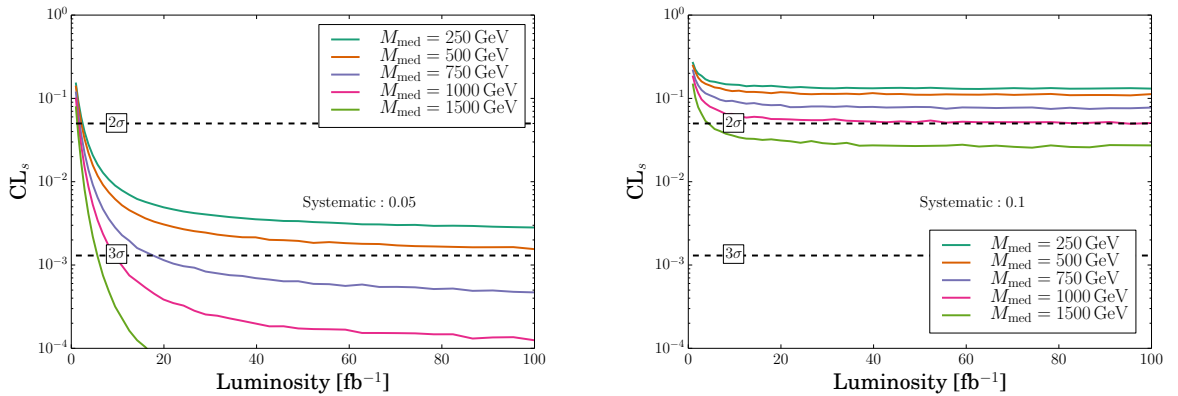systematic uncertainty.

Figure 6.7:   The LHC reach for different M_{med} models. We normalise the cross-
sections for all models to the SM Higgs cross-section with $\mathrm{Br}_{\mathrm{inv}} = 30\%$ and a sys-
tematic uncertainty of 5% (left panel) and 10% (right panel).

6.4.3   Distinguishing Between Models with Different Mediator Masses

For the models which are within the LHC reach, i.e. with M_{med} below the upper
bounds set to be the exclusion contours in Figures 6.5-6.7, the next step is to be
able to distinguish between different models.

This is achieved by comparing the shapes of the kinematic distributions plotted
in Figure 6.4 for different mediator masses. As we increase M_{med}, the visible jets will
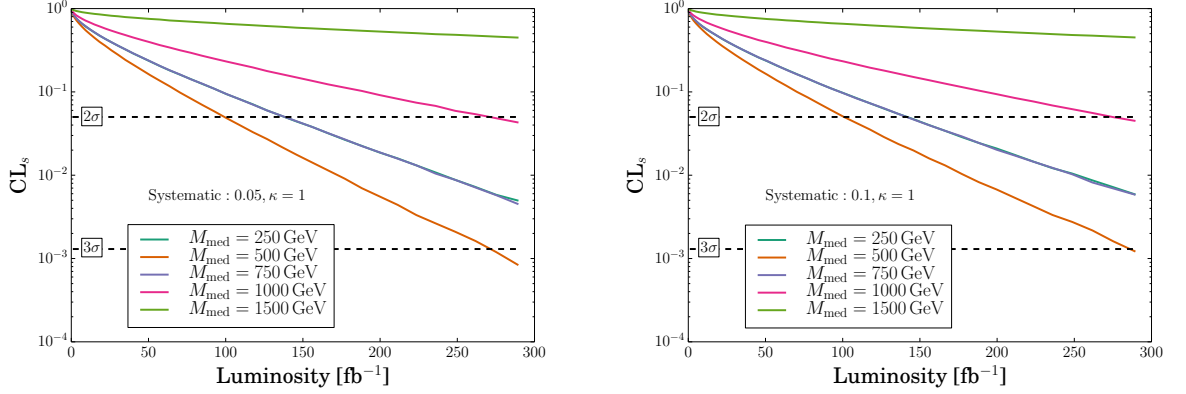
Figure 6.8:   Differentiating the models at $\kappa = 1$ at the LHC. For each value of M_{med}
between 250 and 1500 GeV, the models are compared to the reference model with
a 125 GeV mediator. We assume a systematic uncertainty of 5% (left panel) and
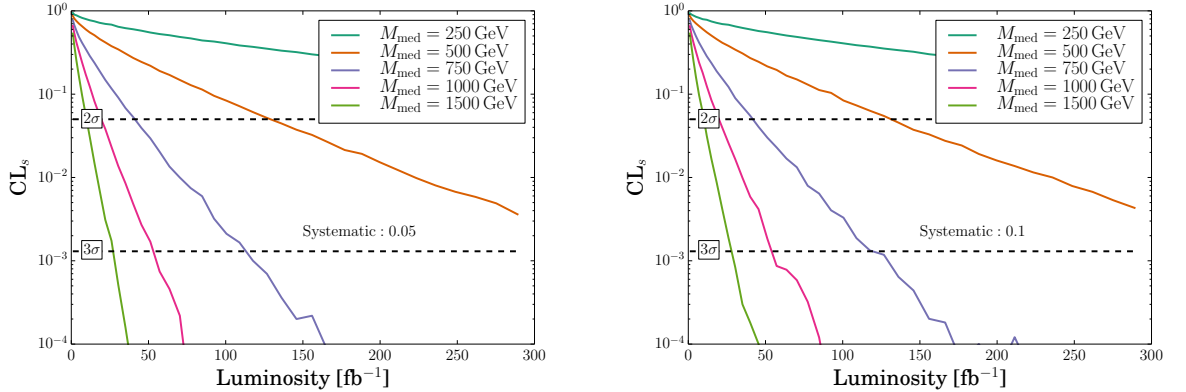10% (right panel).

Figure 6.9:   Differentiating the models with the floating κ parameter defined as in
the caption of Figure 6.7. Models are compared pairwise to the 125 GeV reference
model.

recoil against a heavier object which will change the distribution of the kinematic
variables. We will use this change to distinguish the models with different mediator
masses by the following procedure. Before we even start comparing different models,
we will need an excess of signal events over the SM background in the data after
the VBF cuts. The cross-section of this signal can be used to infer an upper limit
for the mass of the mediator as a function of κ. The question then becomes if we
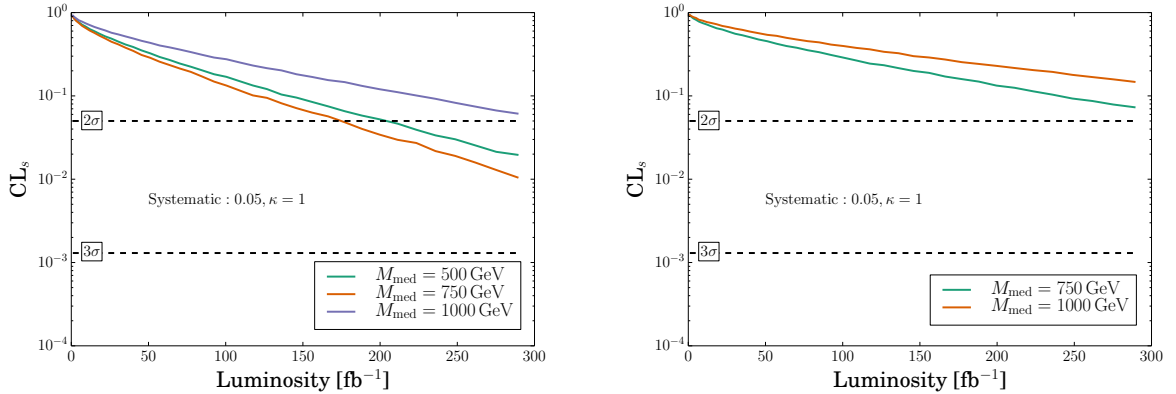can distinguish between the different models that can achieve the measured cross-

Figure 6.10: Differentiating the $\kappa = 1$ models at the LHC. In the left panel we compare to the reference model with $M_{\mathrm{med}} = 250\,\mathrm{GeV}$, and on the right the reference model is 500 GeV. We assume a systematic uncertainty of 5% .

section. We will again use a binned log-likelihood method and will be comparing models pairwise. For each cross-section we select the two extreme models: the first one with the maximal mass, and the second (reference model) with a 125 GeV mediator.

In Figure 6.8, we can see how well one can differentiate the models at the LHC with $\kappa = 1$. Specifically, all the models with $M_{\mathrm{med}} = 250$, 500 and 750 GeV can be distinguished from the 125 GeV mediator. Within our approach, this conclusion is valid even with a relatively high systematic error of 10%. We also note that for $\kappa = 0.15$ it is no longer possible to differentiate any of the models since the cross-section becomes too small.

So far in Figure 6.8, we have characterised the simplified model signals by fixing the scaling parameter κ to either 1 or 0.15. Alternatively, we can set the signal cross-section to a fixed value corresponding to a 30% invisible branching ratio of the SM Higgs. This is shown in Figure 6.9, which leads one to conclude that the models with heavier and heavier mediator masses are easier and easier to distinguish from the reference model. When comparing models with different mediator masses, there are in general two competing effects: the increased difference in the shape of differential distributions and the decrease in the cross-section with the increase of the mediator mass. By fixing the cross-sections in Figure 6.9, the differences between the models are only due to the shapes of differential distributions, while in

Figure 6.8 both effects are important. This explains why, for example, the model with $M_{\mathrm{med}} = 500$ GeV is easier to distinguish than the 250 and 750 GeV models in Figure 6.8.

We also compare models where the reference model is not the 125 GeV Higgs. The results for using 250 GeV and 500 GeV as reference models are shown in Figure 6.10. In the same way as for the 125 GeV Higgs, the cross-section for the reference model is set equal to that of the model we compare it with. We see that the 500 and 750 GeV models can be distinguished from the 250 GeV model at the LHC. At the same time, the 750 GeV model (and above) cannot be distinguished from the 500 GeV reference point.

6.5 Scalar Mediator Models at 100 TeV

We use a similar approach to investigate the model's reach and the ability to distinguish between different models at a future 100 TeV circular proton-proton collider. The signal and background are simulated in the same way as for the LHC analysis, and we use the same binned-log likelihood analysis for exclusion and differentiation of the various models. The main difference is that we use the cuts

$$\not{p}_T > 100\,\mathrm{Gev}\,, \quad M_{jj} > 1200\,\mathrm{GeV}\,, \quad \Delta\phi_{jj} < 0.5\,, \quad \Delta\eta > 5.5\,, \quad p_{T,j} > 110\,\mathrm{GeV}\,, \tag{6.5.15}$$

instead of the normal VBF cuts in (6.4.14), as we need to reduce the background more. We also allow for larger jets by using the anti-kt jet algorithm with $R = 0.8$.

The left panel in Table 6.2 shows the cross-sections for the signal at a future 100 TeV collider, assuming a 100% branching ratio of the scalar mediators to dark matter.

We have set $\kappa = 1$ and assumed a 100% branching ratio of the mediator to $\bar{\chi}\chi$ DM. The cross-sections for SM backgrounds are shown in the table on the right.

Figure 6.11 plots the kinematic distributions for M_{jj}, $\not{p}_T$, $\Delta\eta$, $\Delta\phi_{jj}$ for models with different values of M_{med} and the SM background. We first investigate the exclusion limits at 100 TeV for invisible decays of the 125 GeV Higgs. In Figure 6.12,
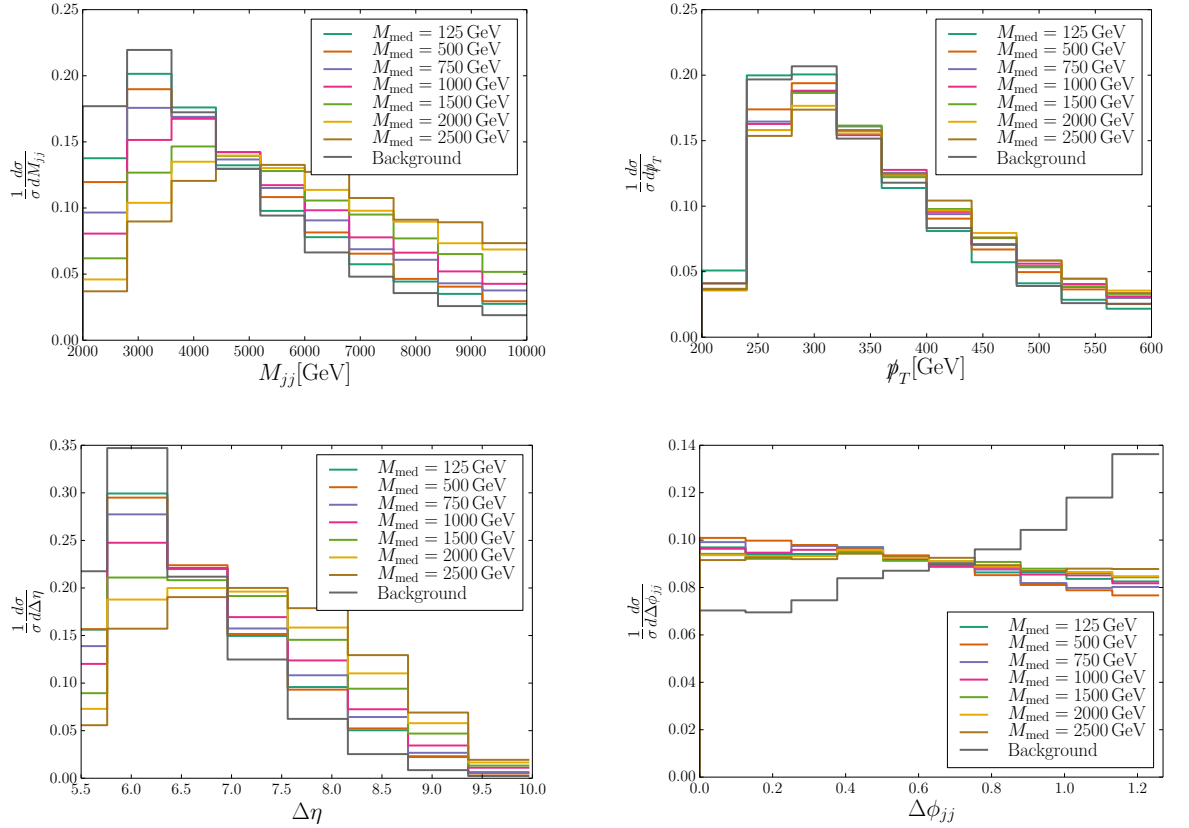
Figure 6.11:   Kinematic distributions for different values of the mediator mass for the signal and for the background at a 100 TeV collider. M_{jj} distributions are shown on the top left panel, $\not{p}_T$ is on top right right, $\Delta\eta$ and ϕ_{jj} distributions are on the bottom left and right panels, respectively.
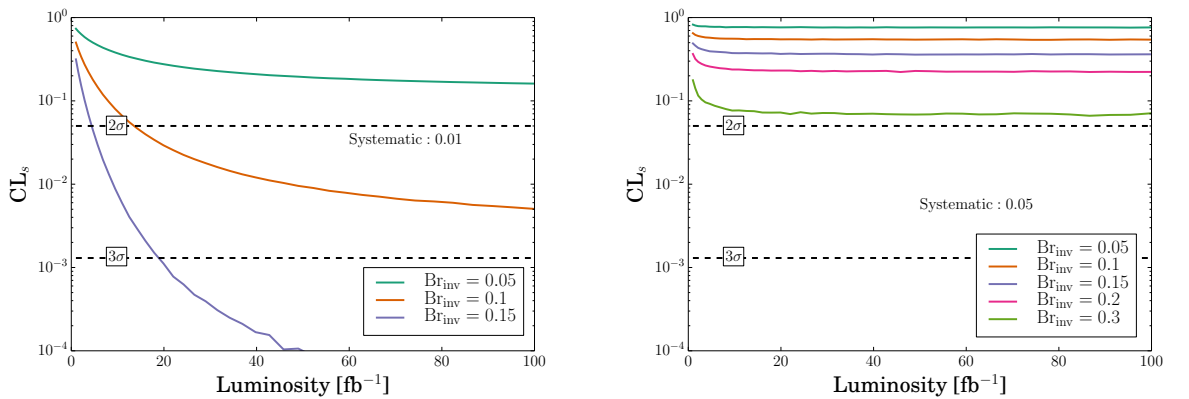

Figure 6.12:   100 TeV reach for excluding invisible decays of the 125 GeV Higgs boson. On the left panel we use a systematic uncertainty of 1%, and the panel on the right corresponds to a 5% systematic uncertainty
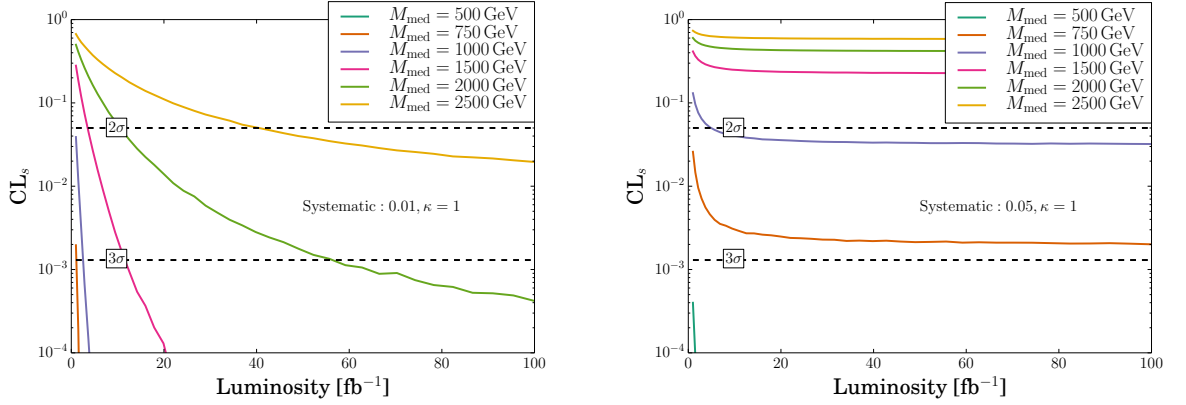
Figure 6.13: 100 TeV reach for different M_{med} models with $\kappa = 1$. On the left panel we use a systematic uncertainty of 1%, and the panel on the right corresponds to a 5% systematic uncertainty.

Figure 6.14: 100 TeV reach for different M_{med} models with $\kappa = 0.15$. On the left panel we use a systematic uncertainty of 1%, and the panel on the right corresponds to 5% systematic uncertainty.
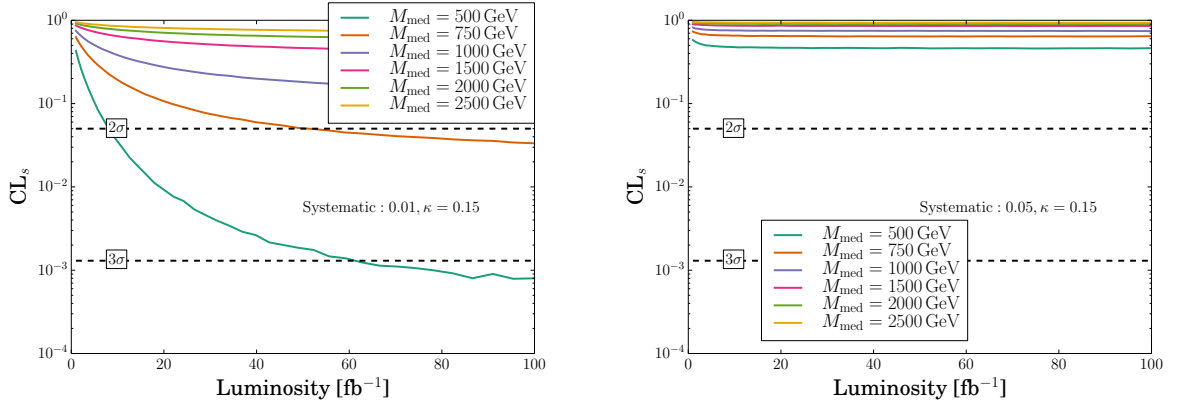
we plot exclusion limits on the branching rations to invisibles and conclude that for small systematic errors one can exclude $\mathrm{Br}_{\mathrm{inv}} \gtrsim 10\%$.

We can now consider simplified models with different values of the mediator mass. In Figure 6.13 we show the expected reach for a 100 TeV collider for these models with $\kappa = 1$ for a 1% and 5% level of systematic uncertainty. Figure 6.14 gives the expected exclusion limits for models with $\kappa = 0.15$. From these figures we conclude that in the case of small systematic uncertainties, the 100 TeV collider would provide a very significant increase in the exclusion reach for new physics

M_{med}	VBF	GGF	Total
125 GeV	120	100	220
500 GeV	76	110	185
750 GeV	53	46	99
1000 GeV	40	20	60
1500 GeV	22	5	27
2000 GeV	14	2	16
2500 GeV	8.7	0.6	9.4

Background	Cross-section(fb)
Zjj	239
W^+jj	298
W^-jj	157

Table 6.2: Cross-sections (fb) at partonic level after the cuts (6.5.15) at 100 TeV.

models with mediator masses up to 2.5 TeV. For a larger systematic uncertainty at the level of 5%, the reach in M_{med} is 1 TeV. For the more restricted case of $\kappa = 0.15$ Higgs-mixing models, a 100 TeV collider could exclude models with up to 750 GeV.
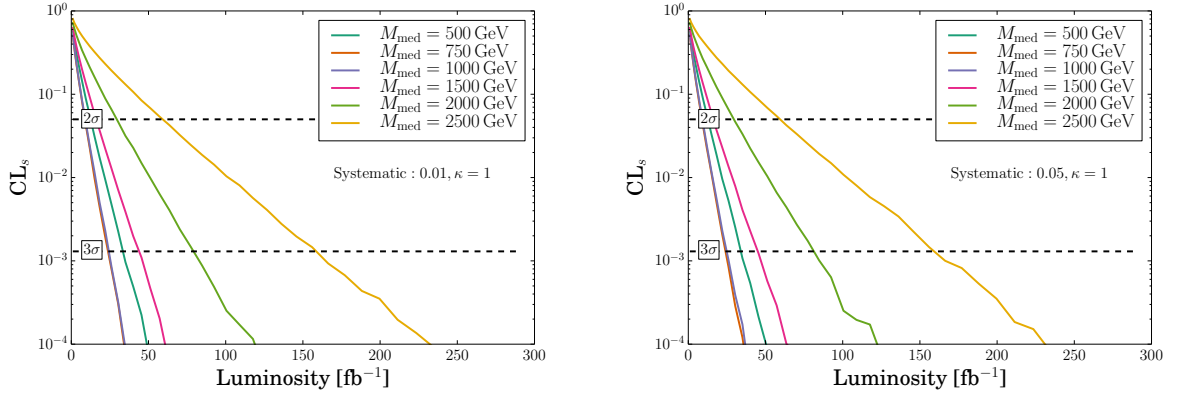

Figure 6.15: Differentiating the models at $\kappa = 1$ at 100 TeV. For each value of M_{med} between 500 and 2500 GeV, the models are compared to the reference model with the 125 GeV mediator. We assume a systematic uncertainty of 1% (left panel) and 5% (right panel).

Finally, as we have done at the LHC energies before, we can use the kinematic distributions at 100 TeV to differentiate pairwise between models with different mediator masses. We first compare each model with a reference model with a 125 GeV mediator. The results for this analysis are presented in Figure 6.15 for $\kappa = 1$ and Figure 6.16 for the models with $\kappa = 0.15$. At $\kappa = 1$, we can distinguish all the

reachable models with mediators up to 2.5 TeV from the 125 GeV reference model. For the small-κ models in Figure 6.16, we can distinguish between the models up to 1 TeV (this requires higher luminosities up to 600 fb^{-1}).
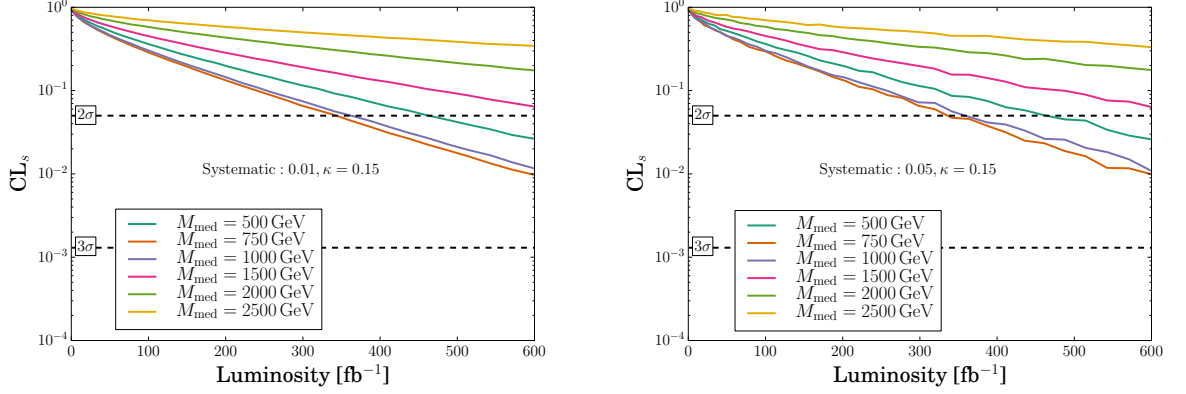

Figure 6.16:   Differentiating the models at $\kappa = 0.15$ at 100 TeV. For each value of M_{med} between 500 and 2500 GeV, the models are compared to the reference model with the 125 GeV mediator. We assume a systematic uncertainty of 1% (left panel) and 5% (right panel).

Figure 6.17:   Differentiating the models at $\kappa = 1$ at a future 100 TeV Collider. For each value of M_{med} between the reference model mass and 2500 GeV, the models are compared to the reference model with the 500 GeV mediator in the left panel and 750 GeV in the right panel. We assume a systematic uncertainty of 5% .

As before, we can also compare to different choices of reference model. In Figures 6.17-6.18, we plot the results with reference models corresponding to mediator

masses of 500, 750, 1000 and 1500 GeV. We conclude that for all the reference models with up to 1 TeV mediator masses we can successfully distinguish all reachable models with higher mass.
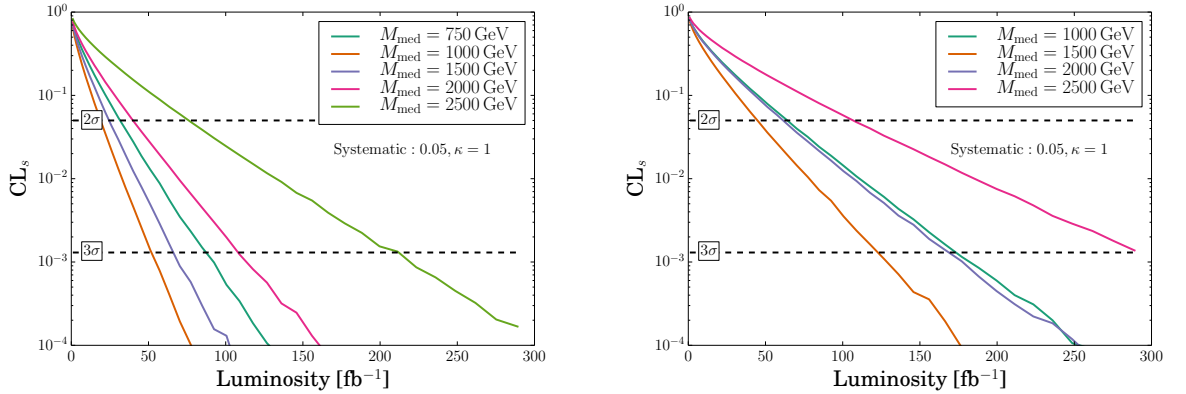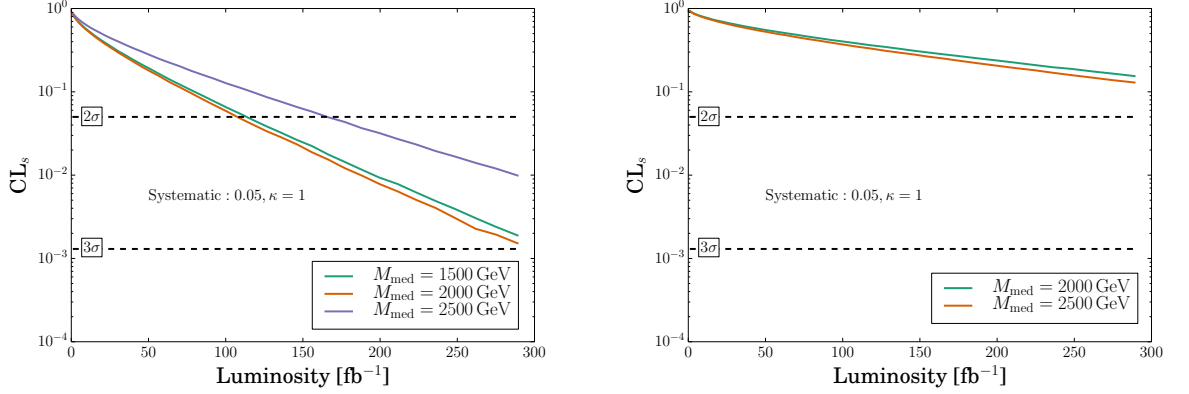

Figure 6.18: Differentiating the models at $\kappa = 1$ at a future 100 TeV Collider. For each value of M_{med} between the reference model mass and 2500 GeV, the models are compared to the reference model with the 1000 GeV mediator in the left panel and 1500 GeV in the right panel. We assume a systematic uncertainty of 5% .

6.6 Summary and Conclusions

We have studied collider limits for simplified models of dark matter where the dark matter is coupled to the Standard Model by a scalar field mediator which interacts with both the SM fermions and the vector bosons. Our main goal was two-fold: First to determine the projected reach of the Run 2 LHC and a future circular hadron collider for excluding such models. Second, to use the kinematic distributions to be able to extract information on the values of the mediator masses. To achieve this we focused on the two-jets-plus-missing-transverse-energy final states. In our case both production mechanisms are important: the gluon fusion process which effectively probes the coupling of mediators to quarks, and the weak vector boson fusion which is due to the interactions with vector bosons.

We found that at the 13 TeV LHC, one can probe simplified models of dark matter with mediator masses up to 750 GeV. At a 100 TeV collider the reach is

increased to 2.5 TeV mediators. These measurements are dominated by systematic uncertainties which we have kept relatively small and have varied between the 1% and 10% level.

In order to 'measure' the mediator mass, which is the most relevant new physics scale of these models at colliders, we have compared the models with different values of M_{med} pairwise. In both cases at 13 and at 100 TeV, we found that we can differentiate between essentially all the discoverable benchmark models we have considered. In particular, we can distinguish a 125 GeV reference model from models with mediator masses of 250, 500 and 750 GeV at the LHC. For the 100 TeV case, the list of distinguishable models extends to 2.5 TeV.

For the more constrained case of the Higgs portal models where scalar mediators mix with the SM Higgs and the mixing angle is small, $\sin^2\theta = 0.15$, the collider reach is reduced due to the overall decrease in the signal cross-section. We found that the LHC reach is 500 GeV for an optimistic 1% systematic uncertainty, and this is increased to 750 GeV at a 100 TeV collider.

Chapter 7

Conclusions

In this thesis we have investigated the collider and the cosmological phenomenology of hidden sector extensions to the SM with a Higgs portal coupling. These models extend the SM by adding a new hidden or dark gauge group with a new scalar degree of freedom that is coupled to the Higgs. We have mainly been interested in models with classical scale invariance where all mass scales are generated dynamically through dimensional transmutation. In Chapter **2**, we showed how to construct SM extensions with CSI. These models come in many shapes: some achieve dimensional transmutation through confinement as in QCD, while most examples in the literature generate mass scales at weak coupling via the Coleman-Weinberg mechanism. In both of these approaches the generated scale is transmitted to the SM via the Higgs portal coupling. For models with CSI to be interesting and viable extensions of the SM, they need to solve the observational problems in the SM which include dark matter, matter-antimatter asymmetry, Higgs stability and neutrino masses, without introducing any new large scales. Constructing and exploring the physics of CSI models that could address these problems was the main motivation of this thesis.

To generate the observed matter-antimatter asymmetry in the Universe we implemented leptogenesis in a CSI model where the SM is extended by a $U(1)_{B-L}$ gauge group in Chapter **3**. Leptogenesis based on right-handed neutrino oscillations avoids the requirements of very heavy right-handed neutrinos in normal leptogenesis scenarios. The SM$\times$ $U(1)_{B-L}$ model explains the small active neutrino mass via a

type 1 see-saw mechanism, and in sizeable parts of the parameter space, with right-handed neutrinos at the GeV scale, we achieved the observed matter asymmetry of the Universe.

We have shown in Chapters **4** and **5** that many different viable dark matter candidates are possible in these hidden sector extensions to the SM. In this thesis, we have investigated scalar dark matter, vector boson dark matter and the possibility to have monopoles of the hidden sector as dark matter. In addition to providing good dark matter candidates, we find that the models with scalar dark matter can successfully stabilise the Higgs potential. If the hidden sector is a non-Abelian SU(2) group, the gauge bosons are stable as there is no kinetic mixing with the SM U(1). This makes the gauge bosons good dark matter candidates. For all of these dark matter models, the next generation of direct detection experiments could discover them or exclude large parts of the parameter space. When the hidden sector gauge group is SU(2) and we have an adjoint scalar, the gauge group is broken to a U(1) and Polyakov 't Hooft monopoles will exist. We have showed that monopoles, which are produced in phase transitions in the early Universe, can make up a significant fraction of dark matter in this model. Both the monopoles and the gauge boson dark matter will have long-range self-interactions which can help to solve the too-big-too-fail and the core-vs-cusp problems with the standard cold dark matter paradigm.

The collider phenomenology of many of the models with dark matter in the hidden sector can be characterised by simplified models where the dark matter is coupled to a mediator that is coupled to the SM quarks and leptons. In Chapter **6**, we showed how it is possible to learn about the mass of a scalar mediator to dark matter at the LHC and a future 100 TeV collider by using the kinematic distributions in the two-jets-plus-missing-energy final state. At the LHC one can probe models with mediator masses of 750 GeV, and at a future 100 TeV collider masses up to 2.5 TeV. With small systematic errors, it would also be possible to distinguish most of the benchmark models where the difference in mediator mass is of the order of 250 GeV.

The results presented in this thesis show that CSI models, and hidden sector models more generally, are interesting and viable BSM models. It is possible to

address the main observational problems of the SM in a minimal way without introducing any new large scales that would destabilise the Higgs mass. Even if the models do not have any smoking-gun signatures they provide a rich phenomenology at colliders, direct and indirect detection experiments and for cosmological observables. With new data from the next run of the LHC and the next generation of DM and cosmological experiments, there are good possibilities to either discover such SM extensions, or to exclude large parts of their parameter space.

Bibliography

[1] V. V. Khoze and G. Ro, *Leptogenesis and Neutrino Oscillations in the Classically Conformal Standard Model with the Higgs Portal*, *JHEP* **10** (2013) 075, [`arXiv:1307.3764`].

[2] V. V. Khoze, C. McCabe, and G. Ro, *Higgs vacuum stability from the dark matter portal*, *JHEP* **1408** (2014) 026, [`arXiv:1403.4953`].

[3] V. V. Khoze and G. Ro, *Dark matter monopoles, vectors and photons*, *JHEP* **1410** (2014) 61, [`arXiv:1406.2291`].

[4] V. V. Khoze, G. Ro, and M. Spannowsky, *Spectroscopy of Scalar Mediators to Dark Matter at the LHC and at 100 TeV*, `arXiv:1505.03019`.

[5] E. W. Kolb and M. S. Turner, *The Early universe*, *Front.Phys.* **69** (1990) 1–547.

[6] P. W. Higgs, *Broken Symmetries and the Masses of Gauge Bosons*, *Phys.Rev.Lett.* **13** (1964) 508–509.

[7] F. Englert and R. Brout, *Broken Symmetry and the Mass of Gauge Vector Mesons*, *Phys.Rev.Lett.* **13** (1964) 321–323.

[8] P. W. Higgs, *Broken symmetries, massless particles and gauge fields*, *Phys.Lett.* **12** (1964) 132–133.

[9] **UA1** Collaboration, G. Arnison et al., *Experimental Observation of Isolated Large Transverse Energy Electrons with Associated Missing Energy at s**(1/2) = 540-GeV*, *Phys.Lett.* **B122** (1983) 103–116.

[10] **UA1** Collaboration, G. Arnison et al., *Experimental Observation of Lepton Pairs of Invariant Mass Around 95-GeV/c**2 at the CERN SPS Collider*, *Phys.Lett.* **B126** (1983) 398–410.

[11] **TASSO** Collaboration, R. Brandelik et al., *Evidence for Planar Events in e+ e- Annihilation at High-Energies*, *Phys.Lett.* **B86** (1979) 243.

[12] D. Barber, U. Becker, H. Benda, A. Boehm, J. Branson, et al., *Discovery of Three Jet Events and a Test of Quantum Chromodynamics at PETRA Energies*, *Phys.Rev.Lett.* **43** (1979) 830.

[13] **PLUTO** Collaboration, C. Berger et al., *Evidence for Gluon Bremsstrahlung in e+ e- Annihilations at High-Energies*, *Phys.Lett.* **B86** (1979) 418.

[14] **JADE** Collaboration, W. Bartel et al., *Observation of Planar Three Jet Events in e+ e- Annihilation and Evidence for Gluon Bremsstrahlung*, *Phys.Lett.* **B91** (1980) 142.

[15] **CDF** Collaboration, F. Abe et al., *Observation of top quark production in $\bar{p}p$ collisions*, *Phys.Rev.Lett.* **74** (1995) 2626–2631, [`hep-ex/9503002`].

[16] **ATLAS Collaboration** Collaboration, G. Aad et al., *Observation of a new particle in the search for the Standard Model Higgs boson with the ATLAS detector at the LHC*, *Phys.Lett.* **B716** (2012) 1–29, [`arXiv:1207.7214`].

[17] **CMS Collaboration** Collaboration, S. Chatrchyan et al., *Observation of a new boson at a mass of 125 GeV with the CMS experiment at the LHC*, *Phys.Lett.* **B716** (2012) 30–61, [`arXiv:1207.7235`].

[18] **CMS** Collaboration, V. Khachatryan et al., *Measurement of the inclusive 3-jet production differential cross section in protonproton collisions at 7 TeVand determination of the strong coupling constant in the TeVrange*, *Eur.Phys.J.* **C75** (2015), no. 5 186, [`arXiv:1412.1633`].

[19] F. Zwicky, *Die Rotverschiebung von extragalaktischen Nebeln*, *Helv.Phys.Acta* **6** (1933) 110–127.

[20] M. Milgrom, *A Modification of the Newtonian dynamics as a possible alternative to the hidden mass hypothesis*, *Astrophys.J.* **270** (1983) 365–370.

[21] D. Clowe, A. Gonzalez, and M. Markevitch, *Weak lensing mass reconstruction of the interacting cluster 1E0657-558: Direct evidence for the existence of dark matter*, *Astrophys.J.* **604** (2004) 596–603, [`astro-ph/0312273`].

[22] **Planck** Collaboration, P. A. R. Ade et al., *Planck 2013 results. XVI. Cosmological parameters*, *Astron. Astrophys.* **571** (2014) A16, [`arXiv:1303.5076`].

[23] **EROS-2** Collaboration, P. Tisserand et al., *Limits on the Macho Content of the Galactic Halo from the EROS-2 Survey of the Magellanic Clouds*, *Astron.Astrophys.* **469** (2007) 387–404, [`astro-ph/0607207`].

[24] **MACHO** Collaboration, C. Alcock et al., *The MACHO project LMC microlensing results from the first two years and the nature of the galactic dark halo*, *Astrophys.J.* **486** (1997) 697–726, [`astro-ph/9606165`].

[25] H. Baer, K.-Y. Choi, J. E. Kim, and L. Roszkowski, *Dark matter production in the early Universe: beyond the thermal WIMP paradigm*, *Phys.Rept.* **555** (2014) 1–60, [`arXiv:1407.0017`].

[26] G. Bertone, *Particle dark matter: Observations, models and searches*, .

[27] J. D. Wells, *Annihilation cross-sections for relic densities in the low velocity limit*, `hep-ph/9404219`.

[28] L. Ackerman, M. R. Buckley, S. M. Carroll, and M. Kamionkowski, *Dark Matter and Dark Radiation*, *Phys.Rev.* **D79** (2009) 023519, [`arXiv:0810.5126`].

[29] L. D. Duffy and K. van Bibber, *Axions as Dark Matter Particles*, *New J.Phys.* **11** (2009) 105008, [`arXiv:0904.3346`].

[30] W. H. Press and P. Schechter, *Formation of galaxies and clusters of galaxies by selfsimilar gravitational condensation, Astrophys.J.* **187** (1974) 425–438.

[31] C. Frenk and S. D. White, *Dark matter and cosmic structure, Annalen Phys.* **524** (2012) 507–534, [`arXiv:1210.0544`].

[32] S. D. M. White, C. S. Frenk, and M. Davis, *Clustering in a neutrino-dominated universe, Astrophys.J* **274** (Nov., 1983) L1–L5.

[33] A. J. Benson, *Galaxy Formation Theory, Phys.Rept.* **495** (2010) 33–86, [`arXiv:1006.5394`].

[34] P. Cushman, C. Galbiati, D. McKinsey, H. Robertson, T. Tait, et al., *Working Group Report: WIMP Dark Matter Direct Detection,* `arXiv:1310.8327`.

[35] L. Baudis, *WIMP Dark Matter Direct-Detection Searches in Noble Gases, Phys. Dark Univ.* **4** (2014) 50–59, [`arXiv:1408.4371`].

[36] M. Cirelli, G. Corcella, A. Hektor, G. Hutsi, M. Kadastik, P. Panci, M. Raidal, F. Sala, and A. Strumia, *PPPC 4 DM ID: A Poor Particle Physicist Cookbook for Dark Matter Indirect Detection, JCAP* **1103** (2011) 051, [`arXiv:1012.4515`]. [Erratum: JCAP1210,E01(2012)].

[37] **Fermi-LAT** Collaboration, A. A. Abdo et al., *Constraints on Cosmological Dark Matter Annihilation from the Fermi-LAT Isotropic Diffuse Gamma-Ray Measurement, JCAP* **1004** (2010) 014, [`arXiv:1002.4415`].

[38] D. Hooper and L. Goodenough, *Dark Matter Annihilation in The Galactic Center As Seen by the Fermi Gamma Ray Space Telescope, Phys. Lett.* **B697** (2011) 412–428, [`arXiv:1010.2752`].

[39] F. Calore, I. Cholis, C. McCabe, and C. Weniger, *A Tale of Tails: Dark Matter Interpretations of the Fermi GeV Excess in Light of Background Model Systematics, Phys. Rev.* **D91** (2015), no. 6 063003, [`arXiv:1411.4647`].

[40] M. R. Buckley, D. Feld, and D. Goncalves, *Scalar Simplified Models for Dark Matter*, *Phys.Rev.* **D91** (2015), no. 1 015017, [`arXiv:1410.6497`].

[41] P. Harris, V. V. Khoze, M. Spannowsky, and C. Williams, *Constraining Dark Sectors at Colliders: Beyond the Effective Theory Approach*, *Phys.Rev.* **D91** (2015), no. 5 055009, [`arXiv:1411.0535`].

[42] M. Chala, F. Kahlhoefer, M. McCullough, G. Nardini, and K. Schmidt-Hoberg, *Constraining Dark Sectors with Monojets and Dijets*, *JHEP* **07** (2015) 089, [`arXiv:1503.05916`].

[43] V. Silveira and A. Zee, *SCALAR PHANTOMS*, *Phys.Lett.* **B161** (1985) 136.

[44] J. M. Cline, K. Kainulainen, P. Scott, and C. Weniger, *Update on scalar singlet dark matter*, *Phys.Rev.* **D88** (2013) 055025, [`arXiv:1306.4710`].

[45] A. G. Cohen, A. De Rujula, and S. Glashow, *A Matter - antimatter universe?*, *Astrophys.J.* **495** (1998) 539–549, [`astro-ph/9707087`].

[46] V. Barger, J. P. Kneller, H.-S. Lee, D. Marfatia, and G. Steigman, *Effective number of neutrinos and baryon asymmetry from BBN and WMAP*, *Phys.Lett.* **B566** (2003) 8–18, [`hep-ph/0305075`].

[47] A. Sakharov, *Violation of CP Invariance, c Asymmetry, and Baryon Asymmetry of the Universe*, *Pisma Zh.Eksp.Teor.Fiz.* **5** (1967) 32–35.

[48] F. R. Klinkhamer and N. Manton, *A Saddle Point Solution in the Weinberg-Salam Theory*, *Phys.Rev.* **D30** (1984) 2212.

[49] C. Jarlskog, *A Basis Independent Formulation of the Connection Between Quark Mass Matrices, CP Violation and Experiment*, *Z.Phys.* **C29** (1985) 491–497.

[50] M. Shaposhnikov, *Baryon Asymmetry of the Universe in Standard Electroweak Theory*, *Nucl.Phys.* **B287** (1987) 757–775.

[51] A. G. Cohen, D. Kaplan, and A. Nelson, *Progress in electroweak baryogenesis*, *Ann.Rev.Nucl.Part.Sci.* **43** (1993) 27–70, [`hep-ph/9302210`].

[52] V. Kuzmin, V. Rubakov, and M. Shaposhnikov, *On the Anomalous Electroweak Baryon Number Nonconservation in the Early Universe*, *Phys.Lett.* **B155** (1985) 36.

[53] L. Fromme, S. J. Huber, and M. Seniuch, *Baryogenesis in the two-Higgs doublet model*, *JHEP* **0611** (2006) 038, [`hep-ph/0605242`].

[54] D. V. Nanopoulos and S. Weinberg, *Mechanisms for Cosmological Baryon Production*, *Phys.Rev.* **D20** (1979) 2484.

[55] M. Fukugita and T. Yanagida, *Baryogenesis Without Grand Unification*, *Phys.Lett.* **B174** (1986) 45.

[56] C. S. Fong, E. Nardi, and A. Riotto, *Leptogenesis in the Universe*, *Adv.High Energy Phys.* **2012** (2012) 158303, [`arXiv:1301.3062`].

[57] M. Plumacher, *Baryogenesis and lepton number violation*, *Z.Phys.* **C74** (1997) 549–559, [`hep-ph/9604229`].

[58] S. Davidson and A. Ibarra, *A Lower bound on the right-handed neutrino mass from leptogenesis*, *Phys.Lett.* **B535** (2002) 25–32, [`hep-ph/0202239`].

[59] D. Buttazzo, G. Degrassi, P. P. Giardino, G. F. Giudice, F. Sala, et al., *Investigating the near-criticality of the Higgs boson*, *JHEP* **1312** (2013) 089, [`arXiv:1307.3536`].

[60] J. R. Espinosa, G. F. Giudice, E. Morgante, A. Riotto, L. Senatore, A. Strumia, and N. Tetradis, *The cosmological Higgstory of the vacuum instability*, *JHEP* **09** (2015) 174, [`arXiv:1505.04825`].

[61] J. Kearney, H. Yoo, and K. M. Zurek, *Is a Higgs Vacuum Instability Fatal for High-Scale Inflation?*, *Phys. Rev.* **D91** (2015), no. 12 123537, [`arXiv:1503.05193`].

[62] A. Shkerin and S. Sibiryakov, *On stability of electroweak vacuum during inflation*, *Phys.Lett.* **B746** (2015) 257–260, [`arXiv:1503.02586`].

[63] L. Susskind, *Dynamics of Spontaneous Symmetry Breaking in the Weinberg-Salam Theory*, Phys.Rev. **D20** (1979) 2619–2625.

[64] G. 't Hooft, *Naturalness, chiral symmetry, and spontaneous chiral symmetry breaking*, NATO Sci.Ser.B **59** (1980) 135.

[65] A. de Gouvea, D. Hernandez, and T. M. P. Tait, *Criteria for Natural Hierarchies*, Phys. Rev. **D89** (2014), no. 11 115005, [`arXiv:1402.2658`].

[66] G. F. Giudice, *Naturalness after LHC8*, PoS **EPS-HEP2013** (2013) 163, [`arXiv:1307.7879`].

[67] S. P. Martin, *A Supersymmetry primer*, `hep-ph/9709356`.

[68] I. Melzer-Pellmann and P. Pralavorio, *Lessons for SUSY from the LHC after the first run*, Eur.Phys.J. **C74** (2014) 2801, [`arXiv:1404.7191`].

[69] N. Craig, *The State of Supersymmetry after Run I of the LHC*, `arXiv:1309.0528`.

[70] S. Weinberg, *Implications of Dynamical Symmetry Breaking*, Phys.Rev. **D13** (1976) 974–996.

[71] K. Agashe, R. Contino, and A. Pomarol, *The Minimal composite Higgs model*, Nucl.Phys. **B719** (2005) 165–187, [`hep-ph/0412089`].

[72] E. K. Akhmedov, V. Rubakov, and A. Y. Smirnov, *Baryogenesis via neutrino oscillations*, Phys.Rev.Lett. **81** (1998) 1359–1362, [`hep-ph/9803255`].

[73] A. Dymarsky, Z. Komargodski, A. Schwimmer, and S. Theisen, *On Scale and Conformal Invariance in Four Dimensions*, `arXiv:1309.2921`.

[74] K. A. Meissner and H. Nicolai, *Conformal Symmetry and the Standard Model*, Phys.Lett. **B648** (2007) 312–317, [`hep-th/0612165`].

[75] W. A. Bardeen, *On naturalness in the standard model*, .

[76] G. Marques Tavares, M. Schmaltz, and W. Skiba, *Higgs mass naturalness and scale invariance in the UV*, Phys. Rev. **D89** (2014), no. 1 015009, [arXiv:1308.0025].

[77] S. Abel and A. Mariotti, *Novel Higgs Potentials from Gauge Mediation of Exact Scale Breaking*, Phys. Rev. **D89** (2014), no. 12 125018, [arXiv:1312.5335].

[78] A. Gorsky, A. Mironov, A. Morozov, and T. N. Tomaras, *Is the Standard Model saved asymptotically by conformal symmetry?*, J. Exp. Theor. Phys. **120** (2015), no. 3 344–353, [arXiv:1409.0492]. [Zh. Eksp. Teor. Fiz.147,399(2015)].

[79] S. R. Coleman and E. J. Weinberg, *Radiative Corrections as the Origin of Spontaneous Symmetry Breaking*, Phys.Rev. **D7** (1973) 1888–1910.

[80] E. Gildener and S. Weinberg, *Symmetry Breaking and Scalar Bosons*, Phys.Rev. **D13** (1976) 3333.

[81] K. Allison, C. T. Hill, and G. G. Ross, *Ultra-weak sector, Higgs boson mass, and the dilaton*, Phys. Lett. **B738** (2014) 191–195, [arXiv:1404.6268].

[82] C. Englert, J. Jaeckel, V. V. Khoze, and M. Spannowsky, *Emergence of the Electroweak Scale through the Higgs Portal*, JHEP **1304** (2013) 060, [arXiv:1301.4224].

[83] R. Hempfling, *The Next-to-minimal Coleman-Weinberg model*, Phys.Lett. **B379** (1996) 153–158, [hep-ph/9604278].

[84] M. Quiros, *Finite temperature field theory and phase transitions*, hep-ph/9901312.

[85] J. Kubo, K. S. Lim, and M. Lindner, *Gamma-ray Line from Nambu-Goldstone Dark Matter in a Scale Invariant Extension of the Standard Model*, JHEP **1409** (2014) 016, [arXiv:1405.1052].

[86] Y. Ametani, M. Aoki, H. Goto, and J. Kubo, *Nambu-Goldstone Dark Matter in a Scale Invariant Bright Hidden Sector*, Phys.Rev. **D91** (2015), no. 11 115007, [`arXiv:1505.00128`].

[87] C. D. Carone and R. Ramos, *Dark chiral symmetry breaking and the origin of the electroweak scale*, Phys.Lett. **B746** (2015) 424–429, [`arXiv:1505.04448`].

[88] M. Heikinheimo, A. Racioppi, M. Raidal, C. Spethmann, and K. Tuominen, *Physical Naturalness and Dynamical Breaking of Classical Scale Invariance*, Mod. Phys. Lett. **A29** (2014) 1450077, [`arXiv:1304.7006`].

[89] O. Antipin, M. Redi, and A. Strumia, *Dynamical generation of the weak and Dark Matter scales from strong interactions*, JHEP **1501** (2015) 157, [`arXiv:1410.1817`].

[90] M. Heikinheimo and C. Spethmann, *Galactic Centre GeV Photons from Dark Technicolor*, JHEP **1412** (2014) 084, [`arXiv:1410.4842`].

[91] C. T. Hill, *Is the Higgs Boson Associated with Coleman-Weinberg Dynamical Symmetry Breaking?*, Phys. Rev. **D89** (2014), no. 7 073003, [`arXiv:1401.4185`].

[92] E. Gabrielli, M. Heikinheimo, K. Kannike, A. Racioppi, M. Raidal, and C. Spethmann, *Towards Completing the Standard Model: Vacuum Stability, EWSB and Dark Matter*, Phys. Rev. **D89** (2014), no. 1 015017, [`arXiv:1309.6632`].

[93] R. Foot, A. Kobakhidze, K. McDonald, and R. Volkas, *Neutrino mass in radiatively-broken scale-invariant models*, Phys.Rev. **D76** (2007) 075014, [`arXiv:0706.1829`].

[94] R. Foot, A. Kobakhidze, K. L. McDonald, and R. R. Volkas, *A Solution to the hierarchy problem from an almost decoupled hidden sector within a classically scale invariant theory*, Phys.Rev. **D77** (2008) 035006, [`arXiv:0709.2750`].

[95] J. Guo and Z. Kang, *Higgs Naturalness and Dark Matter Stability by Scale Invariance, Nucl. Phys.* **B898** (2015) 415–430, [arXiv:1401.5609].

[96] H. Davoudiasl and I. M. Lewis, *Right-Handed Neutrinos as the Origin of the Electroweak Scale, Phys. Rev.* **D90** (2014), no. 3 033003, [arXiv:1404.6260].

[97] C. Tamarit, *Higgs vacua with potential barriers, Phys.Rev.* **D90** (2014), no. 5 055024, [arXiv:1404.7673].

[98] A. Farzinnia and J. Ren, *Higgs Partner Searches and Dark Matter Phenomenology in a Classically Scale Invariant Higgs Boson Sector, Phys. Rev.* **D90** (2014), no. 1 015019, [arXiv:1405.0498].

[99] K. Kannike, A. Racioppi, and M. Raidal, *Embedding inflation into the Standard Model - more evidence for classical scale invariance, JHEP* **06** (2014) 154, [arXiv:1405.3987].

[100] M. Lindner, S. Schmidt, and J. Smirnov, *Neutrino Masses and Conformal Electro-Weak Symmetry Breaking, JHEP* **10** (2014) 177, [arXiv:1405.6204].

[101] P. Humbert, M. Lindner, and J. Smirnov, *The Inverse Seesaw in Conformal Electro-Weak Symmetry Breaking and Phenomenological Consequences, JHEP* **1506** (2015) 035, [arXiv:1503.03066].

[102] A. Farzinnia, H.-J. He, and J. Ren, *Natural Electroweak Symmetry Breaking from Scale Invariant Higgs Mechanism, Phys. Lett.* **B727** (2013) 141–150, [arXiv:1308.0295].

[103] Z. Kang, *FImP Miracle of Sterile Neutrino Dark Matter by Scale Invariance,* arXiv:1411.2773.

[104] K. Allison, C. T. Hill, and G. G. Ross, *An ultra-weak sector, the strong CP problem and the pseudo-Goldstone dilaton, Nucl.Phys.* **B891** (2015) 613–626, [arXiv:1409.4029].

[105] D. A. Demir, M. Frank, and B. Korutlu, *Dark Matter from Conformal Sectors, Phys. Lett.* **B728** (2014) 393–399, [arXiv:1308.1203].

[106] M. B. Einhorn and D. R. T. Jones, *Naturalness and Dimensional Transmutation in Classically Scale-Invariant Gravity*, JHEP **1503** (2015) 047, [`arXiv:1410.8513`].

[107] R. Foot, A. Kobakhidze, and R. R. Volkas, *Stable mass hierarchies and dark matter from hidden sectors in the scale-invariant standard model*, Phys.Rev. **D82** (2010) 035005, [`arXiv:1006.0131`].

[108] K. Ishiwata, *Dark Matter in Classically Scale-Invariant Two Singlets Standard Model*, Phys.Lett. **B710** (2012) 134–138, [`arXiv:1112.2696`].

[109] S. Iso and Y. Orikasa, *TeV Scale B-L model with a flat Higgs potential at the Planck scale - in view of the hierarchy problem -*, PTEP **2013** (2013) 023B08, [`arXiv:1210.2848`].

[110] S. Iso, N. Okada, and Y. Orikasa, *Classically conformal B^- L extended Standard Model*, Phys.Lett. **B676** (2009) 81–87, [`arXiv:0902.4050`].

[111] T. Hambye and A. Strumia, *Dynamical generation of the weak and Dark Matter scale*, Phys.Rev. **D88** (2013) 055022, [`arXiv:1306.2329`].

[112] C. D. Carone and R. Ramos, *Classical scale-invariance, the electroweak scale and vector dark matter*, Phys. Rev. **D88** (2013) 055020, [`arXiv:1307.8428`].

[113] W. Altmannshofer, W. A. Bardeen, M. Bauer, M. Carena, and J. D. Lykken, *Light Dark Matter, Naturalness, and the Radiative Origin of the Electroweak Scale*, JHEP **01** (2015) 032, [`arXiv:1408.3429`].

[114] H. Okada and Y. Orikasa, *Classically Conformal Radiative Neutrino Model with Gauged B-L Symmetry*, `arXiv:1412.3616`.

[115] K. Kawana, *Criticality and Inflation of the Gauged B-L Model*, `arXiv:1501.04482`.

[116] S. Oda, N. Okada, and D.-s. Takahashi, *Classically conformal U(1)' extended standard model and Higgs vacuum stability*, Phys. Rev. **D92** (2015), no. 1 015026, [`arXiv:1504.06291`].

[117] S. Iso, N. Okada, and Y. Orikasa, *The minimal B-L model naturally realized at TeV scale*, *Phys.Rev.* **D80** (2009) 115007, [`arXiv:0909.0128`].

[118] M. Hashimoto, S. Iso, and Y. Orikasa, *Radiative symmetry breaking from flat potential in various U(1) models*, *Phys.Rev.* **D89** (2014), no. 5 056010, [`arXiv:1401.5944`].

[119] S. Iso, N. Okada, and Y. Orikasa, *Resonant Leptogenesis in the Minimal B-L Extended Standard Model at TeV*, *Phys.Rev.* **D83** (2011) 093011, [`arXiv:1011.4769`].

[120] I. Oda, *Classically Scale-invariant B-L Model and Dilaton Gravity*, *Phys.Rev.* **D87** (2013) 065025, [`arXiv:1301.2709`].

[121] V. V. Khoze, *Inflation and Dark Matter in the Higgs Portal of Classically Scale Invariant Standard Model*, *JHEP* **1311** (2013) 215, [`arXiv:1308.6338`].

[122] S. Benic and B. Radovcic, *Electroweak breaking and Dark Matter from the common scale*, *Phys.Lett.* **B732** (2014) 91–94, [`arXiv:1401.8183`].

[123] S. Benic and B. Radovcic, *Majorana dark matter in a classically scale invariant model*, *JHEP* **01** (2015) 143, [`arXiv:1409.5776`].

[124] P. H. Chankowski, A. Lewandowski, K. A. Meissner, and H. Nicolai, *Softly broken conformal symmetry and the stability of the electroweak scale*, *Mod. Phys. Lett.* **A30** (2015), no. 02 1550006, [`arXiv:1404.0548`].

[125] K. Kannike, G. Htsi, L. Pizza, A. Racioppi, M. Raidal, et al., *Dynamically Induced Planck Scale and Inflation*, *JHEP* **1505** (2015) 065, [`arXiv:1502.01334`].

[126] A. Salvio and A. Strumia, *Agravity*, *JHEP* **06** (2014) 080, [`arXiv:1403.4226`].

[127] B. Patt and F. Wilczek, *Higgs-field portal into hidden sectors*, `hep-ph/0605188`.

[128] C. Englert, T. Plehn, D. Zerwas, and P. M. Zerwas, *Exploring the Higgs portal*, *Phys.Lett.* **B703** (2011) 298–305, [arXiv:1106.3097].

[129] A. Falkowski, C. Gross, and O. Lebedev, *A second Higgs from the Higgs portal*, *JHEP* **1505** (2015) 057, [arXiv:1502.01361].

[130] N. Manton, *Topology in the Weinberg-Salam Theory*, *Phys.Rev.* **D28** (1983) 2019.

[131] S. Davidson, E. Nardi, and Y. Nir, *Leptogenesis*, *Phys.Rept.* **466** (2008) 105–177, [arXiv:0802.2962].

[132] T. Asaka and M. Shaposhnikov, *The nuMSM, dark matter and baryon asymmetry of the universe*, *Phys.Lett.* **B620** (2005) 17–26, [hep-ph/0505013].

[133] M. Drewes and B. Garbrecht, *Leptogenesis from a GeV Seesaw without Mass Degeneracy*, *JHEP* **1303** (2013) 096, [arXiv:1206.5537].

[134] R. N. Mohapatra and R. Marshak, *Local B-L Symmetry of Electroweak Interactions, Majorana Neutrinos and Neutron Oscillations*, *Phys.Rev.Lett.* **44** (1980) 1316–1319.

[135] L. Basso, A. Belyaev, S. Moretti, and C. H. Shepherd-Themistocleous, *Phenomenology of the minimal B-L extension of the Standard model: Z' and neutrinos*, *Phys.Rev.* **D80** (2009) 055030, [arXiv:0812.4313].

[136] R. Barbieri, P. Creminelli, A. Strumia, and N. Tetradis, *Baryogenesis through leptogenesis*, *Nucl.Phys.* **B575** (2000) 61–77, [hep-ph/9911315].

[137] A. Pilaftsis and T. E. Underwood, *Resonant leptogenesis*, *Nucl.Phys.* **B692** (2004) 303–345, [hep-ph/0309342].

[138] G. Sigl and G. Raffelt, *General kinetic description of relativistic mixed neutrinos*, *Nucl.Phys.* **B406** (1993) 423–451.

[139] D. Besak and D. Bodeker, *Thermal production of ultrarelativistic right-handed neutrinos: Complete leading-order results*, *JCAP* **1203** (2012) 029, [`arXiv:1202.1288`].

[140] J. S. Schwinger, *Brownian motion of a quantum oscillator*, *J.Math.Phys.* **2** (1961) 407–432.

[141] L. Keldysh, *Diagram technique for nonequilibrium processes*, *Zh.Eksp.Teor.Fiz.* **47** (1964) 1515–1527.

[142] B. Garbrecht and M. Herranen, *Effective Theory of Resonant Leptogenesis in the Closed-Time-Path Approach*, *Nucl.Phys.* **B861** (2012) 17–52, [`arXiv:1112.5954`].

[143] M. Garny, A. Kartavtsev, and A. Hohenegger, *Leptogenesis from first principles in the resonant regime*, *Annals Phys.* **328** (2013) 26–63, [`arXiv:1112.6428`].

[144] J. Casas and A. Ibarra, *Oscillating neutrinos and muon -¿ e, gamma*, *Nucl.Phys.* **B618** (2001) 171–204, [`hep-ph/0103065`].

[145] M. Drewes, *The Phenomenology of Right Handed Neutrinos*, *Int.J.Mod.Phys.* **E22** (2013) 1330019, [`arXiv:1303.6912`].

[146] A. Boyarsky, D. Iakubovskyi, and O. Ruchayskiy, *Next decade of sterile neutrino studies*, *Phys.Dark Univ.* **1** (2012) 136–154, [`arXiv:1306.4954`].

[147] O. Lebedev, *On Stability of the Electroweak Vacuum and the Higgs Portal*, *Eur.Phys.J.* **C72** (2012) 2058, [`arXiv:1203.0156`].

[148] J. Elias-Miro, J. R. Espinosa, G. F. Giudice, H. M. Lee, and A. Strumia, *Stabilization of the Electroweak Vacuum by a Scalar Threshold Effect*, *JHEP* **1206** (2012) 031, [`arXiv:1203.0237`].

[149] L. Basso, S. Moretti, and G. M. Pruna, *A Renormalisation Group Equation Study of the Scalar Sector of the Minimal B-L Extension of the Standard Model*, *Phys.Rev.* **D82** (2010) 055018, [`arXiv:1004.3039`].

[150] G. Degrassi, S. Di Vita, J. Elias-Miro, J. R. Espinosa, G. F. Giudice, et al., *Higgs mass and vacuum stability in the Standard Model at NNLO, JHEP* **1208** (2012) 098, [arXiv:1205.6497].

[151] M. Sher, *Electroweak Higgs Potentials and Vacuum Stability, Phys.Rept.* **179** (1989) 273–418.

[152] M. Lindner, *Implications of Triviality for the Standard Model, Z.Phys.* **C31** (1986) 295.

[153] S. A. Abel, C.-S. Chu, J. Jaeckel, and V. V. Khoze, *SUSY breaking by a metastable ground state: Why the early universe preferred the non-supersymmetric vacuum, JHEP* **0701** (2007) 089, [hep-th/0610334].

[154] M. Gonderinger, Y. Li, H. Patel, and M. J. Ramsey-Musolf, *Vacuum Stability, Perturbativity, and Scalar Singlet Dark Matter, JHEP* **1001** (2010) 053, [arXiv:0910.3167].

[155] O. Lebedev and H. M. Lee, *Higgs Portal Inflation, Eur.Phys.J.* **C71** (2011) 1821, [arXiv:1105.2284].

[156] **ATLAS** Collaboration, G. Aad et al., *A particle consistent with the Higgs Boson observed with the ATLAS Detector at the Large Hadron Collider, Science* **338** (2012) 1576–1582.

[157] **CMS** Collaboration, S. Chatrchyan et al., *Measurement of the properties of a Higgs boson in the four-lepton final state, Phys.Rev.* **D89** (2014), no. 9 092007, [arXiv:1312.5353].

[158] **CMS** Collaboration, S. Chatrchyan et al., *Search for a standard-model-like Higgs boson with a mass in the range 145 to 1000 GeV at the LHC, Eur.Phys.J.* **C73** (2013) 2469, [arXiv:1304.0213].

[159] **ATLAS** Collaboration, *Search for high-mass dilepton resonances in 20 fb^{-1} of pp collisions at $\sqrt{s} = 8$ TeV with the ATLAS experiment,* .

[160] **CMS** Collaboration, C. Collaboration, *Search for Resonances in the Dilepton Mass Distribution in pp Collisions at sqrt(s) = 8 TeV*, .

[161] T. Hambye, *Hidden vector dark matter*, *JHEP* **0901** (2009) 028, [`arXiv:0811.0172`].

[162] T. Hambye and M. H. Tytgat, *Confined hidden vector dark matter*, *Phys.Lett.* **B683** (2010) 39–41, [`arXiv:0907.1007`].

[163] C. Arina, T. Hambye, A. Ibarra, and C. Weniger, *Intense Gamma-Ray Lines from Hidden Vector Dark Matter Decay*, *JCAP* **1003** (2010) 024, [`arXiv:0912.4496`].

[164] J. Evslin and S. B. Gudnason, *Dwarf Galaxy Sized Monopoles as Dark Matter?*, `arXiv:1202.0560`.

[165] J. McDonald, *Gauge singlet scalars as cold dark matter*, *Phys.Rev.* **D50** (1994) 3637–3649, [`hep-ph/0702143`].

[166] C. Burgess, M. Pospelov, and T. ter Veldhuis, *The Minimal model of nonbaryonic dark matter: A Singlet scalar*, *Nucl.Phys.* **B619** (2001) 709–728, [`hep-ph/0011335`].

[167] Y. Mambrini, *Higgs searches and singlet scalar dark matter: Combined constraints from XENON 100 and the LHC*, *Phys.Rev.* **D84** (2011) 115017, [`arXiv:1108.0671`].

[168] A. Djouadi, O. Lebedev, Y. Mambrini, and J. Quevillon, *Implications of LHC searches for Higgs–portal dark matter*, *Phys.Lett.* **B709** (2012) 65–69, [`arXiv:1112.3299`].

[169] I. Low, P. Schwaller, G. Shaughnessy, and C. E. Wagner, *The dark side of the Higgs boson*, *Phys.Rev.* **D85** (2012) 015009, [`arXiv:1110.4405`].

[170] K. Cheung, Y.-L. S. Tsai, P.-Y. Tseng, T.-C. Yuan, and A. Zee, *Global Study of the Simplest Scalar Phantom Dark Matter Model*, *JCAP* **1210** (2012) 042, [`arXiv:1207.4930`].

[171] P. Gondolo and G. Gelmini, *Cosmic abundances of stable particles: Improved analysis, Nucl.Phys.* **B360** (1991) 145–179.

[172] F. D'Eramo and J. Thaler, *Semi-annihilation of Dark Matter, JHEP* **1006** (2010) 109, [arXiv:1003.5912].

[173] G. Belanger, K. Kannike, A. Pukhov, and M. Raidal, *Impact of semi-annihilations on dark matter phenomenology - an example of Z_N symmetric scalar dark matter, JCAP* **1204** (2012) 010, [arXiv:1202.2962].

[174] **LUX** Collaboration, D. Akerib et al., *First results from the LUX dark matter experiment at the Sanford Underground Research Facility, Phys.Rev.Lett.* **112** (2014) 091303, [arXiv:1310.8214].

[175] H.-Y. Cheng and C.-W. Chiang, *Revisiting Scalar and Pseudoscalar Couplings with Nucleons, JHEP* **1207** (2012) 009, [arXiv:1202.1292].

[176] G. 't Hooft, *Magnetic Monopoles in Unified Gauge Theories, Nucl.Phys.* **B79** (1974) 276–284.

[177] A. M. Polyakov, *Particle Spectrum in the Quantum Field Theory, JETP Lett.* **20** (1974) 194–195.

[178] H. Murayama and J. Shu, *Topological Dark Matter, Phys.Lett.* **B686** (2010) 162–165, [arXiv:0905.1720].

[179] S. Baek, P. Ko, and W.-I. Park, *Hidden sector monopole, vector dark matter and dark radiation with Higgs portal*, arXiv:1311.1035.

[180] P. A. Dirac, *Quantized Singularities in the Electromagnetic Field, Proc.Roy.Soc.Lond.* **A133** (1931) 60–72.

[181] E. Bogomolny, *Stability of Classical Solutions, Sov.J.Nucl.Phys.* **24** (1976) 449.

[182] J. Preskill, *MAGNETIC MONOPOLES, Ann.Rev.Nucl.Part.Sci.* **34** (1984) 461–530.

[183] C. G. Sanchez and B. Holdom, *Monopoles, strings and dark matter*, *Phys.Rev.* **D83** (2011) 123524, [`arXiv:1103.1632`].

[184] W. Fischler and W. Tangarife Garcia, *Hierarchies of Susy Splittings and Invisible Photinos as Dark Matter*, *JHEP* **1101** (2011) 025, [`arXiv:1011.0099`].

[185] T. Kibble, *Topology of Cosmic Domains and Strings*, *J.Phys.* **A9** (1976) 1387–1398.

[186] W. Zurek, *Cosmological Experiments in Superfluid Helium?*, *Nature* **317** (1985) 505–508.

[187] G. W. Anderson and L. J. Hall, *The Electroweak phase transition and baryogenesis*, *Phys.Rev.* **D45** (1992) 2685–2698.

[188] M. Dine, R. G. Leigh, P. Y. Huet, A. D. Linde, and D. A. Linde, *Towards the theory of the electroweak phase transition*, *Phys.Rev.* **D46** (1992) 550–571, [`hep-ph/9203203`].

[189] J. L. Feng, H. Tu, and H.-B. Yu, *Thermal Relics in Hidden Sectors*, *JCAP* **0810** (2008) 043, [`arXiv:0808.2318`].

[190] C. Brust, D. E. Kaplan, and M. T. Walters, *New Light Species and the CMB*, *JHEP* **1312** (2013) 058, [`arXiv:1303.5379`].

[191] M. J. Strassler and K. M. Zurek, *Echoes of a hidden valley at hadron colliders*, *Phys.Lett.* **B651** (2007) 374–379, [`hep-ph/0604261`].

[192] M. Pospelov, A. Ritz, and M. B. Voloshin, *Secluded WIMP Dark Matter*, *Phys.Lett.* **B662** (2008) 53–61, [`arXiv:0711.4866`].

[193] N. Arkani-Hamed, D. P. Finkbeiner, T. R. Slatyer, and N. Weiner, *A Theory of Dark Matter*, *Phys.Rev.* **D79** (2009) 015014, [`arXiv:0810.0713`].

[194] A. Sommerfeld, *Uber die beugung und bremsung der elektronen*, *Annalen der Physik* **403** (1931), no. 3 257–330.

[195] J. Hisano, S. Matsumoto, and M. M. Nojiri, *Unitarity and higher order corrections in neutralino dark matter annihilation into two photons*, *Phys.Rev.* **D67** (2003) 075014, [`hep-ph/0212022`].

[196] J. Hisano, S. Matsumoto, and M. M. Nojiri, *Explosive dark matter annihilation*, *Phys.Rev.Lett.* **92** (2004) 031303, [`hep-ph/0307216`].

[197] J. Hisano, S. Matsumoto, M. M. Nojiri, and O. Saito, *Non-perturbative effect on dark matter annihilation and gamma ray signature from galactic center*, *Phys.Rev.* **D71** (2005) 063528, [`hep-ph/0412403`].

[198] M. Cirelli, A. Strumia, and M. Tamburini, *Cosmology and Astrophysics of Minimal Dark Matter*, *Nucl.Phys.* **B787** (2007) 152–175, [`arXiv:0706.4071`].

[199] A. H. Guth and E. J. Weinberg, *Could the Universe Have Recovered from a Slow First Order Phase Transition?*, *Nucl.Phys.* **B212** (1983) 321.

[200] V. Ruutu, V. Eltsov, M. Krusius, Y. Makhlin, B. Placais, et al., *Defect Formation in Quench-Cooled Superfluid Phase Transition*, *Phys.Rev.Lett.* **80** (1998) 1465–1468.

[201] M. J. Bowick, L. Chandar, E. A. Schiff, and A. M. Srivastava, *The Cosmological Kibble mechanism in the laboratory: String formation in liquid crystals*, *Science* **263** (1994) 943–945, [`hep-ph/9208233`].

[202] Y. Zeldovich and M. Y. Khlopov, *On the Concentration of Relic Magnetic Monopoles in the Universe*, *Phys.Lett.* **B79** (1978) 239–241.

[203] J. Preskill, *Cosmological Production of Superheavy Magnetic Monopoles*, *Phys.Rev.Lett.* **43** (1979) 1365.

[204] A. Vilenkin, *COSMIC STRINGS AND OTHER TOPOLOGICAL DEFECTS*, .

[205] D. N. Spergel and P. J. Steinhardt, *Observational evidence for selfinteracting cold dark matter*, *Phys.Rev.Lett.* **84** (2000) 3760–3763, [`astro-ph/9909386`].

[206] J. F. Navarro, C. S. Frenk, and S. D. White, *A Universal density profile from hierarchical clustering*, Astrophys.J. **490** (1997) 493–508, [astro-ph/9611107].

[207] S.-H. Oh, W. J. G. de Blok, E. Brinks, F. Walter, and R. C. Kennicutt, Jr, *Dark and luminous matter in THINGS dwarf galaxies*, Astron. J. **141** (2011) 193, [arXiv:1011.0899].

[208] B. Moore, T. R. Quinn, F. Governato, J. Stadel, and G. Lake, *Cold collapse and the core catastrophe*, Mon.Not.Roy.Astron.Soc. **310** (1999) 1147–1152, [astro-ph/9903164].

[209] M. Boylan-Kolchin, J. S. Bullock, and M. Kaplinghat, *Too big to fail? The puzzling darkness of massive Milky Way subhaloes*, Mon. Not. Roy. Astron. Soc. **415** (2011) L40, [arXiv:1103.0007].

[210] M. Boylan-Kolchin, J. S. Bullock, and M. Kaplinghat, *The Milky Way's bright satellites as an apparent failure of LCDM*, Mon. Not. Roy. Astron. Soc. **422** (2012) 1203–1218, [arXiv:1111.2048].

[211] M. R. Buckley and P. J. Fox, *Dark Matter Self-Interactions and Light Force Carriers*, Phys.Rev. **D81** (2010) 083522, [arXiv:0911.3898].

[212] A. Loeb and N. Weiner, *Cores in Dwarf Galaxies from Dark Matter with a Yukawa Potential*, Phys.Rev.Lett. **106** (2011) 171302, [arXiv:1011.6374].

[213] M. Vogelsberger, J. Zavala, and A. Loeb, *Subhaloes in Self-Interacting Galactic Dark Matter Haloes*, Mon.Not.Roy.Astron.Soc. **423** (2012) 3740, [arXiv:1201.5892].

[214] J. Zavala, M. Vogelsberger, and M. G. Walker, *Constraining Self-Interacting Dark Matter with the Milky Way's dwarf spheroidals*, Monthly Notices of the Royal Astronomical Society: Letters **431** (2013) L20–L24, [arXiv:1211.6426].

[215] S. Tulin, H.-B. Yu, and K. M. Zurek, *Beyond Collisionless Dark Matter: Particle Physics Dynamics for Dark Matter Halo Structure*, Phys.Rev. **D87** (2013), no. 11 115007, [arXiv:1302.3898].

[216] M. R. Buckley, J. Zavala, F.-Y. Cyr-Racine, K. Sigurdson, and M. Vogelsberger, *Scattering, Damping, and Acoustic Oscillations: Simulating the Structure of Dark Matter Halos with Relativistic Force Carriers*, Phys.Rev. **D90** (2014), no. 4 043524, [arXiv:1405.2075].

[217] J. L. Feng, M. Kaplinghat, H. Tu, and H.-B. Yu, *Hidden Charged Dark Matter*, JCAP **0907** (2009) 004, [arXiv:0905.3039].

[218] D. E. Kaplan, G. Z. Krnjaic, K. R. Rehermann, and C. M. Wells, *Atomic Dark Matter*, JCAP **1005** (2010) 021, [arXiv:0909.0753].

[219] S. A. Khrapak, A. V. Ivlev, G. E. Morfill, and S. K. Zhdanov, *Scattering in the attractive yukawa potential in the limit of strong interaction*, Phys. Rev. Lett. **90** (Jun, 2003) 225002.

[220] S. A. Khrapak, A. V. Ivlev, and G. E. Morfill, *Momentum transfer in complex plasmas*, Phys. Rev. E **70** (Nov, 2004) 056405.

[221] S. W. Randall, M. Markevitch, D. Clowe, A. H. Gonzalez, and M. Bradac, *Constraints on the Self-Interaction Cross-Section of Dark Matter from Numerical Simulations of the Merging Galaxy Cluster 1E 0657-56*, Astrophys.J. **679** (2008) 1173–1180, [arXiv:0704.0261].

[222] **CMS** Collaboration, V. Khachatryan et al., *Search for dark matter, extra dimensions, and unparticles in monojet events in proton-proton collisions at $\sqrt{s} = 8$ TeV*, arXiv:1408.3583.

[223] **CMS** Collaboration, V. Khachatryan et al., *Search for new phenomena in monophoton final states in proton-proton collisions at $\sqrt{s} = 8$ TeV*, arXiv:1410.8812.

[224] **ATLAS** Collaboration, G. Aad et al., *Search for new phenomena in final states with an energetic jet and large missing transverse momentum in pp collisions at $\sqrt{s} = 8$ TeV with the ATLAS detector*, `arXiv:1502.01518`.

[225] A. Birkedal, K. Matchev, and M. Perelstein, *Dark matter at colliders: A Model independent approach*, Phys.Rev. **D70** (2004) 077701, [`hep-ph/0403004`].

[226] J. Goodman, M. Ibe, A. Rajaraman, W. Shepherd, T. M. Tait, et al., *Constraints on Light Majorana dark Matter from Colliders*, Phys.Lett. **B695** (2011) 185–188, [`arXiv:1005.1286`].

[227] J. Goodman, M. Ibe, A. Rajaraman, W. Shepherd, T. M. Tait, et al., *Constraints on Dark Matter from Colliders*, Phys.Rev. **D82** (2010) 116010, [`arXiv:1008.1783`].

[228] P. J. Fox, R. Harnik, R. Primulando, and C.-T. Yu, *Taking a Razor to Dark Matter Parameter Space at the LHC*, Phys.Rev. **D86** (2012) 015010, [`arXiv:1203.1662`].

[229] J. Abdallah, A. Ashkenazi, A. Boveia, G. Busoni, A. De Simone, et al., *Simplified Models for Dark Matter and Missing Energy Searches at the LHC*, `arXiv:1409.2893`.

[230] S. Malik, C. McCabe, H. Araujo, A. Belyaev, C. Boehm, et al., *Interplay and Characterization of Dark Matter Searches at Colliders and in Direct Detection Experiments*, `arXiv:1409.4075`.

[231] D. Abercrombie, N. Akchurin, E. Akilli, J. Alcaraz Maestre, B. Allen, et al., *Dark Matter Benchmark Models for Early LHC Run-2 Searches: Report of the ATLAS/CMS Dark Matter Forum*, `arXiv:1507.00966`.

[232] U. Haisch, A. Hibbs, and E. Re, *Determining the structure of dark-matter couplings at the LHC*, Phys.Rev. **D89** (2014), no. 3 034009, [`arXiv:1311.7131`].

[233] T. Robens and T. Stefaniak, *Status of the Higgs Singlet Extension of the Standard Model after LHC Run 1*, Eur.Phys.J. **C75** (2015), no. 3 104, [arXiv:1501.02234].

[234] **CMS** Collaboration, V. Khachatryan et al., *Precise determination of the mass of the Higgs boson and tests of compatibility of its couplings with the standard model predictions using proton collisions at 7 and 8 TeV*, Eur. Phys. J. **C75** (2015), no. 5 212, [arXiv:1412.8662].

[235] D. Lpez-Val and T. Robens, *r and the W-boson mass in the singlet extension of the standard model*, Phys.Rev. **D90** (2014), no. 11 114018, [arXiv:1406.1043].

[236] M. Backovic, K. Kong, and M. McCaskey, *MadDM v.1.0: Computation of Dark Matter Relic Abundance Using MadGraph5*, Physics of the Dark Universe **5-6** (2014) 18–28, [arXiv:1308.4955].

[237] M. Backovic, K. Kong, A. Martini, O. Mattelaer, and G. Mohlabeng, *Direct Detection of Dark Matter with MadDM v.2.0*, arXiv:1505.04190.

[238] O. J. Eboli and D. Zeppenfeld, *Observing an invisible Higgs boson*, Phys.Lett. **B495** (2000) 147–154, [hep-ph/0009158].

[239] C. Bernaciak, T. Plehn, P. Schichtel, and J. Tattersall, *Spying an invisible Higgs boson*, Phys.Rev. **D91** (2015), no. 3 035024, [arXiv:1411.7699].

[240] M. Cacciari and G. P. Salam, *Dispelling the N^3 myth for the k_t jet-finder*, Phys.Lett. **B641** (2006) 57–61, [hep-ph/0512210].

[241] M. Cacciari, G. P. Salam, and G. Soyez, *FastJet User Manual*, Eur.Phys.J. **C72** (2012) 1896, [arXiv:1111.6097].

[242] U. Haisch, F. Kahlhoefer, and J. Unwin, *The impact of heavy-quark loops on LHC dark matter searches*, JHEP **1307** (2013) 125, [arXiv:1208.4605].

[243] J. Baglio, J. Bellm, F. Campanario, B. Feigl, J. Frank, et al., *Release Note - VBFNLO 2.7.0*, arXiv:1404.3940.

[244] K. Arnold, J. Bellm, G. Bozzi, M. Brieg, F. Campanario, et al., *VBFNLO: A Parton Level Monte Carlo for Processes with Electroweak Bosons – Manual for Version 2.5.0*, arXiv:1107.4038.

[245] K. Arnold, M. Bahr, G. Bozzi, F. Campanario, C. Englert, et al., *VBFNLO: A Parton level Monte Carlo for processes with electroweak bosons*, *Comput.Phys.Commun.* **180** (2009) 1661–1670, [arXiv:0811.4559].

[246] J. Alwall, M. Herquet, F. Maltoni, O. Mattelaer, and T. Stelzer, *MadGraph 5 : Going Beyond*, *JHEP* **1106** (2011) 128, [arXiv:1106.0522].

[247] J. Bellm, S. Gieseke, D. Grellscheid, A. Papaefstathiou, S. Platzer, et al., *Herwig++ 2.7 Release Note*, arXiv:1310.6877.

[248] Y. Bai, P. Draper, and J. Shelton, *Measuring the Invisible Higgs Width at the 7 and 8 TeV LHC*, *JHEP* **1207** (2012) 192, [arXiv:1112.4496].

[249] D. Ghosh, R. Godbole, M. Guchait, K. Mohan, and D. Sengupta, *Looking for an Invisible Higgs Signal at the LHC*, *Phys.Lett.* **B725** (2013) 344–351, [arXiv:1211.7015].

[250] T. Junk, *Confidence level computation for combining searches with small statistics*, *Nucl.Instrum.Meth.* **A434** (1999) 435–443, [hep-ex/9902006].

[251] A. L. Read, *Presentation of search results: The CL(s) technique*, *J.Phys.* **G28** (2002) 2693–2704.

[252] J. R. Andersen, M. Rauch, and M. Spannowsky, *Dark Sector spectroscopy at the ILC*, *Eur.Phys.J.* **C74** (2014) 2908, [arXiv:1308.4588].

[253] Z. Chacko, Y. Cui, and S. Hong, *Exploring a Dark Sector Through the Higgs Portal at a Lepton Collider*, *Phys.Lett.* **B732** (2014) 75–80, [arXiv:1311.3306].